BERGISCHE
UNIVERSITÄT
WUPPERTAL

From detectors to data: Thermal Characterization of CMS Outer Tracker modules and Measurement of the top quark mass using $t\bar{t}$+jet events

Dissertation

zur Erlangung des Doktorgrades an der Fakultät
für Mathematik und Naturwissenschaften
Fachbereich Physik
der Bergische Universität Wuppertal

vorgelegt von

Ana Ventura Barroso

aus

Hamburg, 2025

Eidesstattliche Versicherung / Declaration on oath

Hiermit versichere ich an Eides statt, dass ich die vorliegende Dissertationsschrift selbst verfasst und keine anderen als die angegebenen Hilfsmittel und Quellen benutzt habe. Die eingereichte schriftliche Fassung entspricht der auf dem elektronischen Speichermedium. Die Dissertation wurde in der vorgelegten oder einer ähnlichen Form nicht schon einmal in einem früheren Promotionsverfahren angenommen oder als ungenügend beurteilt.

I hereby declare, on oath, that I have written the present dissertation by my own and have not used any resources and aids other than those acknowledged. The written version submitted corresponds to the one stored electronically. The dissertation presented in this form, has not already been accepted in an earlier doctoral procedure or assessed as unsatisfactory.

Hamburg, February 18, 2025

Ana Ventura Barroso

Gutachter der Dissertation:	Prof. Dr. Katerina Lipka
	Dr. Paul Schütze
Zusammensetzung der Prüfungskommission:	Prof. Dr. Katerina Lipka
	Dr. Paul Schütze
	Prof. Dr. Wolfgang Wagner
	Prof. Dr. Dirk Lützenkirchen-Hecht
	Prof. Dr. Jana Günther

Per l'Arnau,
t'estimo i et trobo a faltar

Abstract

This thesis addresses key challenges in modern particle physics by contributing to three critical areas: the development of particle detectors, their calibration and the analysis of data collected in particle physics experiments. Contributions to these areas are presented in the context of the Compact Muon Solenoid (CMS) experiment at the Large Hadron Collider (LHC).

The first part of this work focuses on the development and characterization of a temperature test system (Burn-in) for silicon modules, essential components of the CMS Outer Tracker Upgrade, a central part of the preparation of CMS for the forthcoming High Luminosity LHC running. The Burn-in test involves subjecting the modules to thermal cycling to identify early failures and ensure long-term reliability. This system demonstrated a reliable performance for quality assurance and has been used to conduct thermal characterization measurements of Pixel-Strip modules. In addition, thermal measurements including dees and cooling structures have been performed.

In the second part of this thesis, the contribution to the CMS tracker alignment in the ongoing LHC run at a center of mass energy $\sqrt{s}$=13.6 TeV is presented. Alignment is a critical calibration process that ensures the high precision geometry required for accurate particle tracking. Special attention is given to the interplay between alignment and local pixel reconstruction.

The final part of the thesis presents a measurement of the top quark pole mass, using events where the top quark-antiquark pairs are produced in association with an energetic jet ($t\bar{t}$+jet). The proton-proton collision data at $\sqrt{s} = 13\,\text{TeV}$ are used, collected by the CMS and corresponding to the integrated luminosity of 138 fb^{-1}. This analysis employs machine learning-based techniques to reconstruct the $t\bar{t}$ kinematics. The top quark pole mass is extracted through comparison of the normalized differential cross section of $t\bar{t}$+jet production to the theoretical prediction in quantum chromodynamics at next-to-leading order. The result of this thesis improves the precision of the available CMS public result by a factor of 2 and is the most precise extraction of the top quark pole mass by using $t\bar{t}$+jet production, to date.

Zusammenfassung

Diese Arbeit befasst sich mit zentralen Herausforderungen der modernen Teilchenphysik und leistet Beiträge in drei kritischen Bereichen: der Entwicklung von Teilchendetektoren, deren Kalibrierung sowie der Analyse der in Teilchenphysikexperimenten gesammelten Daten. Diese Beiträge werden im Kontext des Compact Muon Solenoid (CMS) Experiments am Large Hadron Collider (LHC) präsentiert.

Der erste Teil der Arbeit behandelt die Entwicklung und Charakterisierung eines Temperatur-Testsystems (sog. Einbrenntest-Systems) für Siliziummodule. Diese Module sind ein zentraler Bestandteil des CMS Outer Tracker Upgrades, das zur Vorbereitung von CMS auf die LHC-Ära mit hoher Luminosität (HL-LHC) dient. Beim Einbrenntest werden die Module thermischen Zyklen unterzogen, um frühe Ausfälle zu identifizieren und die langfristige Zuverlässigkeit sicherzustellen. Das System hat sich als zuverlässig für die Qualitätssicherung erwiesen und wurde für thermische Charakterisierungsmessungen von Pixel-Strip (PS)-Modulen eingesetzt. Darüber hinaus wurden auch thermische Messungen an Dees und Kühlstrukturen durchgeführt.

Im zweiten Teil der Arbeit wird die Ausrichtung des CMS-Trackers untersucht, ein kritischer Kalibrierungsprozess, der die hochpräzise Geometrie sicherstellt, die für eine genaue Verfolgung der Teilchen erforderlich ist. Ein besonderer Fokus liegt auf dem Zusammenspiel zwischen der Ausrichtung und der Rekonstruktion lokaler Pixel.

Der letzte Teil der Dissertation präsentiert eine Messung der Polmasse des Top-Quarks, basierend auf Ereignissen, bei denen Top-Quark-Antiquark-Paare in Verbindung mit einem energiereichen Jet ($t\bar{t}$+jet) erzeugt werden. Die verwendeten Proton-Proton-Kollisionsdaten wurden bei einer Schwerpunktsenergie von $\sqrt{s} = 13$ TeV vom CMS-Experiment aufgezeichnet und entsprechen einer integrierten Luminosität von 138 fb^{-1}. In dieser Analyse werden maschinelle Lerntechniken eingesetzt, um die Kinematik der $t\bar{t}$ Paare zu rekonstruieren. Die Polmasse des Top-Quarks wird durch den Vergleich des normierten differentiellen Wirkungsquerschnitts der $t\bar{t}$+jet-Produktion mit der theoretischen Vorhersage der Quantenchromodynamik zu nächstführender Ordnung extrahiert. Das Ergebnis dieser Arbeit verbessert die Präzision des verfügbaren öffentlichen CMS-Ergebnisses um den Faktor 2 und stellt die bisher präziseste Bestimmung der Polemasse des Top-Quarks mittels $t\bar{t}$+jet-Produktion dar.

Contents

Introduction

High-energy particle physics seeks to understand fundamental processes through particle collisions, employing the Standard Model (SM) as its theoretical framework. Developed during the latter half of the twentieth century and the beginning of the twenty-first century, the SM successfully describes three of the four fundamental interactions and encompasses all observed elementary particles. However, it is not a complete description of nature, as it fails to address key questions regarding dark matter, the matter-antimatter asymmetry, and the hierarchy of neutrino masses, among others. The SM is viewed as the theory applicable to current experimental energy scales, yet it allows for the addition of new physical phenomena at higher energies.

In experimental particle physics, the search for such new phenomena is pursued through two main strategies: direct searches for new particles predicted by theoretical extensions to the SM, and rigorous tests of the SM itself through precise measurements of known processes. Both strategies rely on data collected in the high-energy particle collision experiments.

Since the first particle accelerators were built in the 1930s, collision energies have continuously increased, necessitating the construction of larger and more sophisticated machines. The Large Hadron Collider (LHC) at CERN, the largest and the most energetic particle accelerator to date, operates at a center-of-mass energy of 13 TeV, with experiments like the Compact Muon Solenoid (CMS) contributing to precision tests of the SM, including the discovery of the Higgs boson, playing a key role in the electroweak symmetry breaking in the SM.

For more accurate and detailed studies of the properties of the particles of the SM, including the Higgs boson, and to achieve higher sensitivity to new physics, the LHC will be upgraded into its High Luminosity (HL-LHC) phase in 2029. The HL-LHC is expected to increase the current instantaneous luminosity of the LHC by a factor of 5. The increased luminosity will pose challenges for the four main experiments at LHC, ATLAS, CMS, ALICE and LHCb, due to higher collision rates, intensified radiation environments, and increased data rates.

This thesis addresses the challenges associated with conducting high-energy physics experiments, organized into three principal sections.

To meet the challenges posed by the HL-LHC, the CMS experiment will undergo a so-called Phase-2 Upgrade, significantly enhancing performance of all the detector subsystems. This upgrade will feature an increased number of readout channels, improved granularity and spatial resolution, and an enhanced coverage in pseudo-rapidity. Additionally, the Outer Tracker will play a key role in mitigating pileup by contributing to the

CMS Level-1 Trigger through a novel on-module transverse momentum (p_T) discrimination method, which allows it to identify high-p_T particles in the strong magnetic field of the CMS detector. These modules have to be built, assembled and tested before being installed in CMS. This first main part primarily focuses on the construction of a setup to perform a quality test of the modules before installation in the detector, known as *Burn-in* test. This thesis focuses on the design and characterization of the test setup, as well as a characterization of the thermal and electrical properties of Pixel-Strip (PS) modules.

The second part is dedicated to a particular detector calibration, namely tracker alignment, in the ongoing data taking (so-called Run 3) of the LHC. The CMS silicon tracking system achieves high-precision tracking of charged particles, this requires accurate knowledge of the tracker geometry, which can shift due to changes in operating conditions and radiation damage. To maintain precision, continuous alignment correction is necessary.

The third part of this thesis utilizes the proton-proton collisions at the LHC at a center of mass energy of 13 TeV, collected by the CMS experiment in 2016-2018 (so called Run 2), aiming at the extraction of the mass of the top quark. The top quark is the most massive known fundamental particle and its mass plays a crucial role in many aspects of the SM. The relation of the masses of the top quark, Higgs boson and W boson is clearly predicted in the SM, however the values of these masses need to be extracted experimentally. High precision and clear theoretical interpretation of the measured top quark mass is necessary not only for stringent tests of the SM, but also to potentially unveil the hints to the SM extensions. This thesis presents the extraction of the top quark pole mass by using events where top quark-antiquark pairs are produced with an additional jet.

The thesis is organized as follows. In Chapter 1, the SM is introduced with the focus on the top quark production. The focus of Chapter 2 is the description of the LHC and the CMS detector. In Chapter 3, the semiconductor tracking detectors are introduced, together with the Phase-2 Outer Tracker Upgrade detailed description of the Pixel-Strip module. In Chapter 4, the construction and commissioning of the Burn-in setup at DESY is described and the characterization of Pixel-Strip modules assembled at DESY is presented. In Chapter 5, the temperature and noise measurements of the modules in conditions close to the operational ones is discussed. In Chapter 6, the methodology for track-based alignment is explained, encompassing the alignment algorithms and validation techniques employed in CMS. Chapter 7 focuses on the measurement of the differential cross section of the top quark-antiquark pairs produced in association with at least one additional jet. Using these measurements, the top quark pole mass is extracted. Finally, the findings of the different parts of the thesis are summarized in the Summary Chapter.

CHAPTER 1

Theoretical framework

Contents

The Standard Model (SM) of particle physics is a quantum field theory, describing the known fundamental particles and their interactions. The elementary particles are the fermions, the leptons and the quarks, and the gauge bosons, which mediate the forces. The SM encompasses strong, weak, and electromagnetic interactions. The strengths of these interactions and the masses of elementary particles are fundamental parameters of the SM. While the relations of these parameters are predicted by the model, their actual values at a certain energy scale have to be determined experimentally. The SM has been investigated, tested and accomplished over decades in particle scattering experiments, in particular in high-energy collider experiments. The facility at the frontier of collision energy, to date, is the Large Hadron Collider (LHC) at CERN, operating with proton or ion beams. This thesis utilizes the data collected by one of the general-purpose LHC experiments, Compact Muon Solenoid (CMS), collected in proton-proton (pp) collisions at the LHC.

The SM has been highly successful in explaining all observed phenomena of particle physics. Yet, this model is incomplete, as it does not account for gravitation, dark matter, or dark energy, suggesting the existence of phenomena beyond the Standard Model (BSM).

The direct searches for BSM at the LHC have not yet been successful, which hints to involvement of energy scales of new physics much beyond those reachable at the LHC. The indirect search for new physics, through e.g. precision measurements of the SM parameters, are very promising, since those might probe higher scales.

This thesis utilizes the LHC pp collision data, collected by the CMS experiment in 2016-2018, to extract the mass of the top quark, the most massive elementary particle. For this purpose, production of top quark-antiquark ($t\bar{t}$) pairs associated with hadronic jets is investigated.

In the following, the SM is introduced, together with the QCD factorization and the relevant models of top quark production.

1.1 The Standard Model of particle physics

The Standard Model follows the principles of quantum mechanics and special relativity, where particles are understood as excitations of quantum fields. The three primary forces in the SM: electromagnetic, weak and strong, are described by quantized fields. Gravitation, formulated in general relativity [1], remains the only known fundamental interaction not included in the SM.

The SM is governed by certain symmetries, leading to fundamental properties of the system that remain unchanged under certain transformations. These symmetries form the foundation for writing down the Lagrangian, L. The theory must respect these symmetries, which means the Lagrangian is constructed to be renormalizable [2] (meaning it can make finite, predictive calculations) while maintaining the symmetries. Noether's theorem [3] states that for every continuous symmetry in a physical system, there is a corresponding conserved quantity. This theorem is a cornerstone in constructing the SM because it links symmetries to conservation laws: Translational symmetry corresponds to the conservation of momentum, rotational symmetry corresponds to the conservation of angular momentum and gauge symmetries are related to the conservation of charges, such as electric charge in electromagnetism. The SM is based on three fundamental symmetry groups: SU(3), SU(2), and U(1). These groups represent different types of gauge symmetries, each associated with one of the fundamental forces of SM. The U(1) symmetry governs the electromagnetic interaction, described by Quantum Electrodynamics (QED) and corresponds to the conservation of the electric charge. The SU(2) gauge symmetry is associated with the weak interaction, which is responsible for processes such as e.g. β-decay. The weak interaction does not conserve parity, meaning it distinguishes between left-handed and right-handed particles. The SU(3) color symmetry group governs the strong interaction, which is responsible for binding quarks together to form hadrons such

as protons and neutrons. The theory of the strong force is Quantum Chromodynamics (QCD). The weak SU(2) and the color SU(3) are non-abelian theories, which imply self-interaction of the vector bosons, transmitting the field [4].

Elementary particles in the SM fall into two categories based on their spin: fermions (with half-integer spin), which include quarks and leptons, and bosons (with integer spin), which mediate forces. All fundamental particles and their interactions are illustrated in Figure 1.1

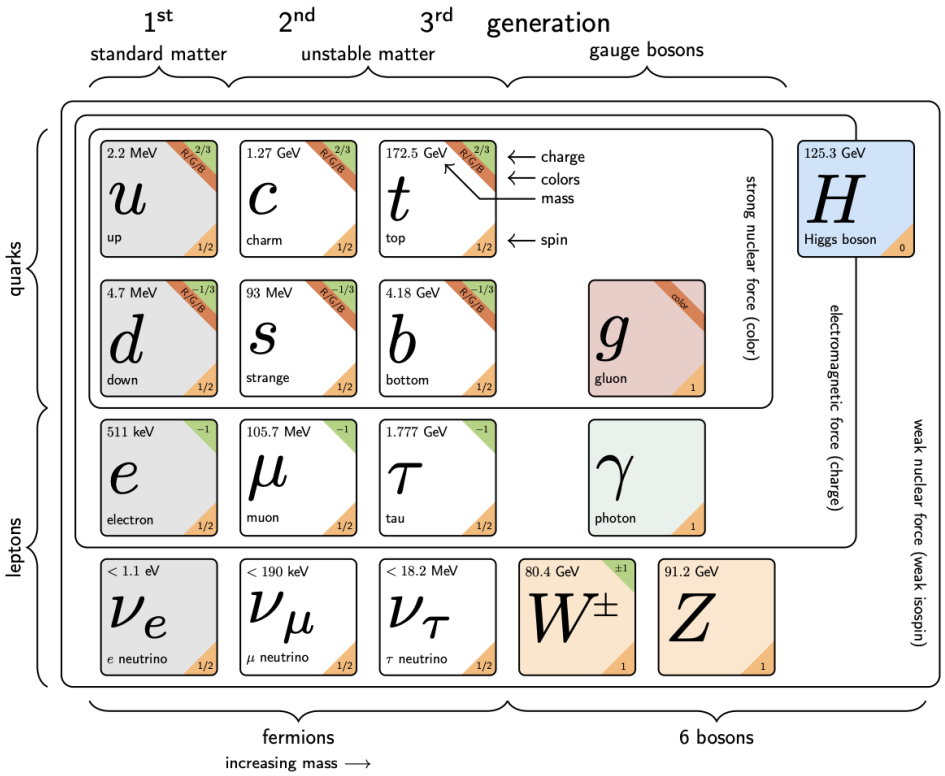

Figure 1.1: Particle content of the Standard Model, including measured mass values, electric charge, and spin quantum numbers for each particle. Figure taken from [5].

Quarks and leptons follow Fermi-Dirac statistics and represent the building blocks of matter. The quarks (u, d, c, s, t, b) participate in all fundamental interactions, while leptons (e, ν_e, μ, ν_μ, τ, ν_τ) do not participate in the strong interactions, and neutrinos are only subject to the weak interaction. Each fermion has a corresponding antiparticle with opposite quantum numbers. The six types (or flavors) of quarks and leptons are sorted into 3 generations (or families) according to their quantum properties. Although all those particles are believed to be elementary, their masses differ by about 12 orders of magnitude between the lightest ν_e and the most massive t quark. The mass of the

elementary particles is understood as a parameter of the Lagrangian of the Standard Model in the context of the Brout-Englert-Higgs mechanism [6, 7], which connects mass and the vacuum.

The Standard Model does not provide an explanation for the number of generations or for large differences in the particle masses. While no fundamental principle forbids a fourth generation, the experimental data, such as the decay rates of the Z boson and neutrino production measurements, have placed strong constraints on its possibility [8].

The fundamental interactions are mediated by the gauge bosons: the W and Z boson transmit the weak interaction, photons mediate the electromagnetic interaction, and the gluons carry the strong interaction. The Higgs boson, the only scalar boson of the SM, is responsible for particle mass generation through the Higgs–Brout–Englert mechanism [6, 7].

The SM mathematical formalism can be illustrated e.g by QED. In this case, the Lagrangian density follows the U(1) gauge group:

$$L_{\mathrm{QED}} = \Psi(i\gamma^{\mu}\partial_{\mu} - m)\Psi - q\Psi\gamma^{\mu}\Psi A_{\mu} - \frac{1}{4}F_{\mu\nu}F^{\mu\nu} \ , \tag{1.1}$$

where Ψ represents the wave function of a fermion, and γ^{μ} are the Dirac matrices. The boson field A_{μ} ensures invariance under local U(1) gauge transformations by defining the covariant derivative as $\partial_{\mu} \rightarrow \partial_{\mu} + iqA_{\mu}$. Here, $F_{\mu\nu}$ is the electromagnetic field tensor, q is the electric charge, and m is the particle's mass. The Lagrangian in Eq. (1.1) describes the interaction of a charged particle, e.g. electron, with the electromagnetic field. The term $q\Psi\gamma^{\mu}\Psi A_{\mu}$ corresponds to the interaction between the particle's current and the photon, while $F_{\mu\nu}F^{\mu\nu}$ represents the photon itself. Since giving the photon mass would violate local symmetry under U(1), it remains massless, resulting in the electromagnetic interaction having an infinite range. The term $q\Psi\gamma^{\mu}\Psi$ can be identified as the current j^{μ} of the electromagnetic interaction, making the interaction term $-qj^{\mu}A_{\mu}$, where q acts as the coupling constant. This is often expressed in terms of the coupling strength $\alpha \approx 1/137$, which defines the strength of the electromagnetic interaction.

Feynman diagrams provide an illustrative way for calculations of particle interactions and are widely used in the particle physics community. These diagrams follow certain rules such as using specific symbols for particles: straight lines for fermions, curly for gluons, wavy for electroweak bosons, and dashed for the Higgs boson.

1.1.1 The Electroweak interaction

The weak interaction, described by Quantum Flavour Dynamics, is the only flavor-changing interaction, allowing quarks to change flavor and leptons to convert to their

corresponding neutrinos (or vice versa). This interaction violates the parity invariance, as demonstrated in e.g. Wu experiment in 1956 [9]. The weak interaction acts on left-chiral particles and right-chiral antiparticles.

The unification of the electromagnetic and weak forces into the electroweak theory, developed by Glashow, Salam, and Weinberg in 1968 [10–12], treats these interactions as a single entity at high energy scales, where the Lagrangian is symmetric under SU(2) $\otimes$ U(1). Below an energy scale related to the vacuum expectation value of the Higgs field, spontaneous symmetry breaking occurs, causing the SU(2) symmetry to break down. This leads to the separation of the unified electroweak force into distinct electromagnetic and weak interactions. The mechanism responsible for this symmetry breaking is the Higgs–Brout–Englert mechanism [6, 7] mechanism, which will be elaborated in Section 1.1.2.

The gauge-invariant Lagrangian of the electroweak theory is given by:

$$L_{\mathrm{EW}} = iL\gamma^{\mu}D_{\mu}L + R\gamma^{\mu}D_{\mu}R - \frac{1}{4}B_{\mu\nu}B^{\mu\nu} - \frac{1}{4}W^{a}_{\mu\nu}W^{a\mu\nu} \ , \tag{1.2}$$

where the covariant derivative gives the propagation of the fermion fields and their interaction with the gauge boson fields and is:

$$D_{\mu} = \partial_{\mu} - i\frac{g'}{2}YB_{\mu} - igT^{a}W^{a}_{\mu} \ , \tag{1.3}$$

where i runs over the values 1–3. The generators Y and T^a are associated with the U(1) hypercharge and the SU(2) weak isospin, respectively. This results in one gauge boson B_μ for U(1) and three gauge bosons W^a_μ for SU(2). The field strength tensors are defined as [13]:

$$B_{\mu\nu} = \partial_{\mu}B_{\nu} - \partial_{\nu}B_{\mu} \tag{1.4}$$

and

$$W^{a}_{\mu\nu} = \partial_{\mu}W^{a}_{\nu} - \partial_{\nu}W^{a}_{\mu} - gf^{abc}W^{b}_{\mu}W^{c}_{\nu} \ . \tag{1.5}$$

The constants g and g' are dimensionless coupling constants and f^{abc} are the structure constants of the SU(2).

The fermion fields are categorized into left-handed and right-handed components. In the SM, left-handed fermions and right-handed antifermions are organized into SU(2) weak isospin doublets with eigenvalues (T, T_3) and chirality of -1. For up-type quarks and neutrinos, the weak isospin is $(1/2, +1/2)$, while for down-type quarks and charged leptons is $(1/2, -1/2)$. Conversely, right-handed fermions and left-handed antifermions form SU(2) weak isospin singlets with eigenvalues $(0, 0)$ and chirality of $+1$.

The charged current weak interaction is maximally parity-violating, acting only on left-chiral particles and right-handed antiparticles. The electroweak interaction charges are the weak isospin T_3 and the weak hypercharge Y, related to the electric charge Q through the Gell–Mann–Nishijima formula [14, 15]:

$$Q = \frac{Y}{2} + T_3 \ . \tag{1.6}$$

The weak charged current interactions can be expressed as a linear combination of the W_μ^1 and W_μ^2 fields:

$$W_\mu^\pm = \frac{1}{\sqrt{2}}(W_\mu^1 \mp W_\mu^2) \ . \tag{1.7}$$

The electromagnetic field A_μ and the neutral current field Z_μ are obtained by rotating the gauge fields:

$$\begin{pmatrix} A_\mu \\ Z_\mu \end{pmatrix} = \begin{pmatrix} \cos\theta_W & \sin\theta_W \\ -\sin\theta_W & \cos\theta_W \end{pmatrix} \begin{pmatrix} B_\mu \\ W_\mu^3 \end{pmatrix} \tag{1.8}$$

where θ_W is the electroweak mixing angle, also known as the Weinberg angle. The relationship between the W and Z boson masses is given by $\cos\theta_W = \frac{m_W}{m_Z}$. The coupling constants g and g' relate to the electromagnetic charge e as $e = g\sin\theta_W = g'\cos\theta_W$. The non-abelian SU(2) symmetry leads to self-interactions among the gauge bosons.

1.1.2 The Brout-Englert-Higgs mechanism

The Lagrangian in Eq. (1.2) shows no mass terms for vector bosons because including them would violate local SU(2) symmetry. However, the existence of massive bosons, as observed experimentally, indicates that this symmetry is broken at low energies.

The electroweak symmetry breaking (EWSB) is explained by the Brout-Englert-Higgs mechanism [6,7], which introduces an isospin doublet of scalar fields, $\phi = (\phi^+, \phi^0)$, without explicitly breaking the SU(2) symmetry. This is achieved by adding a new term to the Lagrangian:

$$L_{\text{Higgs}} = (D_\mu\phi)^\dagger(D^\mu\phi) - V(\phi) \ , \tag{1.9}$$

where the Higgs potential $V(\phi)$ is defined as:

$$V(\phi) = -\rho^2\phi^\dagger\phi + \lambda(\phi^\dagger\phi)^2. \tag{1.10}$$

The minimum of this potential depends on the parameters ρ and λ. For $\lambda > 0$, the potential has two possibilities: when $\rho < 0$, the minimum is trivial ($\phi_{\text{min}} = 0$), but

for $\rho > 0$, an infinite number of degenerate minima exist, and the system spontaneously chooses one, leading to symmetry breaking. In this case, the potential forms a "sombrero" shape, as shown in Figure 1.2.

This phenomenon results in ground-state fields that are no longer invariant under gauge transformations and leads to a non-zero vacuum expectation value (VEV) v. The VEV of the Higgs field is given by:

$$\langle \phi \rangle = \frac{\sqrt{\rho^2}}{\sqrt{2\lambda}}. \tag{1.11}$$

This non-zero VEV is crucial, as it generates masses for the gauge bosons and fermions through their interactions with the Higgs field.

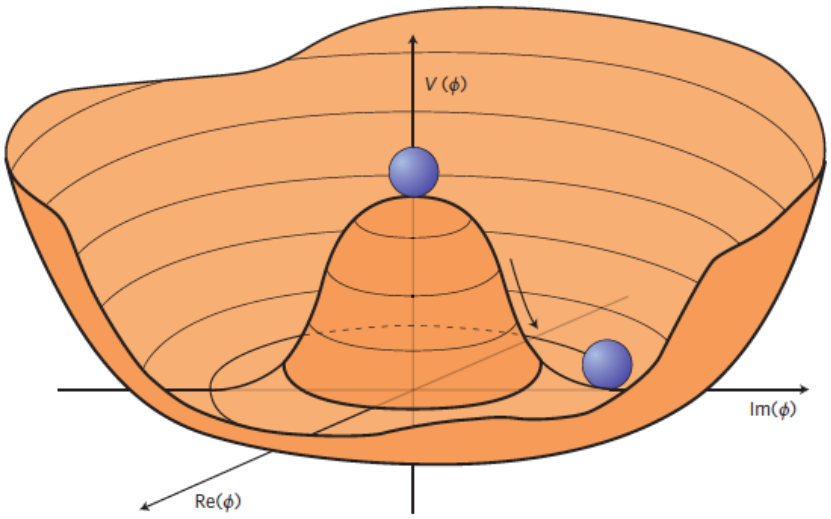

Figure 1.2: Higgs potential in the scenario where $\rho < 0$. The purple marble represents a point chosen at the minimum of the potential, illustrating the spontaneous breaking of symmetry. Figure taken from [16].

Since the physical properties do not depend on the exact minimum due to the symmetry of the Higgs potential $V(\Phi)$, we can choose the minimum as:

$$\Phi_{\text{min}} = \left(0, \frac{v}{\sqrt{s}}\right)^T \quad \text{with} \quad v = \sqrt{\frac{\mu^2}{\lambda}}. \tag{1.12}$$

Expanding the ground-state field around this minimum, the field can be expressed in terms of four degrees of freedom as:

$$\Phi = e^{i\xi_i \sigma_i/2} \begin{pmatrix} 0 \\ v + H \end{pmatrix}, \tag{1.13}$$

where H and ξ_i are real scalar fields. Applying a transformation, called the unitary gauge, eliminates ξ_i so that only H remains.

Upon EWSB, the scalar field is expanded around its new vacuum, and the original gauge bosons mix to form physical particles. The W_1^μ and W_2^μ fields mix into massive W^+ and W^- bosons, while B^μ and W_3^μ combine to form the photon (A^μ) and the Z boson. The mixing of B^μ and W_3^μ is characterized by the Weinberg angle, θ_W, and results in the photon remaining massless, while the $W^\pm$ and Z bosons acquire masses:

$$m_W = \frac{1}{2} v g, \quad m_Z = \frac{1}{2} v \sqrt{g^2 + g'^2}, \tag{1.14}$$

where $v = 246\,\text{GeV}$ is the Higgs vacuum expectation value [17]. The large masses of the W and Z bosons, 80.4 GeV and 91.2 GeV [17] respectively, are responsible for the short range of the weak interaction, while the zero mass of the photon allows for the infinite reach of the electromagnetic force.

The Higgs field itself also acquires a mass after symmetry breaking, given by:

$$m_H = \sqrt{2\lambda} v. \tag{1.15}$$

This mechanism explains how particles in the Standard Model (SM) acquire mass without violating gauge symmetry, as the Higgs field generates mass terms through spontaneous symmetry breaking. The Higgs boson, the last undiscovered component of the SM, was finally observed in 2012 by the ATLAS and CMS collaborations [18, 19], with a mass of about 125 GeV [17]. Additionally, the Higgs mechanism predicts interactions between the Higgs boson and other particles, including vector bosons, as well as Higgs self-interactions.

1.1.3 Fermion mass generation and quark mixing

To explain the fermion mass generation and quark mixing, the SM Lagrangian is extended by introducing a term, that describes the interaction between the Higgs–Brout–Englert field ϕ and the fermions, without breaking the SU(2) symmetry. This interaction is known as the Yukawa interaction [11] and can be expressed as:

$$L_{\text{Yukawa},f} = -\lambda_f (\overline{\Psi_L} \phi \psi_R + \overline{\psi_R} \phi \Psi_L), \tag{1.16}$$

where λ_f is the Yukawa coupling constant, Ψ_L represents the left-chiral weak isospin doublet (such as L_i or Q_i), and ψ_R is the right-chiral singlet (such as u_i, d_i, or e_i). This

term causes fermions to acquire mass proportional to the VEV of the Higgs field through the spontaneous symmetry breaking.

For the quarks, two distinct Yukawa terms are introduced. One generates masses for the down-type quarks and charged leptons, and is given by:

$$L^{Y}_{l+dq} = -y_f(\overline{L}\phi R + \overline{L}\phi R^{\dagger}), \tag{1.17}$$

while the masses for up-type quarks are generated by the term:

$$L^{Y}_{uq} = y_f(\overline{L}\phi^c R + \overline{L}\phi^c R^{\dagger}). \tag{1.18}$$

In both cases, y_f is the Yukawa coupling, defined as:

$$y_f = \frac{m_f}{v}, \tag{1.19}$$

where m_f represents the fermion mass. After symmetry breaking, the mass terms for the quarks and leptons arise, with the coupling strength proportional to the fermion masses. Experimental verification of these couplings has been observed at the LHC, including the coupling of the Higgs boson to third-generation fermions, such as top quarks, bottom quarks, and tau leptons.

Quarks mix between different generations through weak interaction, with a probability driven by the coefficients of the Cabibbo–Kobayashi–Maskawa (CKM) matrix [20, 21]. In the SM, charged current interactions can change quark flavors, allowing quarks to transform into their isospin partners. However, quark mass eigenstates (q) are not the same as their weak eigenstates (q'). The relationship between these are described as:

$$\begin{pmatrix} d' \\ s' \\ b' \end{pmatrix} = V_{\mathrm{CKM}} \begin{pmatrix} d \\ s \\ b \end{pmatrix}, \tag{1.20}$$

where V_{CKM} is the CKM matrix, which takes the form [17]:

$$V_{\mathrm{CKM}} = \begin{pmatrix} V_{ud} & V_{us} & V_{ub} \\ V_{cd} & V_{cs} & V_{cb} \\ V_{td} & V_{ts} & V_{tb} \end{pmatrix} \approx \begin{pmatrix} 0.974 & 0.226 & 0.004 \\ 0.226 & 0.973 & 0.040 \\ 0.009 & 0.040 & 0.999 \end{pmatrix}. \tag{1.21}$$

The elements represent the probabilities of transition from one quark flavor to another and are obtained experimentally. The off-diagonal elements are small, leading to suppressed

transitions beyond the same generation. The element $|V_{tb}| \approx 1$ suggests that the top quark almost exclusively decays into a b quark and a W boson.

The small off-diagonal entries related to the bottom quark lead to suppressed decays of b hadrons, contributing to their relatively long lifetimes, which is useful in experimental identification of b-flavored particles.

In the leptonic sector, a similar mixing matrix could be introduced, known as the Pontecorvo–Maki–Nakagawa–Sakata (PMNS) matrix [22, 23], to explain neutrino oscillation [24, 25]. However, as right-chiral neutrinos are not part of the SM, this extension is not necessary for generating masses for charged leptons. Neutrino oscillations imply that neutrinos must have mass, though their exact values remain unknown, with current experimental limits placing them below 0.8 eV [26].

1.1.4 Quantum Chromodynamics

Quantum Chromodynamics (QCD) is the theory that describes the strong interaction between the quarks and gluons, which carry a unique quantum number known as color charge. It is analogous to electric charge in electromagnetism, but instead of just having two types (positive and negative), color charge comes in three types: red (r), green (g) and blue (b). Quarks are described by color triplets, represented as $Q = (q_{\mathrm{r}}, q_{\mathrm{g}}, q_{\mathrm{b}})^T$, while antiquarks $\bar{Q}$ carry one of the three anti-color charges, respectively. Gluons, the mediators of the strong interaction, carry both a color and an anti-color charge. The QCD Lagrangian, which governs the dynamics of quarks and gluons, can be expressed as [27]:

$$L_{\mathrm{QCD}} = \bar{Q}\left(i\gamma^{\mu}(D_{\mu})_{ij} - m\delta_{ij}\right)Q_j - \frac{1}{4}G^a_{\mu\nu}G^{\mu\nu}_a \quad , \tag{1.22}$$

where the indices μ, ν refer to the four space-time dimensions, while i, j run over the six quark flavors. The covariant derivative D_{μ} describes both the free propagation of quarks and their interaction with gluons and it is represented as $D_{\mu} = \partial_{\mu} - ig_s T_a G^a_{\mu}$. The gluon field strength tensor,

$$G^a_{\mu\nu} = \partial_{\mu}G^a_{\nu} - \partial_{\nu}G^a_{\mu} + g_s f^{abc}G^b_{\mu}G^c_{\nu} \quad , \tag{1.23}$$

accounts for the gluon self-interaction. Here, g_s is related to the strong coupling constant $\alpha_S = g_s^2/4\pi$, and T_a are the generators in the fundamental representation of the SU(3) group, commonly expressed as the Gell-Mann matrices $\lambda_a/2$, with $a = 1...8$ [28]. The last term captures the gluon self-interaction, enabled by the non-zero structure constants f_{abc} in the commutation relation $[T_a, T_b] = if_{abc}T_c$. The resulting gluon self-interactions via three-gluon and four-gluon vertices is illustrated in Feynman diagrams in Figure 1.3.

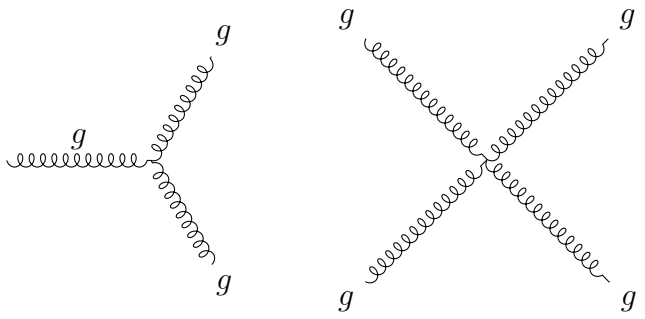

Figure 1.3: Feynman diagrams illustrating the gluon self-coupling vertices.

In calculations beyond the leading order in perturbation theory, corrections to quark and gluon propagators must be accounted for. In Figure 1.4, examples of virtual particle loops, creating ultraviolet divergences in the scattering amplitude calculations are presented. In order to eliminate these infinities, the method of renormalization [29] is applied. In the modified minimal subtraction ($\overline{\text{MS}}$) scheme, these divergences are managed at a renormalization scale, μ_R, with the renormalized parameters being experimentally measurable at a fixed scale Q. The requirement for an observable to be independent of the choice for μ_r leads to the renormalization group equations (RGE) for the coupling and the particle masses.

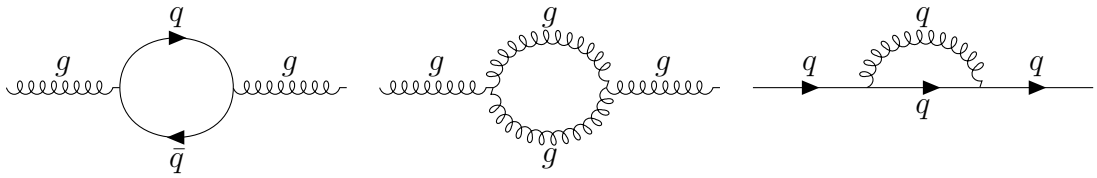

Figure 1.4: Feynman diagrams depicting loop corrections to quark and gluon propagators.

As a result, in QCD, the strong coupling constant α_S and the quark masses become dependent on μ_r, a phenomenon referred to as the "running" of the coupling and masses. The running of these QCD parameters was demonstrated in many experiments, such as [30, 31] for α_S, [32–38] for the running of the bottom quark mass, [39] for the running of the charm quark mass and [40–44] for the running of the top quark mass.

The β function governs the evolution of a coupling constant α_S with energy Q as:

$$\beta(\alpha_S) \equiv \frac{d\alpha_S}{d\ln(Q^2)} \quad . \tag{1.24}$$

At leading-logarithmic approximation, the running of α_S in QCD can be written as:

$$\alpha_S(\mu^2) = \frac{\alpha_S(\mu^2)}{1 + \beta_0 \alpha_S(\mu^2) \ln\left(\frac{Q^2}{\mu^2}\right)} \ , \tag{1.25}$$

where β_0 depends on the number of quark flavors n_f and the number of colors N_c as

$$\beta_0 = \frac{11N_C - 2n_f}{12\pi} \ . \tag{1.26}$$

Here, the first (second) term originates from the contribution of the gluon (quark) loops to the QCD vacuum polarization. With $N_C = 3$ and n_f=6, β_0 is positive and, respectively, the slope of $\beta(\alpha_s) = -\beta_0 \alpha_S^2$ is negative, which defines the running of $\alpha_S(Q)$ as rapidly decreasing with growing energy scale Q.

At very high energies, α_S is very small and the quarks and gluons are treated as asymptotically free [45, 46] in the perturbative calculations.

At low energies (or large distances), in contrast, α_S becomes very large, so that perturbative calculations cannot be applied. Indeed, at large distances, the color contribution to the potential, which can be illustrated as a color string of a certain tension σ between two quarks, rises linearly as σr with the distance r between the quarks. With further rising r, infinite energy would be needed to "free" a quark confined in the color potential. At a certain tension, the string breaks and new $q\bar{q}$ pairs are created. Kinetic energy of the quarks remains partially in the potential of the color string. With a certain energy density of the color field, further $q\bar{q}$ pairs pop up from the vacuum. In the end of this process, called hadronization, colorless states, hadrons, are created. These are then observable experimentally, while confinement prevents colored objects, quarks and gluons, from being observed as free particles. Hadrons are classified into mesons, made of a quark-antiquark pair, and baryons, consisting of three quarks. Further colorless states have been experimentally observed, so-called tetraquarks (pentaquarks), consisting of 4 (5) quarks [47–49].

Of all quarks, the top quark is unique in that it does not hadronize due to its large mass, which causes it to decay via the electroweak interaction into a b-type quark and a W boson before hadronization can occur [17].

In the $\overline{\text{MS}}$ scheme, the RGE describes how the quark mass m depends on the energy scale μ. Typically, the $\overline{\text{MS}}$ mass is reported at the energy scale corresponding to the mass value itself, denoted as $m(m)$.

An alternative method for quark mass definition is the on-shell, or pole mass, scheme [50]. In this approach, the mass parameter is defined to match the pole in the quark propagator,

similar to how free particle masses are defined in e.g. QED. Self-energy corrections up to the mass scale are absorbed into this definition. However, due to nonperturbative QCD effects, the top quark pole mass has an inherent ambiguity, known as the renormalon problem [50]. The pole and $\overline{\text{MS}}$ masses can be converted into each other, with the relation at one-loop level as:

$$m_{\text{pole}} = m(m)\left(1 + \frac{4}{3\pi}\alpha_S(m)\right) \quad . \tag{1.27}$$

Another short-distance quark mass definition that bridges the gap between the pole and $\overline{\text{MS}}$ mass is the MSR scheme [51]. The relationship between the pole and MSR masses is given by the equation:

$$m_{\text{pole}} = m_{MSR} + R\sum_{n=1}^{\infty} a_n^{MSR}\left(\frac{\alpha_S(R)}{4\pi}\right)^n . \tag{1.28}$$

In this scheme, a_n^{MSR} are decoupling coefficients, and R represents an additional arbitrary scale. As $R \to 0$, the MSR mass approaches the pole mass, while for $R = m(m)$, it behaves like the $\overline{\text{MS}}$ mass. Like the $\overline{\text{MS}}$ mass, the MSR mass is free from renormalon ambiguities, with all self-energy corrections between the scales R and m absorbed into its definition.

1.2 Hadron collider physics

In high-energy pp collisions, e.g. at the LHC, the internal structure of both protons is resolved. The quantum properties of the proton are described by the three valence quarks: two up quarks and one down quark. The structure of the proton is however much more complicated, involving gluons which split into further (sea) $q\bar{q}$ pairs. All these constituents are referred to as partons. The details of the proton structure are expressed in terms of parton distribution functions (PDFs), related to the probability to find a parton of a particular flavor in the proton, carrying a certain fraction x of the proton momentum.

In a collision of two protons, the partons of each proton participate in the primary interaction, known as the hard scattering. As a result, further particles are produced. The factorization theorem of QCD allows calculating a cross section of any process in pp collision as a convolution of the PDFs of both protons and the partonic cross section.

After the primary interaction, the final-state partons can further fragment, building a parton shower (PS), with decreasing energy of the partons in the shower, those hadronize and freeze out as colorless hadrons. While the hard interaction, and partially fragmentation, can be calculated perturbatively, the hadronization is modeled using phenomenological

methods. In practice, PS and hadronization are simulated using Monte Carlo (MC) event generators. These tools are crucial for modeling high-energy pp collisions and understanding the processes leading to the production of final-state particles.

1.2.1 QCD Factorization and Parton Distribution Functions

In pp collisions at the LHC, the strong interaction governs a wide variety of processes. The QCD factorization theorem [52] separates the short-distance (perturbative) and long-distance (non-perturbative) effects by introducing a factorization scale μ_F. This scale typically represents the smallest scale at which a physical process can be resolved, and it is introduced to remove infrared divergences caused by collinear initial-state radiation. The long-distance effects, where perturbative calculations are not possible, are mostly absorbed into the PDFs. The production cross section for a given process $pp \to ab + X$ can be expressed as a convolution of the PDFs and the partonic cross section and is given by:

$$\sigma_{pp\to ab+X} = \sum_{i,j} f_i(x_1, \mu_F^2) f_j(x_2, \mu_F^2) \hat{\sigma}_{ij\to ab}(\hat{s}, \mu_F^2, \mu_R^2, \alpha_S)\, dx_1\, dx_2 \ . \tag{1.29}$$

Here, $f_i(x_1, \mu_F^2)$ and $f_j(x_2, \mu_F^2)$ are the PDFs of each incoming proton, giving the probability of interaction between the partons i and j, carrying the momentum fractions x_1 and x_2 of the proton momenta at a factorization scale μ_F^2. The $\hat{\sigma}_{ij\to ab}$ represents the partonic cross section, which is calculated perturbatively using matrix element (ME) calculations. The center-of-mass energy of the partonic system is denoted by $\hat{s} = x_1 x_2 s$, where s is the center-of-mass energy of pp collision. While the scale dependence (evolution) of the PDFs can be calculated in QCD using the Dokshitzer–Gribov–Lipatov–Altarelli–Parisi (DGLAP) equations [53–55], their x dependence cannot yet be calculated from the first principles and needs to be extracted from the experimental data.

Precise knowledge of PDFs is essential to describe the initial state in pp collisions. The PDFs are commonly determined in so-called QCD analyses, based on the measurements in deep-inelastic scattering (DIS) experiments and the data from hadronic collisions [56, 57]. In modern PDF sets, the measurements from HERA [58], Tevatron [59], and the LHC are used [60–63]. The CMS experiment has provided significant insights into the PDFs by using jet, $t\bar{t}$, and electroweak boson production [64–66].

The scales μ_F and μ_R are not physical parameters and their choice is arbitrary. The observable cross-section, however, must remain independent of the scale choice. In fixed-order calculations, only a few terms in the perturbative series can be taken into account, which introduces a dependence on the scale choice, resulting in theoretical uncertainty in the cross-section predictions.

1.2.2 Modelling pp collisions

Comparison between experimental data and the theoretical predictions involves two components: a robust modeling of the physical process and a precise simulation of the detector response. The experimentally observable stable (detector-level) particles must be traced back to the original partons produced during the hard interaction (parton-level objects). This requires an accurate description of the development of the PS including fragmentation, hadronization, and particle decays.

Monte Carlo simulation

To simulate pp collisions, Monte Carlo (MC) event generators are employed, which are based on probabilistic models. The MC generators combine the MC calculations with phenomenological models to create the most accurate depiction of actual collisions, simulating the entire chain from the hard interaction at high energy scales to the lower energy scales, where hadronization and particle decays occur. An illustration of a simulated hadron collision event using a MC generator is shown in Figure 1.5. The partons (blue) of the initial protons (black) participate in the hard interaction (represented by a red circle), with their kinematics described by the PDFs. The hard collision is surrounded by a tree-like structure representing Bremsstrahlung, simulated by SM, in light red. The underlying event interaction is indicated by a purple cluster, which represents a secondary hard scattering event. Additionally, yellow lines represent soft photon radiation. The hadronization is shown by light green clusters, and the subsequent decay of hadrons into stable final-state particles is represented by dark green clusters.

The initial partons participating in the interaction are selected probabilistically according to the PDFs, with the outgoing particles' types and kinematics provided by ME calculations. Hard scattering can generate massive particles like the Higgs boson, W and Z bosons, and the top quark, which are approximated by short-lived resonances. To include higher-order corrections in the scattering amplitude and simulate soft and collinear emissions, PS models are employed. These models further extend the simulation by approximating soft interactions, hadronization, and hadronic decays through phenomenological methods.

Emissions from the initial state particles are referred to as initial-state radiation (ISR), while emissions from the products of the hard scattering or their subsequent decays are known as final-state radiation (FSR). Fixed-order perturbative calculations are used to describe well-separated emissions, whereas parton shower PS models are employed to simulate soft and collinear emissions.

Since emissions are present in both fixed-order calculations of the ME and PS models, there is a risk of double counting. This is addressed by using matching and merging

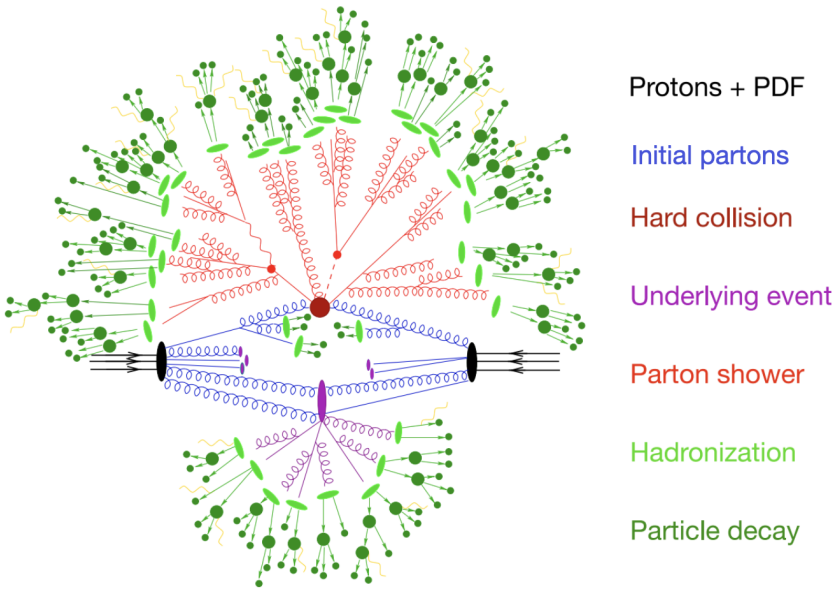

Figure 1.5: Sketch of pp collision simulated by a MC event generator. Figure taken from [67] (modified).

schemes, such as MLM [68] at LO and FxFx [69] at NLO, to reconcile the two approaches. The PS models, which simulate soft and collinear emissions at lower scales, need to be corrected for the hardest emissions since the ME calculations handle well-separated emissions precisely.

Additionally, the interactions of the proton remnants can produce additional particles through Multiple Parton Interactions (MPIs), which are part of so-called underlying event (UE). These interactions are described by phenomenological models, which are tuned using experimental data to better capture the underlying physical processes [70]. Moreover, interference effects between color-charged particles are treated through color reconnection models, further enhancing the accuracy of the simulation.

Hadronization models, such as the string [71] and cluster [72] models, describe how colored final-state particles recombine into color-neutral hadrons. The string model, for example, characterizes interactions between quarks and antiquarks via gluons, modeled as linear potential color-flux tubes called strings. As these strings stretch and break, they produce $q\bar{q}$ pairs until neutral hadrons are formed.

Detector simulation

In addition to the physics modeling, a full simulation of the detector response is necessary. At the CMS experiment, the detector response is simulated using the Geant4 package [73].

The particles emerging from the MC simulation, called "generator-level" particles, are propagated through this detector simulation and their interactions with various detector components, such as the magnetic field, material scatterings, and bremsstrahlung, are modeled.

This detailed simulation ensures that the behavior of particles is accurately reproduced as they traverse the detector, including how they are affected by the detector's unique geometry and environment. The outputs of this simulation, referred to as "detector-level" objects, are treated similarly to real collision data and serve as the input for particle reconstruction and identification algorithms. The detector simulation is finely tuned to match real collision data, ensuring a high level of accuracy and realism in the comparison between the MC-generated events and the experimental observations.

1.3 The top quark

The existence of third-generation quarks was first postulated by Makoto Kobayashi and Toshihide Maskawa in 1973 to explain the CP violation observed in kaon decays [20]. With the discovery of the b quark at Fermilab in 1977 [74], the existence of a third generation of quarks was confirmed, sparking the search for the top quark, named by Haim Harari in 1975 [75]. Initial searches for the top quark, such as those conducted at the Large Electron Positron (LEP) collider, were based on the assumption that its mass was smaller than that of the W boson, allowing it to be a decay product of the W. However, the LEP experiments did not find the top quark, and the final combined results indicated a much higher top quark mass than expected, leading to a shift in the search strategy. It was not until 1995 that the CDF and D0 collaborations reported the discovery of the top quark in proton-antiproton collisions at Fermilab [76, 77].

With a pole mass of about 172.5 ± 0.70 GeV [17], the top quark is the most massive particle in the SM. Its large mass and short lifetime, approximately 5×10^{-25} s (significantly shorter than the hadronization time of $1/\Lambda_{QCD} \approx 3 \times 10^{-24}$ s) causes the top quark to decay before hadronization. It is the only quark which does not hadronize, so that the bare-quark properties, such as spin and electric charge are directly transferred to the top quark decay products, and can be studied experimentally.

The top quark mass, m_t, plays a crucial role in both QCD and EW sectors of the SM, significantly affecting the relation of the masses of the Higgs boson through loop corrections. These corrections are closely linked to the hierarchy or naturalness problem, as they require fine tuning to offset large contributions to the Higgs potential parameter, in order to keep the Higgs mass at its relatively small observed value [78].

Moreover, loop corrections from the top quark also affect the quartic coupling in the Higgs potential. The relationship between m_t, α_S, and the Higgs boson mass plays a key

role in determining the behavior of the Higgs quartic coupling at higher energy scales. This relationship, drives the stability of the SM electroweak vacuum, as illustrated in Figure 1.6. While current experimental measurements can exclude vacuum instability, further improvement in precision is needed to determine whether the vacuum is stable or meta-stable [79].

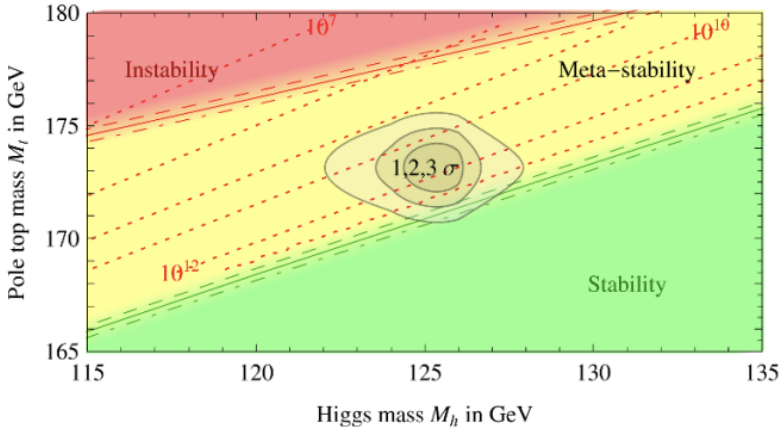

Figure 1.6: Regions of instability (red), meta-stability (yellow) and stability (green) of the SM EWK vacuum as a function of the masses of the top quark and Higgs boson. Figure taken from [79].

Furthermore, in SM the masses of the top quark, W boson, and Higgs boson are related via vacuum corrections. With two of the masses known, the third can be obtained in so-called global EW fit [80–82]. Any observation of deviation from this predicted relationship would hint to new physics. Tension between the value of m_t obtained in EW fits and the measurements of m_t by the ATLAS and CMS collaborations [80] suggest the need for further precise m_t extraction to unambiguously test the SM and explore potential new physics.

1.3.1 Top quark production and decay

In hadron collisions, top quarks can be produced either as a single quark via the weak interaction, or strongly as $t\bar{t}$ pairs. Pair production is induced through gluon fusion or quark-antiquark annihilation, as illustrated in Figure 1.7.

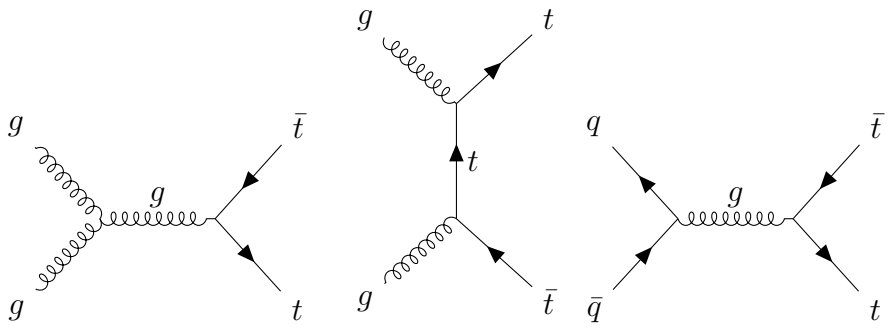

Figure 1.7: Feynman diagrams representing $t\bar{t}$ production at LO. The left and middle diagrams depict the gluon-gluon fusion process in the s- and t-channels, respectively. The rightmost diagram shows quark-antiquark annihilation.

The work in this thesis considers $t\bar{t}$ production in pp collisions at the LHC, where the gluon-gluon fusion process dominates. The cross section for $t\bar{t}$ production has been measured at the LHC at different center-of-mass energies and compared with theoretical predictions at next-to-next-to-leading order (NNLO) plus next-to-leading-log (NNLL) accuracy in QCD, showing very good agreement as illustrated in Figure 1.8.

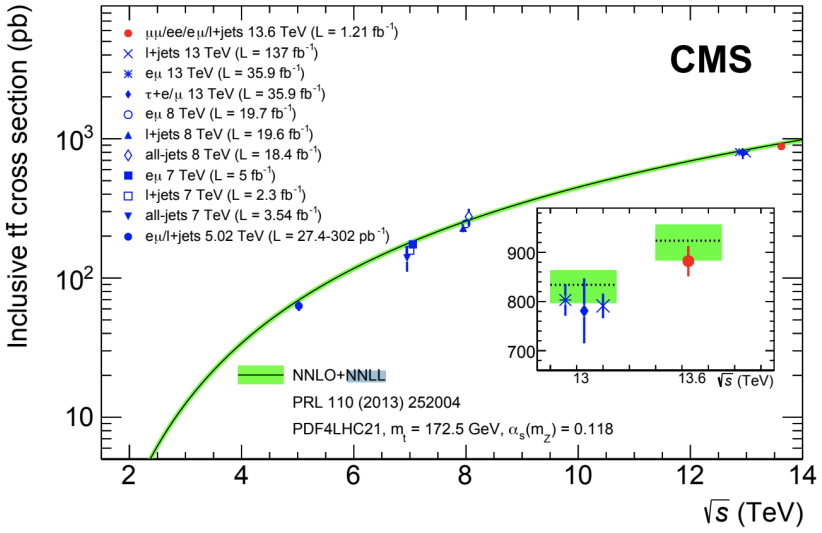

Figure 1.8: CMS $t\bar{t}$ production cross section at different center-of-mass energies ($\sqrt{s}$) and compared the results to NNLO QCD predictions with NNLL resummation. Uncertainties in the theoretical predictions include scale variations, PDFs, and $alpha_s$, with all calculations assuming $m_t = 172.5\,\text{GeV}$. An inset highlights differences between 13 TeV and 13.6 TeV measurements and predictions. Figure taken from [83].

The top quark decays almost exclusively into a W boson and a b quark. The $t\bar{t}$ production channels are categorized based on the decay modes of the W bosons, as illustrated in Figure 1.9. If both W bosons decay into leptons, the event is classified as dileptonic, while if both W decay into quark pairs, it is considered fully hadronic. The lepton+jets category arises when one W decays leptonically, and the other one hadronically. The dileptonic channel, despite its smaller branching ratio, provides the cleanest signal with the smallest background. In contrast, the fully hadronic channel has the largest branching fraction but is heavily affected by QCD multijet background. The semileptonic channel has intermediate properties.

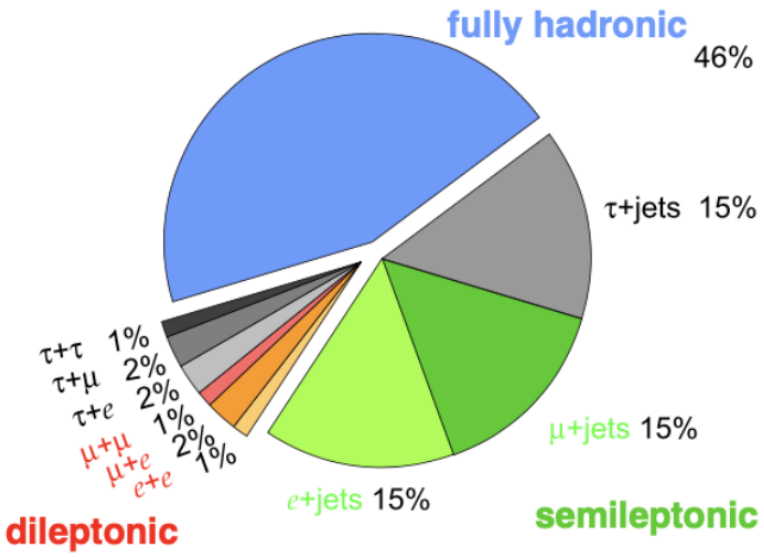

Figure 1.9: Branching ratios and the resulting final states from $t\bar{t}$ production. Figure taken from [84].

1.3.2 Top quark mass

The top quark mass m_t is a fundamental parameter of the SM, with its value and precision being essential for the SM tests and searches for new physics.

In CMS, the value of m_t is extracted either directly, based on kinematic reconstruction of the top-quark decay products, or indirectly by using e.g. inclusive or differential $t\bar{t}$ production cross sections. In direct measurements, m_t is obtained from the fit to the invariant mass of the top quark's decay products or other related observables, reaching a precision of about 0.4 GeV [85]. Despite their high precision, direct measurements rely on MC simulation of the final-state distributions, which are compared to experimental

results. The details of the PS simulation introduce an additional uncertainty in the interpretation of the results of direct measurements, referred to as m_{MC}, in terms of the Lagrangian parameter m_t in a certain renormalization scheme. Studies suggest that m_{MC} can be related to the pole mass m_{pole}, with an additional uncertainty of approximately $\pm$ 0.5 GeV, depending on the specific MC generator used [86]. Furthermore, m_{MC} is often found to approximate the MSR mass at a scale of $R = 1$ GeV [87].

In the indirect measurements, the value of m_t is extracted from comparison of the measured parton-level cross sections to the fixed-order theoretical predictions implying the top-quark mass in a certain renormalization scheme, e.g. pole mass m_{pole} or the running mass in the MS scheme, $m_t(m_t)$, introduced in section 1.1.4. In CMS, m_{pole}, the pole mass has been extracted with an uncertainty below 1 GeV by using differential $t\bar{t}$ cross sections. Also, the value of $m_t(m_t)$ was obtained and the running of the top-quark mass at next-to-leading order (NLO) and next-to-next-to-leading order (NNLO) was illustrated [40, 41, 88]. A summary of the results m_t measurements by the CMS collaboration is presented in Figure 1.10.

While direct measurements focus on kinematic properties, the theoretical definition of the top quark mass remains subtle. The top quark's short lifetime prevents hadronization, allowing for a definition of the pole mass m_{pole} as the real part of the propagator's pole.

The analysis presented in this thesis focuses on extracting the top quark mass from an observable that can be calculated perturbatively at NLO, as explained in section 1.4. This method offers a direct link to the pole mass, avoiding the uncertainties tied to MC-based measurements. This approach aims to provide a precise and theoretically consistent determination of the top quark mass.

1.4 $t\bar{t}$ production in association with one jet

In this thesis, the value of the top quark pole mass, m_t^{pole}, is extracted from events where a $t\bar{t}$ pair is produced in association with at least one energetic jet ($\mathrm{t\bar{t}}$ + jet). It has been demonstrated that the invariant mass of the $\mathrm{t\bar{t}}$ + jet system, $m_{\mathrm{t\bar{t}+jet}}$, is highly sensitive to the value of m_t^{pole} [89]. The observable ρ is defined as:

$$\rho = \frac{2m_0}{m_{t\bar{t}+1jet}} \tag{1.30}$$

where m_0 is an arbitrary scaling constant set to 170 GeV, close to the expected value of m_t^{pole}. The analysis presented in this thesis employs the ρ observable to extract m_t^{pole} and builds upon the work of Ref. [90] making use of a larger dataset and improved reconstruction.

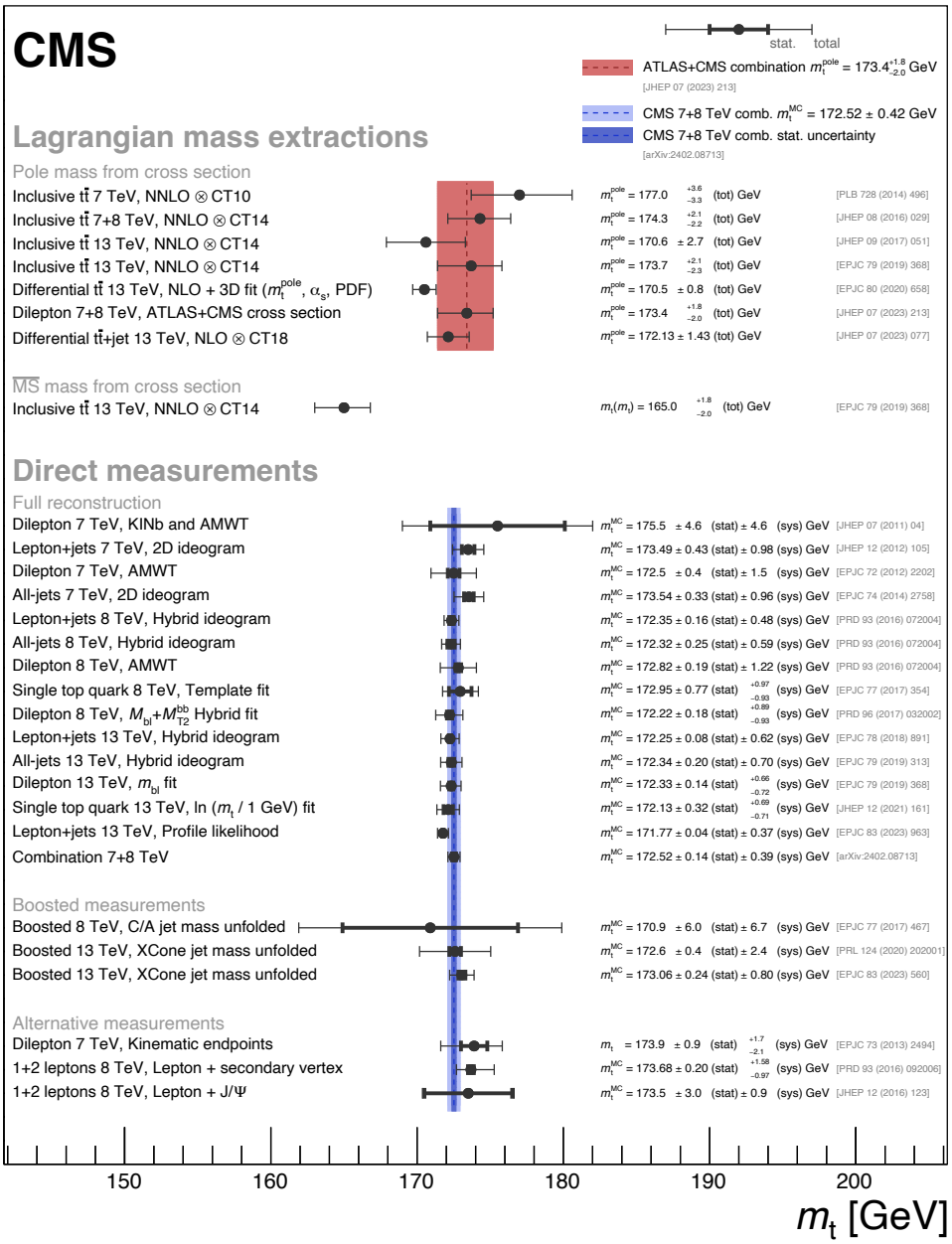

Figure 1.10: Recent results obtained by the CMS experiments on the value of the top mass. Figure taken from [83].

The sensitivity of the observable ρ to m_t^{pole} is quantified using a sensitivity measure $S(\rho)$, defined as:

$$S(\rho) = \sum_{\Delta=\pm 3 \text{ GeV}} \frac{R(\rho, m^t_{\text{pole}}) - R(\rho, m^t_{\text{pole}} + \Delta)}{2|\Delta| R(\rho, m^t_{\text{pole}})}, \tag{1.31}$$

where R represents the normalized differential cross section of $\mathrm{t\bar{t}}$ + jet production as a function of ρ. This measure quantifies how the cross section changes with m_t^{pole}. To compare the sensitivity between $\mathrm{t\bar{t}}$ + jet and $\mathrm{t\bar{t}}$ production, the invariant mass of the $\mathrm{t\bar{t}}$ + jet system in the ρ calculation is replaced with the invariant mass of the $\mathrm{t\bar{t}}$ pair. As shown in Figure 1.11 for $\sqrt{s} = 13$ TeV, both processes show increased sensitivity near the $\mathrm{t\bar{t}}$ production threshold. However, the $\mathrm{t\bar{t}}$ + jet process displays a significantly higher sensitivity beyond the threshold region compared to the $\mathrm{t\bar{t}}$ system alone.

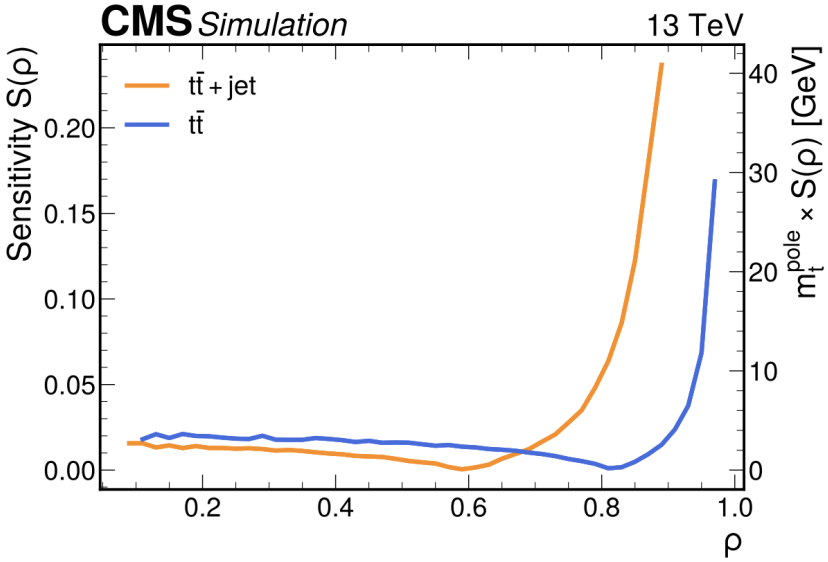

Figure 1.11: Sensitivity of $R(m_{\text{pole}},)$ to the top quark mass both $\mathrm{t\bar{t}}$ + jet (blue) and $\mathrm{t\bar{t}}$ production (orange), using equation 1.31. Figure taken from [83].

The m_t^{pole} sensitivity of the R distribution is depicted in Figure 1.12, where the curves are normalized to unity and intersect at $\rho \approx 0.65$, a point where the observable shows no sensitivity to the m_t^{pole}. Greater sensitivity to m_t^{pole} is observed near the $\mathrm{t\bar{t}}$+jet production threshold, corresponding to $\rho > 0.65$. Conversely, for larger values of $m_{t\bar{t}+\text{jet}}$ (i.e., ρ of about 0.55), the sensitivity diminishes.

The theoretical prediction for $\mathrm{t\bar{t}}$ + jet production is calculated at NLO precision [91] in QCD, favoring the pole mass scheme for defining the top quark mass. This choice

is based on its appropriateness of m_t^{pole} near the production threshold. The process is modeled using the POWHEG ME generator, which efficiently computes predictions and simulates events with subsequent showering via Pythia MC [92]. Recent studies have suggested using a dynamic scale for the renormalization and factorization scales, improving perturbative convergence [93]. The defined scale, $H_T^B/2$, incorporates the transverse momenta of the top quark, antiquark, and an additional jet. By varying μ_r and μ_f, theoretical uncertainties are assessed. In comparison to the standard choice of the scales as $\mu_r = \mu_f = m_t^{pole}$, the dynamic scale results in reduced and symmetric scale uncertainty for the $R(\rho)$ distribution [94].

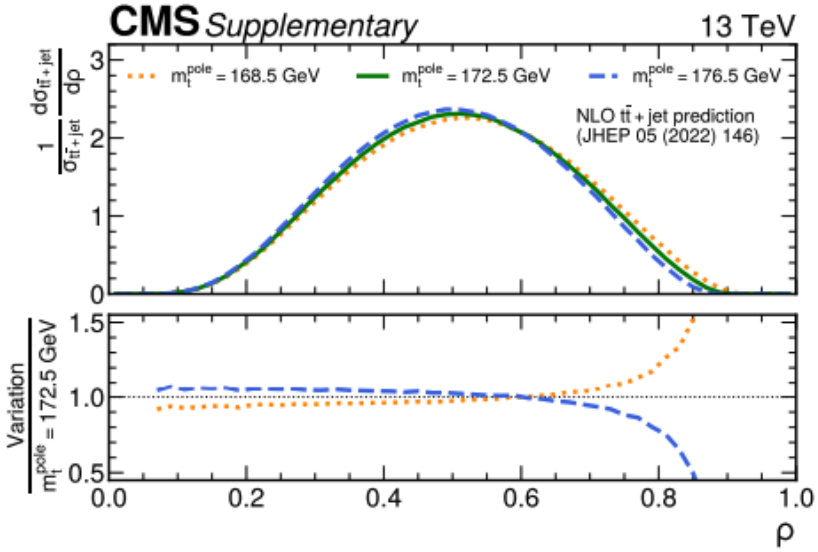

Figure 1.12: Normalized differential cross section for $t\bar{t}$ + jet as a function of ρ for three different assumptions of the top quark mass: 168.5 GeV (orange), 172.5 GeV (green), and 176.5 GeV (blue). The lower panel displays the ratio relative to the central value of 172.5 GeV. Figure taken from [5].

CHAPTER 2

The LHC and the CMS experiment

Contents

The studies presented in this thesis were performed with the collision data recorded with the CMS detector at the Large Hadron Collider (LHC) at CERN. The LHC is the world's largest particle accelerator, and it is described in the following section. In the LHC, the protons are accelerated, and collided at several interaction points (IPs), one of which is surrounded by the CMS detector.

The structure and components of the CMS detector are detailed in section 2.2, the reconstruction techniques used in Compact Muon Solenoid (CMS) are explained, with a focus on the objects relevant for this thesis in section 2.3. Finally, section 3.2.1 introduces the High Luminosity LHC upgrade.

2.1 The Large Hadron Collider

The LHC [95] is located at the Swiss-French border 100 meters beneath the surface. With a circumference of 27 kilometers and a design center-of-mass of 14 TeV, it is the world's largest and most powerful particle accelerator. Its primary goals are testing the

predictions of the Standard Model (SM) and searching for new physics. Reaching these goals is ensured by the high center-of-mass energy and collecting large amounts of data.

The current collider uses a series of accelerators, shown in Figure 2.1, to bring protons or heavy ions to ultimate target energies of 7 TeV or 2.76 TeV, respectively. For the acceleration of protons, hydrogen atoms are stripped of electrons and accelerated to 160 MeV in the Linear accelerator 4 (LINAC4). These are then passed through the Proton Synchrotron Booster (PSB) to reach 2 GeV. Subsequently, they are accelerated to 26 GeV by the Proton Synchrotron (PS) and further to 450 GeV by the Super Proton Synchrotron (SPS). Finally, the proton beam is split in two beams, which are transferred into separate counter directional beam pipes within the LHC. There, they are accelerated to the current target energy of 6.8 TeV. This energy level has been achieved through numerous improvements and upgrades, increasing from 4 TeV during 2009 – 2013 (Run 1), to 6.5 TeV in 2016-2018 (Run 2), and reaching 6.8 TeV in the ongoing Run 3.

The LHC consists of two beam pipes housed in vacuum tubes, structured into eight straight sections known as "insertions" and connected by curved arcs called "sectors". Each sector contains 154 superconducting dipole magnets (totaling 1,232), which operate at 1.9 K, to bend the particle beams [96]. Quadrupole, sextupole, octupole, and decapole magnets are used to focus the beam and correct for magnetic field imperfections or other effects, such as chromatic aberration due to small energy variations inside a bunch. Additionally, eight RF cavities per beam, operating at 4.5 K, accelerate protons from 450 GeV to their final energy.

Proton beams interact at four key interaction points (IPs) in the LHC tunnel, with collisions consisting of 2808 bunches of up to 1.15×10^{11} protons each, occurring every 25 ns and creating around 40 million collisions per second. These IPs house the LHC's main experiments: ATLAS [97] and CMS, which are general-purpose detectors, as well as LHCb [98], which studies bottom quark processes, and ALICE [99], which focuses on heavy-ion collisions.

2.1.1 Luminosity at the LHC

Besides center of mass energy, driven by the energy of the beams, a key parameter of an accelerator is luminosity (L), which quantifies the number of particle interactions per second. The number of observed events N of a given process with a cross section σ is given by the relation $N = L \cdot \sigma$, where σ. The luminosity is a parameter of the machine and is defined as:

$$L = \frac{N_b^2 n f_t \gamma}{4\pi \epsilon_n \beta^*} \tag{2.1}$$

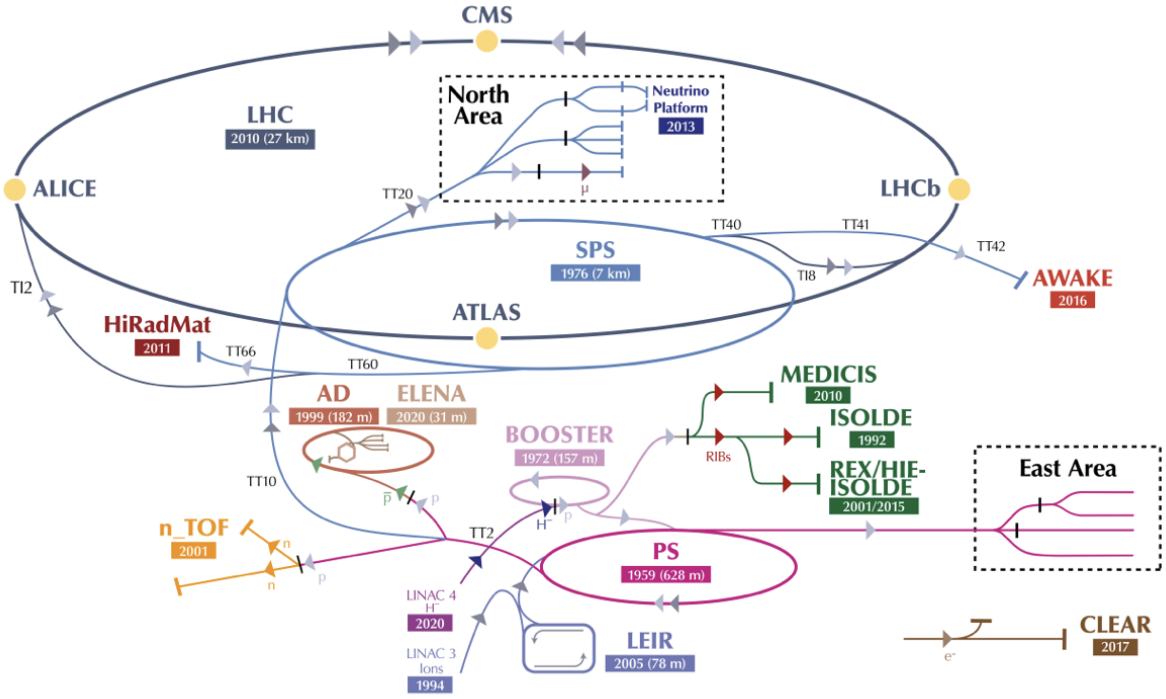

Figure 2.1: Schematic of the CERN accelerator complex. Particles undergo a series of preaccelerations performed at different stages of the complex, from the nucleon source, through linear accelerators and boosting rings, ending with the nominal energy reached in the LHC storage ring. Figure taken from [95].

The luminosity can be optimized by adjusting the parameters in Eq. (2.1), such as the number of protons per bunch (N_b), the number of bunches per beam (n), the revolution frequency (f_t), and the beta function ($\beta*$) which refers to the beam focusing at the interaction point.

In the context of the LHC, a "Run" denotes a specific period of data-taking during which the collider is operational, separated by shutdowns for maintenance, upgrades, and preparations for the subsequent phase. Each Run is characterized by unique beam energies and intensities. Run 1, conducted between 2010 and 2012, marked the LHC's first operational phase, colliding protons at center-of-mass energies of $\sqrt{s} = 7\,\text{TeV}$ (2010–2011) and $\sqrt{s} = 8\,\text{TeV}$ (2012). Run 2, spanning from 2015 to 2018, operated at a higher energy of $\sqrt{s} = 13\,\text{TeV}$. At the time of writing, Run 3 is ongoing (2022–2025), with the LHC achieving an energy of $\sqrt{s} = 13.6\,\text{TeV}$.

Instantaneous luminosity measures the collision rate at a specific moment in time, reflecting the current performance of the collider and is expressed in $\text{cm}^{-2}\text{s}^{-1}$. In contrast, cumulative luminosity, or integrated luminosity, represents the total number of collisions

delivered over a period, calculated by integrating the instantaneous luminosity over time. It is typically expressed in fb^{-1} and determines the size of the dataset available for physics analyses.

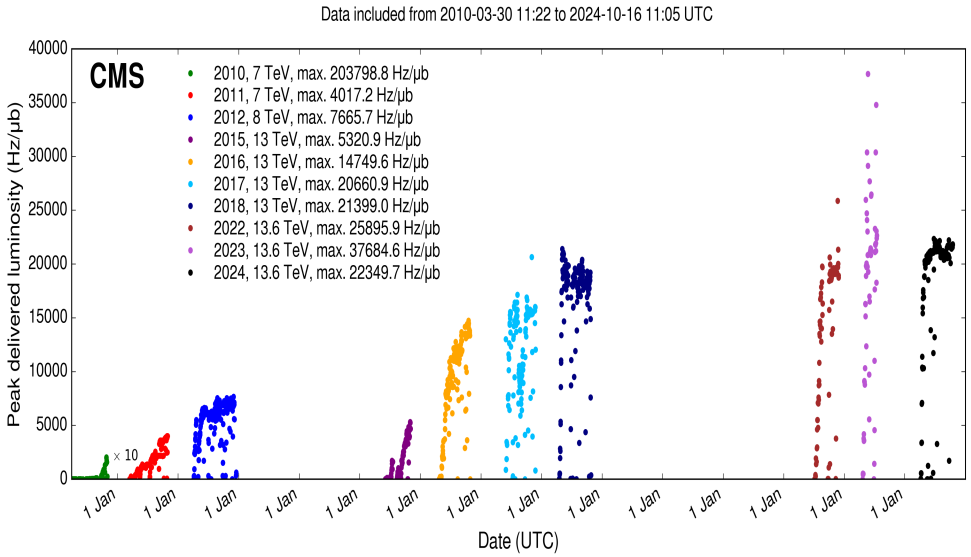

Figure 2.2: Peak luminosity as a function of day delivered to CMS during stable beams and for pp collisions, 2010 (green), 2011 (red), 2012 (blue), 2015 (purple), 2016 (orange), 2017 (light blue), 2018 (navy blue), 2022 (brown), 2023 (light purple) and 2024 (black). Figure taken from [100].

Figure 2.2 illustrates the evolution of the peak instantaneous luminosity of the LHC as a function of time, highlighting the distinct periods of data collection during the various years of operation. The plot also delineates the separation of data-taking Runs by extended shutdown periods, during which the LHC underwent significant maintenance and upgrades.

The design luminosity of the LHC is 10^{34} cm^{-2} s^{-1}, obtained by optimizing parameters in Eq. (2.1). By the end of Run 2 in 2018, the LHC achieved a proton beam energy of 6.5 TeV, approaching its design goal of 7 TeV, and reached a peak instantaneous luminosity of 2.1×10^{34} cm^{-2} s^{-1}, more than double the original design value. This increase was made possible by significant upgrades to the LHC's injection chain magnets. Already in the middle of Run 3 at a center-of-mass energy of 13.6 TeV, the LHC reached a record integrated luminosity of 196.4 fb^{-1} as seen in Figure 2.3

The data analyzed in this thesis was collected by the CMS detector during Run 2, where protons were collided at a center-of-mass energy of 13 TeV.

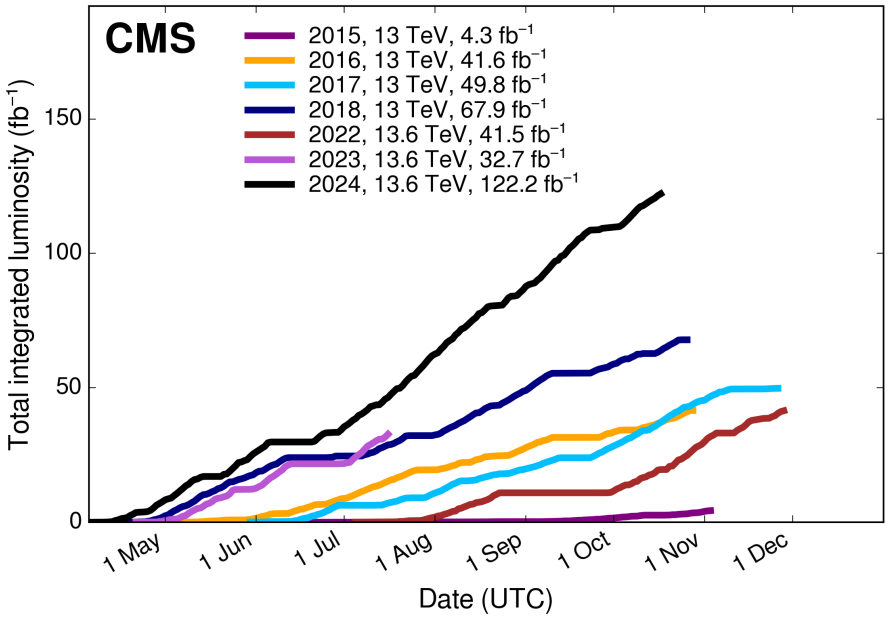

Figure 2.3: Cumulative luminosity as a function of day delivered to CMS during stable beams and for pp collisions, 2010 (green), 2011 (red), 2012 (blue), 2015 (purple), 2016 (orange), 2017 (light blue), 2018 (navy blue), 2022 (brown), 2023 (light purple) and 2024 (black). Figure taken from [101].

2.2 The Compact Muon Solenoid

The Compact Muon Solenoid (CMS) detector, located at Point 5 of the LHC near Cessy, France, about 100 meters underground, is one of the four major experiments at the Large Hadron Collider (LHC). It is a general-purpose detector capable of detecting and measuring different kinds of particles and processes, making it versatile enough to explore a broad spectrum of high-energy physics. It has a cylindrical shape, measures 21.6 meters in length, 15 meters in diameter, and weighs 14,000 tons. The two independent experiments, CMS and ATLAS, with similar capabilities but different detector designs, are intended to cross-validate the achieved results. This redundancy ensures that any significant findings, such as the discovery of new particles or phenomena, can be confirmed independently by both detectors, enhancing the reliability of the results and increasing their precision through combinations. The most profound result was the discovery of the Higgs boson [18, 19] in 2012.

The CMS detector features a 3.8 T solenoid magnet at its core (Section 2.2.1), designed to

bend the trajectories of charged particles produced in collisions. Located inside the core and in the return field are several subsystems arranged in layers, each playing a crucial role in particle detection. The silicon tracking system (Section 2.2.2) records the paths of charged particles. Electromagnetic and hadronic calorimeters (Section 2.2.3) measure the particle energy using scintillator materials. Muon chambers (Section 2.2.4), located at the outermost part of the detector, track muons through gaseous detectors.

Besides the cylindrical part (the barrel) of the detector, the CMS also features endcaps, which help to maximize particle detection, covering a large fraction of the (4π) solid angle around the interaction point. Figure 2.4 shows a sectional view of the CMS detector illustrating its subsystems and detection technologies.

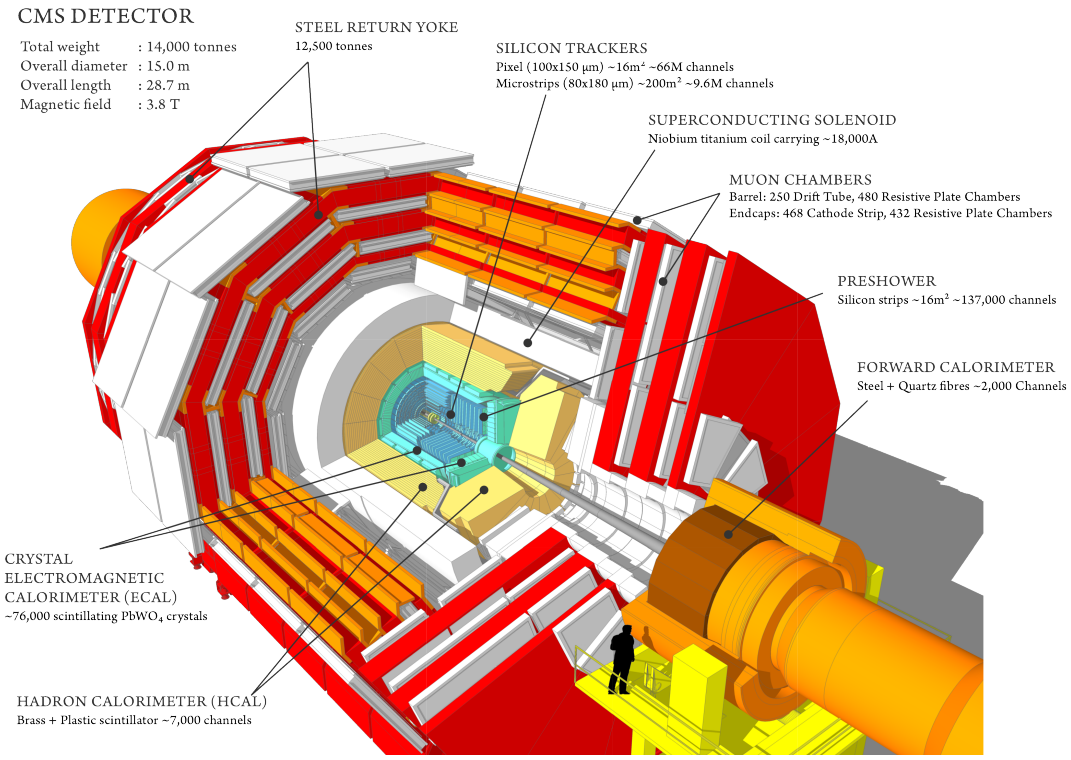

Figure 2.4: Schematic view of the CMS with its subdetectors. Figure taken from [102].

Coordinate Systems

The CMS detector employs a right-handed reference coordinate system where the x-axis points towards the LHC center, the y-axis points upwards, and the z-axis follows the beamline. As the layout of the detector is a cylinder, the cylindrical coordinates are frequently used. The polar angle θ and azimuthal angle ϕ, measured with respect to

the particle direction, help define the pseudorapidity (η) which quantifies how centrally a particle is produced, ranging from 0 for a particle aligned with the transverse plane ($\theta = 90\ ^\circ$) to infinity for a particle moving along the beamline ($\theta = 0^\circ$). It is defined as $\eta = -\ln[\tan(\theta/2)]$. Another important quantity is rapidity (y), defined as $y = \frac{1}{2}\ln\left(\frac{E+p_z}{E-p_z}\right)$. In high-energy scenarios, where a particle's momentum far exceeds its mass, η and y become approximately the same. The angular separation between two particles, ΔR, is calculated as $\Delta R = \sqrt{(\Delta\eta)^2 + (\Delta\phi)^2}$, which provides a useful measure for analyzing particle pairs in collisions.

The advantage of using pseudo-rapidity instead of the polar angle is that it better aligns with the rapidity of a particle, which remains invariant under longitudinal boosts (along the beam axis) in a Lorentz frame. This means that for highly energetic particles, the difference in pseudo-rapidity is a Lorentz invariant quantity, making it a more practical measurement in particle physics.

In addition to the pseudo-rapidity, the transverse momentum $\vec{p_T}$, which represents a particle's momentum in the transverse (x-y) plane is crucial. The magnitude of this transverse momentum is given by $\vec{p_T} = \sqrt{p_x^2 + p_y^2}$. Since the colliding beams do not carry momentum in the transverse plane, the sum of all transverse momenta in a single collision should equal zero. Any deviation from zero is attributed to undetectable particles, such as neutrinos. The missing transverse momentum $\vec{p_T^{miss}}$, defined as the negative vector sum of the transverse momenta of all detected particles, helps to reconstruct neutrino momenta or indicate the presence of undetected particles.

2.2.1 The Superconducting Solenoid

The magnet system is crucial for the performance of the CMS detector, particularly in measuring the particle momentum. To achieve good muon momentum resolution at energies around 1 TeV, the CMS features a powerful superconducting solenoid made of Niobium-Titanium, which generates a 3.8 T magnetic field. This solenoid, measuring 12.5 m in length and 6.3 m in diameter, is the largest of its kind. It is surrounded by a steel structure that serves both as support and as a return yoke for the magnetic field. The magnetic field enables the measurement of the momentum and charge of particles produced in collisions through the Lorentz force, which bends charged particles' trajectories. Inside the solenoid, the tracking and calorimeter systems are positioned. The Solenoid has niobium-titanium layers cooled by a cryostat system using liquid helium at 4.7 K. The steel return yoke, made up of five barrel wheels and six endcap disks, also acts as a filter by absorbing tails of hadronic showers and improving the muon purity.

2.2.2 Tracking system

The silicon tracking detector is crucial for reconstructing the trajectories and measuring the momenta of charged particles originating from the collision. It is designed to offer excellent spatial resolution and minimal material interference to avoid high impact by multiple scattering. Positioned within a 3.8 T magnetic field, the tracking detector is used to determine the particles' momenta from the curvature of their trajectories, which are bent due to the Lorentz force [17]:

$$p[\mathrm{GeV}/c] = 0.3qBr \tag{2.2}$$

where B represents the magnetic field strength in Tesla, q is the particle's charge, and r is the curvature radius in meters.

The CMS silicon tracker consists of 18 barrel layers and 15 forward discs, covering a total surface area of 210 m^2. It extends from a radius of 4 cm to 110 cm from the interaction point and has a length of 540 cm, symmetrically covering a pseudo-rapidity range of $|\eta| < 2.5$. The innermost layers are high-resolution silicon pixel detectors, while the outer layers are silicon strip detectors. Figure 2.5 provides a cross-section of the tracker layout.

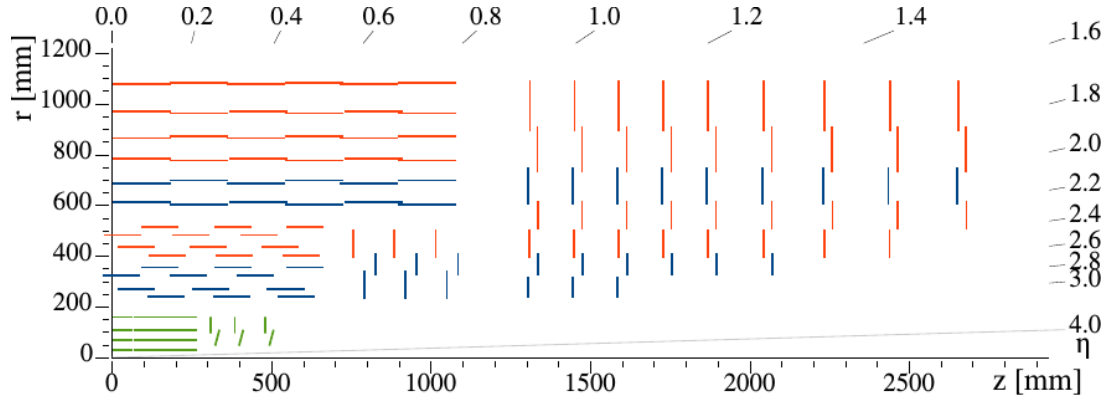

Figure 2.5: Diagram of a quarter of the silicon tracker layout in the r-z view, showing the location of the pixel tracker (green) and the strip tracker (red and blue). Figure taken from [103].

Pixel Tracker

Located closest to the interaction point, the pixel tracker copes with high particle flux and demands stringent performance criteria, including high rate capability, radiation tolerance, and good tracking resolution. Following the Phase-1 upgrade in 2017, the pixel detector now features four barrel layers (BPIX) of 54 cm length, positioned at radii of

2.9, 6.8, 10.9, and 16.0 cm, along with three endcap disks (FPIX) extending from radii of 4.5 to 16.1 cm. The pixel modules consist of 270 μm and 286 μm thick silicon sensors with rectangular pixel cells sized 100 $\times$ 150 μm^2, totaling 66 million readout channels. Signal processing is managed by the PSI46 ASIC [104], providing position measurements with a resolution between 10 and 20 μm [105].

Strip Tracker

The strip tracker surrounds the pixel detector, extending the tracker volume to the full radius of 110 cm and length of 540 cm. It includes four Tracker Inner and Outer Barrel layers (TIB, TOB), four Tracker Inner Disks (TID), and two Tracker Endcaps (TEC), with 14 layers in the barrel and 12 in each endcap. In the outer regions, where radiation and occupancy are lower, the granularity is reduced by a larger pitch. The strip tracker modules feature silicon sensors with thicknesses of 320 μm and 500 μm and strip pitches ranging from 80 μm to 180 μm, amounting to 9.3 million readout channels [106]. These modules are designed for cost-effective mass production with simple silicon sensor layouts, analog readout electronics, and low-mass support infrastructure. Performance varies, with resolutions in the innermost layer ranging from 23 to 34 μm in the $r - \phi$ direction and 23 μm in the z direction, and in the outermost layer resolutions of 35 to 53 μm in $r - \phi$ and 52 μm in z direction [107].

2.2.3 The Calorimeters

The calorimeter detectors are designed to measure the energy of particles by using high-density materials that cause incoming primary particles to produce a cascade of secondary particles, a process known as a particle shower. Two types of particle showers are observed: electromagnetic showers, initiated by electrons and positrons and photons, and hadronic showers, initiated by hadrons. Electromagnetic showers result from energy losses via bremsstrahlung and electron-positron pair production, resulting in a large number of low energetic particles. Absorption of those in scintillators leads to a number of photons correlating to the primary particle's energy. Hadronic showers, dominated by the strong force, involve hadron creation and decay, while also generating a fraction of electromagnetic showers. Energy is also absorbed and measured.

To gather both energy and position data of showering particles, the calorimeters are segmented. This segmentation allows for the distinction of multiple particles and jets, which can then be matched to particle trajectories recorded in the tracker system. Positioned directly behind the tracker, first the electromagnetic calorimeter (ECAL) is located, and

focuses on detecting electrons and photons, while the hadron calorimeter (HCAL) is responsible for measuring hadron energy and is located outside the ECAL. Both systems are designed to fit within the magnet structure.

The Electromagnetic Calorimeter

The Electromagnetic Calorimeter (ECAL) covers pseudorapidities up to $|\eta| < 3$ and is composed of a barrel layer (EB) and two endcap layers (Preshower Detector and the Endcap ECAL). The barrel region contains 61,200 Lead-Tungstate ($PbWO_4$) crystals, while the endcap region holds 7,324 crystals. $PbWO_4$ was selected due to its short radiation length ($X_0 = 0.89$ cm), small Moliere radius (2.2 cm), fast light emission (80% emitted within 25 ns), and high radiation hardness. The radiation length represents the distance required to reduce an electron's energy by a factor of 1/e, this causes EM showers to be compact and improves spatial resolution and separation of showers. The Moliere radius indicates the lateral spread of an electromagnetic shower within the material.

The crystals measure 22×22 mm^2 in the barrel region and 28.6×28.6 mm^2 in the endcap, with lengths of 230 mm and 220 mm, respectively [107]. In both the barrel (EB) and endcap (EE), scintillation photons are detected using silicon avalanche photodiodes (APD). In the endcap region, the ES serves as a pre-shower detector in front of the EE, consisting of two layers of silicon strip modules with a 1.9 mm pitch, placed behind lead disks at depths of $2X_0$ and $3X_0$. This additional material allows for sampling of the shower profile and estimating energy deposits. A transverse section of the CMS ECAL is shown in Figure 2.6.

During Run 2, the energy resolution for electrons determined from Z boson decays in proton-proton collision data ranged from 2 to 5%, depending on the electron pseudorapidity [108].

The Hadronic Calorimeter

The Hadron Calorimeter (HCAL) is based on the principle of sampling calorimetry. In this design, alternating layers of an absorbing material, here brass plates, and a scintillating material, here plastic scintillators, allow for the detection of secondary particles produced within particle showers. This setup increases the probability that the particle showers are contained within the calorimeter, as the absorber material can be selected independently of its scintillating properties. The HCAL is divided into four sections: the Hadron Barrel (HB), the Hadron Outer (HO), the Hadron Endcap (HE), and the Hadron Forward (HF). A transverse section of a quarter of the CMS HCAL is shown in Figure 2.7.

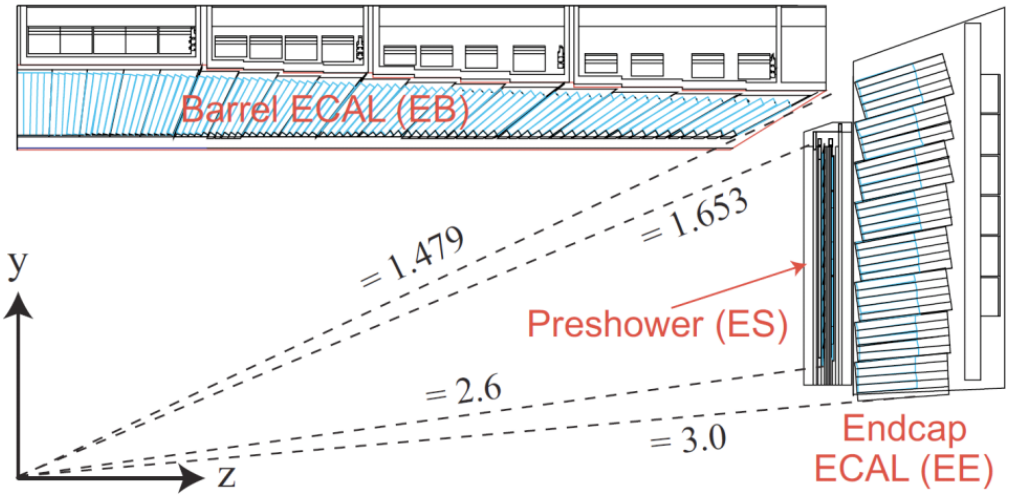

Figure 2.6: Transverse section of the Electromagnetic Calorimeter, illustrating their geometrical arrangement. Figure taken from [109].

The HB covers the region of $|\eta| < 1.4$, with photon detection performed via Hybrid Photo-Detectors (HPD). The HE, covering the region $1.3 < |\eta| < 3$, uses the same materials but employs Silicon Photomultipliers (SiPM) for photon detection. The HO, located between the solenoid magnet and the muon chambers, is composed of plastic scintillators connected to Wavelength Shifter Tubes (WLF) and SiPMs. Lastly, the HF, positioned beyond the endcaps, extends the coverage to up to $|\eta| < 5$, with quartz fibers attached to Photomultiplier Tubes and steel as the absorbing material. The energy resolution for the barrel layers was measured in test beams to be [111]:

$$\sigma_E = \frac{84.7\%}{\sqrt{E(\text{GeV})}} + 7.6\% \tag{2.3}$$

For the HF, the resolution is [112]:

$$\sigma_E = \frac{280\%}{\sqrt{E(\text{GeV})}} + 11\% \tag{2.4}$$

The resolution of the HCAL is worse than that of the ECAL because hadronic showers are more complex, involving nuclear interactions and energy losses that are harder to measure accurately. Additionally, hadronic showers can cause energy leakage and non-uniform response, while electromagnetic showers are more predictable and confined to a smaller volume resulting in better precision.

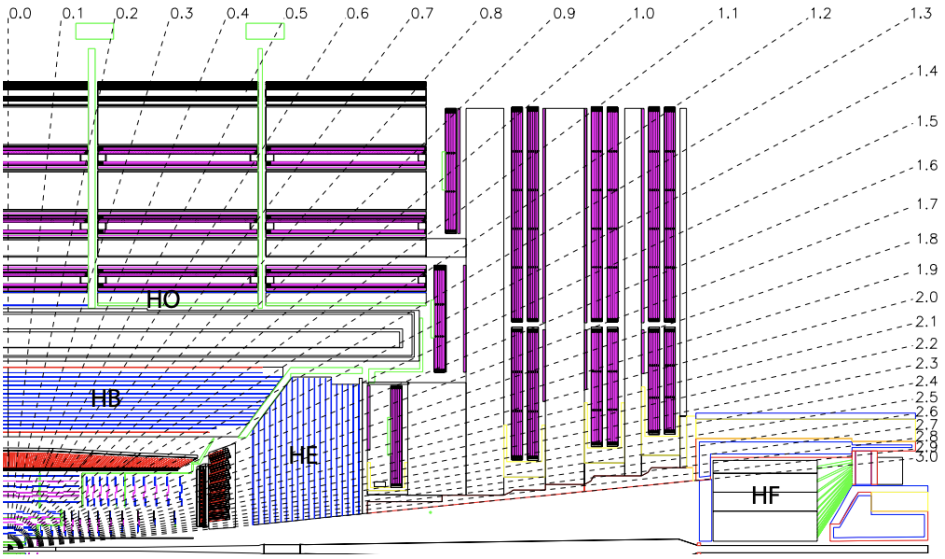

Figure 2.7: Longitudinal view of the CMS detector the locations of the hadron barrel (HB), endcap (HE), outer (HO) and forward (HF) calorimeters. Figure taken from [110].

2.2.4 Muon system

The Muon System consists of three sections, using four types of gaseous detector, each utilizing different technologies and embedded within the flux return yoke, as shown in Figure 2.8: Drift Tube chambers (DT), Cathode Strip Chambers (CSC), Resistive Plate Chambers (RPC), and triple-foil Gas Electron Multipliers (GEM).

In the barrel region ($|\eta| < 1.2$), where the muon rate and residual magnetic field are relatively low, 250 DT are used. These chambers are organized into four layers (MB1, MB2, MB3, MB4) interleaved with the magnet return yoke. With a maximum drift length of 2.0 cm, they provide a single point resolution of approximately 200 μm.

In the forward region, where both the muon rate and magnetic field are higher, 468 cathode strip chambers are deployed, covering up to $|\eta| < 2.4$. Each trapezoidal CSC consists of six gas gaps with a plane of radial cathode strips and perpendicular anode wires. CSC data are used in the CMS Level-1 Trigger system and offer a spatial resolution of around 200 μm.

Resistive Plate Chambers (RPCs) are utilized in both the barrel and endcap regions, covering the pseudo-rapidity range up to $|\eta| < 2.1$. They are arranged as 36 chambers mounted in two rings within the endcap stations and operated in avalanche mode for consistent operation at high rates. RPCs provide fast response times, good time resolution, but with coarser position resolution compared to DTs and CSCs.

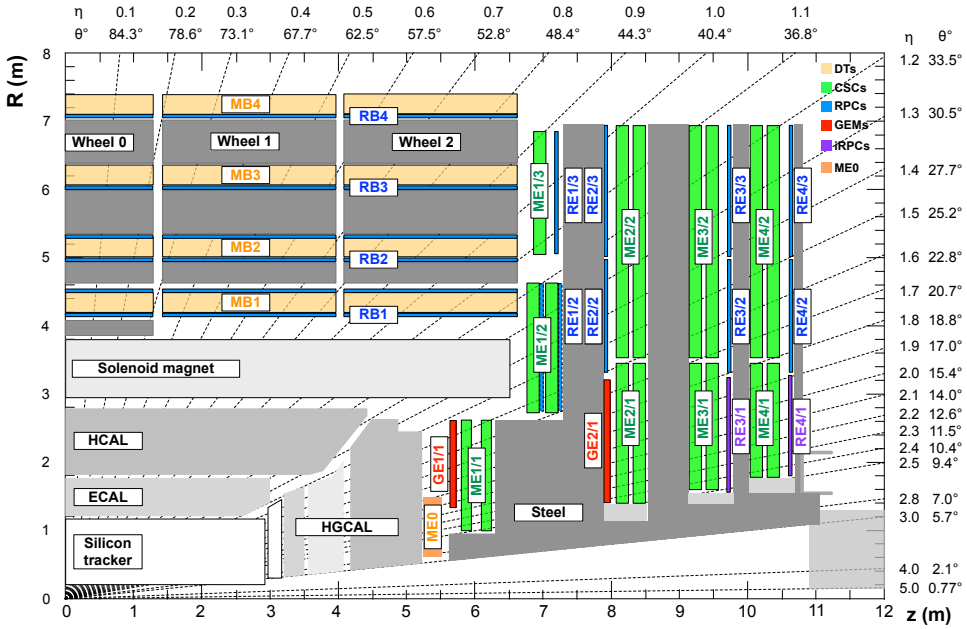

Figure 2.8: Transverse section of a quadrant of the CMS detector, highlighting the muon systems. Figure taken from [113].

In the most recent muon system upgrade, GEMs were introduced in the range $1.6 < |\eta| < 2.4$. Their purpose is to reduce background triggers while maintaining high trigger efficiency for low transverse momentum muons.

2.2.5 The Trigger and Data Acquisition Systems

At design luminosity, the LHC achieves an effective collision rate of up to 1 GHz due to multiple proton-proton interactions occurring within each 40 MHz bunch crossing. This produces a massive amount of data that requires a highly efficient data acquisition system. Since only a small fraction of these events can technically be stored, a two-level trigger system is used to filter the most interesting physics events. Some of the rare events occur at frequencies of less than 1 Hz, allowing for efficient data collection while rejecting the majority of background events [114].

The trigger system is composed of two levels. The first is the Level-1 Trigger (L1T), which provides a fast, hardware-based selection of wanted events. Using trigger primitives from the ECAL, HCAL and Muon systems, the L1T applies predefined selection criteria. If an event meets these criteria, a Level-1 Accept (L1A) signal is generated, with a latency of 3.9 μs. During this latency, data from all subdetectors recorded for this event are buffered

and sent to the central Data Acquisition (DAQ) system if accepted. This reduces the frequency of read out events to 100 kHZ

The second level is the High-Level Trigger (HLT), which performs more detailed event processing through software-based algorithms on a large CPU farm. The HLT reduces the data rate further by selecting the relevant events based on their physics content. It can allocate more time for decision-making ($\geq$ 40 ms per event), enabling the use of more complex algorithms than L1T. Data is buffered and processed by the Readout Builder Network (RBN), which operates at transfer rates up to 800 Gbs, before reaching the data storage.

The entire process is monitored and controlled by the Run Control and Monitor System (RCMS), which interfaces with both the DAQ and Detector Control systems, ensuring smooth operation and data flow throughout.

2.3 Physics object reconstruction

Reconstruction refers to the process of interpreting raw data from a particle detector to identify and measure the properties of particles produced in high-energy collisions, also known as physics objects. The reconstruction of all final state objects produced in a pp collision in the CMS detector implies the identification of particles such as electrons, muons or jets from the raw data acquired by the detector subsystems. It is the first step for starting a measurement and separate the signal events from the background contributions. Particles are identified, and their kinematic properties measured by combining the information coming from the various subdetectors.

The Particle Flow algorithm

CMS uses the Particle Flow (PF) [115] algorithm to reconstruct all stable or long-lived particles in an event by performing a global identification combining information from the different subdetectors. PF provides a list of candidates classified as photons, electrons, muons, jets, and their energy-momenta four-vectors, and observables such as p_T^{miss}. It aims to achieve a high-resolution reconstruction and efficient identification of these particles. The concept is illustrated in Figure 2.9

The first step is the reconstruction of the different PF elements: tracks from the tracking system (section 2.2.2), energy clusters from the calorimeters (section 2.2.3) and muon candidates from the muon system (section 2.2.4).

The tracking system provides precise measurements of charged particle trajectories combining the information from the pixel and the strip trackers with the muon systems.

Figure 2.9: The Particle Flow algorithm achieves a full event reconstruction by identifying and reconstructing all final-state particles, including photons, electrons, muons, charged hadrons, and neutral hadrons. Figure taken from [115].

These tracks are extrapolated (or interpolated for the muons) to the calorimeters and are matched to the clusters, which are defined as the deposited energy in adjacent calorimeter cells. The combination of this information is known as *block*.

The PF algorithm employs unique criteria to identify and distinguish particles from each other. The cleanest signal comes from the muon system, therefore muons are the first to be identified. The second reconstructed candidates are electrons, which creates photons coming from bremsstrahlung processes, these electrons are identified by extrapolating and matching the tracks to the Electromagnetic Calorimeter (ECAL) clusters. The remaining tracks are considered to come from charged hadrons, which are reconstructed from the track information and matched to the cluster energies in the calorimeters. Finally, the energy clusters that are not associated to any particle track are attributed to photons and neutral hadrons.

Primary vertex reconstruction

The collision between proton bunches generates multiple interactions that are spread along the beam axis, as illustrated in Figure 2.10. The location and the associated uncertainty of pp interaction vertices in each event is reconstructed by combining information from the available reconstructed tracks, see section 6.3. The primary vertex (PV) is the interaction point with the largest value of the sum of associated p_T^2 and represents a hard scattering process. The other vertices are referred to as pileup vertices and are important to correct the Monte Carlo (MC) simulations.

For PV reconstruction, the first step is to select the tracks. The reconstructed tracks need to fulfill a set of quality criteria such as being produced promptly in the primary inter-

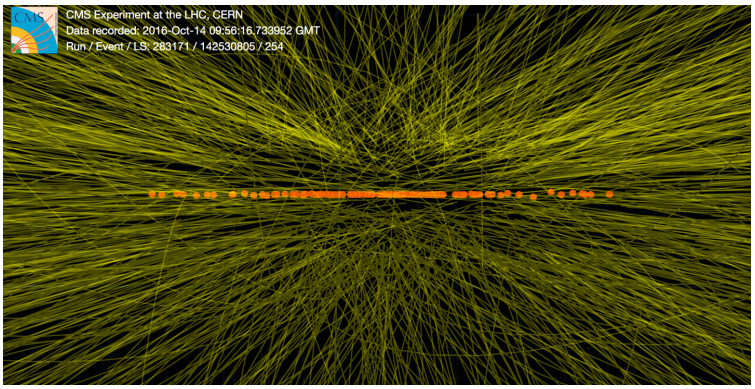

Figure 2.10: The image depicts a collision event captured by the CMS detector during the 2016 data collection period. The yellow lines in the image correspond to the reconstructed tracks of particles, while the orange dots represent the reconstructed interaction vertices. Figure taken from [116].

action region, having a maximum significance value of the transverse impact parameter with respect to the center of the beam spot and having a minimum amount of strip and pixel hits associated with a track. The chosen tracks are then grouped based on their z-coordinates at the point where they are closest to the center of the beam spot. After the identification of vertex candidates, an adaptive vertex fitter is used to determine the x, y and z coordinates of the vertex [117].

Muon reconstruction

There are two types of tracks pertaining to muon reconstruction: the ones that are reconstructed in the muon system, known as standalone muon track, and the tracker tracks which are reconstructed in the inner tracker. Initially, those tracks are independently reconstructed and then used as input for the muon track reconstruction.

In CMS, the muon reconstruction uses two approaches, which are based on either reconstructing a Global muon or reconstructing a Tracker muon.

Global muon tracks are built by matching standalone-muon tracks with tracker tracks. Signals from cathode strip chambers (CSC), drift tubes (DT) and resisistive plate chambers (RPC) are reconstructed to determine the muon hit positions and its timing information. By applying the Kalman-filter technique to combine this information, standalone-muon tracks are formed. Upon finding a match, the algorithm determines the best trajectory by fitting the tracks and segments in the muon detectors. From this fit, the transverse momentum (p_T) of the muon is precisely determined, using the curvature induced by the magnetic field and the energy losses in the calorimeters.

Tracker-muon tracks are built the other way around, starting from tracker-tracks with high p_T that are then propagated to the muon system. If there is a signal from at least one DT or CSC segment that matches the extrapolated track, a tracker-muon track is constructed.

The efficiency for reconstructing a muon, either as a global muon track or as a tracker muon track, within the acceptance of the muon system is approximately 99% [118].

Electron and photon reconstruction

Electrons, being charged particles, produce hits in the silicon tracker while also leaving energy deposits in the ECAL. Photons deposit energy in the ECAL as well but, being neutral particles, do not leave a trace in the silicon tracker [108].

As an electron or photon travels through the tracker, it may interact. The electron can emit bremsstrahlung photons, while the photon may be converted into an electron-positron pair. Thus, when they reach the ECAL, they are no longer a single particle but a shower coming from multiple electrons or photons. In the case of photons, the shower is expected to be less smeared, since the tracks are not bent.

For reconstructing photons or electrons, the first step is to identify energy clusters in the ECAL, which are groups of adjacent detector elements that have recorded energy deposits. Cluster formation involves grouping together consecutive crystals with energy deposits above a specific threshold. The next step involves combining these clusters to form a super cluster (SC), which helps in grouping together the electrons and photons from bremsstrahlung and pair conversion, thus allowing the measurement of the primary particle's total energy. Among these clusters, the one with the highest energy in a specific region is selected as the seed cluster, which serves as the center of the super cluster.

The electron curvature changes when loosing energy for bremsstrahlung and the energy loss distribution is non-Gaussian. Therefore, all electron/photon candidates in the event are fitted with a dedicated algorithm based on a Gaussian sum filter (GSF) [119]. If the track is compatible with an electron trajectory it is matched with a SC and becomes an electron candidate. The reconstructed SC with no matching tracks are identified as photons candidates.

Jet reconstruction

Quarks and gluons emitted in a collision cannot exist freely due to color confinement (chapter 1). Instead, they undergo a process called hadronization, in which they fragment into a shower of stable hadrons, such as protons, neutrons or pions. These hadrons are

emitted in a collimated cone around the original parton's direction. Therefore, they are grouped as a single object referred to as jet. The hadronic jets are reconstructed with the anti-k_{T} algorithm [120]. The algorithm defines a distance measure between pairs of particles, defined as:

$$d_{ij} = \min\left(\frac{1}{p_{\mathrm{T},i}^2}, \frac{1}{p_{\mathrm{T},j}^2}\right) \frac{\Delta R_{ij}^2}{R^2} \tag{2.5}$$

where $p_{\mathrm{T},i}$ and $p_{\mathrm{T},j}$ are the transverse momenta of particles i and j, ΔR_{ij} is the angular distance between particles i and j in the rapidity-azimuthal plane, and R is the cone size.

The distance between a particle i and the beam is also computed,

$$d_{iB} = \frac{1}{p_{\mathrm{T},i}^2}. \tag{2.6}$$

This distance is used to determine whether a particle is sufficiently isolated from the beam to be considered itself as a jet. If $d_{iB} < d_{ij}$ then particle i is identified as a jet and removed from the list of particles. Otherwise, particles i and j are clustered into a jet and the four-momentum vector of the new object is computed. This is repeated until all particles are clustered into jets. Therefore, the total momentum of the resulting jet is defined as the sum of the momenta of its constituent particles.

To mitigate the effects of pileup vertices, charged PF candidates not associated to the PV are excluded from the clustering procedure by the charged hadron subtraction algorithm (CHS) [121]. To further account for neutral particles, pileup-per-particle-identification (PUPPI) [122] algorithm is used. It estimates the probability of each particle to have originated from pileup by assigning a weight and removes the neutral hadron contributions. PUPPI is an extension of the CHS algorithm, also shown in Figure 2.12.

B-Jets identification

Jets can be categorized into two main types: light flavor jets and heavy flavor jets. Light flavor jets typically arise from the fragmentation of gluons or up, down, or strange quarks. On the other hand, heavy flavor jets originate from the fragmentation of bottom or charm quarks. Jets coming from b quarks, also called b jets, play a crucial role in top quark reconstruction, since top quarks decay almost exclusively into a b quark and a W boson. The presence of a b jet in an event serves as a manifestation for a possible top quark candidate. Identification of b jets (b-tagging) is based on the properties of b-flavoured hadrons, namely their large mass and in turn long lifetime of about 1.5 ps [17]], with the corresponding decay length of few mm leading to a corresponding secondary vertex signature in the tracker, as illustrated in Figure 2.11.

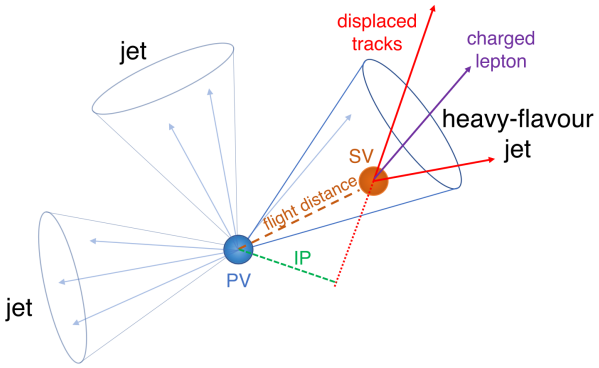

Figure 2.11: Schematic representation of a b jet, where a b hadron travels a few millimeters from the primary vertex (PV) before it decays, resulting in a secondary vertex (SV) and displaced tracks, as well as a charged lepton. Figure taken from [123].

Furthermore, in the b hadron decay chain it is common to encounter leptons, in particular muons. These two properties are used in machine learning based classifiers algorithms specially designed to distinguish b jets from c and light flavor jets, such as [124].

Missing transverse momentum

Missing transverse momentum refers to the imbalance in detected transverse momentum in a collision event. It arises when some particles produced in the collision escape detection or are undetected. This can happen if the particles are neutrinos, which interact weakly with the detector and escape it without leaving a trace. Another possibility is the generation of weakly interacting neutral particles such as hypothetical dark matter candidates that are unlikely to interact with the material of the detectors.

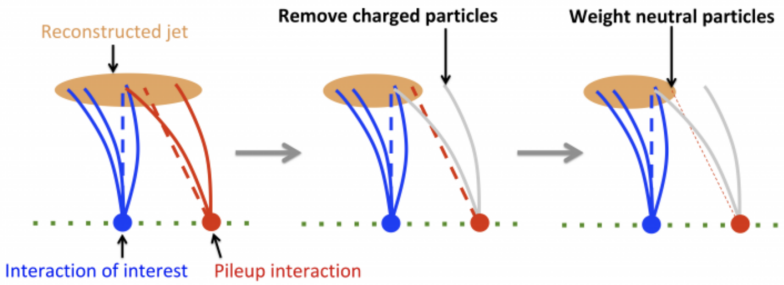

Figure 2.12: Mitigation of pileup effects in jet reconstruction. Pileup contributions are mitigated from jets through two methods: subtracting charged hadron energies (CHS, middle) or weighting the particle four momenta based on their probability of originating from the primary vertex (PUPPI, right). Figure taken from [125].

The missing transverse momentum, $p_{\mathrm{T}}^{\mathrm{miss}}$, is defined as the negative vector sum of the momenta in the plane perpendicular to the beam of all reconstructed particles in an event:

$$p_{\mathrm{T}}^{\mathrm{miss}} = \left|\vec{p}_{\mathrm{T}}^{\,\mathrm{miss}}\right| = \left| - \sum_{i}^{N_{PFobj.}} \vec{p}_{\mathrm{T},i} \right|. \tag{2.7}$$

Since $p_{\mathrm{T}}^{\mathrm{miss}}$ reconstruction uses every reconstructed particle coming from the PF algorithm, any additional correction to the reconstruction such as jet and lepton energy corrections must be propagated to $p_{\mathrm{T}}^{\mathrm{miss}}$. It is also sensitive to contributions from pileup. For mitigating this effect, the PUPPI missing transverse momentum coming from PUPPI jets is used.

CHAPTER 3

CMS Outer Tracker Upgrade for HL-LHC

Contents

In particle physics experiments, tracking detectors are fundamental to reconstruct the trajectories of charged particles and infer their basic properties, such as momentum and charge. Track reconstruction becomes particularly challenging in a high-pileup environment. For this purpose, various detector technologies have been developed and are continuously improved. The silicon-based detectors are chosen for the Outer Tracker of the CMS experiment. Extensive reviews on silicon detectors can be found, e.g. in [126–129].

For the High Luminosity LHC (HL-LHC), the upgrade aims to address the challenges that come with high luminosity, featuring an extended tracking acceptance, reduced material budget, increased radiation tolerance, and improved granularity. The upgrade features a new tracker with the introduction of new silicon detector modules, including the Pixel-Strip (PS) module, which combines strip and so-called macro-pixel sensors. This chapter introduces the basics of silicon tracking detectors and discusses the aspects of the design, assembly, and functionality of the silicon PS modules.

3.1 Silicon Tracking Detectors

Tracking detectors, designed to map charged particle trajectories and infer momentum and charge, play a crucial role in particle physics experiments like CMS. In high-luminosity environments, where many interactions occur simultaneously, tracking efficiency and spatial resolution are vital. Silicon semiconductor detectors are preferred due to their ability to generate and process signals from drifting electron-hole pairs created by incident charged particles. Silicon's low ionization energy and good compatibility with microelectronics enable the production of fast signals in lightweight and large area sensors, which is essential for experiments with high collision rates like those at the LHC.

Interaction of charged particles with matter

Charged particles, such as protons, electrons, and ions, interact with matter primarily through electromagnetic force. As these particles traverse a material, they lose energy via ionization and excitation of the atoms along their path. This process leads to a signal formation in a tracking detector.

The energy loss per unit distance traveled by a charged particle is quantitatively described by the Bethe-Bloch formula [130]:

$$-\frac{dE}{dx} = 4\pi m_e r_e^2 z^2 c^2 \rho \frac{N_A Z}{A} \frac{1}{\beta^2} \left[\frac{1}{2} \ln \frac{2m_e \gamma^2 \beta^2 c^2 T_{max}}{I^2} - \beta^2 - \frac{\delta(\beta\gamma)}{2} - \frac{C(\beta\gamma, I)}{Z} \right] , \quad (3.1)$$

where z and β are charge and velocity of the projectile particle, Z and A are atomic number and atomic mass of the medium, respectively, I is the mean excitation energy, T_{max} is the maximum possible energy transfer to a shell electron during a central collision, δ accounts for the density correction, which is significant at high energies, and C/Z is a shell correction, relevant for small β values. Additionally, m_e is the mass of the electron, r_e is the classical electron radius, c is the speed of light in a vacuum, ρ represents the density of the material through which the particle travels and γ is the Lorentz factor.

The energy loss described by Eq. (3.1) accounts primarily for ionization and excitation processes. However, at higher incident energies, radiation losses, particularly Bremsstrahlung, become increasingly significant and must be considered.

Fig. 3.1 illustrates the differential energy loss for muons across various incident particle momentum regimes. In the Bethe regime, which spans from approximately 5 MeV/c to 5 GeV/c, the minimum ionization represents the lowest energy deposited in the absorbing material. A particle at this energy is referred to as a Minimum Ionizing Particle (MIP).

The Bethe-Bloch formula predicts the average energy loss of charged particles as they pass through a material, but this energy loss varies significantly around the average due

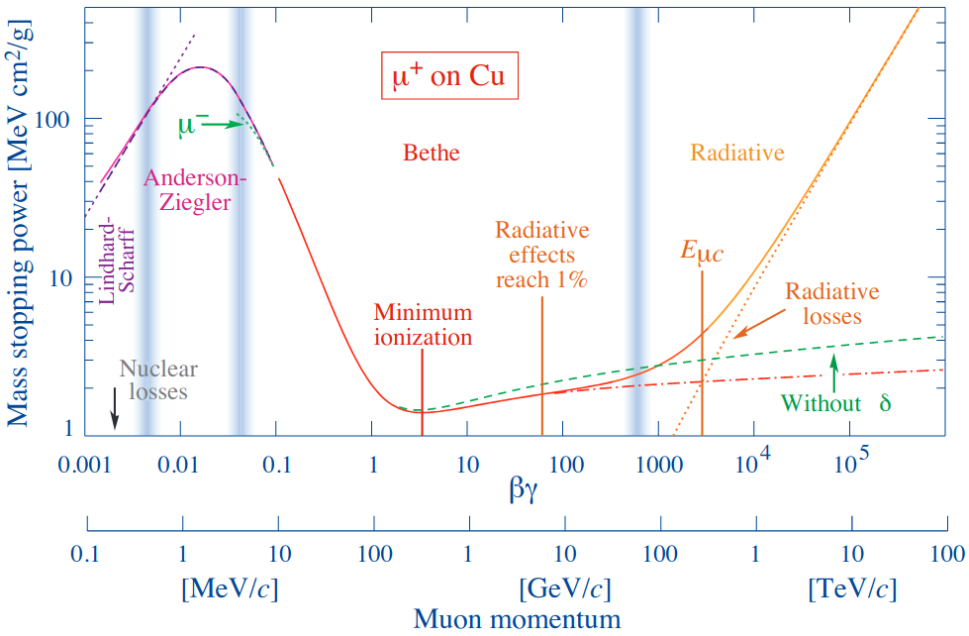

Figure 3.1: Mass stopping power $< -dE/dx >$ for positive muons in copper as a function of $\beta\gamma = p/Mc$ and momentum. The solid curve indicates the total stopping power. Figure taken from [17].

to statistical fluctuations. These fluctuations are described by the Landau-Vavilov distribution, which characterizes the probability of energy loss by charged particles. The distribution is asymmetric, resembling a Gaussian curve with a pronounced tail towards higher energy losses. This tail is largely due to the presence of δ-electrons, knocked out of their atomic orbits by the passing charged particle, with sufficient energy to cause further ionization in the material.

The total number of electron-ion pairs created, is derived from the total energy loss experienced by the particle. This total ionization is influenced by both primary ionization (direct ionization by the incident particle) and secondary ionization (caused by delta electrons).

3.1.1 Semiconducting detectors and silicon sensors

Semiconductors are materials with electrical properties that lie between those of conductors and insulators, making them essential in particle detection. Their defining feature is the distinct energy band structure: the valence band, fully occupied by electrons, and the conduction band, which is partially filled or empty. The energy gap between these bands, known as the bandgap, is crucial for their behavior. In silicon, a widely used

semiconductor, the bandgap is 1.12 eV. At room temperature, this allows electrons to thermally excite from the valence to the conduction band, enabling controlled conductivity. At lower temperatures, semiconductors behave like insulators as fewer electrons gain enough energy to cross the bandgap.

The semiconducting properties of silicon make it an ideal material for tracking detectors. When a charged particle traverses a silicon detector, it deposits energy, exciting electrons from the valence band to the conduction band and creating electron-hole pairs. In this context, a "hole" represents the absence of an electron in the valence band. As electrons move to the conduction band, these vacancies, or holes, can also move through the lattice as positive charge carriers, contributing to electrical conductivity.

Figure 3.2 provides a schematic representation of the working principle of a semiconducting detector. The illustration shows how a passing charged particle ionizes the silicon, generating electron-hole pairs, which are then separated and collected under the influence of an applied electric field. This charge collection enables the detection of the particle's path and energy deposition.

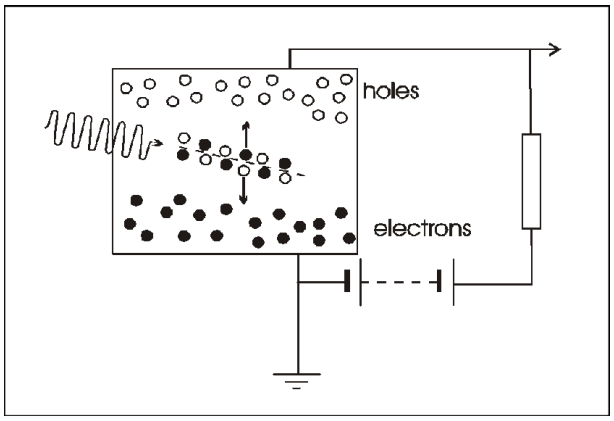

Figure 3.2: Semiconductor detector principle. Figure taken from [131].

Due to silicon's relatively low ionization energy (W=3.62 eV), it generates a high number of charge carriers compared to other materials like diamond or gaseous detectors. This property reduces statistical fluctuations in the number of charge carriers produced, a key factor for achieving high precision in particle tracking.

Statistical fluctuations in charge carrier production are further minimized in silicon by the Fano factor, which quantifies deviations from the Poisson distribution typically expected in ionization processes. For silicon, the Fano factor is approximately 0.115, which significantly reduces statistical noise. This correction distinguishes silicon detectors from larger, irregular energy loss fluctuations described by the Landau-Vavilov distribution, enhancing their precision.

These properties, combined with silicon's robust performance and scalability, make it the material of choice for the majority of modern tracking detectors in particle physics, including the CMS tracker.

The pn-Junction

The conduction properties of semiconductors like silicon can be regulated through so-called doping, by introducing impurity atoms. When silicon is doped with a group-V element, such as arsenic, it introduces an extra loosely bound electron near the conduction band, creating what is known as n-type silicon. This additional electron can be easily excited into the conduction band, enhancing the material's conductivity. Conversely, doping silicon with a group-III element, such as boron, creates an incomplete bond that introduces an acceptor level just above the valence band. This level tends to attract an electron from a neighboring silicon atom, resulting in the creation of a hole in the valence band, forming p-type silicon. These two types of doped silicon, n-type and p-type, are fundamental in semiconductor technology, allowing for controlled manipulation of electrical properties.

When a minimum ionizing particle traverses a silicon sensor of 300 μm, the expected number of generated charge carriers is around 10^9, nonetheless, the expected signal is only about 10^4. To distinguish the signal from this noise contribution, it is necessary to reduce the number of free charge carriers. For this purpose, a pn-junction is formed by combining p-doped and n-doped silicon. In the p-doped region, holes dominate, with the Fermi level (theoretical energy level at which an electron has a 50% probability of being occupied at thermodynamic equilibrium.) near the valence band, while in the n-doped region, electrons are the majority carriers, with the Fermi level near the conduction band. At the interface between these regions, a diffusion current arises as electrons and holes move across the boundary and recombine, forming a depletion zone devoid of free charge carriers.

The depletion zone creates a space-charge region (SCR) due to the remaining ionized atoms, which produces an electric field that prevents further diffusion and maintains the depletion of free carriers. Fig. 3.3 illustrates the SCR, highlighting the space charge across the junction.

The electrostatic potential $\Phi(x)$ across the SCR can be expressed as:

$$\Phi(x) = \begin{cases} -\frac{N_A}{2\epsilon_r\epsilon_0}(x+d_p)^2, & -d_p < x < 0 \text{ (p-doped region)} \ , \\ \frac{N_D}{2\epsilon_r\epsilon_0}(x+d_n)^2, & 0 < x < d_n \text{ (n-doped region)} \ , \end{cases} \tag{3.2}$$

where d_p and d_n are the boundaries of the depletion region, N_A and N_D are the doping concentrations, and ϵ_r and ϵ_0 are the relative permittivity (or dielectric constant) of the

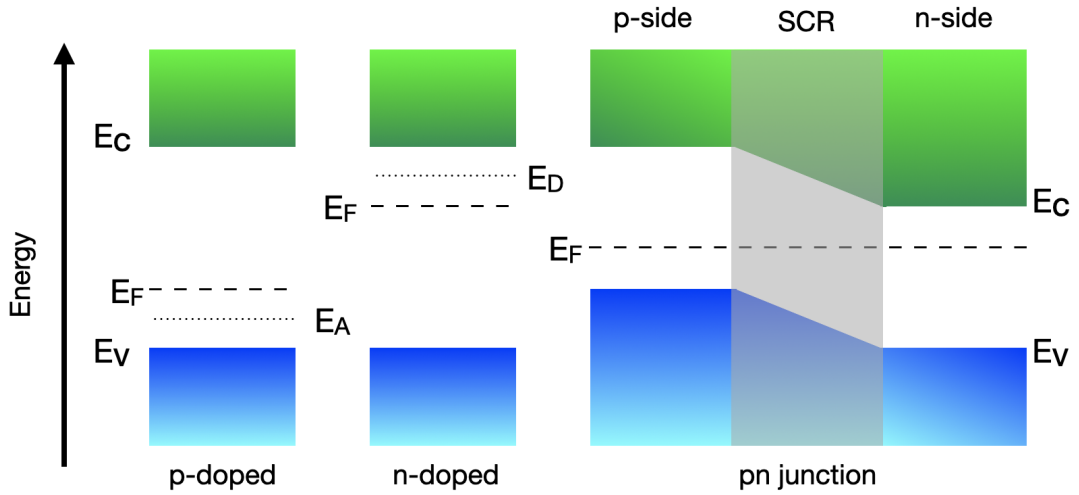

Figure 3.3: Band structure and energy levels of n-doped and p-doped silicon. The acceptor (E_A, left) and donor (E_D, center) energy levels introduced by the dopant alter the Fermi energy E_F of the material. When joining them (right) a common Fermi level develops and a space-charge region (SCR) forms.

material and the vacuum permittivity respectively. The built-in voltage U_{bi} across the pn-junction caused by the remaining ionized atoms is given by:

$$U_{bi} = \frac{|N_{\text{eff}}| \cdot d^2}{2\epsilon_r \epsilon_0} \quad , \tag{3.3}$$

where d is the total thickness of the SCR, and $N_{\text{eff}} = N_D - N_A$ is the effective doping concentration.

Applying an external bias voltage U_{bias} can adjust the SCR thickness $d(U_{\text{bias}})$, calculated as:

$$d(U_{\text{bias}}) = \sqrt{\frac{2\epsilon_r \epsilon_0}{N_{\text{eff}}} \cdot (U_{\text{bias}} - U_{bi})} \quad . \tag{3.4}$$

This voltage can either increase or decrease the extent of the depletion region, referred to as reverse biasing or forward biasing, respectively. The depletion voltage U_{dep}, at which the SCR and the electric field span the entire sensor thickness D, is:

$$U_{\text{dep}} = \frac{|N_{\text{eff}}| \cdot D^2}{2\epsilon_r \epsilon_0} \quad . \tag{3.5}$$

Typically, U_{dep} ranges from few tens of V to 500 V for silicon sensors in particle physics. The capacitance C of the sensor depends on the SCR thickness and therefore the U_{bias} as shown in Eq. (3.4), and is given by:

$$C = \frac{A_{\text{pn}}\epsilon_r\epsilon_0}{d(U_{\text{bias}})} \propto \begin{cases} \sqrt{\frac{\epsilon_r\epsilon_0|N_{\text{eff}}|}{2U_{\text{bias}}}}, & \text{for } U_{\text{bias}} \leq U_{\text{dep}} \\ \frac{\epsilon_r\epsilon_0}{D}, & \text{for } U_{\text{bias}} > U_{\text{dep}} \end{cases} . \tag{3.6}$$

Here, A_{pn} is the p-n junction surface area. The capacitance can be used to measure the depletion voltage. At full depletion, C decreases with higher bias voltage, allowing U_{dep} to be identified from a measurement of the capacity as a function of U_{bias}.

If the bias voltage exceeds U_{dep}, an additional electric field forms, leading to a leakage current, also known as reverse current. This current is a crucial property as it impacts the sensor's noise and power consumption. The leakage current is caused by thermally excited electrons and can be exacerbated by impurities or radiation-induced defects. The temperature dependence of leakage current is described by:

$$I(T_2) = I(T_1) \cdot \left(\frac{T_2}{T_1}\right)^2 e^{\frac{-E_{\text{eff}}}{2k_B}\left(\frac{1}{T_2}-\frac{1}{T_1}\right)} , \tag{3.7}$$

where $E_{\text{eff}} = 1.21$ eV is the effective bandgap energy. Operating the sensor at lower temperatures reduces leakage current.

The comprehensive understanding of the pn-junction, depletion voltage, capacitance, and leakage current is crucial for optimizing the design of silicon sensors for particle detection.

Sensor Segmentation

Most modern silicon sensors are built using planar structures, with the silicon wafer, or sensor bulk, typically produced through the Float Zone (FZ) [132] process, which allows for specific resistivity in silicon ingots. Alternative methods like Czochralski (Cz) or Magnetic Czochralski (MCz) [132] are also used, offering better radiation hardness after being sliced into wafers. The silicon bulk undergoes photolithographic structuring, etching, implantation, and material deposition to create position-sensitive devices.

The surface of the silicon bulk is segmented into strips or pixels acting as electrodes to detect the location of charge carriers generated by a traversing particle. The simplest example of segmentation is the p-in-n sensor, as shown in Figure 3.4 (left). In a common p-in-n sensor configuration, p^+ doped implants are placed on the n doped bulk's surface, with an n^+ doped backplane on the opposite side. These n^+ and p^+ are implants with higher doping concentrations than the bulk. This forms a pn-junction, causing holes to

drift towards the implants and electrons towards the backplane when a particle passes through. An isolation layer, usually made of SiO_2, and a metalization layer on top.

Another configuration, n-in-n sensors (Figure 3.4 right), uses n^+ doped implants in an n-type bulk with a p^+ backplane. This design includes an additional doped region between the n^+ implants, implemented using the p-spray or p-stop technique to manage the electric field and prevent electron accumulation near the surface.

The distance between implants, known as the sensor pitch, is governed by factors like the need for space for readout electronics, the amount of readout channels and the desired granularity and position resolution of the sensor.

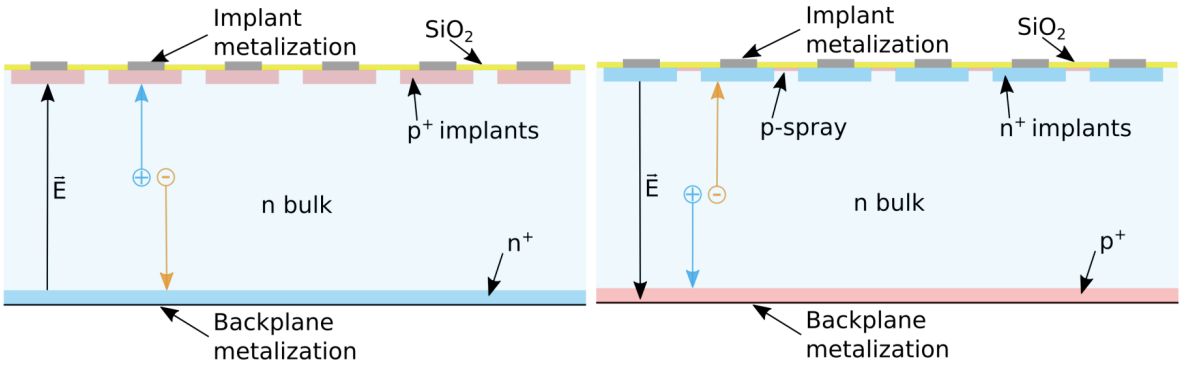

Figure 3.4: The sensor is segmented to achieve high-resolution estimation of particle traversal, as illustrated for both p-in-n (a) and n -in-n (b) sensors. Figure taken from [133].

Signal Formation

Signal formation in silicon sensors comprises the movement of charge carriers (electrons and holes) created by a particle passing through the sensor bulk. These carriers are separated by the electric field from reverse biasing, causing electrons and holes to move towards the sensor's implants or backplane, depending on the bulk doping. As these charge carriers move, a signal is induced on the electrode surface, which can be recorded as a current or voltage.

The critical factor in signal induction is the movement of charge carriers towards the electrodes, not just the collection of charges. This process is described by the Shockley-Ramo Theorem [134, 135]. The key observable is the total induced charge (Q), and the Charge Collection Efficiency (CCE) is defined as the ratio of the total induced charge to the initially deposited charge (Q_0). A good CCE is crucial for the detection performance.

3.1.2 Signal Processing

The signal generated by a particle traversing a silicon sensor typically consist of tens of thousands of electrons collected from a few to hundreds of nanoseconds. This signal is processed by a dedicated Front-End (FE) electronic circuit, which converts the signal into digital data for further analysis.

The charge is first amplified using a Charge Sensitive Amplifier (CSA). The CSA integrates the input current and produces a voltage proportional to the signal charge.

A test charge injection circuit allows the front-end electronics to be tested without the actual sensor connected. This circuit injects a known charge using a calibration capacitor (C_{inj}) to simulate the effect of a particle traversing the sensor.

Pulse shaping is applied to filter the amplifier's voltage step, producing a pulse that returns to the baseline after a finite time. This limits the bandwidth (reducing electronic noise) and constrains pulse width, ensuring that signals can be distinguished from each other. For example, detectors at the LHC require a timing precision of at least 25 ns, necessitating that the rise time of the shaped signal is below this threshold.

Signal discrimination distinguishes particle-induced signals from noise. A discriminator identifies analog signals exceeding a predefined voltage threshold. This allows noise signals below the threshold to be filtered out, optimizing the threshold to detect low signals, while excluding noise.

The final stage in the signal processing chain is the readout stage, where the digital signal undergoes further processing, such as determining the particle's position in the sensor, time of arrival, or signal amplitude. In high-energy physics experiments like those at the LHC, this stage often includes an on-chip buffering connected to a trigger system that selects a fraction of the recorded hits to be transmitted and stored centrally for detailed analysis, reducing the data volume transmitted to the back-end system for further processing like particle track reconstruction or momentum measurement.

3.1.3 Noise

During the operation of silicon sensors, the signal generated by a traversing particle competes with the statistical fluctuations happening inside the volume of the detector. These fluctuations come from multiple sources and are collectively referred to as noise. It is essential to ensure that the noise levels are minimized, as the signal from traversing particles is only detectable if it exceeds the noise generated by the detector. The total noise, quantified as the equivalent noise charge (Q_n), is the result of four main contributions, and its amplitude can be modeled by summing them in quadrature.

The leakage current (I_L) in a sensor, caused by the thermal excitation of charge carriers, is temperature-dependent and can significantly contribute to the overall current, alongside the intended signal from particle excitation and ionization. It introduces a noise component, also known as **shot noise**, which scales with temperature and the signal peaking time (t_p) of the readout electronics. It can be expressed as [129]:

$$Q_{IL} = \frac{e}{2} \cdot \sqrt{\frac{I_L \cdot t_p}{q_e}} \ , \tag{3.8}$$

where e represents Euler's number and q_e is the electron charge.

The second contribution comes from **capacitance noise**, which is dominated by the sensor capacitance (C_d). This capacitance is primarily determined by the area of the sensor implant. The noise due to capacitance is given by [129]:

$$Q_{Cd} = a + b \cdot C_d \ , \tag{3.9}$$

where a and b are parameters specific to the readout electronics, related to the preamplifier where b is primarily determined by the intrinsic voltage noise of the chip and t_p.

The third contribution is **thermal noise**. It arises from the random motion of charge carriers due to thermal kinetic energy and contributes continuously to the overall noise level. It can be divided into two contributions.

The **parallel thermal noise**, originating from the bias resistance (R_p) scales with temperature and the signal peaking time (t_p) and is described by [129]:

$$Q_{Rp} = \frac{e}{q_e} \cdot \sqrt{\frac{k_B T \cdot t_p}{2R_p}} \ , \tag{3.10}$$

where k_B is the Boltzmann constant and T represents the temperature.

Finally, the **serial thermal noise**, associated with the series resistance (R_S), scales with temperature and is proportional to the sensor capacitance (C_d) [129]:

$$Q_{RS} = C_d \cdot \frac{e}{q_e} \cdot \sqrt{\frac{k_B T \cdot R_S}{6t_p}} \ . \tag{3.11}$$

To mitigate capacitance noise, optimizing the sensor design is essential, while thermal noise can be reduced by cooling the sensor during operation. Pixel detectors by design

exhibit lower noise in contrast to strip detectors that have longer sensor strips which collect charge over a larger area, leading to higher intrinsic noise per channel. Additional noise minimization techniques include shielding the sensor from external interference (electromagnetic interferences and pickup noise coming from surrounding electronics, power supplies or environmental sources) and optimizing the readout electronics, all of which are crucial for maintaining a good signal-to-noise ratio in high-precision silicon sensors.

3.1.4 Radiation Damage

Silicon detectors used in particle physics experiments face substantial damage due to the large number of highly energetic particles traversing them. This radiation exposure leads to alterations in several sensor properties, degrading the detector performance over time. Radiation damage affects silicon sensors primarily through two mechanisms: bulk damage and surface damage. Bulk damage occurs when high-energy particles displace silicon atoms, disrupting the crystal lattice. Surface damage, on the other hand, is caused by ionizing radiation, leading to trapped charges in the insulating layers of the sensor, which in turn causes shifts in the electric fields and increased noise.

Radiation damage in silicon sensors leads to changes in several key properties, significantly affecting detector performance. One of them is the increase in leakage current, which occurs as radiation-induced defects in the silicon bulk create new energy levels within the bandgap. These levels facilitate the thermal generation of electron-hole pairs, thereby increasing the leakage current, which contributes to a rise in the detector's power consumption.

To quantify the radiation exposure of silicon sensors, the neutron equivalent fluence (Φ_{eq}) is used. This measurement standardizes the radiation damage caused by different types of particles, such as neutrons, protons, and pions, by matching their effects to the damage caused by 1 MeV neutrons in silicon. The increase in leakage current is linearly dependent on this fluence, providing a direct relationship between the radiation damage and the operational degradation of the detector, as shown in Figure 3.5.

Although unirradiated sensors typically exhibit negligible leakage current, irradiated sensors can experience a substantial rise in current, especially at higher temperatures, leading to significant power dissipation and heat generation. In case of insufficient cooling, this can cause a thermal runaway, where the device overheats, emphasizing the critical need for efficient cooling systems in radiation-exposed detectors. Further detailed discussions on radiation damage can be found in [136, 137].

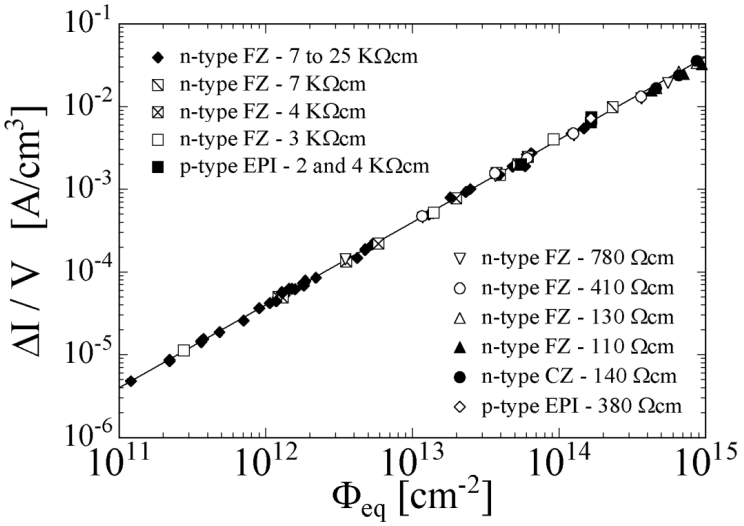

Figure 3.5: Leakage current as a function of neutron equivalent fluence for silicon detectors produced via various fabrication technologies and different bulk doping. Figure taken from [136].

3.1.5 Tracking

Particle tracking is the process of reconstructing the trajectory of charged particles as they pass through a tracking detector in the magnetic field. In high energy physics experiments, the tracking detectors are typically composed of multiple layers arranged in linear or cylindrical configurations. As particles traverse each layers, signals are recorded at the corresponding position of the detector. These records are captured by integrated front-end electronics. The curvature of the particle's trajectory is used to determine its momentum.

The first step in particle tracking is hit clustering, where the goal is to group adjacent sensor channels that were fired by the same particle. The charge deposited by the particle is often collected across multiple sensor implants due to charge diffusion, Lorentz drift in the magnetic field, or the angle at which the particle traverses the sensor. Clustering algorithms are applied to determine the centers of these clusters, representing the most probable position of the traversal, which can then be transformed from local sensor coordinates to a global reference frame for track reconstruction. Several clustering algorithms can be used depending on the charge-sharing topology [138].

Hit clustering plays a critical role in improving the position resolution of the tracking system by ensuring that all the charge generated by the particle is included. The detection process uses a discrimination threshold, and the readout can be binary or non-binary, depending on whether only hit information or the full signal amplitude, respectively, is

recorded. The method for calculating the cluster center differs between these approaches. If part of the charge remains undetected, it can negatively impact the accuracy of position determination.

Based on the cluster information, track reconstruction is performed, by using the cluster positions in a global frame of reference. The effects like multiple scattering, which occurs when particles are deflected by the material along their path, have to be considered. Various tracking algorithms are used depending on the required performance characteristics, such as scalability, speed, or resolution [139]. The best-fitted track is then used to determine the particle's momentum, charge, and the origin (vertex).

3.2 The High Luminosity LHC Upgrade

3.2.1 High Luminosity LHC Upgrade

A significant upgrade of the Large Hadron Collider (LHC) is scheduled for 2026-2029, known as the High Luminosity LHC (HL-LHC) [140] phase. During this period, the LHC is expected to reach peak instantaneous luminosities of up to 7.5×10^{34} cm^{-2} s^{-1} at a center-of-mass energy of 14 TeV. Over a decade, the HL-LHC aims to accumulate integrated luminosities up to 3000 fb^{-1} at the CMS and ATLAS experiments. This upgrade will allow high-precision measurements of rare SM processes and open new possibilities for discoveries beyond the Standard Model. For example, it will enable precise measurements of the Higgs boson's couplings to fermions, including the rare Higgs-muon interaction, as well as the Higgs boson's self-coupling.

To achieve these goals, extensive upgrades to the accelerator complex will be required, which will present significant challenges for the LHC experiments due to increased particle density, data rates, and radiation levels. One of the biggest challenges will be handling pileup (the number of overlapping collisions per bunch crossing), which could reach up to 200. To manage this, the detectors will need upgrades to improve data bandwidth, radiation resistance, and trigger capabilities.

Large Hadron Collider Upgrade

The HL-LHC upgrade will necessitate changes to beam parameters, including increasing the number of particles per bunch, improving beam focusing, increasing the number of bunches in the storage ring, and maximizing the overlap of colliding bunches at the interaction points. These improvements will rely on advanced Nb-Ti and Nb_3Sn superconducting

magnets, superconducting radio-frequency cavities for beam rotation and high-power superconducting links. Novel concepts will also be implemented for beam control, vacuum, cryogenics and machine protection to handle the increased demands on the accelerator complex.

CMS Phase-2 Upgrade

The HL-LHC's higher luminosity will create a more challenging environment for the CMS experiment, demanding improvements in the detector granularity, resolution and pileup mitigation. The increased number of collisions will result in harsher radiation conditions, particularly in the innermost regions of the tracker, where neutron equivalent fluences of 2.3×10^{16} neq/cm^2 will be recorded. To cope with these challenges, various CMS subsystems will be upgraded for improved radiation hardness and new data acquisition and trigger concepts will be introduced.

Key upgrades include the High Granularity Calorimeter (HGCAL) in the Endcap Calorimeter, which will combine silicon sensors and scintillators to provide detailed 3D measurements of particle showers [141, 142]. Another important addition is the MIP Timing Detector (MTD), which will allow precise Time-of-Flight (ToF) measurements with 30 ps precision, significantly mitigating the pileup by distinguishing spatially adjacent collisions in time [143].

The upgraded Silicon Tracker will play a critical role in handling the increased data, featuring more channels, better spatial resolution, and enhanced pseudo-rapidity coverage for improved track and vertex reconstruction. A novel p_T discrimination system will be introduced in the Outer Tracker, allowing it to contribute directly to the Level-1 Trigger by selecting high transverse momentum tracks. This feature will help to sustain the new target trigger rate of 750 kHz.

This thesis primarily focuses on the upgrade of the CMS Tracker, with a particular emphasis on the Outer Tracker. The next section outlines the major advancements and highlights the key concept of transverse momentum (p_T) discrimination. Additionally, it delves into the design and implementation of this concept within the corresponding tracker modules, specifically focusing on one of the two module designs, the Pixel-Strip (PS) module, covering the mechanical and electronic design, the assembly process, the quality control tests focusing on the burn-in test where modules are exposed to temperature cycles from room temperature to operation temperature during at least 24h (chapter 4) and integration of modules into the detector structure (chapter 5).

3.3 Outer Tracker Phase-2 Upgrade

The HL-LHC is designed to reach peak instantaneous luminosities of up to $7.5\times10^{34}\,\mathrm{cm^2s^{-1}}$. This will allow CMS and ATLAS to collect integrated luminosities of the order of $300\,\mathrm{fb^{-1}}$ per year and up to $3000\,\mathrm{fb^{-1}}$ during the HL-LHC projected lifetime of ten years. The HL-LHC is expected to operate at a centre-of-mass energy of 14 TeV and with a bunch spacing of 25 ns.

The current CMS tracker was designed to operate efficiently at an instantaneous luminosity of $1.0\times10^{34}\,\mathrm{cm^{-2}s^{-1}}$, handling an average pileup of 20-30 collisions per bunch crossing and an integrated luminosity of up to 500 $\mathrm{fb^{-1}}$. However, with the expected radiation damage, particularly in the innermost layer where a fluence of $3.6\times10^{15}\,\mathrm{neq/cm^2}$ is anticipated, the performance of the tracker will degrade, affecting the pixel charge collection efficiency, resolution, and strip tracker sensor properties among others. As a result, the current tracker will need to be replaced for the HL-LHC phase.

The Phase-2 Upgrade of the CMS tracker will introduce significant improvements, incorporating new concepts and design modifications to meet the rigorous performance requirements necessary for achieving the CMS physics goals. The upgrade will consist of an Inner Tracker (IT) made of silicon pixel detector modules and an Outer Tracker (OT) with detector modules combining strip and macro-pixel silicon sensors, as shown in Figure 3.6.

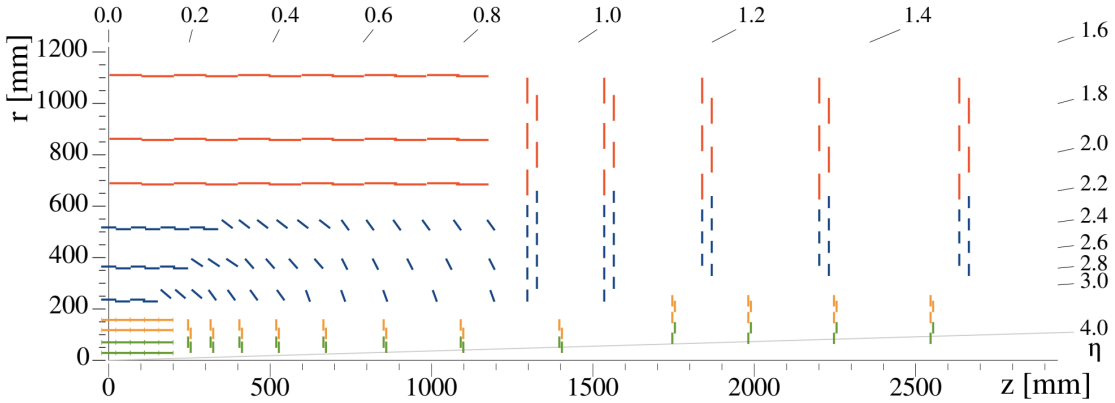

Figure 3.6: Schematics of a quarter of the tracker layout in r-z view indicating the position of the Inner Tracker in green and yellow, and the Outer Tracker in red and blue. Figure taken from [107].

Key goals for the Phase-2 tracker upgrade include extending the tracking acceptance up to a pseudo-rapidity of $|\eta| = 4$, reducing the material budget to enhance calorimetry performance and overall event reconstruction, ensuring radiation tolerance and full efficiency

at an integrated luminosity of up to 3000 fb^{-1} without maintenance for the Outer Tracker, increasing granularity to maintain low readout channel occupancy under high pileup conditions, contributing to the Level-1 trigger to manage the increased event rate, improving two-track separation for better track finding in energetic jets, and implementing robust pattern recognition for efficient track finding, especially at the High Level Trigger.

The Phase-2 tracker upgrade has several key goals. It aims to extend the tracking acceptance up to a pseudo-rapidity of $|\eta| = 4$ and reduce the material budget to improve calorimetry performance and event reconstruction. Additionally, it must ensure radiation tolerance and maintain full efficiency up to 3000 fb^{-1} of integrated luminosity without requiring Outer Tracker maintenance. It also aims to increase granularity to keep readout channel occupancy low in high pileup conditions, contribute to the Level-1 trigger to handle the higher event rate, enhance two-track separation for better track finding in energetic jets, and implement robust pattern recognition for efficient track finding, especially at the High Level Trigger.

3.3.1 Transverse Momentum Discrimination

In the HL-LHC phase, the CMS Level-1 Trigger (L1) system will play a crucial role in managing the increased data rate by selecting events characterized by higher particle momenta. To realize this selection, the Outer Tracker will include modules with fast on-board momentum discrimination capabilities, allowing the system to tag high-momentum particles before they reach the triggering system.

This on-board transverse momentum (p_T) discrimination is achieved using a combination of a strong magnetic field (3.8 T in CMS) and a stack of two closely spaced silicon sensors. When charged particles pass through the magnetic field, they are bent according to their p_T, with low p_T particles having a large curvature, whereas high-p_T particles follow straighter paths. Therefore, the module can discriminate between them by fixing a programmable search window. The spatial displacement between the signals (hits) in the bottom (seed layer) and top (correlation layer) sensors depends on the particle's p_T, assuming they come from the IP. Hits within a programmable search window are combined to form a "stub", a short track segment that signifies a particle with a p_T above the threshold. The search window in CMS will be set to reject particles with a p_T below 2 GeV, however this threshold can be changed if needed. These stubs will serve as the Outer Tracker's contribution to the Level-1 Trigger. A schematic representation of the concept is shown in Fig. 3.7.

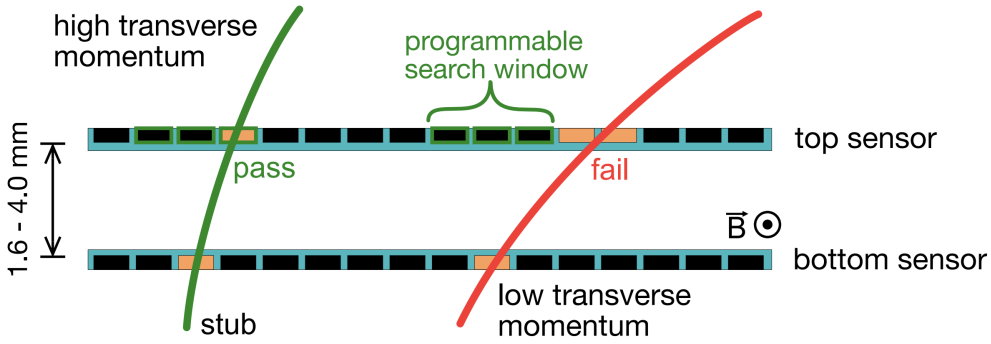

Figure 3.7: Illustration of the transverse momentum discrimination concept. Figure taken from [144].

3.4 PS Module

In the Outer Tracker, the p_T discrimination concept is implemented in two types of modules: Strip-Strip (2S) modules and Pixel-Strip (PS) modules. Both module types use a stack of two silicon sensors, manufactured as high-resistive n-on-p technology, and are separated by dedicated spacers. The PS modules, which are the focus of this work, use Aluminium-Nitride (Al-N) spacers, and they come in three spacing variants: 1.6 mm, 2.6 mm, and 4.0 mm, ensuring consistent p_T discrimination across different module positions in the detector.

The PS module is designed with a higher granularity, featuring a macro-pixel sensor (PS-p) on the bottom and a strip sensor (PS-s) on top, to handle the higher track density in the inner regions of the Outer Tracker. This design helps to maintain acceptable occupancy levels and provides sufficient resolution. The front-end electronics in the PS modules are implemented as four hybrid circuits, which include two Front-End Hybrids (FEHs) responsible for reading out the sensors and processing the data. Additionally, the PS modules feature separate Power and Readout Hybrids for power distribution and data transmission, respectively. At the Deutsches Elektronen Synchrotron (DESY) laboratory, more than 1120 PS modules with a spacing of 4.0 mm will be assembled.

3.4.1 PS module layout

The PS module silicon sensors are designed primarily with radiation hardness in mind, crucial for operating efficiently over a projected 10-year lifespan in a high luminosity environment. The sensors are made from high-resistivity float zone silicon using n-on-p

technology. The design ensures an adequate signal-to-noise ratio for minimal ionizing particles under extreme fluence conditions. Two types of sensors are used: AC-coupled strip sensors (PS-s) and DC-coupled macro-pixel sensors (PS-p), each manufactured on 6-inch wafers with the thicknesses and implant configurations selected to ensure stability and performance. Fig. 3.8 shows an exploded view of a PS module, showing all components and their assembly.

The PS-s sensor features an active volume of 290 µm thickness and a surface of 98.14 × 49.16 mm^2, with 960 AC-coupled strips on each long side. Each strip is 23.472 mm long, with a pitch of 100 μm, which affects the sensor's high voltage stability and interstrip capacitance. Maintaining a proper width-to-pitch ratio helps balance the electric field, reducing the risk of discharges or other high-voltage instabilities while ensuring efficient signal collection. The strip implants are connected to a global biasing system using polysilicon resistors.

The PS-p sensor has a similar active thickness and surface area, but it features a macro-pixel matrix of 32 × 960 DC-coupled cells. The macro-pixels are arranged with a pitch of 100 μm for normal cells and 200 μm for edge cells. The larger edge pitch helps in simplifying the readout architecture and managing boundary effects while ensuring the overall performance remains effective for tracking. This difference in pitch across the sensor balances resolution in the active area and stability near the edges. Punch Through Structures are employed to connect each pixel to the global bias grid.

The Front-end electronics for the PS module comprise various circuits for processing and transmitting data. The complex data handling is achieved through a system that reads out data from individual strips and pixels and transmits it to the back-end system via optical links.

The PS-s sensor's data is read out by Short Strip ASICs (SSAs) connected to the sensor via wire bonds. The SSA encodes and processes strip signal information. The digitized hit information is sent to paired MPAs for further processing.

The PS-p sensor's data is managed by a set of Macro-Pixel ASIC (MPA) chips, which handle both pixel readout and p_T discrimination logic. Each MPA processes data from 1920 pixels arranged in a 16 × 120 matrix. The data flow includes hit data deserialization, Level-1 (L1) data formatting and stub finding.

Each FEH (Front-End Hybrid) holds eight SSAs and a Concentrator Integrated Circuit (CIC) to aggregate and manage data before transmission. The CIC also handles data from the MPAs, compresses and truncates L1 and stub data, and ensures alignment to the 40 MHz sampling clock. The set of MPA chips bump bonded onto the PS-p sensor conforms the so-called MaPSA.

The Read-Out Hybrid (ROH) integrates a low-power Gigabit Transceiver (lpGBT) for data aggregation and serialization and a Versatile Link Plus (VTRx+) optotransceiver

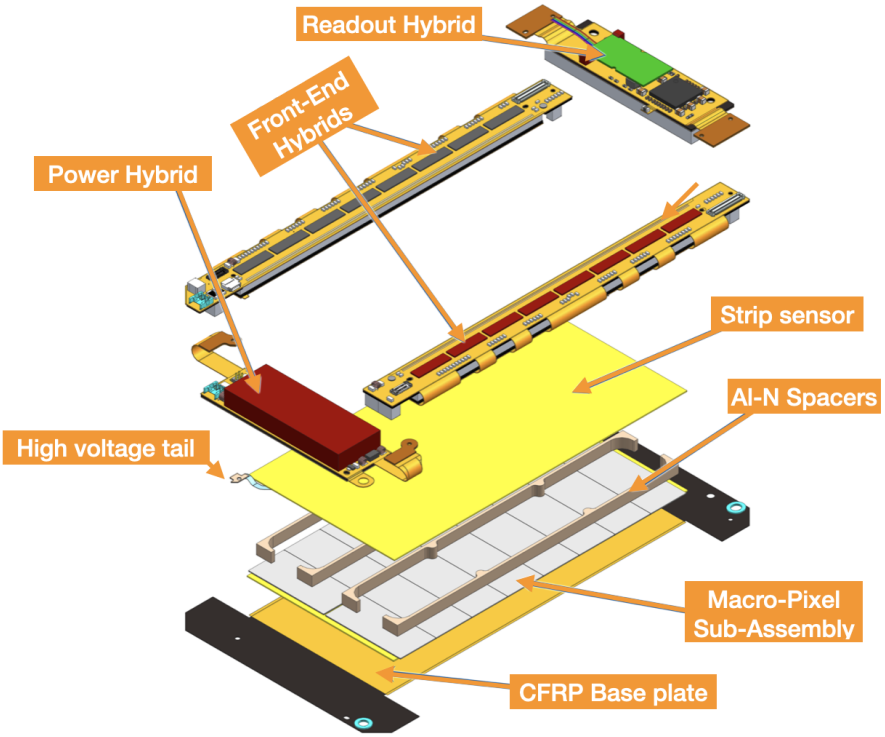

Figure 3.8: Exploded view of a PS module. Figure taken from [145].

module for optical communication. It connects to FEHs and manages data transmission between the module and the back-end system. The lpGBT features high-speed bidirectional optical links and interfaces with the CICs for data transmission. The VTRx+ provides radiation-hard optical data communication, ensuring reliable high-speed data transfer.

The Power Hybrid (POH) manages the power distribution for all PS module components through cascaded DC-DC conversion stages. It converts an 11 V input to required local supply voltages using the so-called bPOL converter designed at CERN and includes filters and shielding to protect against electromagnetic interference.

Mechanically, the PS module is designed for compactness and thermal efficiency. It uses high thermal conductivity materials like Al-N and Carbon Fiber Reinforced Polymer (CFRP) to enable a good heat transfer and ensure minimal differential expansion between components.

3.4.2 PS Module Assembly

The module assembly process is crucial for the precise functionality of the module itself, especially for implementing the p_T discrimination concept. This process can be divided into two phases: the bare module assembly and the functional module assembly.

The assembly procedure follows a semi-automated routine developed to improve both precision and efficiency in module production. While automation enhances accuracy, several manual interventions remain essential to ensure reliable assembly. Before beginning the assembly of a bare module, preparatory steps are required, including quality control of each component and tasks like attaching the Kapton isolator, securing inserts to the base plate, affixing the HV tail to the PS-s sensor and wire bonding and encapsulating the HV tail.

The initial step in assembling the bare module consist of gluing the MaPSA to the CFRP base plate. Following this, Al-N spacers are glued to the PS-s sensor. Once the glue has fully cured both in the MaPSA and baseplate assembly and in the PS-s sensor with spacers, they are glued together. This process uses a combination of fast-curing epoxy ($\sim$20 minutes) and slow-curing epoxy ($\sim$24 hours), the latter being radiation-hard to ensure that the module meets all performance standards. The inclusion of fast-curing epoxy in specific points facilitates the production of up to four modules per day.

This semi-automated process combines manual actions, such as placing components in the gluing robot, with automated actions such the alignment during gluing. The system is operated via a control GUI which guides the operator through each step of the assembly sequence. Once the epoxy has fully cured, each module undergoes a metrology check to ensure a sensor-to-sensor alignment within specifications.

Before starting the functional module assembly quality control of the different components has to be done, such a skeleton test where the different hybrids are electronically tested. Then, the hybrid circuits, the Power Hybrid (POH), Front-End Hybrids (FEH), and Readout Hybrid (ROH) are glued to the assembled bare module, aligning the components via alignment pins. The next step is wirebonding, where aluminum wires connect the MaPSA and PS-s sensor to the two FEHs, accomplished via an aluminum wedge bonding technique. After bonding, the wires are encapsulated to protect them from breaking since they are really delicate, resulting in a fully assembled and functional PS module.

The detailed assembly process is shown in Fig. 3.9 showing as well the quality control procedures done at each step.

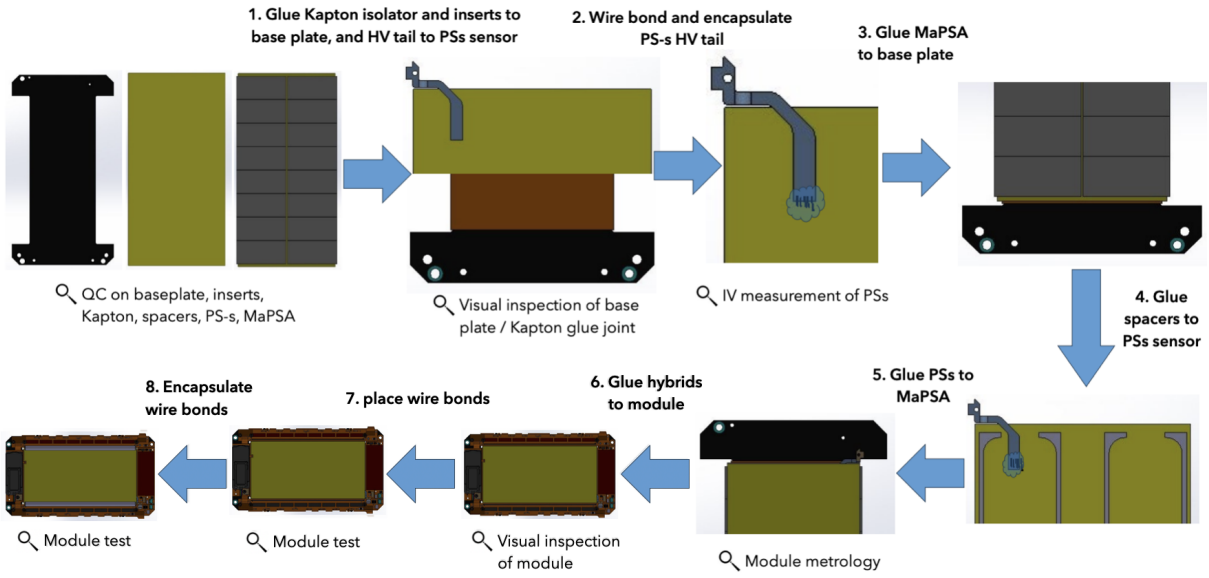

Figure 3.9: Workflow of the assembly for a PS module using the semi-automated assembly. Figure taken from [146].

3.4.3 PS Modules built at DESY

At DESY, 10 PS modules have been successfully built so far. Table 3.1 shows detailed information about each module and the component versions used in this work. The first four modules, classified as prototype modules, were built to demonstrate the feasibility of constructing PS modules at DESY, assess the functionality of the facilities and equipment, and determine the required personnel and time for module assembly. Additionally, this phase was crucial for testing the modules' functionalities, as well as conducting integration and burn-in tests. This phase also allowed for the optimization of the assembly process in preparation for the full-scale production.

During the prototype phase, several issues affecting functionality were identified, prompting modifications in subsequent modules. These changes were implemented in the "*kickoff* series" modules, which comprise the last three modules built so far, being PS_26_05_DSY-00101 one of them.

The hybrids from the kickoff batch represent an advanced stage of the design with many issues observed with the prototype hybrids rectified. The modules assembled with kickoff batch hybrids were never intended to be used in the final detector but they allowed to further study the designs. It was observed that after a design change between prototype and kickoff hybrids the flexible tail connecting the ROH with the left and right FEH of a module became too brittle leading to cracks and broken electrical connections when

Table 3.1: List of PS modules built at DESY

Name	ROH	lpGBT	CIC	POH	Spacer	Grounding
PS_26_05_DSY_00002	v1	v0	v1	v2	2.6 mm	common ground plane
PS_40_05_DSY_00003	v1	v0	v1	v2	4 mm	common ground plane
PS_40_05_DSY_00004	v1	v0	v1	v2	4 mm	common ground plane
PS_40_05_DSY_00005	v2	v1	v2	v2	4 mm	common ground plane
PS_26_05_DSY-00101	v2	v1	v2.1	v3	2.6 mm	common ground plane

the connection was made during the module assembly. In the transition to the preseries hybrids this issue was solved by a change to the cover layer of the hybrid tails. In addition, increased cold noise from the MPAs was observed, which necessitated changes to the filter circuits on the POH.

3.5 Outer Tracker layout and mechanics

The schematic layout of a quarter of the Phase-2 Outer Tracker is shown in Fig. 3.10, centered around the interaction point and aligned with the beam pipe along the z-axis. The Outer Tracker is divided into three sections: the Tracker Barrel Pixel-Strip (TBPS) surrounded by a blue rectangle, the Tracker Barrel Two Strip (TB2S) in a red rectangle, and the Tracker Endcap Double-Discs (*TEDD*), in black.

The Outer Tracker has a length of about 5 m and a radius of approximately 1.2 m. The TBPS and TB2S sections each consist of three concentric barrel layers, covering $|z| < 1200$ mm. The TBPS is equipped with PS modules (blue), while the TB2S uses 2S modules (orange). Beyond these, the TEDD region, covering $1200 \text{ mm} < |z| < 2700$ mm, contains five endcap double-discs. These discs have PS modules in the inner rings and 2S modules in the outer rings, completing the structure of the Outer Tracker Phase-2. The focus of this work is on the TEDD.

3.5.1 TEDD

The Tracker Endcap Double-Disks (TEDD) consist of five *double-disks* per endcap, with each double-disk comprising two *disks*, each made from two identical half-disk support structures called *Dees*. The Dees are described in detail in Section 3.5.2. Each double-disk is equipped with PS and 2S modules on both its front and back sides to ensure full area coverage with silicon sensors. The modules are arranged in 15 rings, alternating between

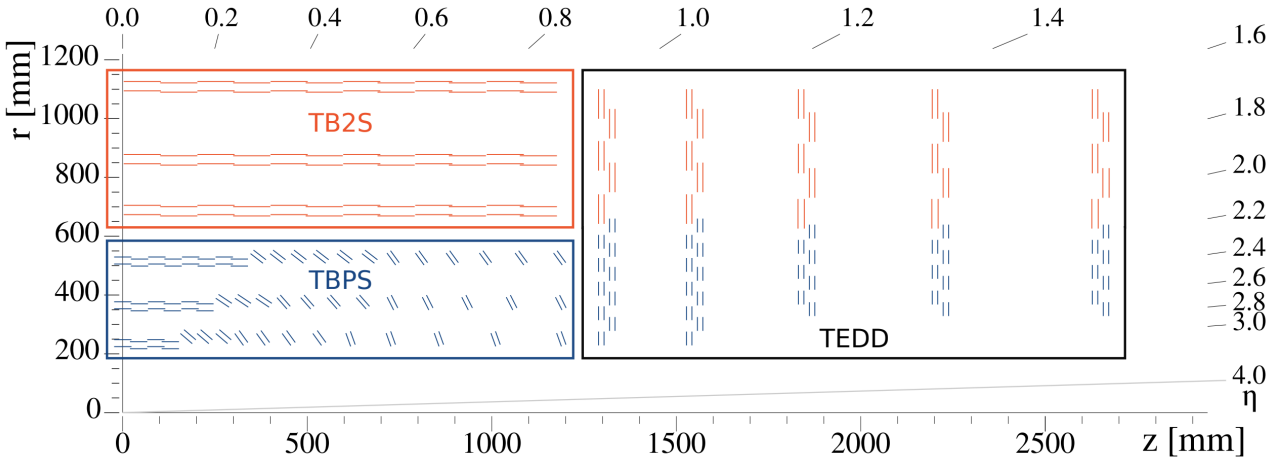

Figure 3.10: Schematics of a quarter of the tracker layout in r-z view indicating the position of the Outer Tracker and the thre main components. Figure taken from [107].

odd-numbered rings (red and black) on the front and the back of odd Dees and even-numbered rings (green and blue) on even Dees. As shown in Fig. 3.11 bottom, combining odd and even disk the full coverage is achieved.

As can be seen from Fig. 3.10, the first two Double-Disks have a smaller inner radius and are called TEDD1. It contains all 15 rings, while the remaining three double-disks, also known as TEDD2, are populated in rings 4 to 15.

The five double-disks of each TEDD will be connected via two inner half-shells at the bore and eight longitudinal bars at the outer radius. The Dee is equipped with inserts at the outer and inner edges to install this mechanical superstructure. Additional support rings between the disks provide extra stiffness. Fig. 3.12 shows the final TEDD structure after assembly. A total of 40 Dees are required to build both endcaps. DESY is responsible for producing all TEDD1 Dees. Furthermore, eight TEDD1 Dees and eight TEDD2 Dees will be equipped with modules at DESY, while four TEDD2 Dees will be integrated at IP2I Lyon and shipped to DESY for the construction of the double-disks.

3.5.2 Dee

The main purpose of a Dee is to support and cool the 2S and PS modules, while also contributing to their grounding. The Dee is also contributing to the global mechanical structure of the TEDD. The Dee is designed as a sandwich structure with carbon fiber facing and a lightweight sandwich core. It comprises mechanical inserts for the mounting of the modules and for the installation of the global mechanics. Each Dee has six embedded

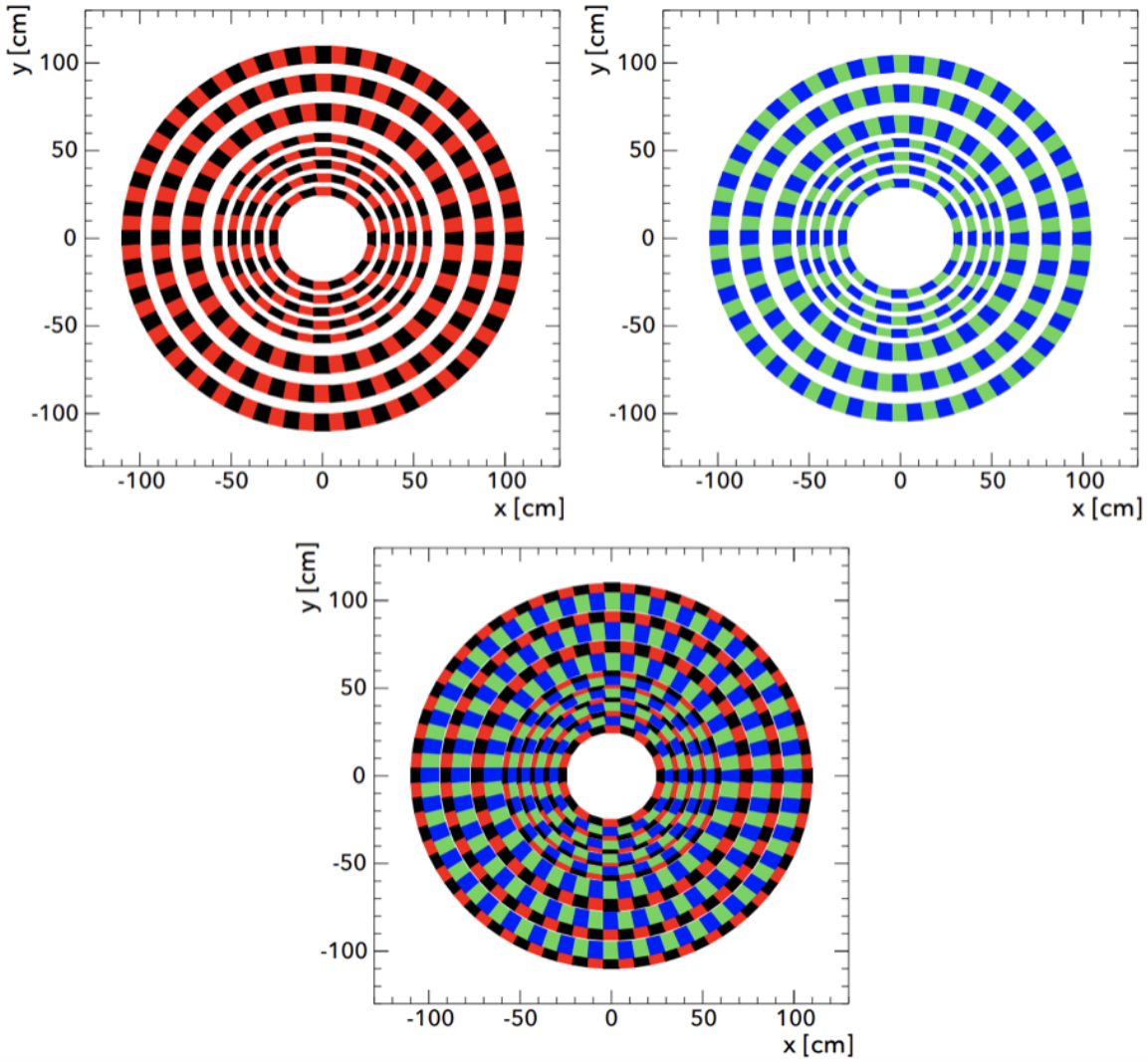

Figure 3.11: Configuration of modules on the odd (top left) and even (top right) disks, and the assembled double-disk (bottom). Figure taken from [147].

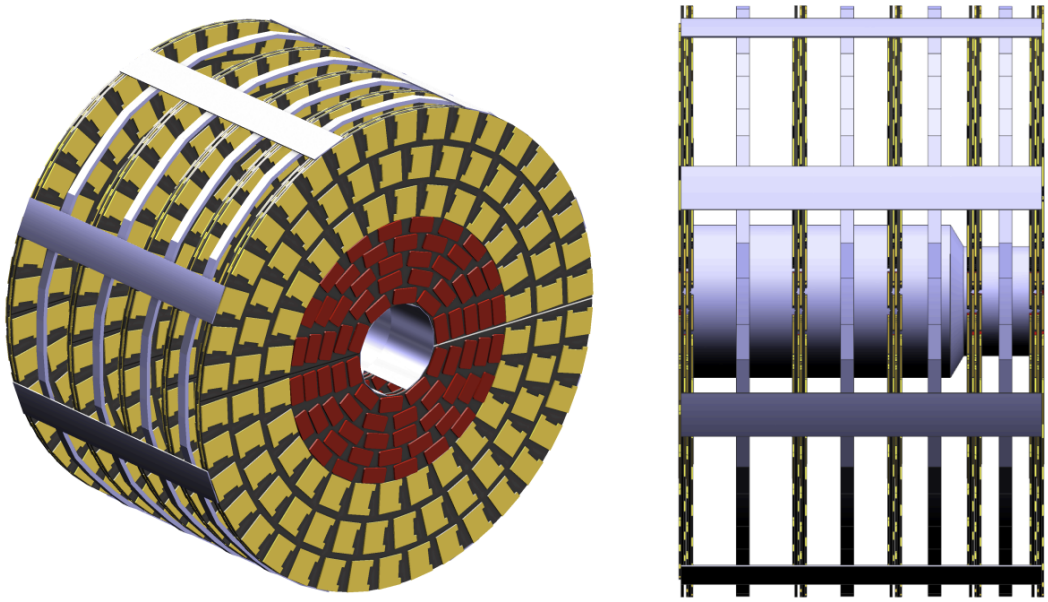

Figure 3.12: 3D CAD drawings of the TEDD made of five double-discs and populated with 2S and PS modules. Figure taken from [147].

cooling pipes inside the sandwich. The 2S inserts are directly connected to the cooling pipe. For the PS modules carbon foam block with a high thermal conductivity are placed in this sandwich. It facilitates a cooling of the Dee surface to allow for a large area cooling of the PS modules [148].

Fig. 3.13 shows an exploded view of the different components that conform the Dee.

To ensure full sensor coverage, the Dee features a step at the edge where it connects to another Dee, creating an overlap region with a reduced sandwich thickness. This design maximizes symmetry and minimizes the number of different Dee types, with the step placed on opposite sides.

Cooling

The Phase-2 tracker cooling system will use evaporative CO_2 in a liquid pumped cycle, serving both the Outer and Inner Tracker. The choice of CO_2 is motivated by its high-pressure evaporation, allowing for smaller, lower-mass tubing compared to conventional refrigerants. This minimizes pressure drops and temperature variation along the pipes. The high latent heat of CO_2 enables lower flow rates, while its low viscosity supports efficient heat transfer with small-diameter pipes. Additionally, CO_2 is radiation-hard,

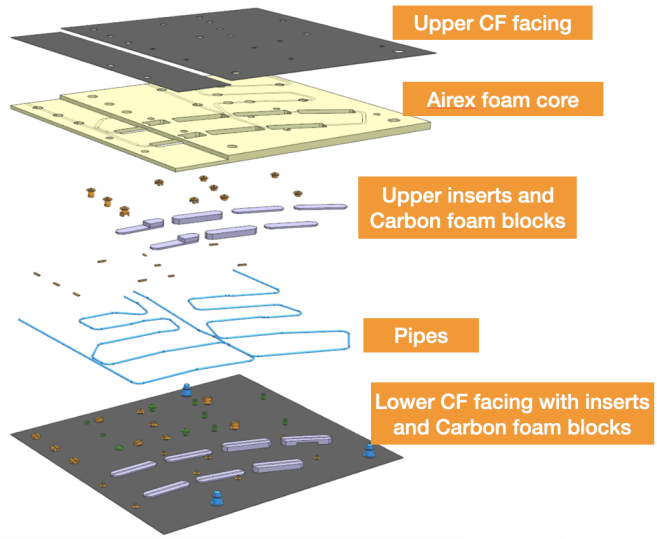

Figure 3.13: Exploded view of a small scale Dee prototype, showing all elements of the Dee construction. Figure taken from [148].

cost-effective, and environmentally friendly compared to other cooling options. However, it must be kept at high pressure, which requires careful safety considerations.

Inside the Dee, there are six cooling pipes arranged in overlapping sectors and routed in two tiers within the Dee's sandwich structure. This two-tiered design allows the cooling pipes to cross neighboring sectors without requiring 3D pipe bending. The six cooling sectors are routed with a rather symmetrical design for sectors 1 and 6, 2 and 5, and 3 and 4 as shown in Fig. 3.14.

The cooling system sustains the temperature of about -35 °C at the outlet of the Dee cooling pipes, crucial for sensor performance after radiation exposure. Cooling inserts or heat spreaders, embedded in the support structures, ensure thermal management for both 2S and PS modules. The PS modules, with higher power density, require large-area cooling contacts through CFRP base plates and thermal interface materials (TIM). The cooling inserts for both module types serve not only thermal management but also as structural support, positioning, and fixation of the modules on the Dee.

3.5.3 Dee integration

Dee integration involves mounting the 2S and PS modules onto the Dee structure. The Dee, especially with installed modules, cannot be handled manually, thus a dedicated

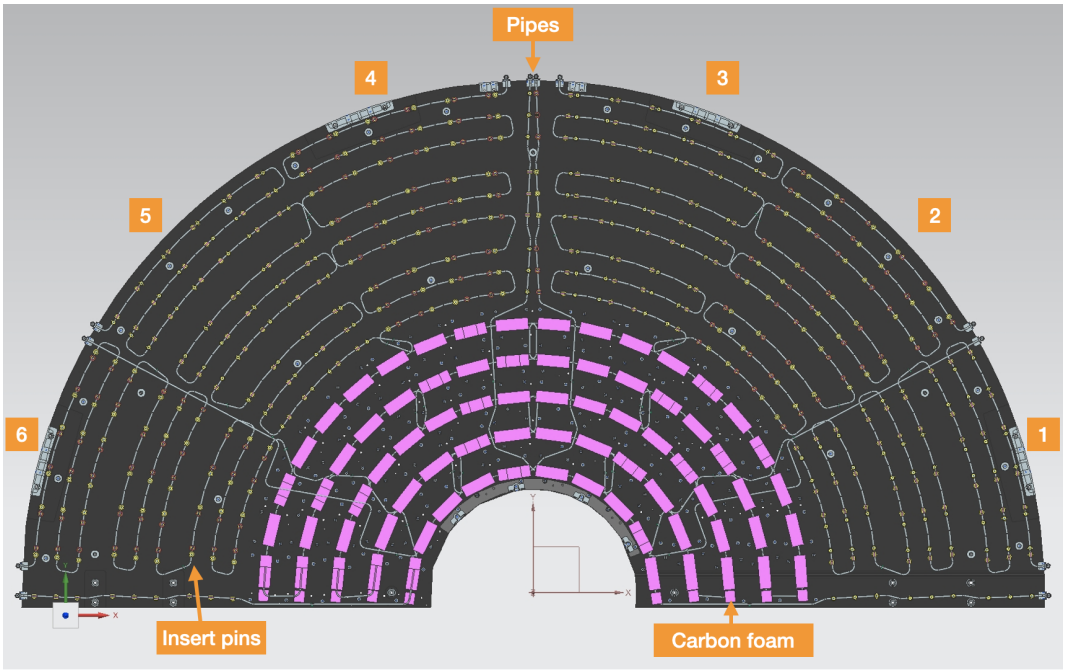

Figure 3.14: CAD drawing of a TEDD1 Dee showing the cooling pipes, the insert pins and the carbon foam blocks. The numbers indicate the different cooling sectors.

holding structure, the Arc frame, has been designed to support each Dee throughout most of the integration process. It holds the Dee on the outer radius and is made of 40 mm thick Aluminum. The Arc frame uses support fingers with radially constraint sliders to securely hold the Dee, while a crossbar provides additional support at the inner radius of the Dee, which is needed during transport and specific integration steps. The Arc frame interfaces with all tooling systems, allowing for seamless integration, transport and assembly. When forming a ring for the assembly, of a disk, two Arc frames can be connected.

For the module integration, the Arc frame is mounted on an assembly trolley, enabling a rotation around the horizontal axis to adjust the angle and height for optimal positioning, as can be seen in Fig. 3.15. Up to 84 PS and 96 2S modules must be installed per Dee, with a complex routing of services to temporary patch panels on the Arc frame. The operator follows a guided integration sequence using a dedicated software to ensure that sufficient space is available for all cables and fibers, and progress is recorded in a construction database. The modules are positioned using aluminum inserts, with additional inserts provided for Dee coordinate system definition, Dee-to-Dee and Disk-to-Disk assembly, and support for the patch panel ring and global TEDD mechanics mounting.

Mounting a PS module onto a Dee involves several critical steps to ensure proper position-

ing, thermal management, and electrical grounding. First, the module must be attached to the Dee, with thermal contact established between the base plate and Dee using a thermal interface material (TIM). The main option is a silicone-based, two-component thermal gap filler. This self-curing material, which does not require heat treatment, provides a tacky but robust interface. It is applied using a stencil that matches the module's size, with the gap filler spread evenly using a squeegee. After placing the module, a slight in-plane circular motion ($\sim$1 mm radius) is performed to ensure proper surface contact between the module and the Dee. Cooling performance tests are currently ongoing.

An alternative option is using thermal pads with a 0.2 mm thickness, which is crucial to prevent weakening of the spring fingers responsible for grounding. The thermal pads also allow for easy placement and removal of the module. This option has been used mainly for comparison of the cooling performance, but not tested for long-term performance and radiation hardness. It is not expected to be used in the detector.

For module placement on the TIM, the baseline method involves using two positioning pins screwed into the Dee insert. It is important to avoid overtightening, as this can bend the base plate, and even with careful handling, inserts or glue connections can break. If the base plate breaks, the module will not be secured properly. The recommended procedure is to tighten the screws only lightly, increasing tightness slightly after the TIM cures, and applying a drop of screw fixation to prevent the screws from loosening during transport. Since the module lacks a fixation hole at the fourth corner, there is a small clamp on the Dee, which can be placed on top of the base plate and fastened to ensure proper contact between the base plate and the Dee.

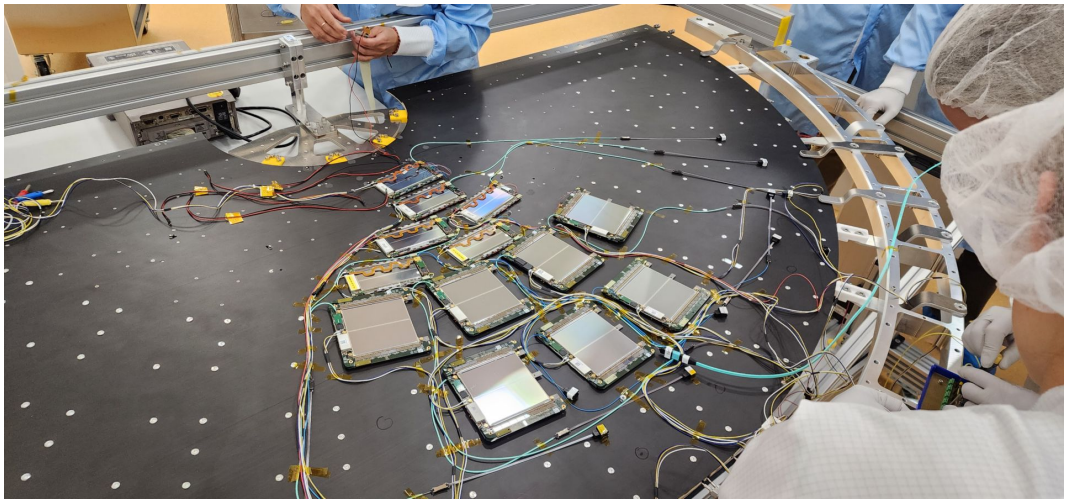

Figure 3.15: Photo of a prototype Dee mounted on the arc frame, with a total of 13 modules (7 2S and 6 PS), from the Integration test performed at DESY.

For 2S modules, the mounting procedure is comparatively simpler. Each module is directly placed onto six cooling inserts, which include a positioning pin for accurate alignment and a designated cooling surface. Since no TIM is applied in this configuration, a torque of 10 cNm is used to ensure optimal thermal contact.

3.5.4 Services

Services refer to the optical and electrical connections (both low voltage and high voltage) for the modules. These services are routed radially on the surface of the double-disk structure to a patch panel (PP0) located at the periphery.

The modules are organized into optical groups. Each optical group consists of 1 to 5 modules that are bundled into a single fiber optic cable. These groups are further aggregated into multi-fiber bundles (MFBs), which can contain up to 12 modules. Each double disk has 18 electrical and 12 optical patch panels, evenly split between the top and bottom parts.

Cooling loops for adjacent Dees connect in parallel to a cooling manifold near the PP0, with a single pair of cooling lines running longitudinally to the appropriate service channel. Figure 3.16 shows a CAD view of the PP0 patch panel with all the services included.

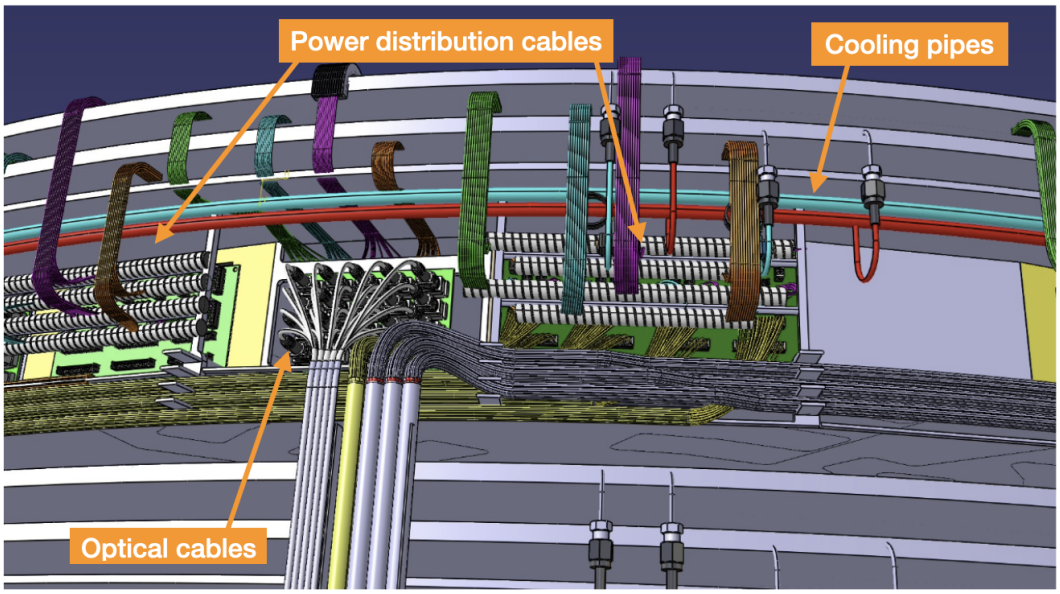

Figure 3.16: CAD view of the PP0 region with the services included.The red and cyan pipes correspond to the cooling system, while the multi-colored cables ascending toward the two side panels represent the power distribution cables. The central cable bundle corresponds to the optical fibers. Figure taken from [148].

From the PP0, longitudinal services connect to a second patch panel (PP1) located on the inner wall of the magnetcryostat, near the tracker bulkhead. The PP1 is connected to the cooling plants located in the service cavern via insulated rigid coaxial transfer lines. In the coaxial transfer lines the innermost pipe will carry cold liquid CO_2 towards the detector. That pipe is placed inside a bigger pipe which returns two-phase CO_2 from the detector.

To prevent water condensation on cold surfaces, dry nitrogen (or dry air during maintenance for safety) is injected into the tracking volume, bulkheads, and cable channels. These areas are sealed with vapor barriers, though not fully leak-tight. The dry gas ensures that the dew point remains low, preventing condensation. The gas is supplied by an existing membrane and dryer system, with nitrogen backups available. Heating foils are used to keep external surfaces above the dew point.

Routing for both optical fibers and power cables on the Dee surface is carefully planned to accommodate the L1-trigger design. The existing tracker power supply system will be completely replaced with a new low voltage (LV) supply system providing approximately 100 kW at 13–14 V, divided between 2S and PS systems. The high voltage (HV) system will deliver up to −800 V for sensor bias, managing about 2 mA of leakage current per module in high-radiation areas. Both LV and HV systems will have module-level granularity to simplify failure mitigation.

CHAPTER 4

Burn-in Tests of CMS Outer Tracker Modules

Contents

During the production phase of the Outer Tracker, thousands of assembled modules will undergo a thorough qualification process at several stages of the assembly. The goal is to conduct a series of functional tests to characterize each module, address potential issues such as defective electronic components, and ensure that only modules of sufficient quality are integrated. These tests will evaluate both the mechanical and electrical performance of the assembled modules. All qualification results will be recorded in a central database to track each individual module's status and performance quality.

The process begins with the room-temperature qualification of different components, which comprises electrical, communication and functionality checks, as well as visual inspection (metrology). Next, the quality control including metrology and functionality test of the assembled module follows, also at room temperature. Then, the modules undergo

thermal cycling tests, also known as Burn-in tests. The qualification process concludes with integration tests on final mechanical structures, such as TEDD Dees.

This thesis addresses building and commissioning of the Burn-in setup at DESY and the characterization of the prototype and kickoff PS modules assembled by DESY by using this setup.

4.1 Burn-in Test

The primary objective of a Burn-in test is to ensure the full detector functionality not only at room temperature but also at the target operational temperature of -35 °C. In addition, the module's long-term operation is verified, as the CMS Tracker is expected to remain functional for at least a decade. Furthermore, the module functionality after undergoing several warm-up and cool-down cycles is validated.

Throughout each cycle of the testing setup, the module undergoes thermal cycling, transitioning from room temperature to operational temperature several times within a 24-hour period (typically 5 or 6 cycles). During this process, measurements of the current as a function of the bias voltage (I-V measurements) and of the electrical noise are performed to assess the module's performance at both room and operational temperature.

4.2 Burn-in system

The Burn-in setup uses a commercial refrigerator as a thermally isolated unit, the enclosure allows maintaining controlled temperature and humidity levels while ensuring a dark environment for the modules. Inside the refrigerator, a support structure for module carrier plates can accommodate up to ten modules, while temperature and dew point sensors monitor the environmental conditions. The current status of the two Burn-in setups is shown in Figure 4.1 (right).

To regulate the temperature of the carrier plate, cooling pipes connect the support structure to a chiller system. Dry air is injected into the refrigerator to reduce the humidity, and a magnetic interlock prevents access during measurements and protects the modules from damage through condensation. The Controller Board, engineered by Fermi National Accelerator Laboratory (FNAL), manages the interlock mechanism and reads out temperature and dew point data. Voltage to the modules is supplied by power supplies housed in a rack. The readout system employs a Field Programmable Gate Array (FPGA) based circuit board which is controlled with a software framework designed, among other functionalities, to perform noise measurements. This setup is integrated into a software

developed by FNAL, known as OtSDAQ, which oversees the entire system and ensures that all components are interconnected as illustrated in Figure 4.1 (left). The entire setup is located inside a clean room known as the Detector Assembly Facility (DAF). This allows to maintain controlled temperature and humidity levels inside the clean room where the modules must be stored after the Burn-in test and to ensure a clean atmosphere with a controlled amount of dust particles in the air.

At DESY, two Burn-in setups are being built, such that the large number of modules can be tested on site.

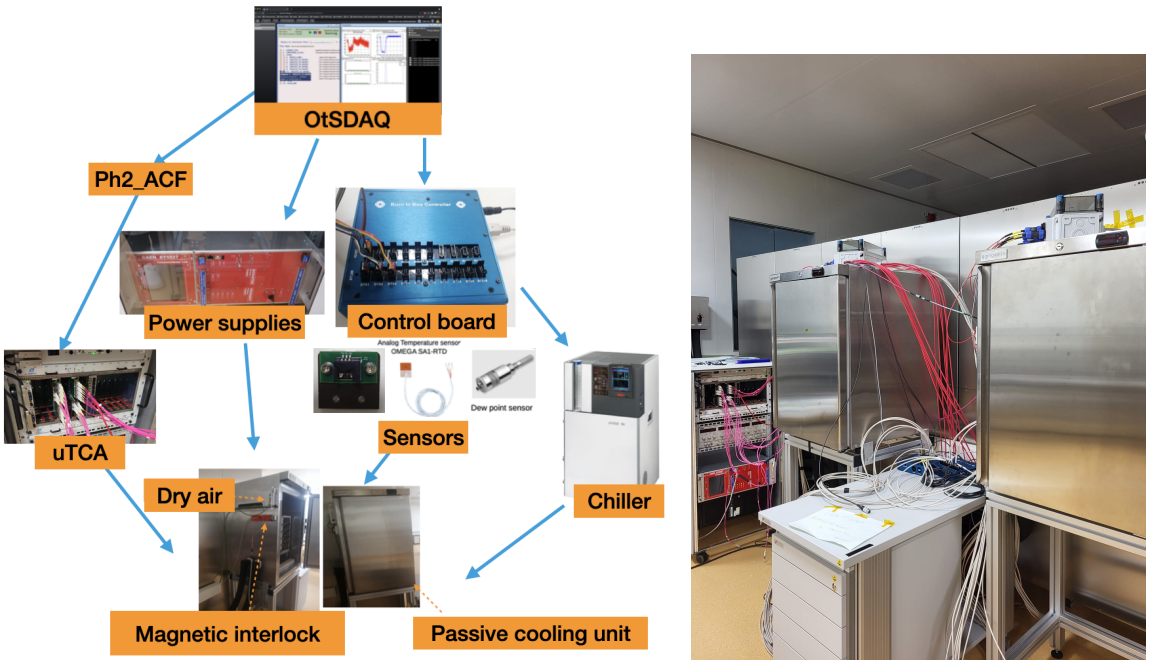

Figure 4.1: Schematics of the Burn-in system on the left, showcasing the different components and how they are interconnected. On the right, the two Burn-in setups installed in the DESY clean room are shown.

4.2.1 The chilling unit and the cooling box

The Huber Unistat 525w chilling unit [149] precisely regulates temperatures within the experimental setup. It uses Novec 7200 as a cooling fluid [150], including ethoxynonafluorobutane ($C_4F_9OC_2H_5$). The chiller operates with a water-cooled refrigeration system, maintaining temperatures from -55 °C to 250°C. With a cooling power of 1.5 kW at -40 °C it ensures efficient temperature control even at extreme conditions. The chiller can be remotely controlled via null modem which is achieved through the controller box (section 4.2.4).

The passive cooling unit, a commercial refrigerator ggmgastro TKSG568N [151] is used and referred to as the cold box. It has been mechanically altered and equipped with the infrastructure needed for the test. In Figure 4.2, a sketch of the cold box with the carrier structure inside is shown.

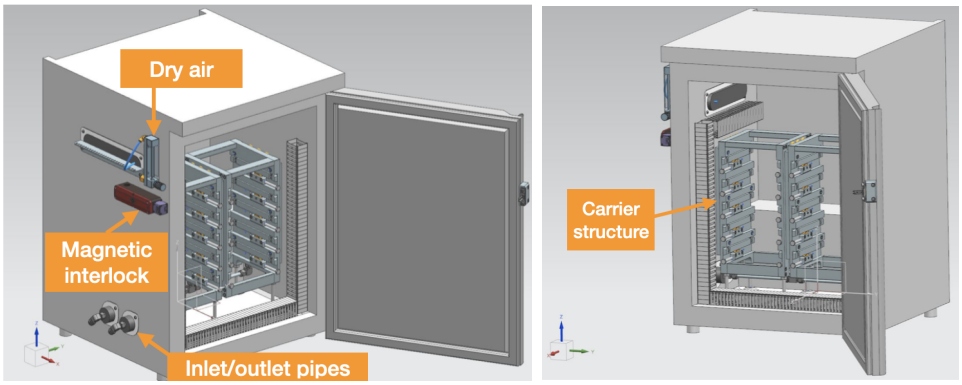

Figure 4.2: Visualization of the passive cold box showcasing the different appliances and services.

Since the chiller serves both Burn-in setups, and an additional setup within the clean room, a distribution box is required, regulating the connection to the setup in use. The inlet and outlet pipes connect the chiller to the cold box. These pipes enter the cold box and are connected to the carrier structure.

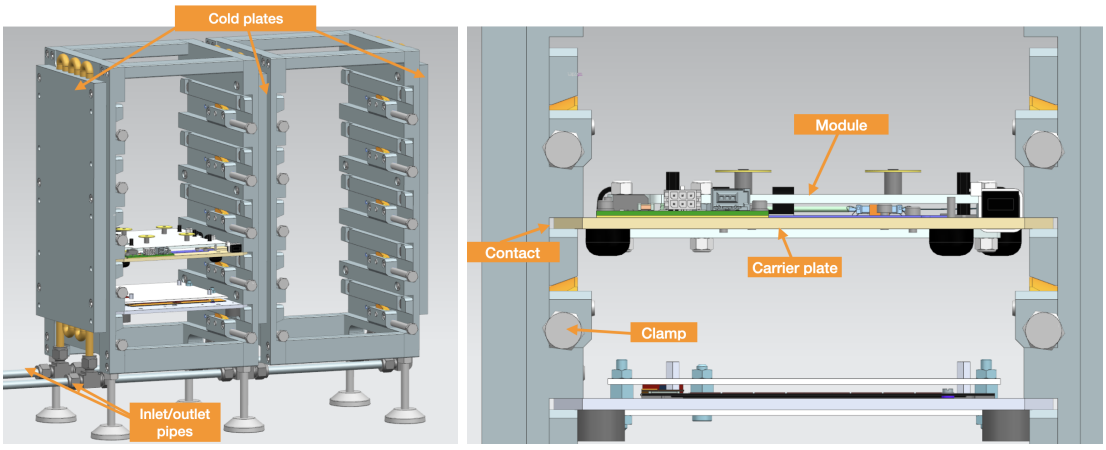

Figure 4.3: The carrier structure placed inside the cold box with a detailed view of one of the sockets with a module in place.

The carrier structure provides a stable and secure frame for the carrier plates, ensuring that they remain fixed in position during the test. It consists of two columns of 5 sockets

each, which allows for simultaneous test of up to 10 modules. The carrier structure is made of Aluminum and features three cold plates [152] as active cooling element for both columns. The middle plate is shared by both columns. The lower part of the structure houses the inlet and outlet pipes, which connect to copper pipes inside the cold plates. Each socket has two clamps to secure the carrier plate in place, as cooling is achieved through direct contact between the carrier plate and the frame as illustrated in Figure 4.3. The cooling contact to the module is achieved by the contact between the carrier plate and the carbon fiber base plate.

The clean room has a central system of dry air with nominal dew point of -70 °C. Dry air is supplied to the cold box through a flowmeter that regulates the flow rate. For operation the flow is set at 80 l/min and, once the dew point has reached -45°C, is set to 7.5 l/min.

4.2.2 Carrier plate and adapter board

The module carrier plate ensures the handling and protection of the module while allowing for electrical testing and encapsulation of the module wires, all without requiring the module to be removed from the carrier plate. Photographs of the carrier plate are shown in Figure 4.4. The carrier plate also allows the cooling, connection and support of the module during the Burn-in test.

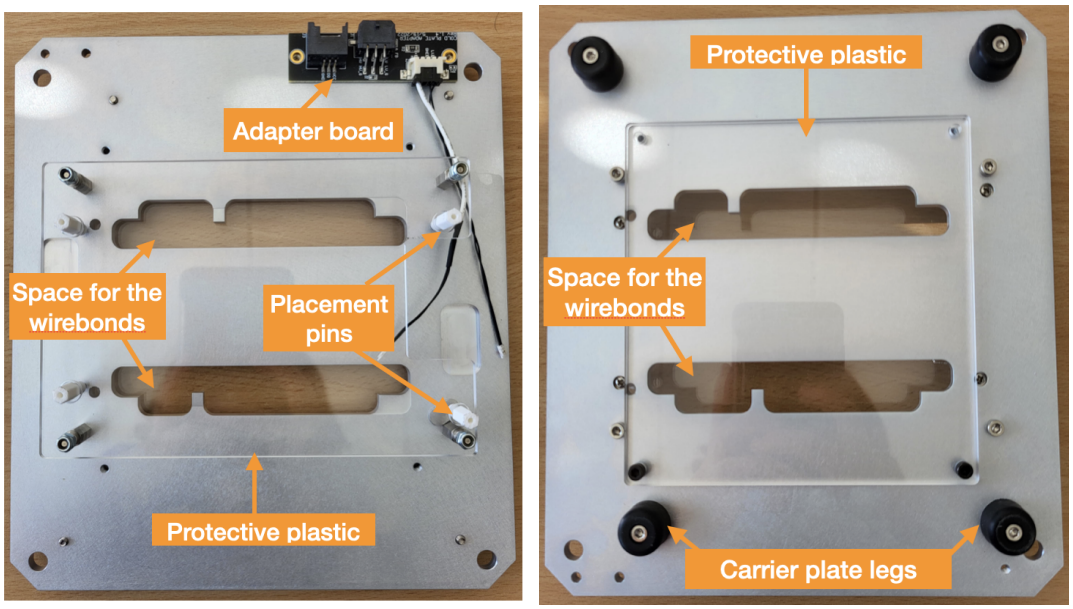

Figure 4.4: Top (left) and bottom (right) view of the carrier plate.

An adapter board and a temperature sensor clip are attached to the carrier plate as

shown in Figure 4.5. The adapter board consists of two connectors, in and out, one of which connects the adapter with the Low Voltage (LV) and High Voltage (HV) that is transmitted through the adapter board to the connector linked to the module. This adapter board has been introduced due to the fragility of the HV/LV connector in the module. This way, the cables are directly plugged in to the module, which mitigates the necessity for toggling those connectors on a regular basis, reducing the probability of breaking them. Once a module is built, it is mounted to a carrier plate for storage. The module remains mounted on a carrier plate until the dee integration. During the tests, the cable on the module is connected to the adapter board, which in turn is connected to the CAEN system, powering the module. The clip temperature sensor monitors the temperature of the carrier plate at all times during the test.

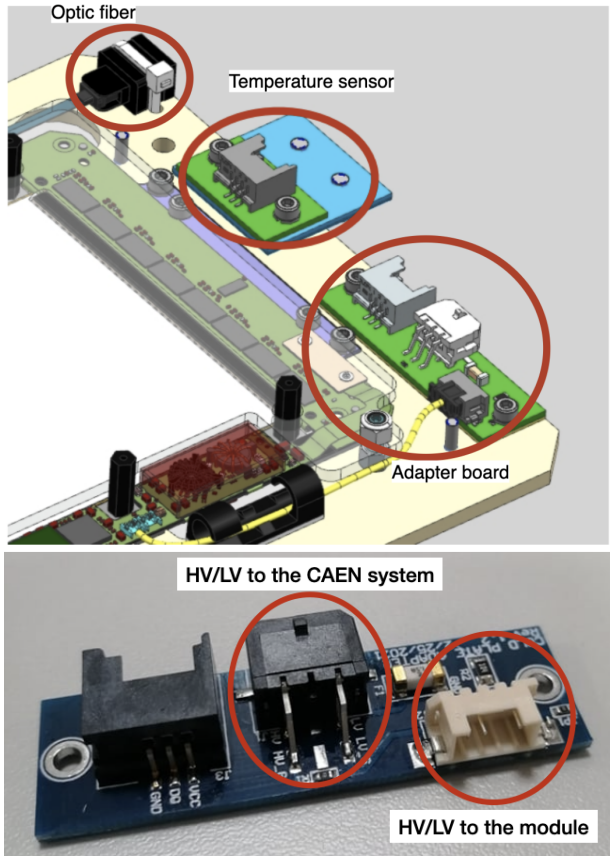

Figure 4.5: The adapter board and the temperature sensor installed on a carrier plate (top). The adapter board with the connections (bottom).

4.2.3 Temperature and dew point sensors

The temperature and humidity inside the cold box are monitored during the test, ensuring the safety of the modules and verifying the temperature cycles. For this purpose, the dew point and temperature sensors are used (Figure 4.6).

Both the environmental temperature and the module temperature are monitored. Two different kinds of temperature sensors are used. For the air temperature inside the cold box, a resistance temperature detector (OMEGA SA1-RTD) is used with an analog read-out. Two such sensors are placed in the cold box, one on the top and the other one on the bottom. Their working range is from 260 °C to -73 °C with an accuracy of ±0.06% at 0 °C [153]. For the module temperature as shown in the previous section a temperature clip is used, which can be easily attached and detached from the carrier plate. It is a one-wire DS18B20+ sensor, read out digitally. Its working range is from 125 °C to -55 °C with an accuracy of ±0.5 °C [154].

Figure 4.6: Sensors installed inside the cold box. The temperature clip with the wire sensor (left), resistance temperature detector (RTD) (middle) and dew point sensor (right).

Maintaining the temperature within a few degrees of the nominal value is crucial to ensure reproducibility. Additionally, monitoring the dew point is essential to prevent condensation, which could harm the modules. During the Burn-in test, the temperature of the carrier plate needs to vary between +20°C and -35°C. The dew point which is monitored with the dew point sensor DMT143 must be below -40°C. The dew point measurement range goes from 60 °C to -70 °C and has an accuracy of ±2 °C [155].

During operation, the cold box must not be opened, as the sudden change of temperature and humidity can severely harm the module, especially in the case of condensation. Additionally, while the module is operated with a high bias voltage (around 600V), the environment must remain dark to not saturate and damage the silicon sensors. For this

purpose, a magnetic interlock is installed on the cold box (Figure 4.7). It locks the door during operation and it is unlocked when the test is finished, the temperature is back to room temperature and the modules are powered off.

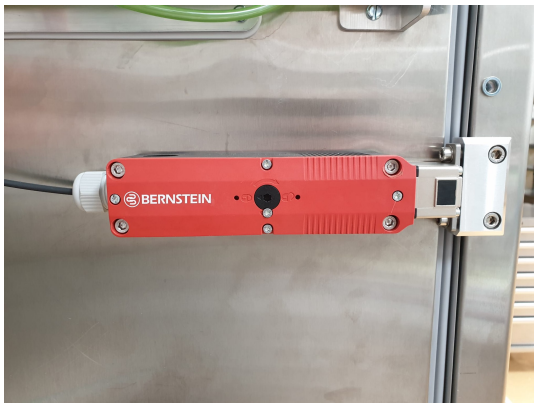

Figure 4.7: Magnetic interlock installed on the outside of the cold box.

The cabling schematics for the RTDs, dew point sensors, and the magnetic interlock are shown in Figures A.1 to A.3.

4.2.4 Burn-in Box Controller

The Burn-in Box Controller is a microprocessor that interfaces the sensors and the chiller and communicates with the control PC [156]. It monitors the temperature and dew point of the box by reading various sensors through the Interface Board. This Interface board is a printed circuit board that connects the electronic board with the different sensors. It uses relays to activate or deactivate the magnetic interlock and the dry air system. These relays also serve as a safety feature, when the software adjusts the machines to restore proper humidity levels if an anomaly is detected, or sending a message to shut down the power for the modules to protect them. The Burn-in Box Controller is operated by a software explained in section 4.2.7.

4.2.5 Power supplies

The modules undergo a series of tests, for which they are powered individually, with two cold boxes designed for ten modules each, so that 20 channels for high and low voltage must be available. Three low voltage (LV) supply modules of the type CAEN A2519C [157] and two high voltage (HV) supply modules of the type CAEN A7435DN [158] are used.

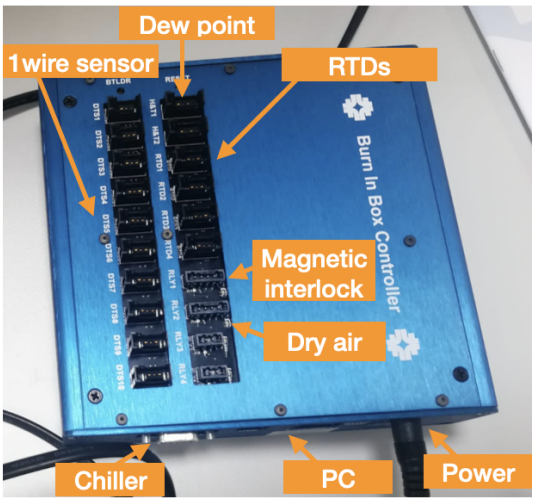

Figure 4.8: Controller Box highlighting all connections with the different components of the Burn-in setup.

They are connected to a Multichannel Power supply of the type CAEN SY5527 [159]. In total, the CAEN system provides 24 HV channels and 24 LV channels, and it can be controlled remotely via Ethernet.

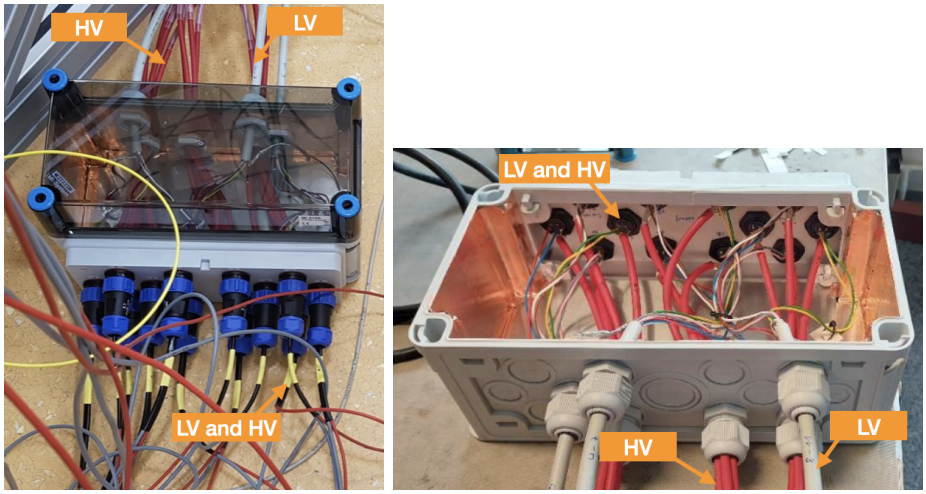

Figure 4.9: Customized patch box, as seen from the front with the cables connected to the modules labeled as LV and HV (left). The connections of the cables coming from the CAEN system are shown in a rear view (right).

Since each detector module needs both LV and HV, a patch box connecting the CAEN system and the modules has been designed and built for this setup. The HV CAEN module

provides one channel per cable, while for the LV CAEN module, one cable provides voltage for four channels. Therefore, the customized cables for the CAEN modules are attached to the box [160]. Inside the box, each LV cable is separated into different channels and each channel is combined with one of the HV channels. As an output, 12 cables delivering LV and HV each to a single module's adapter board have been designed and produced. The patch box is shown in Figure 4.9. More details and specifications can be found in Figure A.4.

4.2.6 Readout System

For data readout, the DTC system introduced in Chapter 3 is planned for the Outer Tracker. However, since the DTC system is not yet available, the micro-DAQ, Trigger, and Control (μDTC) system has been selected as an interim solution for the prototyping and production phases. The μDTC system is built around the FC7 board [161], an FPGA-based circuit board, programmed with a versatile FPGA firmware to support testing needs.

The FC7 board, shown in Figure 4.10, is a core component of the hardware readout system and features an FPGA along with peripherals such as external memory and FPGA Mezzanine interfaces. It is an adaptable Advanced Mezzanine Card (AMC) [162] that adheres to the micro-Telecommunications Computing Architecture (uTCA) [163] form factor. This board is widely used in data acquisition and control applications and is built around the Xilinx Kintex-7 FPGA [164] and the FPGA Mezzanine Card (FMC) Standard [165]. The FC7 offers multiple configurable I/O options and Multi-Gigabit Transceivers (MGT) capable of bandwidth of up to 10 Gbps, allowing for custom processing logic through specialized μDTC firmware developed for this application [144].

In addition to the FPGA, the FC7 board includes additional components and functionalities. It features a card edge AMC connector, ensuring compatibility with uTCA infrastructures and bench-top use. The board provides high-speed connectivity and supports multiple data transfer protocols to the back plane. It also includes two FPGA Mezzanine Card (FMC) connectors for flexible access to FPGA I/O.

The lpGBt on a module's readout hybrid, described in section 3.4.1, connects to the back-end system (FC7) via optical fiber. Each Burn-in box hosts 10 modules, each requiring two optical fiber to transmit data. To limit the number of cables inside the box, a custom design of fiber optics, known as "exapus" is used, as shown in Figure 4.10. The exapus fibers consolidate twelve individual fibers into one ribbon. Outside the Burn-in box, a commercial off the shelf connector is needed to fan out one cable into twelve individual fibers. These fibers connect to optical transceivers on FMC cards hosted in an FC7 board.

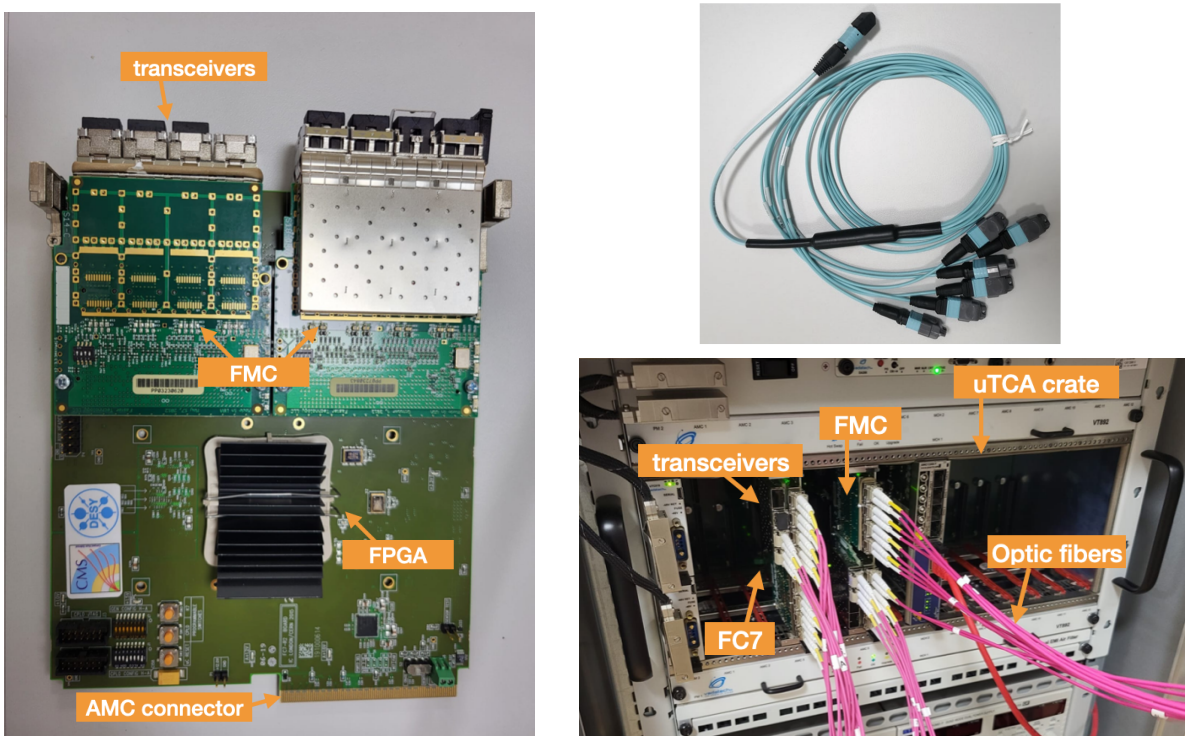

Figure 4.10: An FC7 AMC (left), indicating the back plane AMC connector, the FPGA and the two FPGA mezzanine cards with the transceivers. On the bottom right, the uTCA crate with two FC7 with fiber optics connected to the transceivers in the FMC is shown. The upper right photo shows the "exapus".

4.2.7 Software

The Burn-in system uses two different software applications: Off The Shelf DAQ (OTSDAQ) for operating the Burn-in Box Controller and the Phase-2 Acquisition and Control Framework (Ph2ACF) for performing the readout of the modules.

The Ph2ACF [144] is a software framework designed for the control and readout of the CMS Phase-2 Tracker detector and written in C++. Additionally, this framework is used to develop control and test routines essential during the prototyping and production phases of both the Inner Tracker and Outer Tracker modules.

The OTSDAQ Burn-in Software [166] manages the Burn-in Box Controller by monitoring temperature and dew point sensors and communicating with the chiller, the magnetic interlock, and possibly the dry air system (digital controller to be installed). It also controls the power supplies. Based on the OTSDAQ software developed by FNAL, this ready-to-use Data Acquisition (DAQ) system has been adapted to the specifications of

the chiller available for the setup at DESY. This software incorporates Ph2ACF to control the modules. It is used through a web-based Run Control GUI as shown in Figure 4.11.

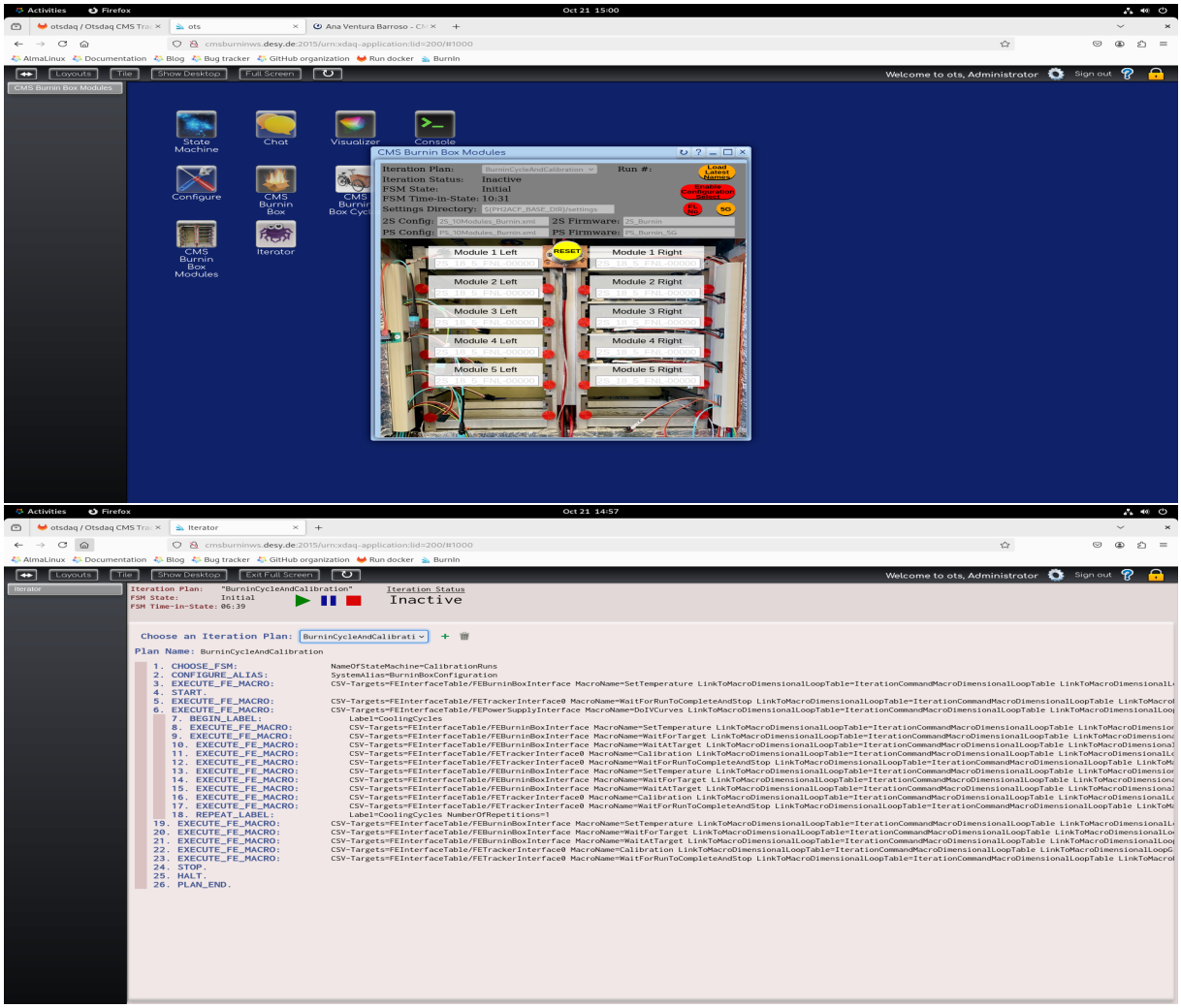

Figure 4.11: Screenshot of the main page of OTSDAQ software (left) and the Burn-in box interface stating the commands to follow (right).

This GUI allows the user to automatize the whole process, from registering the modules that have been loaded on the Burn-in, starting temperature cycles and noise measurements, to the upload and storage of the data in the CMS database. For the measurements presented in this thesis, this software was not yet fully available, so that the system needed to be controlled manually. After most of the measurements have been accomplished, the GUI was also developed as a part of the work presented in this thesis and became fully functional. It will be further used in the production phase of the modules.

4.3 Setup commissioning

The commissioning of the Burn-in setup at DESY is critical for the module production and integration for the CMS Phase-2 Tracker Upgrade. DESY is responsible for testing 1120 PS modules that will be built on site, in addition to the 800 2S modules produced by RWTH Aachen and integrated at DESY.

In order to effectively cope with the requirements, two separate Burn-in setups are needed. This necessity arises mainly from the volume of modules that must be tested. In addition, the technical limitations of the FC7 board require to have two boards. The FC7 board is capable of reading up to 12 modules simultaneously, but it is restricted to processing only one type of module, either 2S or PS, at a time.

The commissioning process involves the systematic evaluation and validation of the Burn-in infrastructure to ensure the reliability and performance of the detector modules under conditions that are as close as to operational conditions as possible. This includes verifying that the setup can achieve the desired temperature and dew point within reasonable time, and ensuring that both setups can be operated simultaneously without any loss of functionality.

Dew point measurement

Monitoring the dew point is essential to prevent condensation, which could harm the modules. During the Burn-in test, the temperature will decrease to -35 °C. Under these conditions, the dew point must be below -40 °C. To measure the dew point inside the cold box, the dew point sensor described in Section 4.2.3 is used. Dry air is introduced through a small pipe at the top of the cold box. Tests (not shown in this thesis) with different flow rates have demonstrated that a higher flow rate allows the target dew point to be reached more quickly. Therefore, an optimal flow rate, around 80 L/min, is used for all measurements.

The modules have proven to be highly sensitive to humidity, with some modules exhibiting variations in breakdown voltage and noise levels in response to small variations of the dew point. Further, it is important to verify that the dew point requirements are fulfilled throughout the entire volume of the cold box. For instance, there could be higher humidity affecting modules positioned farther from the dry air injection, compared to those closer to it. To verify the uniformity of humidity across the box, measurements of the dew point have been performed with the sensor in three different positions. The dew point sensor has been placed in the bottom, the middle and the top of the cold box, while keeping the dry air pipe in a fixed position. As Figure 4.12 shows, there is a minor variation in the dew point between the different positions during the initial phase of dry air flushing

(up to 100 minutes) that can be attributed to the dry air distribution inside the cold box. However, once stable, all three positions indicate a safe dew point level to operate the modules. It's important to note that in this case, it took approximately 5 hours to reach the dew point due to the measurement being conducted at +20°C. As temperature decreases, the dew point also decreases. In this scenario, the focus was not solely on the time required to achieve a safe dew point, but rather on evaluating performance across different positions within the setup. This is why the measurement spanned 2 days, to assess stability and performance variation over time and across different locations.

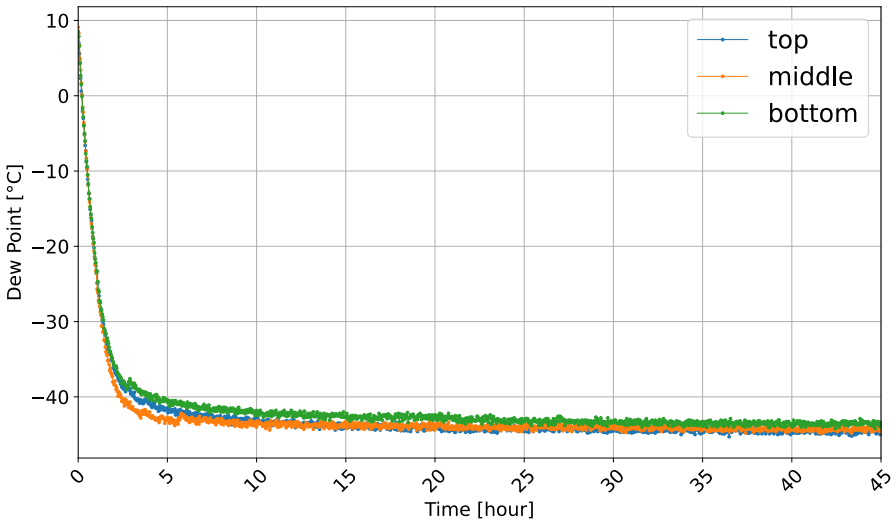

Figure 4.12: Dew Point in the cold box as a function of time for three different positions of the sensor inside the cold box: in the bottom (green), in the middle (blue) and in the top of the box (red).

Based on this measurement, it can be concluded that the dew point levels throughout the cold box are quite uniform. This uniformity ensures that humidity will not compromise the safety and performance of the modules during testing. Therefore, the Burn-in setup is adequately prepared in this regard.

Cooling performance

Monitoring the temperature is essential to ensure that temperature cycles can be conducted accurately and that the temperature is known at any given time. The Burn-in test should last 24 hours, during which as many cycles as possible are performed. Therefore, the cooling performance is critical and must be optimized to reduce the time needed

either to cool down or to warm up the modules. During the Burn-in test the temperature varies between 20 °C to -35 °C.

To estimate the temperature of the modules inside the cold box, the temperature clip sensor described in section 4.2.3 is used. This temperature clip is attached to the carrier plate and located in the warmest place of the carrier structure which was found to be the top right shelf. The carrier plate has a PS module with LV on.

Figure 4.13 shows the temperature on the carrier plate inside the cold box as a function of time while the chiller is cooling the structure starting from room temperature. To achieve the fastest response, the chiller set point is configured to -50 °C for the ramp down and changed to -37 °C when the targeted temperature has been reached, to maintain it over time. The time needed for achieving the desired temperature (-35 °C) is around thirty minutes. About one hour is needed for temperature stabilization (varying by less than 0.5 °C). In this case, the chiller set point is at -37 °C and the stable temperature reached is -33.5 °C. Due to the lack of optimization of the chiller, the set point was not low enough to maintain the targeted -35 °C. In other measurements it was proven that by lowering the set point of the chiller to -40 °C the desired temperature was reached within thirty minutes. Therefore, the cool down is fast enough for performing the Burn-in test.

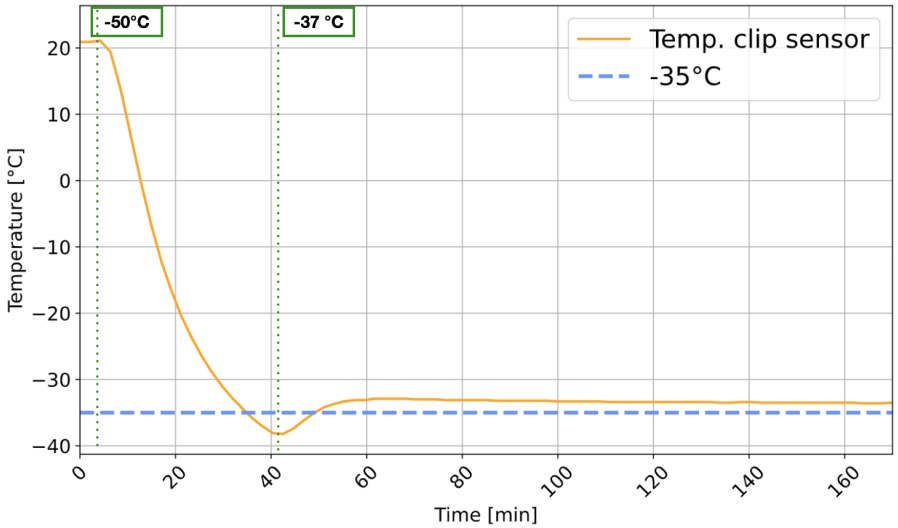

Figure 4.13: Temperature measured at the carrier plate as a function of time for the cooling down process. A set point of -50 °C has been configured to reach the temperature and then a set point of -37 °C to stabilize it. The blue dotted line indicates the temperature target of -35 °C.

For the return to room temperature process, Figure 4.14 shows the temperature measured at the carrier plate as a function of time. The chiller set point is configured at +25 °C.

The desired +20 °C are achieved within thirty minutes, which is within the specifications for the Burn-in process.

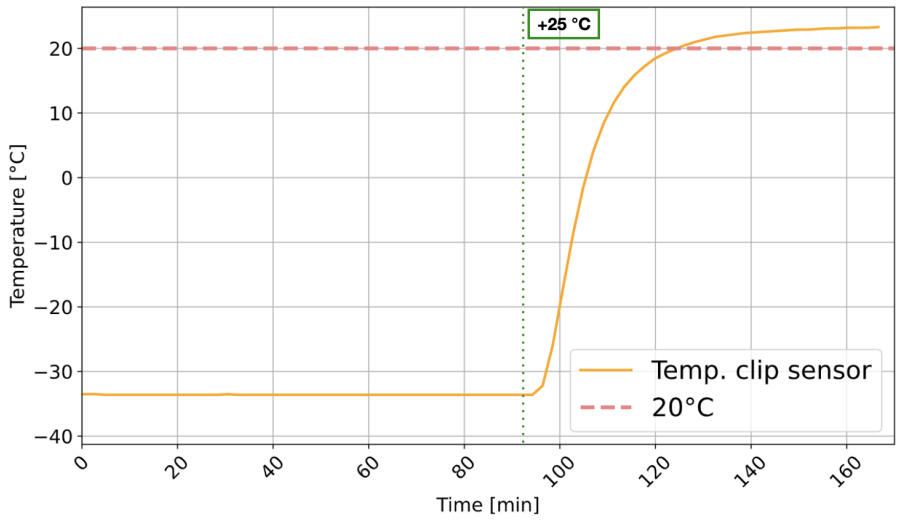

Figure 4.14: Temperature measured at the carrier plate as a function of time for the warming up process. A set point of +25 °C has been configured. The red dotted line indicates the temperature target of 20 °C.

These measurements have demonstrated, that an entire temperature cycle can take around 1 hour and 30 minutes, allowing for 16 temperature cycles within a 24-hour period, considering only warming up and cooling down. This performance was good, but further improvements are planned. The chiller parameters can be optimized to reduce the time required for both processes and to eliminate the need for selecting extreme set points.

Parallel operation of two Burn-in setups

For highest efficiency of the tests, the two Burn-in setups built at DESY need to be operated in parallel. To ensure the viability of such operation, it is critical to evaluate the chiller's capacity to supply both cold boxes at the same time. Furthermore, estimate of time required for a temperature cycling of both boxes is crucial to ensure the conceptualization of the Burn-in procedure.

To evaluate the performance in a parallel scenario, one temperature cycle has been performed without modules on the carrier plates running both cold boxes in parallel. The temperature measurement is performed on four different carrier plates located in two different positions inside each cold box. One sensor is located in the bottom left position,

which is the closest to the inlet pipe, of both boxes. The other sensor is located in the top right position, the furthest from the inlet cooling pipe.

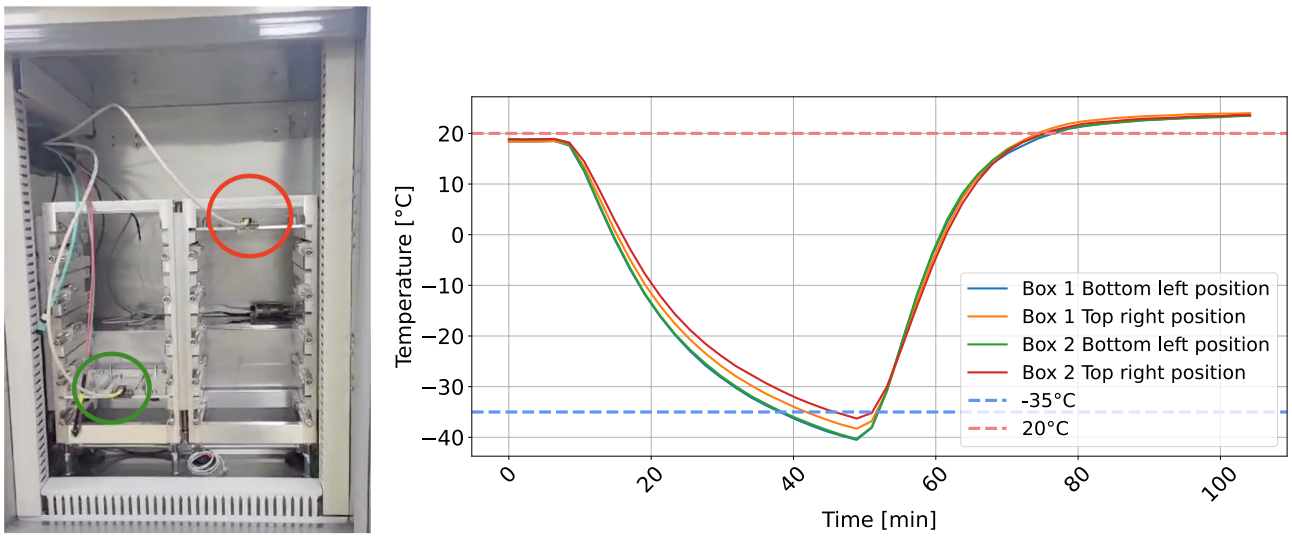

Figure 4.15: On the left, an image of the inside of one of the cold boxes with two carrier plates highlighted in red and green. On the right, a graph showing the temperature as a function of time for the four sensors inside the cold boxes. The dotted blue and red lines indicates the -35 °C and 20 °C temperature target, respectively.

In Figure 4.15, the position of the sensor and the temperature profiles for different positions within the cold boxes as a function of time are shown. When operating both boxes in parallel, the time required for reaching the target temperature of -35 °C is approximately 40 minutes, while warming up to 20 °C takes about 30 minutes. The cooling performance of the chiller is sufficient to cool both boxes to the desired temperature within a reasonable time. Variations in temperature between different positions are observed, depending on their distance from the inlet pipe. Sensors located closer to the cooling inlet, reach the desired temperature more rapidly than those in the top right position.

A small discrepancy is also noted between the two boxes in the upper sensor position: the second box reaches the operating temperature a few minutes later than the sensor in the same position in the first box. This discrepancy most likely arises due to longer pipes and greater thermal losses between the chiller and Box 2 in comparison to Box 1.

Based on these results, operating both Burn-in boxes in parallel is feasible. Measurements using dummies with heating loads that mimic the PS modules have demonstrated that both setups can reach the desired temperature within an acceptable time. In case it is feasible to separate 2S and PS modules for the test, due to the higher heating load of

the PS modules compared to the 2S modules, box 1, being closer to the chiller, will be used for the PS modules to compensate for the temperature difference between the boxes. Conversely, box 2, which is farther from the chiller, will be used for the 2S modules, which have a lower heating load.

4.4 Characterization of PS Modules Using the Burn-in Setup

PS modules will be operated at about -35 °C to maintain their performance and reliability even after substantial irradiation. Understanding their behavior in these conditions, including noise levels and leakage current, as well as the heat dissipation of each module component, is critical. In addition, the efficiency of the cooling system must be ensured. This section presents the findings from various temperature measurements performed on PS modules. In addition to these temperature studies, the noise dependence on the operation temperature and the module's ability to withstand extreme temperatures without damage were investigated. The impact of different module configurations on noise levels was also examined.

Qualitative temperature measurement using an IR camera

The initial step in identifying the heat dissipation of the different components within the module involves performing a qualitative measurement to determine the optimal locations for gluing temperature sensors. To achieve this, a temperature distribution characterization of the PS module without cooling was conducted. This qualitative assessment utilized an infrared (IR) camera to accurately capture and analyze the temperature variations across the module. Since mounting the camera inside the cold box proved challenging and this was only a qualitative measurement, images were taken at room temperature outside the Burn-in setup. In this scenario, it was not necessary to have the module in a closed and controlled environment. Additionally, a 3D-printed carrier plate was constructed to facilitate taking photos of both the top and bottom parts of the module. The aluminum carrier plate only has an opening for the wire bond, as shown in Figure 4.4. Photos of the powered module, both without performing noise measurements and while performing measurements, reveal how different components dissipate heat.

Figure 4.16 displays the top part of the module PS_40_05_DSY_00004. The bottom left image shows the IR profile of the module when it is powered, but no measurement is being performed. The hottest spot, reaching around 40 °C, is the optical transceiver. The DCDC converter is expected to be a hot spot, however it is covered with a shield.

Due to the shield's reflective surface, its temperature is not captured accurately by the IR camera. The bottom right image illustrates that during a measurement, the Front-End (FE) hybrids also dissipate substantial heat, as they are actively engaged in the readout process.

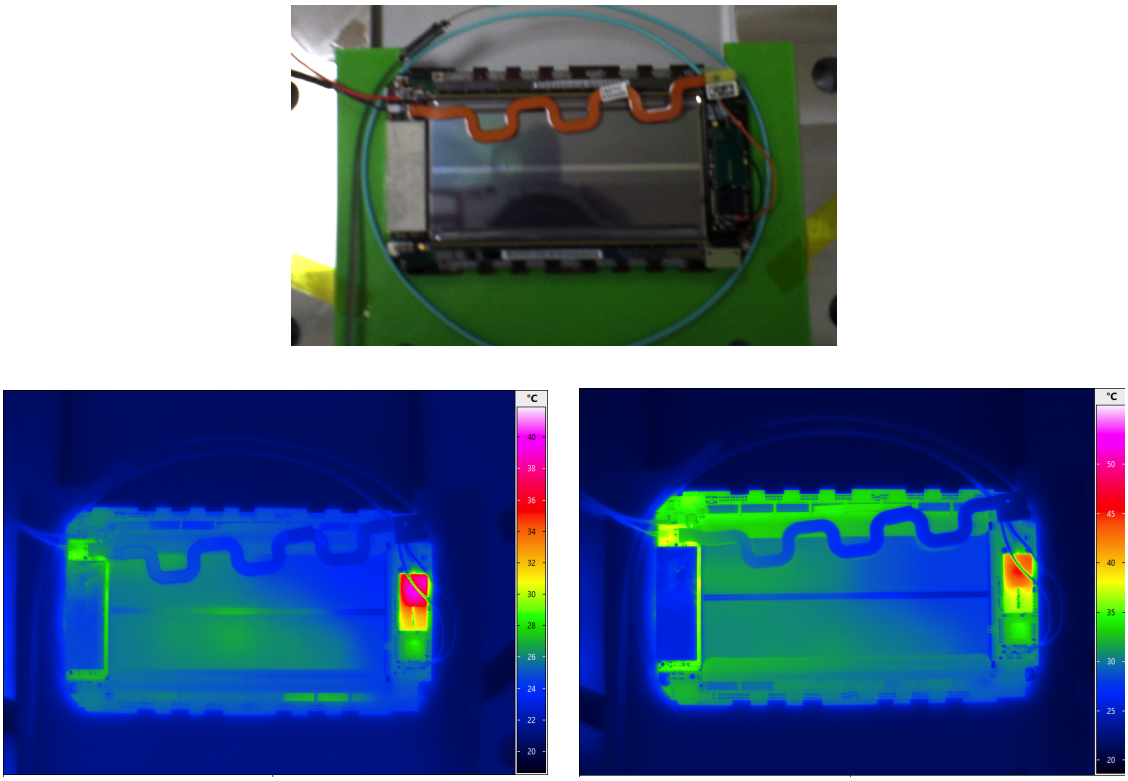

Figure 4.16: The top view of module PS_40_05_DSY_00004 on a 3D printed carrier plate (upper). In the bottom row IR photos of the module powered (lower left) and after configuring the chips (lower right) are presented. The color scale indicates the temperature measured by the IR camera.

Figure 4.17 shows the bottom view of the PS_40_05_DSY_00004 module. The top right image displays the IR profile of the module when it is powered, but no measurements are performed. The bottom row shows the module during a measurement, with the left photo taken at the start and the right photo taken after a few minutes. It is observed that the base plate becomes warmer where the DC-DC converter is located when powered with a temperature of around 30 °C, while the rest of the module remains below 30 °C. Once the measurement starts, the heat dissipation in the DCDC converter increases, causing the base plate to warm up. Additionally, the FE hybrid increases its heat dissipation as well, becoming more active during the readout. After a few minutes of operation, the base plate under the DCDC converter heats up to about 50 °C.

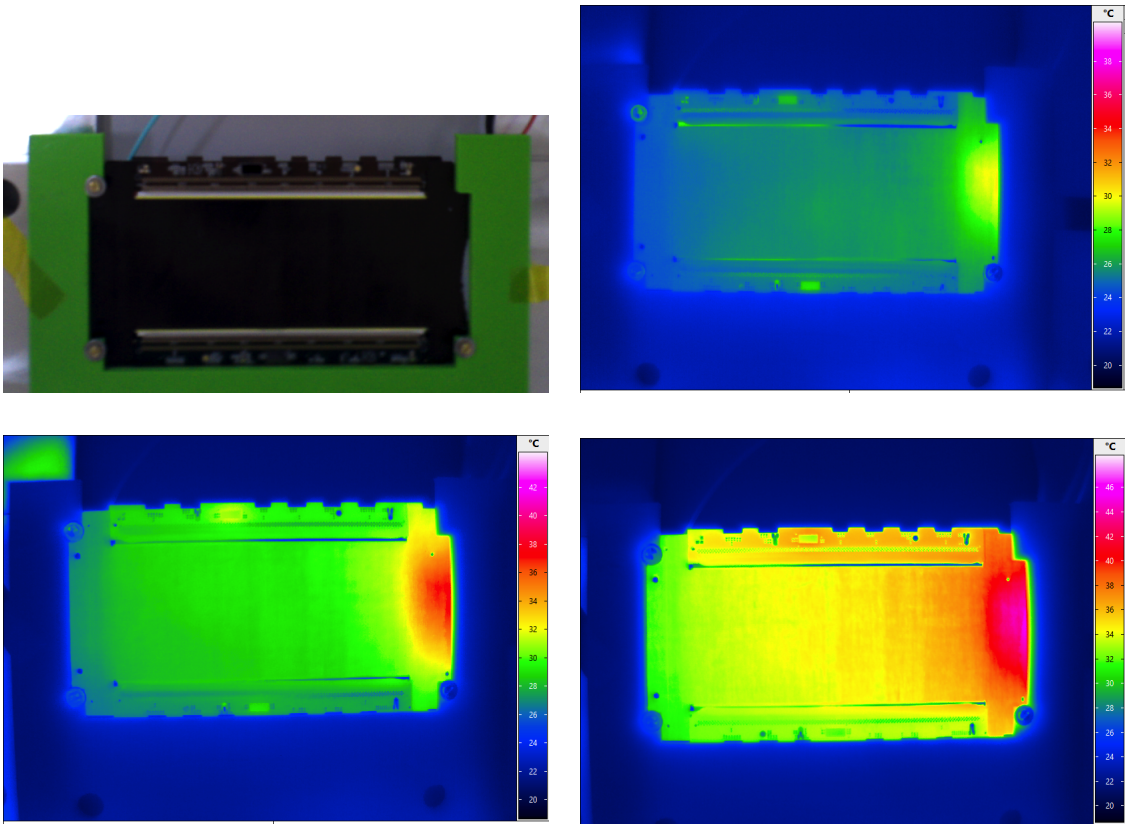

Figure 4.17: Bottom view of the PS_40_05_DSY_00004 module on a 3D printed carrier plate (upper left). The IR photo of the module powered without performing a measurement (upper right). The IR photos of the powered module when the measurement started (lower left) and after a few minutes of performing the measurement (lower right) are shown. The color scale indicates the temperature measured by the IR camera.

The module PS_26_05_DSY_00002 was also measured with the IR camera. To overcome the issue of reflection by the shielding of the DCDC converter in Figure 4.16, this component was covered with black tape, as shown in Figure 4.18. In the bottom left image, the module is powered on, but no measurements are being taken. In the bottom right image, a measurement is in progress. Similar to the PS_40_05_DSY_00004 module, the optical transceiver is observed to have a temperature of around 40 °C. The DCDC converter reaches temperatures of about 46 °C. During the measurement, the heat dissipation of the FE hybrid increases again due to the readout process. In this case, only one side of the FE hybrid is heating up because this module has only one functional hybrid.

With these measurements, the highest heat dissipation points have been identified. Although the heat distribution observed is not entirely accurate due to the use of a 3D-

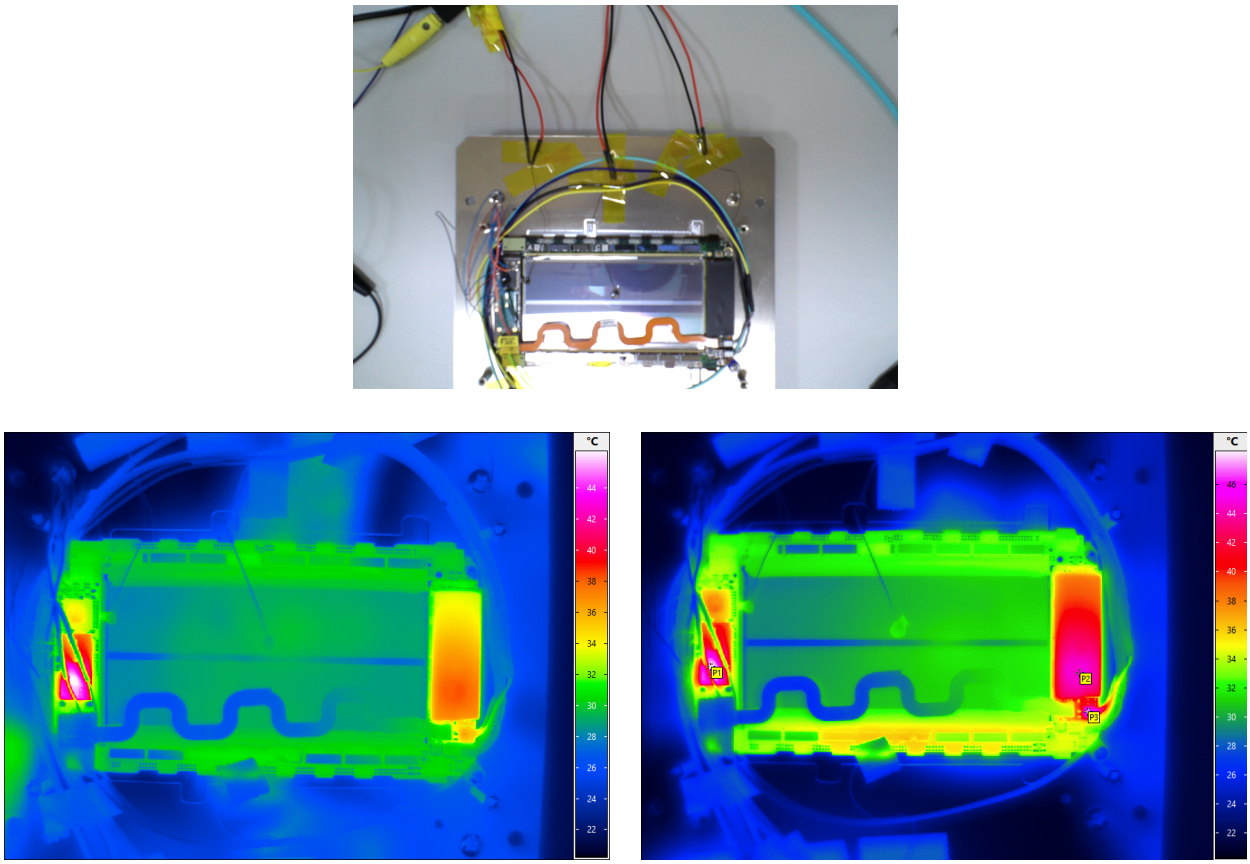

Figure 4.18: Top view of the module PS_26_05_DSY_00002 in a carrier plate (upper). The IR photos of the module powered without performing a measurement (lower left) and while performing a measurement (lower right) are shown. The color scale indicates the temperature measured via the IR camera.

printed plastic carrier plate instead of the actual aluminum plate for the first module, and the lack of cooling, this assessment provides valuable insights. It assists in making informed decisions on where to glue the temperature sensors and perform a quantitative analysis.

Temperature characterization

To obtain quantitative measurements of the temperature profile in the module at room temperature and during the cooling process, seven thermistors were attached to the module PS_26_05_DSY_00002. These thermistors were strategically positioned to assess the thermal homogeneity across the module and evaluate the quality of the thermal con-

tact with the cooling, taking into account the hot spots identified by the IR studies. The specific locations of these thermistors are illustrated in Figure 4.19:

- on top of the optical transceiver (VTRx+), located on the Readout Hybrid (in pink);
- on top of the DCDC converter shield, on the Power Hybrid (brown);
- on the low-power Gigabit Transceiver (lpGBT), located on the Readout Hybrid (orange);
- on the functional Front-End Hybrid (blue);
- in the base plate, next to one of the insert pins (purple);
- at the edge of the Strip sensor, next to temperature sensor on the hybrid (green);
- in the middle of the Strip sensor of the non-functional hybrid (red).

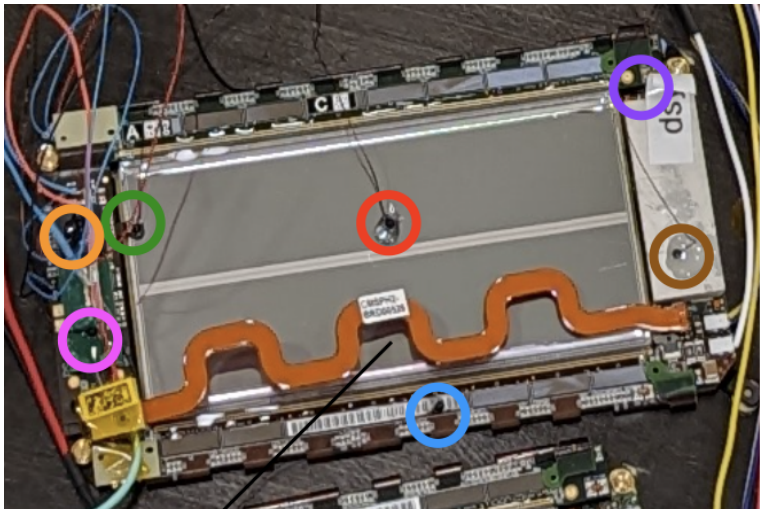

Figure 4.19: Photograph of the module with the positions of the seven thermistors indicated via colored circles.

Once the thermistors are attached to the module, a thermal cycle is performed, ranging from the room temperature (20 °C) to the operating temperature (-35 °C), while measuring the temperature at all seven positions. This measurement has been performed using the Burn-in setup described in section 4.2. To reach the desired temperature when cooling down, the set point of the chiller is configured to be -35 °C, while for warming up, it is set to 25 °C. Throughout the entire measurement, the dew point has remained below -40 °C.

The measurement begins with the module unpowered to observe the cooling process without any heat dissipation. Subsequently, the module is powered on to study the behavior under operating conditions and a noise measurement is taken, since, as shown in the IR studies, this increases the heat dissipation due to an increase in the current. Finally, the module is powered off again, and the entire structure is warmed up to the room temperature.

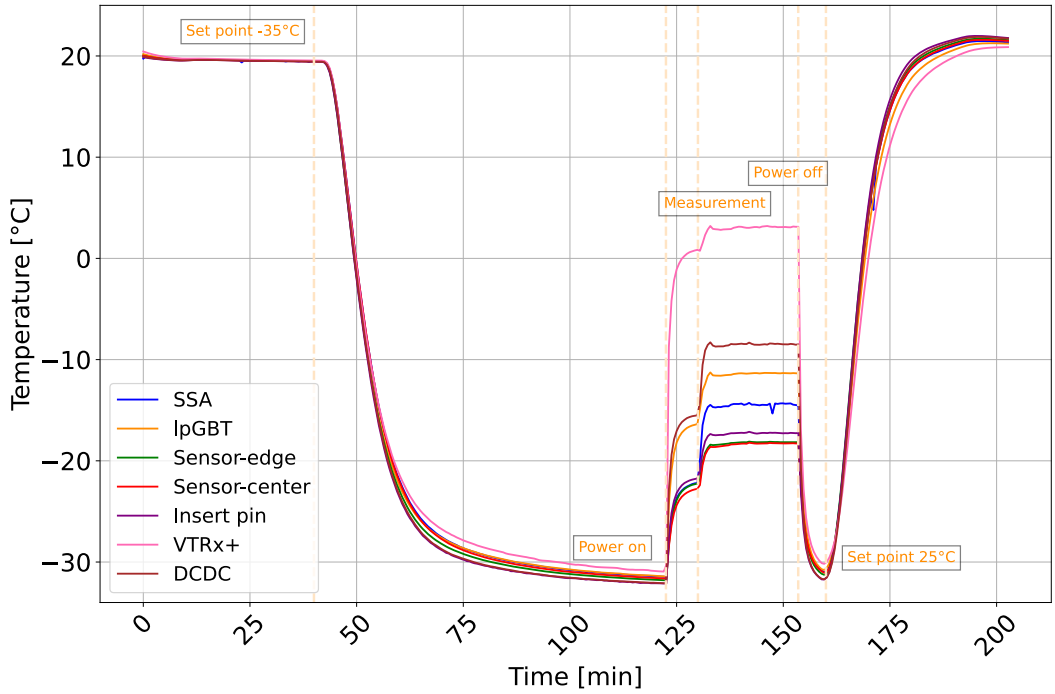

Figure 4.20: Temperature as a function of time during a test sequence, measured via the seven thermistors glued on onto PS_26_05_DSY_00002 module, following the color scheme shown in Figure 4.19.

Figure 4.20 indicates that the setup requires approximately one hour to reach a more or less stable temperature (around -32 °C) to be able to perform a measurement. The difference between the set temperature of the chiller and the achieved temperature is around 3 °C.

Initially, the Burn-in setup is maintained at +20 °C without the module being powered. After a few minutes, the chiller is set to -35 °C, resulting in relatively uniform temperature across the various components of the module while cooling down. When the module is powered on (LV/HV on), the highest temperature is recorded at the optical transceiver, with temperature of around 3 °C. The thermistors located at the lpGBT and the DCDC

converter also indicate high temperatures when the module is powered and configured (-12 °C and -8 °C, respectively), which is attributed to high heat dissipation.

At the start of the noise measurement, a significant temperature increase is observed in the FE hybrid (labeled as SSA). This is due to localized power dissipation during configuration and readout. The two thermistors placed on the silicon sensor (green and red) demonstrate that the Strip sensor is efficiently cooled both at the edges and in the center. After the module is powered off (LV/HV off), all the components cool down within about 5 minutes and uniformly. The warm up process takes around thirty minutes, and it is quite uniform for the different components, as well.

Calibration and noise measurements

In the noise measurement, electrical fluctuations in the output of the detected signal are assessed. These fluctuations can originate from various sources, including leakage current, sensor capacitance, and thermal noise. Consequently, noise is a critical indicator of the quality and performance of each front-end channel and is used to optimize the module's design and operation. Specifically, determining the noise level is essential for selecting the optimal signal threshold that maximizes cluster detection efficiency during the module operation.

First, the reliable communication with the module needs to be ensured. The module startup sequence involves a series of control and configuration procedures on the front-end chips and the back-end FC7 board to ensure the system is ready for operation. These procedures are categorized into optical link establishment, front-end data alignment, and back-end data alignment. The optical link establishment ensures a stable communication with the lpGBT chip, while the data alignment prepare the data transmission chain from the front-end chips to the back-end board. The alignment procedure implies the adjustment of the phase of the data signals with the different components of the module, and ensures that the data is synchronized and thus correctly sampled and decoded.

The next step is the threshold equalization, a critical calibration procedure. This process ensures that the relative position of the signal threshold with respect to the baseline is uniform across all channels, despite inherent variations due to manufacturing differences. The procedure requires setting a target signal threshold where hit occupancy is around 50% and then adjusting the trimming voltage of each front-end channel, such that the hit occupancy is uniform across all channels in response to the same injected charge.

Following the threshold equalization, a noise measurement is conducted to identify electrical fluctuations in the output signal, which are indicative of the quality and performance of each front-end channel. For binary readout chips like the MPA and SSA, noise is assessed using a so-called S-Curve measurement, which consists of scanning the signal

threshold and recording the hit occupancy. At very high thresholds, no signal pulse is detected, resulting in zero hit occupancy for each front-end channel. As the signal threshold decreases toward the signal pulse range, hit occupancy rises to 100%, forming the S-Curve. This curve captures signal fluctuations at the pedestal, allowing for the inference of corresponding electronic noise. Figure 4.21 shows the S-Curve for one channel of a single SSA front-end channel on a single chip.

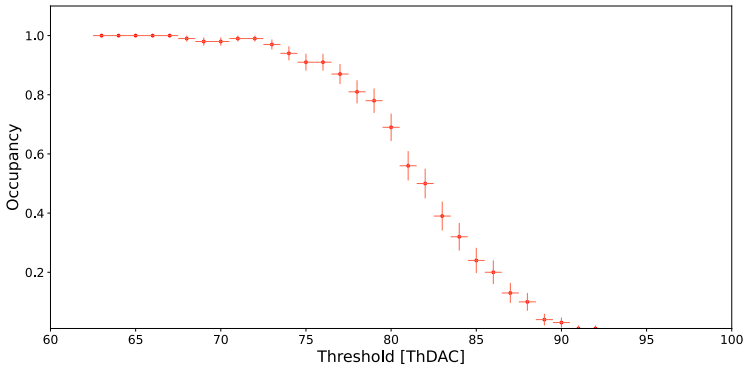

Figure 4.21: S-Curve measurement for one channel of a single SSA.

For each channel, assuming a Gaussian distributed fluctuations, the S-Curve is fitted using an error function:

$$f(x) = \frac{1}{2}\mathrm{erf}(\frac{x-\mu}{\sqrt{2}\sigma}) \ , \tag{4.1}$$

where the pedestal (μ) and the front-end channel noise (σ) are extracted.

In Figure 4.22, the noise performance for the left FEH (FEH-L) of the investigated module PS_26_05_DSY_00002 as a function of temperature is presented. The module is biased with a voltage of -300 V. The dew point during the measurement was between -54 °C and -58 °C, and the carrier plate temperatures ranged from 25 °C to -40 °C. The noise is expressed in ThDAC digital units, which corresponds to the number of electron-hole pairs generated in the sensor required to exceed the threshold. For the SSA 1 ThDAC unit corresponds to about 250 e^- and for the MPA it corresponds to 94 e^-. Each SSA reads out 120 strips, and each MPA chip connects to 1920 channels. The noise value shown in the figure represents the mean noise of all channels in each chip, with the error bars indicating the standard deviation of the mean within the chip.

Figure 4.22a displays the noise values for the different SSA chips. The noise increases with temperature, as expected, since thermally induced electronic fluctuations in the analog input circuit are reduced at lower temperatures. The maximum noise value is around 4.30 ThDAC at 20 °C and below 4 ThDAC at -40 °C, which is well within the acceptable range, as an SSA is considered noisy at a threshold of 5 ThDAC. Additionally, the minimum

value consistently being above 3 ThDAC confirms that there are no disconnected wire or bump bonds. In Figure 4.22a, SSA 3 and 4 are not shown. These two chips have identical I2C addresses in this module. Consequently, individual configuration was not possible, and the noise scan could not be performed. This issue has been resolved in subsequent modules.

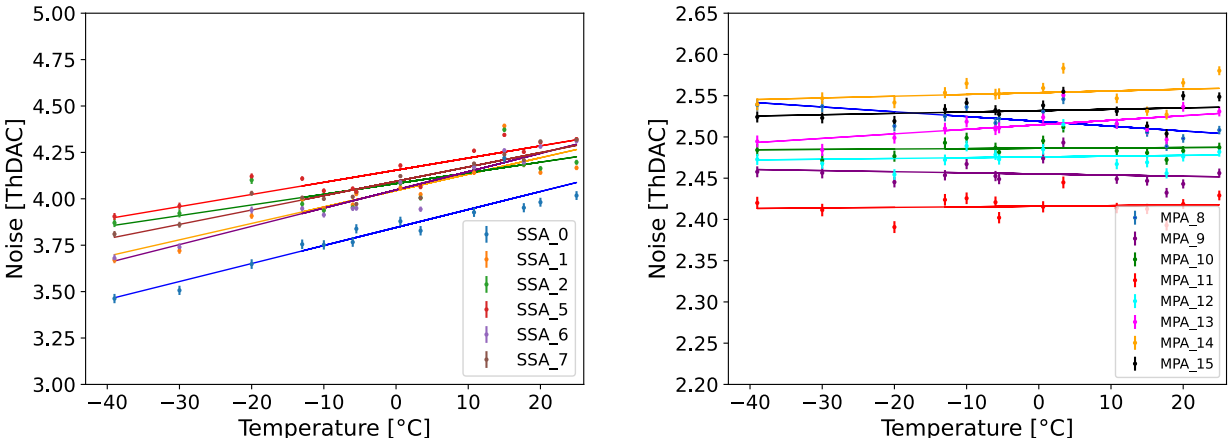

Figure 4.22: Noise levels in units of ThDAC as a function of the carrier plate temperature for the SSAs (left) and the MPAs (right) for FEH-L of PS_26_05_DSY_00002 module.

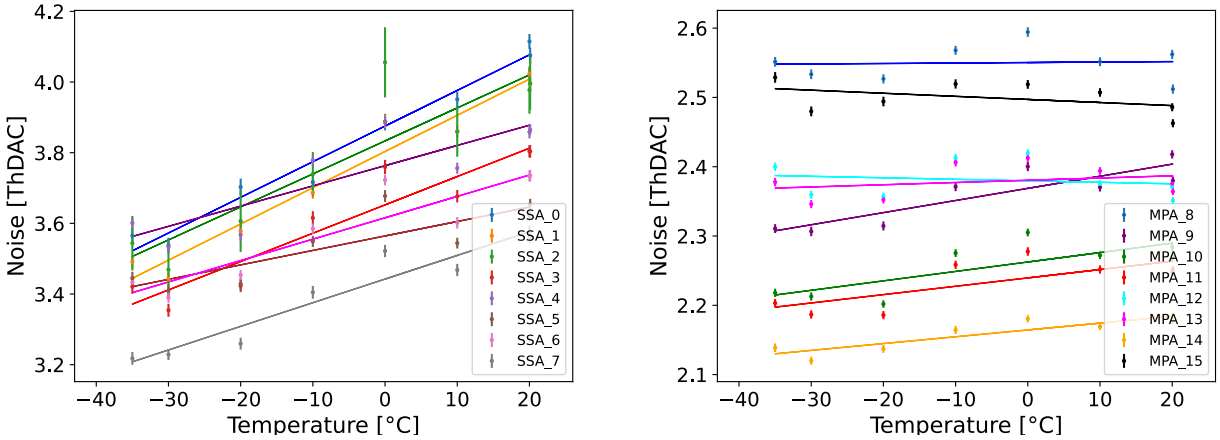

Figure 4.23: Noise levels in units of ThDAC as a function of the carrier plate temperature for the SSAs (left) and the MPAs (right) for FEH-R of PS_26_DSY-00101 module.

Figure 4.22(b) presents the noise values for the MPA chips, where the noise levels remain constant as functions of temperature. The reason is the noise of a pixel sensor being

intrinsically lower than that of a strip sensor due to lower capacitance. Consequently, the impact of low temperatures is more pronounced for the SSA than for the MPA. The measurements show a consistent noise level of approximately 2.5 ThDAC or 225 e across the different MPAs, indicating that this module is performing well, as the classification criteria for an MPA, considering the noise levels between 2 and 4 as acceptable.

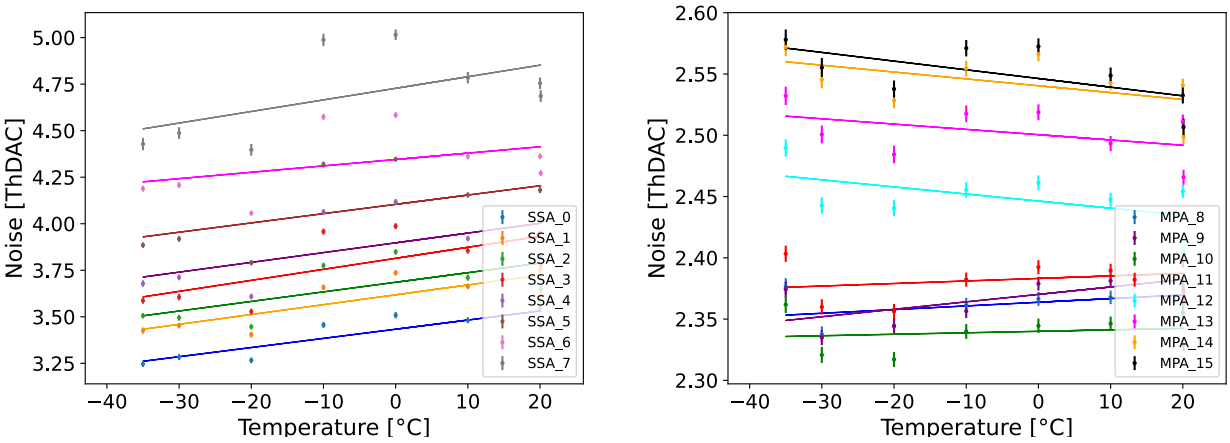

Figure 4.24: Noise levels in units of ThDAC as a function of the carrier plate temperature for the SSAs (left) and the MPAs (right) for FEH-L of PS_26_DSY-00101 module.

These measurements were repeated with the module PS_26_DSY-00101, as shown in Figures 4.23 for the right FEH (FEH-R) and 4.24 for the left FEH (FEH-L). Both hybrids exhibit behavior similar to the PS_26_05_DSY_00002 module. The MPA noise levels remain constant at different temperatures, with values between 2.1 ThDAC and 2.6 ThDAC, indicating good module performance. For the SSAs, a similar trend as in the aforementioned module is observed, with the noise levels increasing with temperature. Notably, on the FEH-R, the highest noise level is measured in SSA_0 and the lowest comes from SSA_7, while on the FEH-L, the opposite pattern is observed. This difference is attributed to the position of the SSAs in the FEH: those situated closer to the POH exhibit higher noise levels. Additionally, the noise levels for the last three SSAs on the FEH-L are consistently higher than those on the FEH-R, exceeding 4 ThDAC regardless of the temperature. This increase in strip noise towards the POH is not yet fully understood. Figure 4.25 shows the noise per channel for the SSAs at -35 °C. The FEH-R displays expected noise values, while FEH-L shows the increasing noise level towards the higher channels, resulting in a higher mean noise value in SSA chips 5, 6 and 7, as compared to FEH-R. This trend is observed in all kickoff modules. The channels around 340 that show noise level of 0 correspond most likely to disconnected wire bonds, while the ones that show high noise are attributed to a scratch on the sensor shorting 4

channels together.

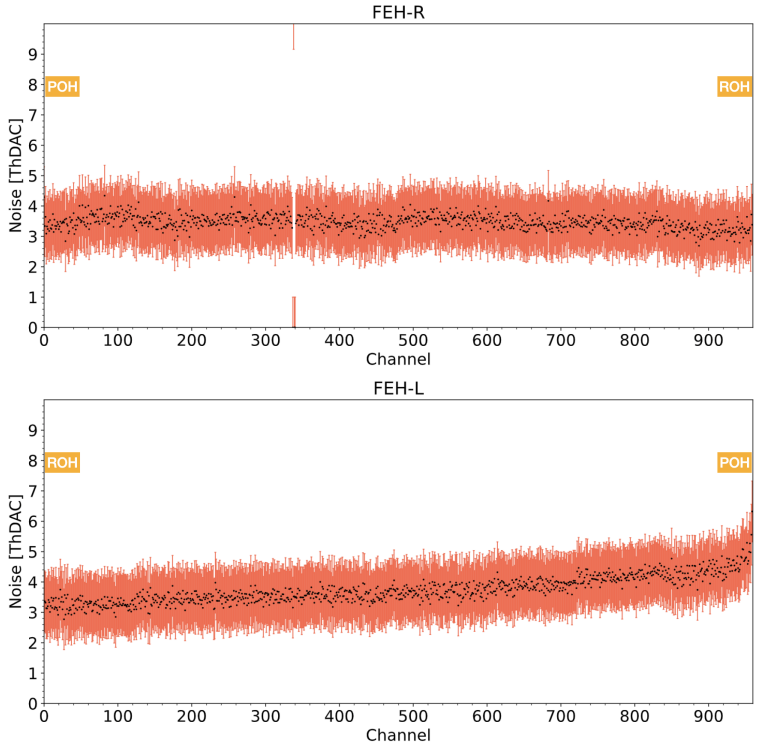

Figure 4.25: Noise measurement for the PS_26_DSY-00101 module per channel for FEH-R on the top and FEH-L on the bottom.

Despite certain channels in the FEH-L exhibiting elevated noise levels (ranging from 5 to 6 ThDAC), the average noise value remains below 5 ThDAC (equivalent to 1250 electrons), thereby deeming it acceptable for installation in the detector. If this issue with the noise tail persists in the production modules, an optimal solution would involve establishing different thresholds for each chip, whereby the channels affected by the tail would be assigned higher thresholds, while channels located further from the POH would maintain lower thresholds.

Threshold equalization

Threshold equalization, also known as trimming, is a calibration process that adjusts the signal threshold relative to the signal baseline (pedestal) for each analogue front-end readout channel. This ensures uniform signal detection across all channels despite variations in pedestal values due to process differences. In the MPA and SSA chips,

where the signal threshold is shared among all channels, equalization is achieved by fine-tuning the trimming voltage. The procedure is typically performed with signal injection, utilizing the chips' asynchronous readout feature. The threshold equalization procedure begins by defining and configuring a target signal threshold at the pulse amplitude where the hit occupancy is approximately 50%, modifying the pedestal definition from the signal baseline to the signal amplitude. Subsequently, the trimming voltage for each front-end channel is adjusted to shift the signal threshold relative to the pedestal, ensuring all channels achieve the same 50% hit occupancy with the same injected charge.

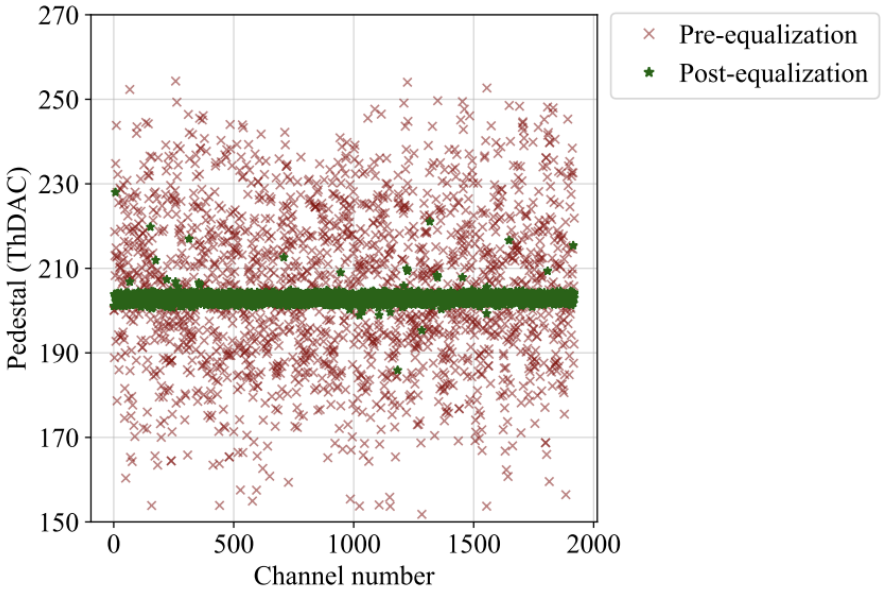

Figure 4.26: Threshold equalization results for a single MPA chip, showing the pre-equalization and post-equalization pedestal for each front-end channel. The y-axis corresponds to the pedestal in digital units (ThDAC) and the x-axis corresponds to the channel number [144].

Figure 4.26 shows a distribution of pedestals for an MPA chip before and after the threshold equalization procedure, performed with an injected pulse amplitude of 77 CalDAC units (where a single unit corresponds to 220 e^-). Thus, a 77 CalDAC amplitude is approximately equivalent to 1 MIP. It should be noted that some front-end channels may fail the equalization procedure. This failure is mainly because the offset required to equalize their corresponding signal threshold exceeds the maximum offset that can be configured on the trimming configuration register.

This trimming procedure, particularly for the MPAs, requires a significant amount of time to complete, whereas it is less time-consuming for the SSAs. Given the importance

of conducting as many cycles as possible during the Burn-in test and understanding the impact of the trimming procedure on noise measurements, a study has been conducted to evaluate the necessity of performing the trimming procedure several times. This study aimed to determine whether trimming needs to be performed before each noise measurement, only once at the beginning, or once per temperature change. For this study, five noise measurements were conducted using the PS_26_05_DSY_00002 module biased at −300 V. Every time a trimming measurement is performed, the thresholds per channel are stored into a configuration file that is used to set the trimming voltage for the subsequent noise measurement.

- Measurement 1: this initial measurement was performed at +20 °C, during which both the trimming and noise measurements were carried out. The resulting trim settings were stored into a configuration file.
- Measurement 2: also conducted at +20 °C, this measurement did not include a trimming procedure. Instead, the configuration file from Measurement 1 was loaded to assess the consistency of noise measurements without re-trimming.
- Measurement 3: conducted at -35 °C, this measurement included both trimming and noise measurements. The trim setting determined from this trimming measurement were stored into a separate configuration file.
- Measurement 4: also conducted at -35 °C, this measurement omitted the trimming step. Instead, the configuration file from Measurement 3 was loaded to determine if noise measurements remained consistent without re-trimming at this temperature.
- Measurement 5: this final measurement was performed at -35 °C, focusing solely on a noise measurement. The configuration file from Measurement 1, which contained trimming data obtained at +20 °C, was used to evaluate the impact of using a trimming configuration from a different temperature setting.

The results of the study are presented in Figure 4.27 for the various SSAs and MPAs, illustrating the mean noise value per measurement. The data indicates that the mean noise value per readout chip remains relatively stable across different measurements as expected. The difference for the SSA between measurements 1 and 2 with 3, 4 and 5 is because of the temperature dependence of the noise in the SSA.

Figure 4.28 shows the pedestal for each measurement for the different SSAs and MPAs. The pedestal is defined as the baseline level of the signal in the absence of any true particle-induced signal. The trimming procedure involves adjusting the trimming voltage for individual front-end channels to equalize the signal thresholds across the channels. This adjustment shifts the signal threshold relative to the pedestal, potentially altering the pedestal value itself. For the measurements where the trimming procedure was performed

(1 and 3), the spread of the pedestal is minimal. In the Measurement 2 and Measurement 4, no trimming was performed and the values from the previous configuration file were used. These measurements exhibit a slightly larger spread in the SSA. The spread in the MPA is quite similar. For the Measurement 5, where the trimming was conducted at a different temperature, the spread of the pedestal noise is significantly larger.

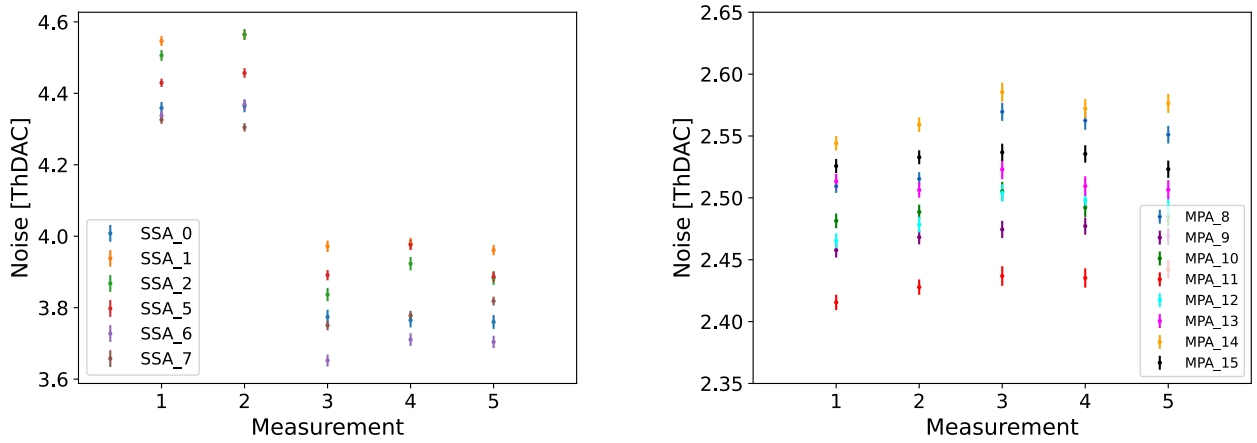

Figure 4.27: Mean value of the noise level for SSAs (left) and MPAs (right) for the different measurements.

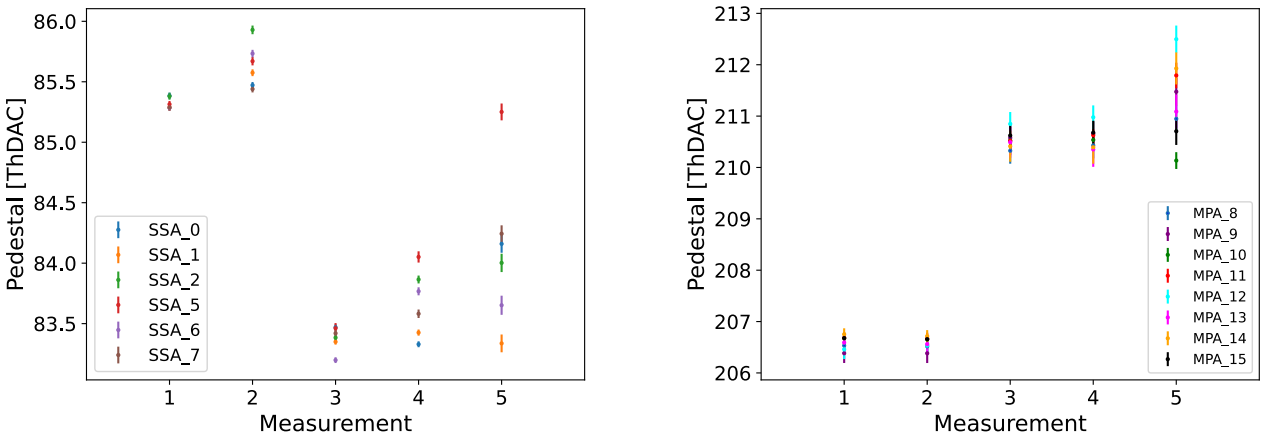

Figure 4.28: Mean value of the pedestal level for SSAs (left) and MPAs (right) for the different measurements.

Additionally, a closer examination of the S-curves reveals differences between the measurements. The S-curves for Measurement 4 and Measurement 5 for SSA_7 and MPA_15 are shown in Figure 4.29. The threshold as a function of the channel and the occupancy is shown. For the SSA, the S-curves appear quite similar between the two measurements, indicating consistent performance. In contrast, the MPA exhibits a noticeable degradation in the width of the pedestal distribution when using a trimming file acquired at a different temperature, compared to using the trimming values acquired at the corresponding temperature.

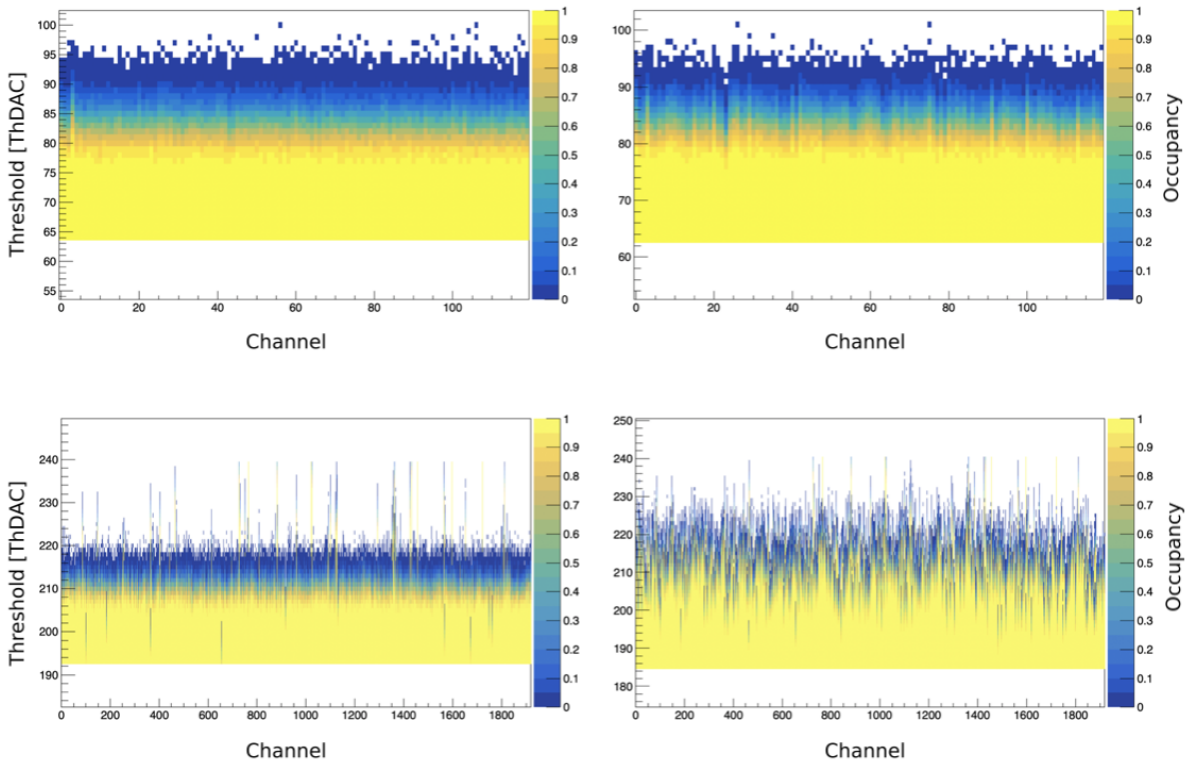

Figure 4.29: S-Curves for a single SSA chip (upper) and a single MPA chip (lower) for measurements 4 (left) and 5 (right).

These observations suggest that while the mean noise values remain stable, individual channels are affected by temperature changes. This implies that while trimming might not be required before each data acquisition, performing a trimming at the specific operational temperature is crucial to maintain optimal noise performance and signal quality. Furthermore, irradiation is anticipated to impact the trimming voltage, thereby requiring regular trimming calibrations of the modules.

Current and noise measurement at different Low Voltage configurations

The modules are designed to operate with a LV of 10.5 V. This voltage is regulated within the Power Hybrid (POH), where the point-of-load (POL) DC-DC converter ASIC is situated. This ASIC, known as bPOL12V [167], was developed at CERN to facilitate more efficient power distribution. It has a maximum nominal input voltage of 12 V and a minimum operational voltage of 6 V.

Reducing the LV can impact the overall power consumption and the noise characteristics of the modules. To investigate the effects of varying the LV, a series of studies were conducted with LV values ranging from 10.5 V to 6 V. The goal was to evaluate how noise levels are affected by lower voltages, in order to determine whether power savings can be achieved without compromising signal integrity.

This study was conducted using the PS_26_05_DSY-00101 module at a temperature of +20 °C with a dew point of -40 °C. Noise measurements were performed for different LVs values, starting at 10.5 V and decreasing until the module could no longer power on. Below 7 V, noise measurement were no longer possible due to communication issues, and below 6.3 V, the module could not be powered on. During the noise measurements, the module was biased at a voltage of −300 V. The LV values along with their respective current and power consumption are shown in Table 4.1.

Table 4.1: Current and power consumption of the module as a function of Low Voltage values.

Low voltage [V]	Current [mA]	Power consumption [W]
10.5	710	7.46
10	739	7.39
9.5	776	7.38
9	815	7.34
8	916	7.33
7	1028	7.22

It can be observed that the current increases as the low voltage decreases, this is to compensate for the need to maintain power consumption constant. The overall power consumption decreases slightly due to the voltage reduction outweighing the current increase.

Figures 4.30 and 4.31 illustrate the noise levels for the SSAs and MPAs chips, across different LV settings for both hybrids. For the SSAs lower LV settings correlate with reduced noise levels of around 0.1 and 0.2 ThDAC. On the FEH-R, the highest noise level is measured in SSA 0 and the lowest comes from SSA 7, while on the FEH-L, the opposite

pattern is observed. This difference may be explained by the position of the SSAs in the FEH, since those closer to the POH exhibit higher noise levels. Additionally, the noise levels for the last three SSAs on the FEH-L are consistently higher than those on the FEH-R as seen in previous measurements.

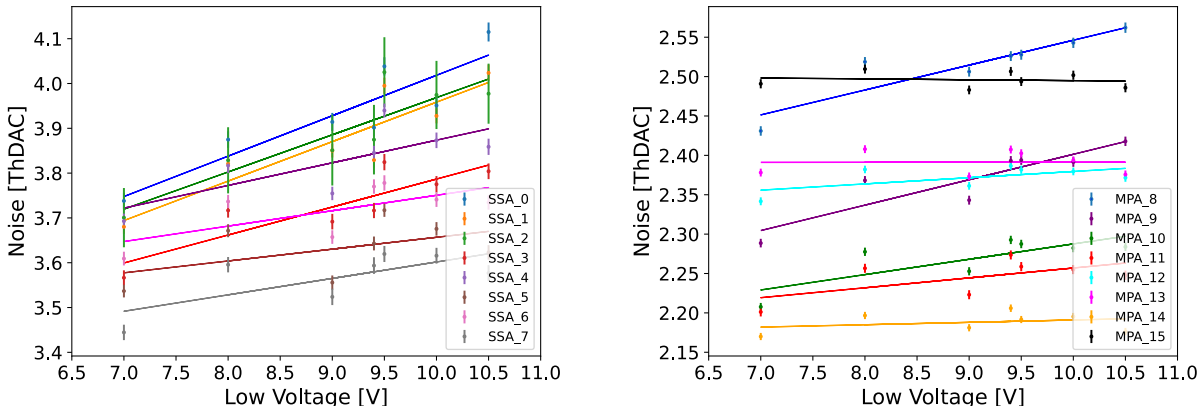

Figure 4.30: Noise as a function of the Low Voltage level for the SSAs (left) and the MPAs (right) for FEH-R of PS_26_05_DSY-00101 module.

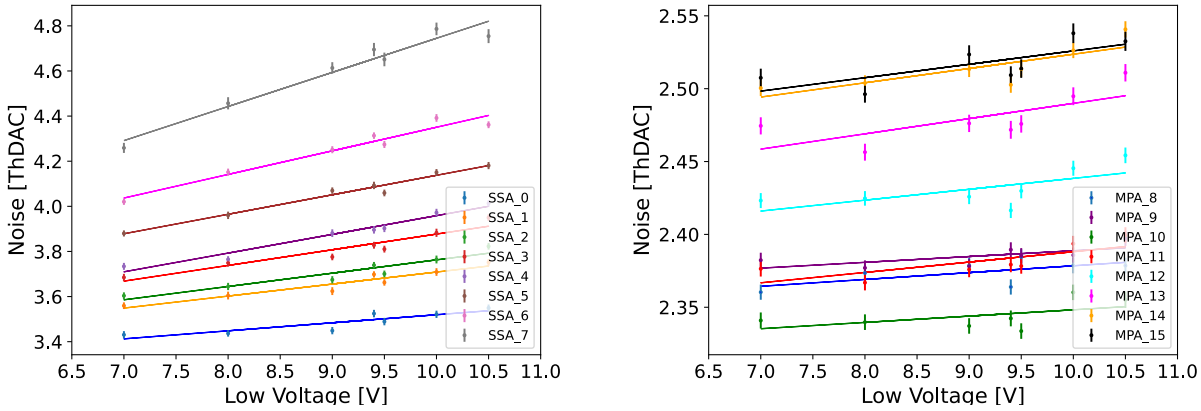

Figure 4.31: Noise as a function of the Low Voltage level for the SSAs (left) and the MPAs (right) for FEH-L of PS_26_05_DSY-00101 module.

Figure 4.32 displays noise measurements from all SSA channels of FEH-R and FEH-L at two LV settings, 10.5 V and 7 V. Slight noise reduction is observed in the FEH-L without noticeable enhancement in the tail effect. Therefore, while lowering LV decreases noise

in the SSA, it does not address the noise issue observed in FEH-L. The FEH-R is not affected by the tail effect.

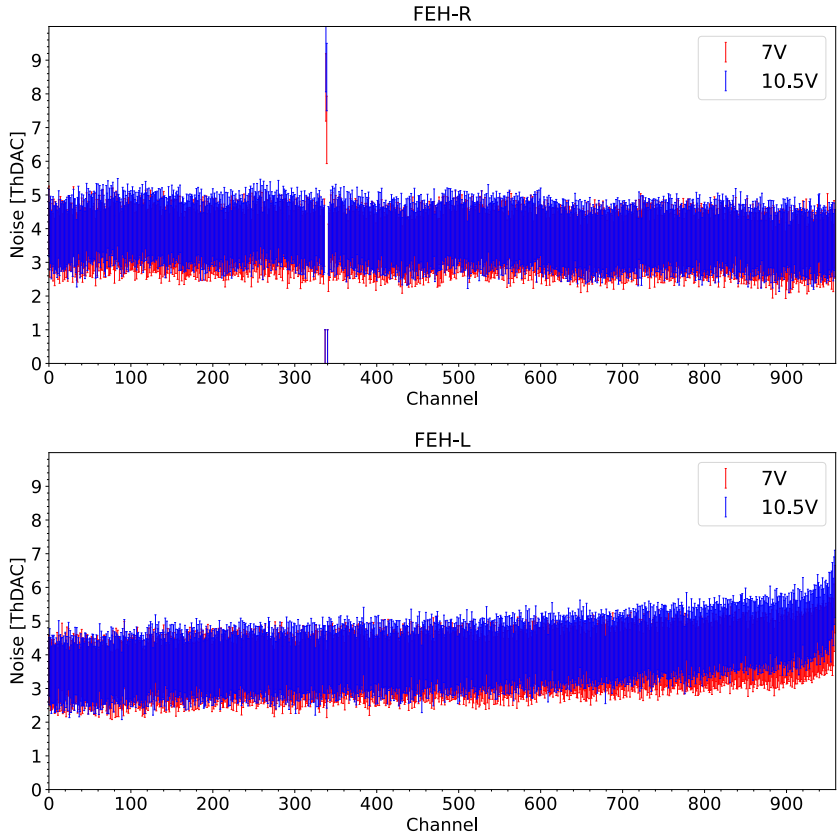

Figure 4.32: Noise measurement with Low Voltage levels of 10.5 V (blue) and 7 V (red) for FEH-R (upper panel) and FEH-L (lower panel) of PS_26_05_DSY-00101 module.

Extreme cold test

While the target operation temperature of the modules is -35 °C, testing the modules at extreme temperature conditions is crucial to ensure their reliability in case the temperature might drop unexpectedly.

For this test, the PS_26_05_DSY_00002 module was used, biased at −300 V and cooled down. A critical constraint was the minimum temperature that the chiller can reach, -55 °C, which corresponds to a temperature of -45 °C on the carrier plate. The test procedure began at 20 °C, gradually cooling down to -45 °C, and then warming back up to 20 °C. Throughout this process, four measurements were taken at specific temperature

points: two at around the room temperature (at the beginning and at the end) and two at around -45 °C. This measurement consists of threshold equalization, noise measurement, and the measurement of the leakage current (I) as a function of the bias voltage (V), referred to as IV characterization. Throughout these temperature cycles, the dew point remained consistently below -60 °C as indicated in Figure 4.33.

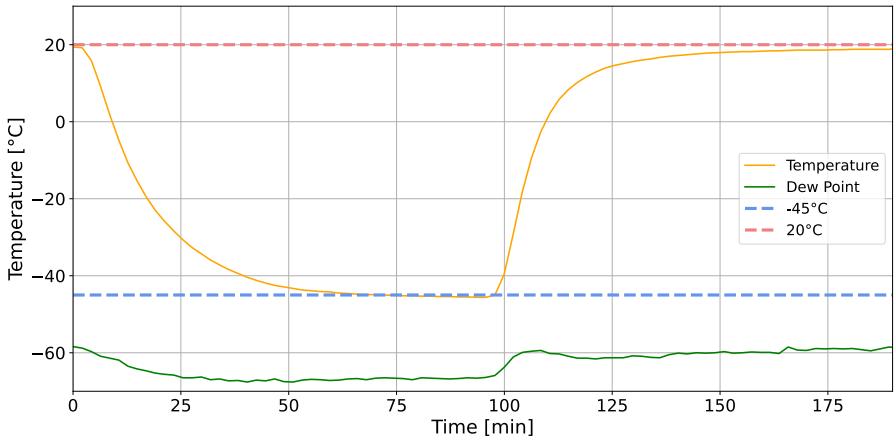

Figure 4.33: Temperature measured on the carrier plate (blue) and dew point (orange) as a function of time for the extreme cold test in the Burn-in system.

Figure 4.34 shows the average noise values per SSA (left) and MPA (right) across the four different measurements. The results indicate that the module functions well throughout the temperature cycle, with noise levels remaining below 5 ThDAC for the SSA and below 4 ThDAC for the MPAs. This proves that the module can handle extremely cold temperatures down to -45 °C, without receiving damage.

The aforementioned IV characterization involves measuring the leakage current as a function of the bias voltage applied to the silicon sensors. This measurement is essential for evaluating electrical properties such as the leakage current at the target operational voltage and, the breakdown voltage, which are critical characteristics of the sensor regarding their operation in the experiment. The IV curves shown in Figure 4.35 appear almost identical. Typically, lower temperatures result in lower leakage currents (Eq. (3.7)), but this is not observed. The reason is the dominant influence of the VTRx+, as it emits light which hits the detector and affects the leakage current. To reduce this effect, production modules will include a plastic cap, placed on the top of the VTRx+, which will absorb these photons.

The modules are designed to operate at 600 V. However, due to radiation damage over time, the operational voltage may gradually increase to 800 V. Consequently, it is essential

to ensure that the module can withstand up to 800 V. Figure 4.35 shows that the breakdown voltage for this module is above 600 V before and after the extreme cold conditions. Furthermore, it was observed that the module is mechanically capable of withstanding high voltage, as no discharges were detected at any point during the measurements.

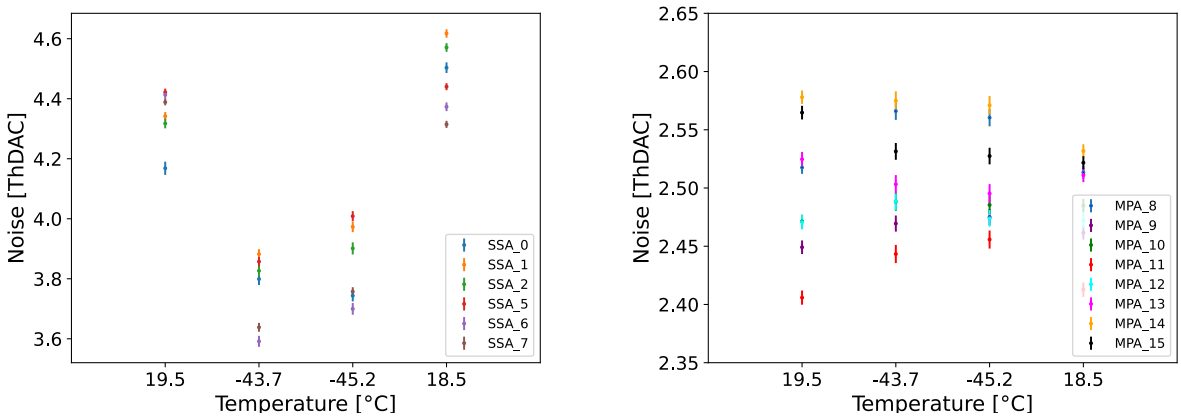

Figure 4.34: Noise for SSAs (left) and MPAs (right) for the measurements at room temperature and at -45 °C.

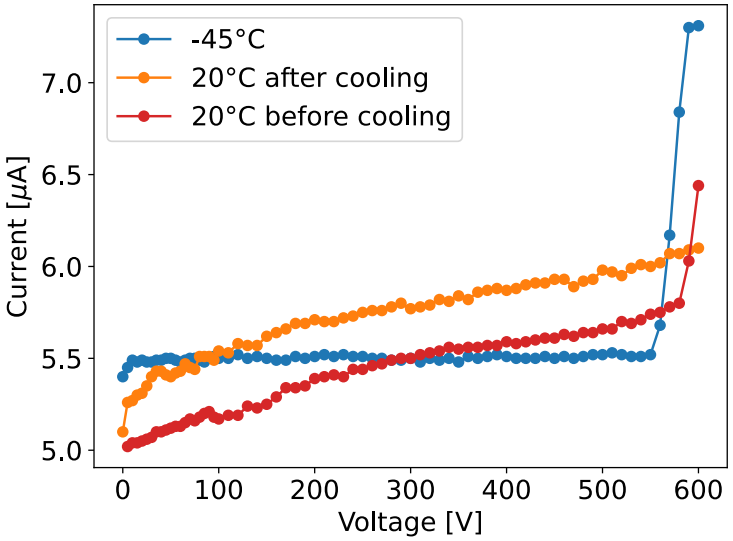

Figure 4.35: IV measurement results from the PS_26_05_DSY_00002 module performed at+20 °C before the cooling (red), -45 °C (blue) and at +20 °C (orange) after the temperature cycle.

The comprehensive data obtained in these measurements demonstrate that the modules can withstand extreme conditions and confirm that the modules can operate reliably under the desired conditions, exhibiting acceptable noise levels, leakage current and breakdown voltage. These studies will be important in designing the quality assurance procedure for the Burn-in process.

4.5 Burn-in Test of a PS module

Upon completion of the Burn-in setup and its commissioning phase, an initial, 24-hour Burn-in test was conducted. Despite the setup not being fully automated yet, the test was executed successfully and replicates a potential sequence of the quality control procedure performed using the Burn-in setup.

The PS_26_05_DSY_00002 module underwent a comprehensive Burn-in test designed to emulate the full qualification process required for all modules before integration into the TEDD. The test protocol comprised optimizing the chiller set points and considering the time needed for each measurement. This allowed for the performance of eight complete temperature cycles, during which trimming, noise and IV measurements were taken at every time a stable temperature was reached.

Figure 4.36 illustrates the temperature cycles performed over a 24-hour period. The orange line represents the temperature recorded on the carrier plate of the module, oscillating between +20 °C and -35 °C. The green line indicates the dew point, consistently staying below -60 °C. The blue dotted line marks the -35 °C target temperature and the red dotted line +20 °C, while the gray dots indicate the instances of the 16 successful measurements taken. Note that the noise measurement at cycle 11 failed due to a communication failure and is not included in the following.

From the Figure 4.36, it can be observed that the dew point increases with rising temperatures and decreases as the temperature drops, as expected. Measurements are performed at sufficiently stable temperature conditions. After the completion of a measurement, the set point of the chiller is changed. The average time between two measurements is 1.5 hours. The chiller set point chosen for low temperature measurements is -40 °C. This results in a carrier plate temperature of -34.5 °C, slightly above the target temperature. It is assumed, that reaching a carrier plate temperature of -35 °C will not increase the time required per temperature cycle significantly. A possible further improvement would be the optimization of the chiller parameters.

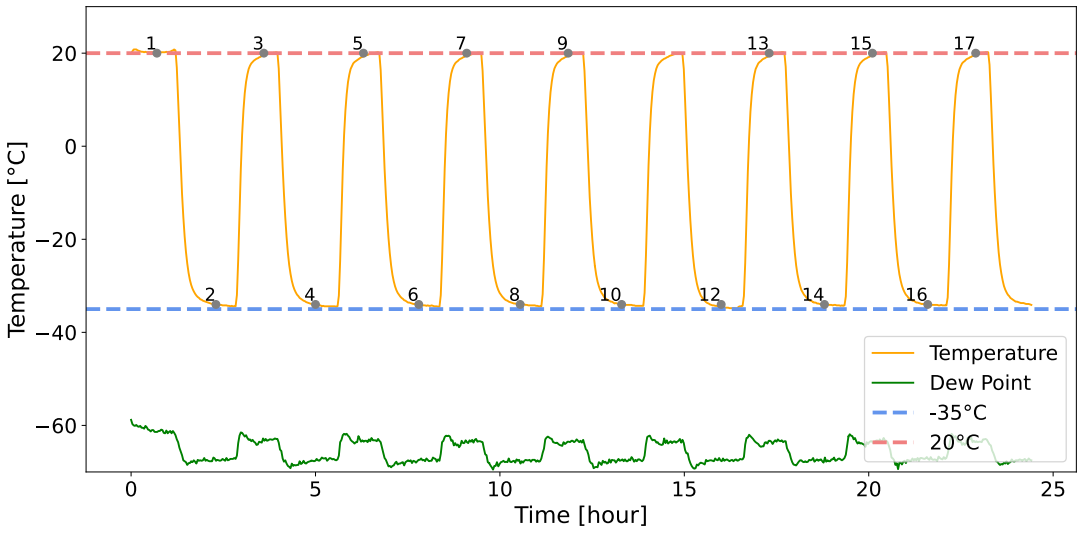

Figure 4.36: Temperature measured on the carrier plate (orange) and dew point (green) as a function of time for the Burn-in test spanning 24h. The gray dots represent the 16 successful measurements performed.

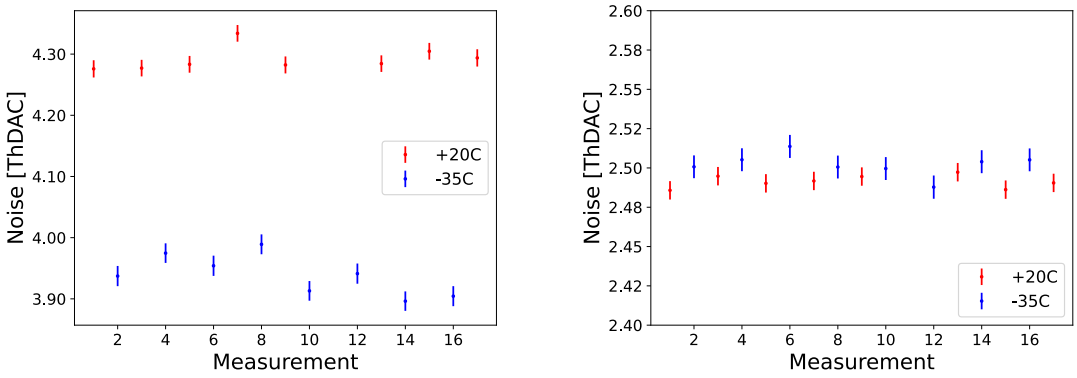

Figure 4.37: Mean value of the noise per channel for SSAs (left) and MPAs (right) for the different measurements taken during the Burn-in test.

Figure 4.37 displays the average noise values for all SSAs (left) and MPAs (right) for each measurement. Red dots represent measurements taken at room temperature (+20 °C), while blue dots represent those taken at the operational temperature (-35 °C). The error bars are the standard deviation of all channels.

For the SSAs, the noise measured at -35 °C is lower than that at +20 °C, which is expected due to reduced thermal noise at lower temperatures. Conversely, for the MPAs,

the temperature does not significantly affect the mean noise values. The noise levels remain within the specifications of less than 5 ThDAC for strips and less than 4 ThDAC for pixels. For a detailed view of the noise performance of individual SSA and MPA chips, refer to Figures A.5 and A.6 respectively.

A noise measurement takes approximately 10 minutes for the PS_26_05_DSY_00002 module because only one hybrid is operational. For a fully functioning module the noise measurement duration extends to about 20 minutes.

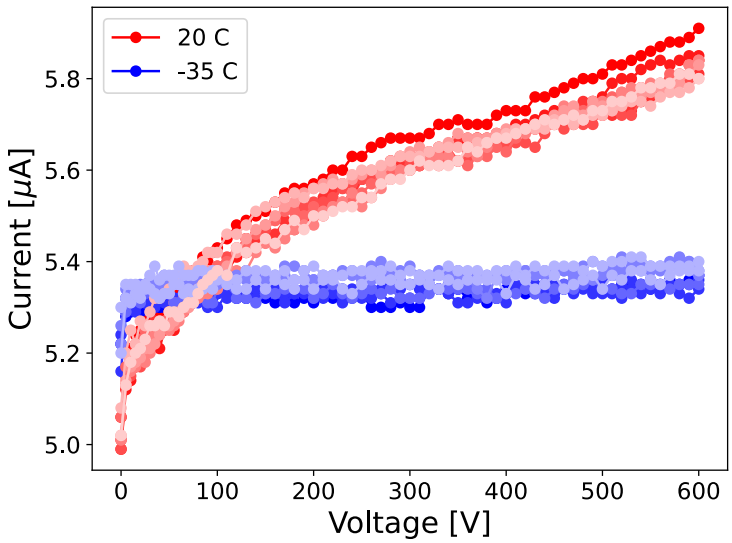

Figure 4.38: IV measurement from PS_26_05_DSY_00002 module showing the 16 measurements performed during the 24h test. The measurements are performed at +20 °C (shades of red) and at -35 °C (shades of blue).

Figure 4.38 shows the current of the module as a function of the voltage (IV curve), measured at +20 °C and at -35 °C. As expected, the leakage current at lower temperatures is reduced, compared to that at higher temperatures, indicating reduced thermal noise at the operational temperature of -35 °C. Naively one would expect a much bigger difference for this temperature change, in this case the VTRx light is major driver of the leakage current in this test over the temperature and bulk leakage current.

Over the 24 hours of continuous HV power and multiple temperature cycles, the noise levels and IV curves of PS_26_05_DSY_00002 module remained consistent. This outcome indicates that the module successfully withstood the test conditions. Consequently, if subjected to the actual Burn-in test, this module would qualify for an integration into the TEDD.

4.6 Conclusion and prospects

The hardware part of the Burn-in setup has been successfully built and commissioned. The Burn-in system has demonstrated its capability for performing a full temperature cycle in around 1 hour, reaching the -35 °C required while maintaining the dew point under -40 °C in all the measurements.

Extensive studies characterizing PS modules and prototypes have been performed within this project. This has led to several changes and had an impact on the design of the final module itself.

Full Burn-in tests have been performed, demonstrating the readiness and capability of the setup, albeit with only one module so far. Despite the fact that the Burn-in test performed 8 full cycles, for production modules, maybe fewer cycles will be performed. This adjustment is necessary because the module used in this test has only one working hybrid, while for production modules with two hybrids, the time required for noise measurements will effectively be doubled. Additionally, current limitations in performing parallel noise measurements for multiple modules necessitate ongoing firmware and software improvements, as testing a single PS module with both hybrids working, currently takes around 20 minutes.

Furthermore, the DESY setup can run two Burn-in setups simultaneously, allowing up to 20 modules to be tested at once. This capability presents two scenarios:

- Alternating Usage: One setup is used, while the other is loaded with modules, alternating between them. This optimizes the time needed for performing a temperature cycle, as all the power of the chiller is focused on one setup. This approach also ensures more accurate temperature control. Additionally, noise measurements of 2S modules only take a couple of minutes, whereas PS modules require around 20 minutes. Therefore, a setup with only 2S modules could perform more cycles compared to one with only PS modules.

- Parallel Usage: If time constraints are critical, both setups can be used in parallel. In this case, one controller box acts as the master and the other as the slave, both reading temperature and dew point sensors, but only one controlling the chiller. Software modifications to enable this functionality are currently under development. The main challenge with this approach is that both setups need to follow the same temperature cycle. Consequently, if one setup is loaded with 2S modules and the other with PS modules, the 2S modules will need to wait for the PS modules to complete their noise measurements.

Decisions regarding the final protocol for Burn-in testing are still pending, considering the capabilities of similar setups at other centers. One proposed option is to perform noise

measurements and IV curves at only a few of the temperature cycles, including the first and the last cycle.

This work has still some ongoing and future tasks not covered in this thesis. These include an optimization of the chiller parameters and thorough test of the full capacity of the Burn-in setup with 20 modules to ensure temperature cycles can be performed efficiently at maximum capacity. Until the 20 modules are available, dummy heat loads are used. The installation of the final software, which is a centralized development within all Burn-in centers, is in progress.

For concluding the temperature studies a kickoff module, representing advanced stage of the module design, has been equipped with thermistors during assembly for detailed temperature monitoring. This module will soon be tested in the Burn-in setup.

CHAPTER 5

Integration Tests of CMS Outer Tracker Modules

Contents

5.1 Introduction

Although important module characterization measurements could be conducted using the Burn-in setup, described in chapter 4, it does not fully represent the cooling methods of the actual CMS experiment. Therefore, a sector test structure was constructed, containing a single Dee cooling sector. This setup allows for tests with controlled humidity and temperature, offering conditions that more closely resemble the final installation of the modules in the experiment.

In this chapter, temperature measurements for the module PS_26_05_DSY_00002 in various positions on the support structure are presented, as well as noise measurements for this and three additional PS modules built at DESY. Additionally, a *mockup* structure has been developed to further refine the cooling performance, by enabling tests with different

thermal interface materials (TIM). So far, the PS_26_05_DSY_00002 module has been tested using a thermal pad, while tests with thermal gap filler are envisaged.

This chapter further presents a comparison of the noise measurements obtained from the sector test and the mockup structure during an integration test at DESY.

5.2 Sector test setup

The sector test setup developed at DESY is designed to evaluate one cooling sector of the Dee, by using CO_2. This setup, shown in Figure 5.1, includes an isolated box, large enough to accommodate an entire cooling sector, equipped with a lid to allow for the temperature and humidity control.

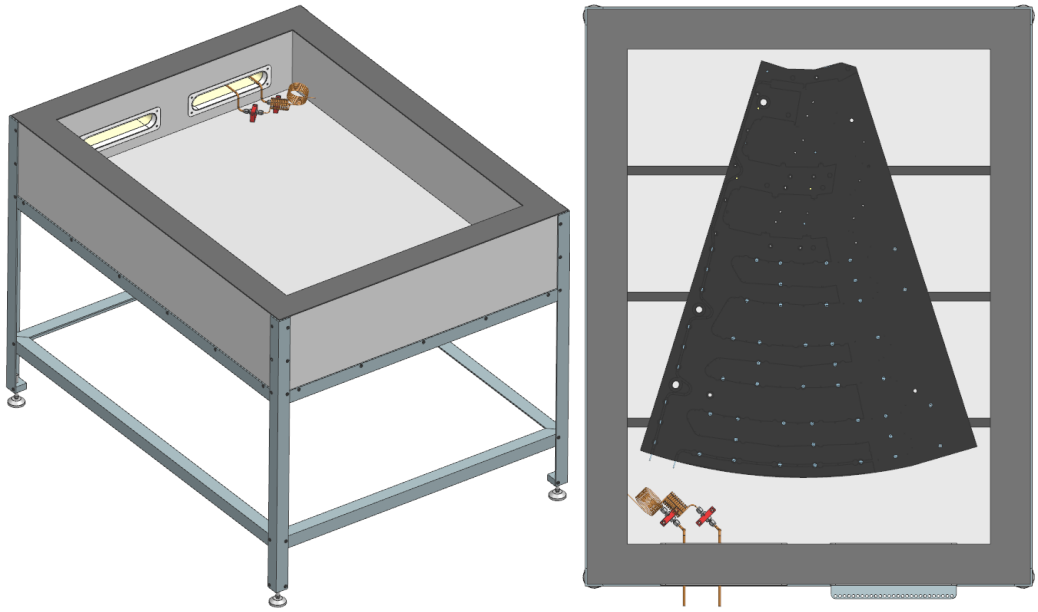

Figure 5.1: 3D CAD drawing of the sector test setup with copper pipes (left panel), and a single cooling sector installed inside the sector test setup (right panel).

To regulate the humidity level, a dry air supply is incorporated. The setup includes inside the box a Vaisala dew-point sensor, a PT1000 temperature sensor, a relative humidity sensor, and 20 PT100 temperature sensors for continuous monitoring of the internal conditions, read out via Keithley DAQ6510 with two Keithley 7700 modules positioned outside the chamber. Additionally, the sector test setup features a rack with a CAEN system to power the modules, along with several FC7 boards and optical fibers for the module readout. For cooling, the setup utilizes a *Monoblock Approach for Refrigeration Technical Application* (MARTA device) connected to the cooling sector under test via copper pipes.

Monoblock Approach for a Refrigeration Technical Application

The MARTA [168] is a compact cooling device, shown in Figure 5.2, based on two-phase CO_2 cooling. This device allows for a precise control of the temperature from the room temperature down to -35°C, providing good thermal stability. It is based on the Two-Phase Accumulator Controlled Loop technology developed at CERN [169]. MARTA features two cooling loops: the primary loop uses an R507 chiller, while the secondary loop circulates CO_2 via a fluid pump. CO_2 flows through the pipes where the temperature of the inlet and outlet pipes equalizes. The thermal load in the experimental setup evaporates CO_2, which is condensed and sub-cooled in a heat exchanger. The system controls the CO_2 temperature by adjusting the saturation temperature in an accumulator with an electrical heater, achieving the desired set-point temperatures. The lowest attainable temperature depends on the experiment's heat load and ambient heat loss.

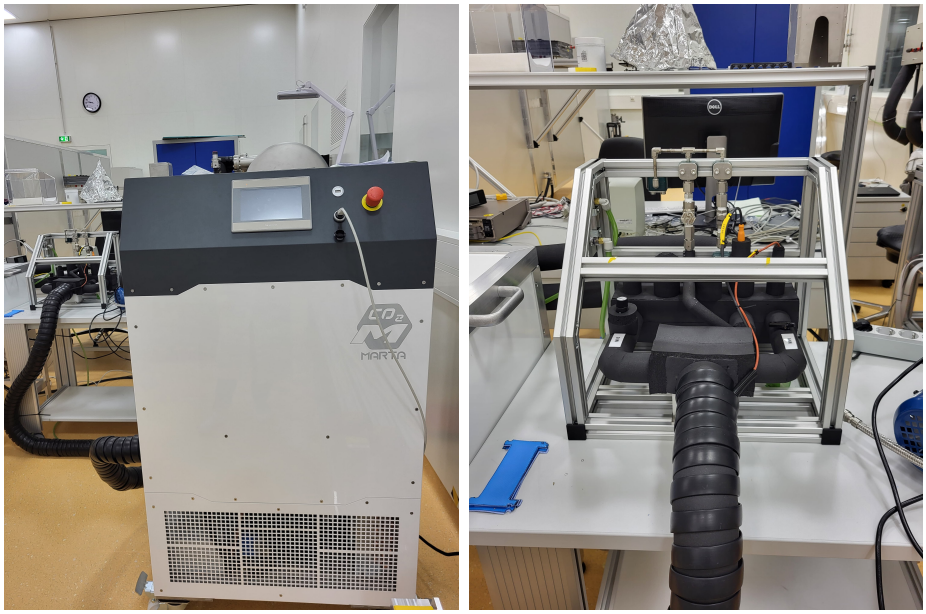

Figure 5.2: Photo of the MARTA setup on the left and of the valves and pipes box on the right.

5.2.1 Temperature Characterization of the Cooling Sector

To evaluate the PS_26_05_DSY_00002 module under conditions that closely resemble its final installation in the Dee, the sector test setup was employed. Given that only a single cooling sector was used in this setup, a uniform cooling across the entire Dee sector could not be achieved. As a result, the temperature distribution across the modules varied

depending on their position within the Dee. To investigate the extent and the impact of these cooling variations, temperature measurements of the PS_26_05_DSY_00002 module were conducted in two different positions.

As illustrated in Figure 5.3, the optical board (VTRx+ and lpGBT) is not directly cooled from below, as the cooling block does not extend to its position. In Figure 5.4, the power board (DCDC converter) lacks direct cooling. Both the VTRx+ and the DCDC converter are the warmest spots of the module during its operation as mentioned in Chapter 4.

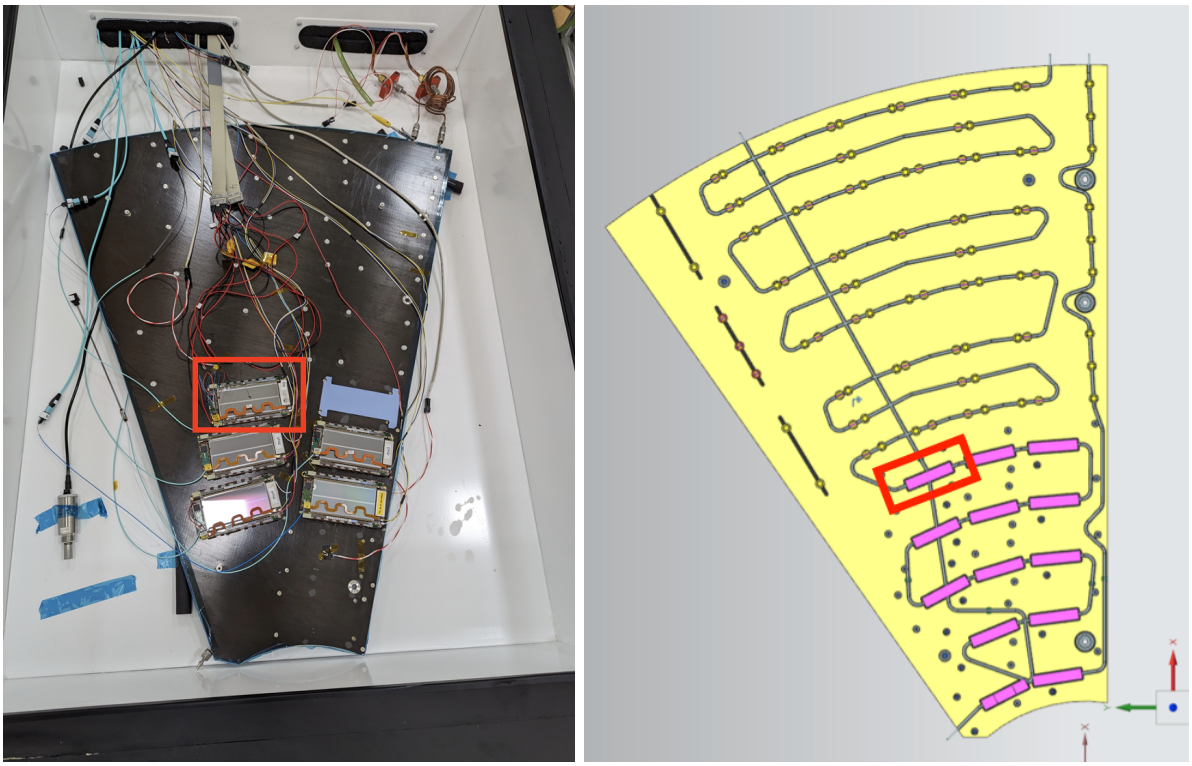

Figure 5.3: Left panel: the photograph of the single cooling sector, with the PS_26_05_DSY_00002 module installed on the left (highlighted with a red square). Right panel: a CAD drawing of the cooling sector with the carbon foam blocks (pink) and the position of the module (red square). The modules are installed in the Dee sector using a thermal pad (blue).

The modules are installed in the Dee sector using a thermal pad to enhance thermal conductivity between the Dee and the base plate of the module. This ensures sufficient heat transfer, crucial for maintaining optimal operating temperatures during the operation. These thermal pads are cut to the shape of the base plate, have a thickness of 0.5 mm and a thermal conductivity of 3 W/mK [170]. Furthermore, four additional PS

modules can be seen installed in the sector test in the same manner. Noise measurements were conducted on all of these modules sequentially, and the results will be presented in Section 5.4. However, for temperature measurements, only the PS_26_05_DSY_00002 module had thermistors attached to it. As a result, comprehensive temperature data was collected exclusively for this module.

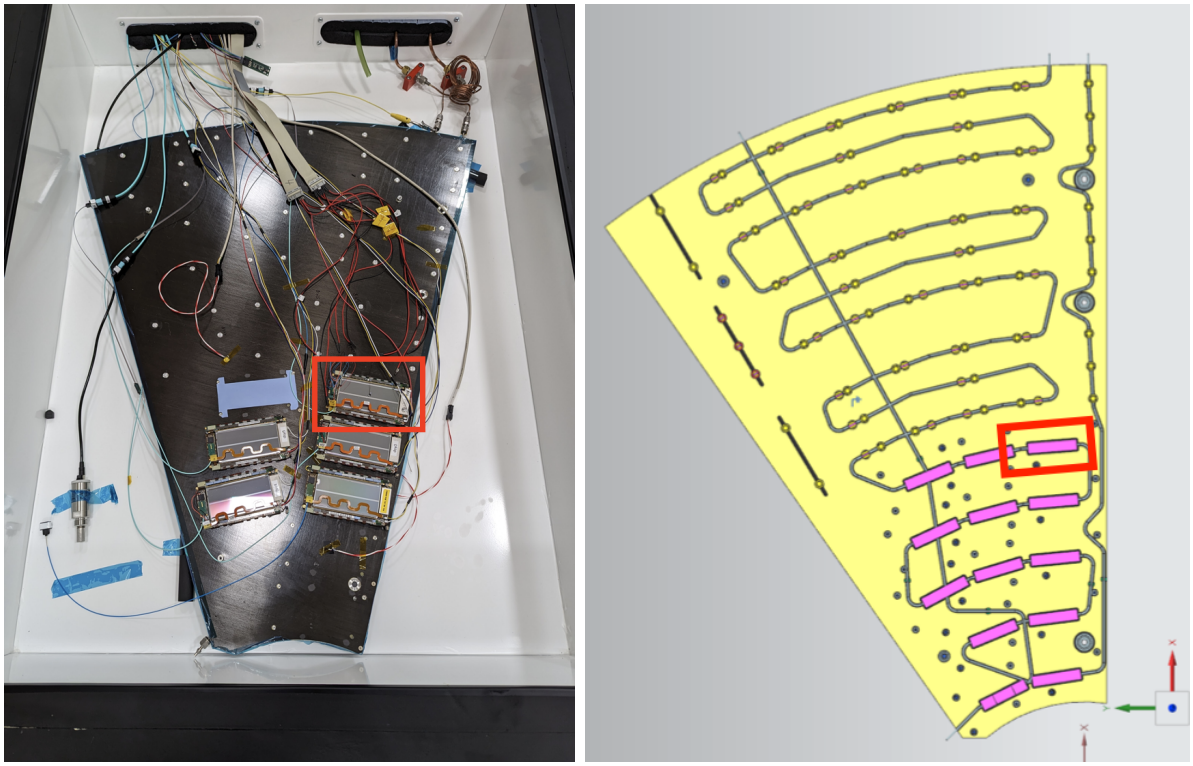

Figure 5.4: Left panel: a photograph of the single cooling sector of a Dee mounted in the sector test setup, with the PS_26_05_DSY_00002 module installed on the right (highlighted by a red square). Right panel: a CAD drawing of the cooling sector with the carbon foam blocks (pink) and the position of the module (red).

The temperature measurements involve a thermal cycle controlled by the MARTA system. The measurement starts at room temperature, followed by a cool down phase with a set point of −35 °C. Various tests, such as noise or IV measurements are conducted while the module is maintained cooled, then it is gradually warmed up to 20 °C. Throughout the process, the dew point remains consistently below -50 °C, ensuring a dry environment and thus preventing condensation. When the module was biased, it was set to a voltage of 300 V. The temperatures on the module were recorded using the thermistors described in Chapter 4.

Figure 5.5 presents the temperature measurements for the module PS_26_05_DSY_00002

positioned on the left side of the Dee sector (as shown in Figure 5.3). Initially, the module is unpowered, and the MARTA system is off, resulting in all thermistors registering a uniform temperature of 20 °C. After 30 minutes, the MARTA set point is adjusted to -35 °C, and the different components of the module begin to cool at varying rates.

The thermistors located on the sensor, SSA, insert pin, and DCDC converter exhibit a similar temperature trend, dropping to -30 °C[1]. However, the thermistors on the VTRx+ and lpGBT show a less steep temperature slope and a higher (by ≈5 °C) final temperature, presumably due to the amount of material between the base plate and the respective thermistors, or due to an indirect cooling contact, which impedes thermal conductivity.

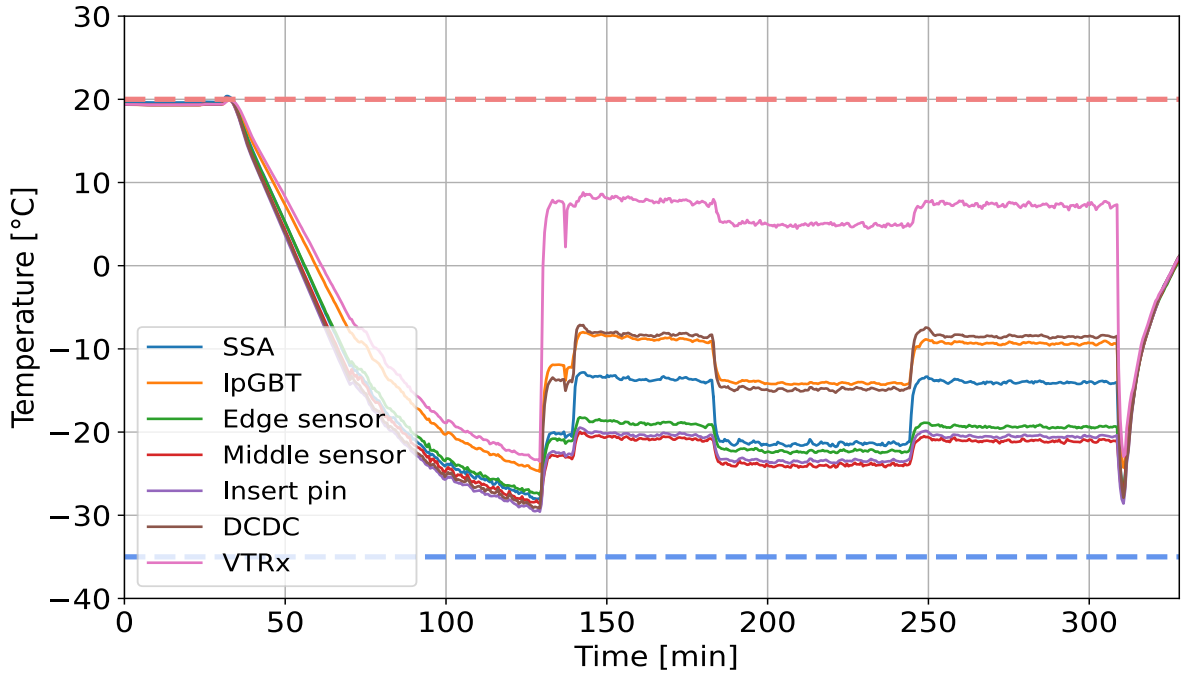

Figure 5.5: Temperature as a function of time, measured via the seven thermistors glued onto PS_26_05_DSY_00002. The module is located in the position shown in Fig. 5.3. The red (blue) dotted line marks the temperature of 20 °C (-35 °C)

After approximately 130 minutes, the module is powered on, leading to a noticeable increase in temperature across all thermistors by 5 °C to 35 °C. The VTRx+ shows the highest temperature, reaching nearly 10 °C, while the lpGBT and DCDC converter also warm up significantly, reaching -6 °C. The SSA and the thermistor near the sensor's edge

[1]Precision on temperature measurements is of the order of 0.1 °C

(next to the ROH) record slightly higher temperatures (-20°C) compared to those at the insert point and in the center of the sensor (-23°C). This rise in temperature is primarily due to heat dissipation in the POH and laser components in the ROH.

At around 140 minutes, a noise measurement was performed, leading to a temperature increase for the time of this measurement. The module's current consumption rises (∼600 mA), leading to further heat dissipation. Notably, the SSA shows the most significant temperature increase, reaching -12°C, as the readout chips become active. Once the noise measurement is completed and the module returns to its initial current consumption (∼400 mA), the temperatures decrease accordingly.

A second noise measurement at approximately 250 minutes shows a similar pattern. Following this, an IV measurement is conducted, which is not noticeable in the temperature trend. After that, the module is powered off, causing the temperature of all components to drop below -20 °C. This quick drop in temperature demonstrated that the ambience temperature inside the structure plays a big role in the cooling speed. Finally, after 320 minutes, the MARTA system is turned off, and the module undergoes a uniform warm-up as all thermistors return to 20 °C.

Figure 5.6 presents the temperature measurements for the module PS_26_05_DSY_00002 positioned on the right side of the Dee sector (as depicted in Figure 5.4). Initially, with the module unpowered and the MARTA system off, all thermistors uniformly register a temperature of 20°C.

After 10 minutes, the MARTA set point is adjusted to -35 °C, initiating the cooling of the module's various components. At around 50 minutes, an increase in dry air flow (around 35 l/min) is implemented to ensure a safe dew point, which temporarily disrupts the cooling process. Since the dry air is at room temperature, this causes a brief rise in the module's temperature. After approximately 20 minutes, the dry air flow is reduced back to 25 l/min, allowing the module's temperature to drop again, reaching -30 °C.

After 100 minutes, an IV measurement is started, resulting in a temperature increase across the module, with the VTRx+ warming up to 5 °C. The DCDC converter's temperature rises to -12 °C, while the lpGBT remains at -15 °C. The SSA and the temperature sensor at the insert pin stays below -20 °C, with the thermistors on the silicon sensor recording the lowest temperatures of -25 °C. Following the IV measurement, the module is powered off, causing all thermistors to cool down to -30 °C.

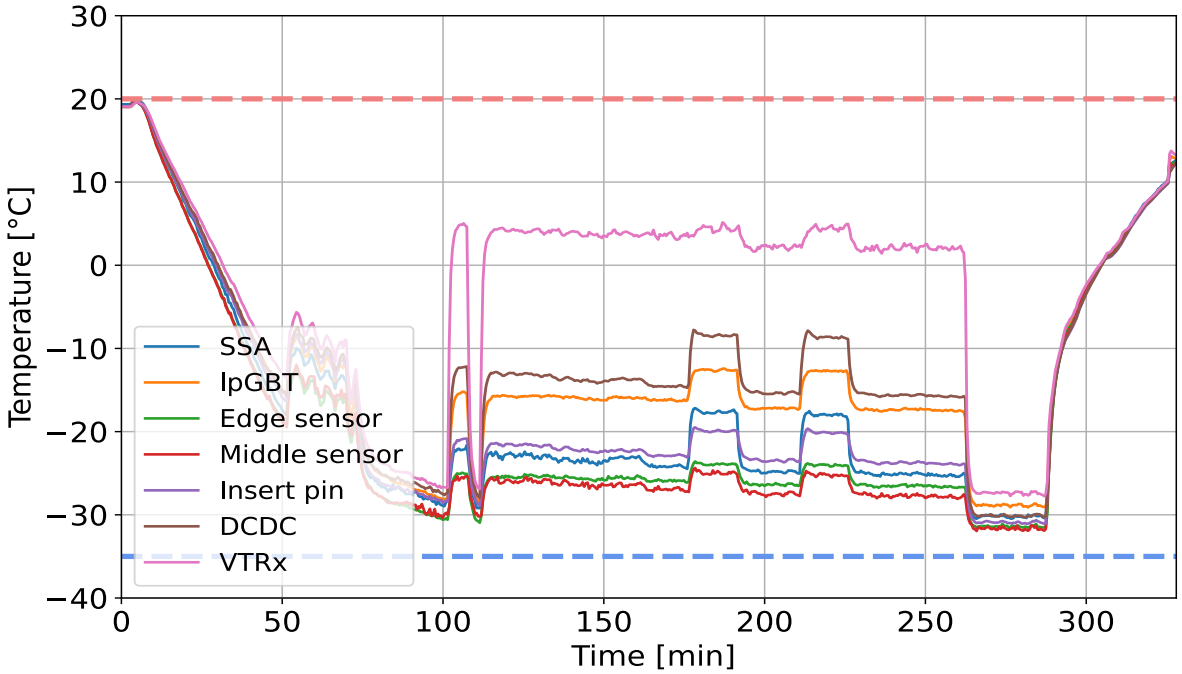

Figure 5.6: Temperature as a function of time, measured via the seven thermistors glued onto PS_26_05_DSY_00002. The module is located in the position shown in Fig. 5.4. The red (blue) dotted line marks the temperature of 20 °C (-35 °C)

During the two noise measurements performed at 180 and 220 minutes, there is another temperature rise due to the increased current while communicating with the FC7. The SSA exhibits a significant temperature increase, reaching -18 °C, due to chip activity. The DCDC converter's temperature increases to -9 °C, while the lpGBT remains at -13 °C. During these measurements, the silicon sensors (thermistors at the sensor's edge and center) reach a maximum temperature of -25 °C.

After 4 hours, the module is powered off, and the temperatures of nearly all components drop to -30 °C. Finally, as MARTA is switched off, the module undergoes a uniform warm-up.

These findings highlight the impact of cooling differences between the two positions tested. As shown in Figure 5.5, as the ROH is not efficiently cooled, the VTRx+ temperature rises to nearly 10°C during the measurements. In contrast, as illustrated in Figure 5.6, once the ROH receives adequate cooling, the VTRx+ reaches only 5 °C, indicating a significant temperature difference of 5 °C when proper cooling is applied to the ROH. A similar trend is observed for the lpGBT, which exhibits a temperature above -10 °C, as

presented in Figure 5.5, compared to approximately -15 °C in Figure 5.6. The DCDC converter, however, does not show a substantial temperature difference between the two positions. This indicates that the thermal coupling of the base plate to the POH is better than the coupling between the base plate and the ROH.

Overall, when the ROH is efficiently cooled, the module's average temperature is lower, as evidenced by the temperatures on silicon measured at both the center and edge of the sensor. In both scenarios, the temperature of the silicon remains below -25°C, which, as will be discussed in section 5.4, correlates with acceptable noise levels and it is crucial for the sensor performance after irradiation.

5.3 Thermal mockup structure

The previous measurements were conducted using a Dee prototype, which does not fully reflect the final design and expected performance in terms of cooling. To address this limitation, a specialized support structure resembling the Dee has been developed at DESY. This thermal mockup is designed to hold and cool a single PS module and is equipped to support CO_2 cooling. Additionally, it allows for the testing of different TIM and provides a more accurate assessment of the module's thermal behavior under conditions closer to those in the final installation.

The thermal mockup is designed to simulate the conditions of the inner most ring on the even Dee (ring 2). As illustrated in Figure 5.7, the base of the structure is an aluminum cooling plate with holes that accommodate insert pins to secure the module in place. On top of this, a 3D-printed plastic frame contains a carbon fiber facing, into which the first half of the carbon foam blocks are embedded. The CO_2 cooling pipes traverse across these blocks and are covered by additional carbon foam to completely encase the pipes. On top of this assembly, an AIREX foam layer is added, followed by a final layer of carbon fiber reinforced plastic onto which the module is installed.

The thermal mockup is equipped with 12 PT100 sensors, strategically placed to monitor the temperature across different parts of the structure, as shown in Figure 5.8. Sensor 1 is attached to the inlet pipe, while sensor 2 is positioned on the outlet pipe. Sensors 3, 4, 5, and 6 are embedded in holes within the carbon foam blocks. Sensors 7 to 12 are installed on top of the carbon fiber (CF) facing, with sensors 8 and 12 positioned below the DCDC converter, and sensors 7, 9, 10, and 11 located beneath the sensor/base plate.

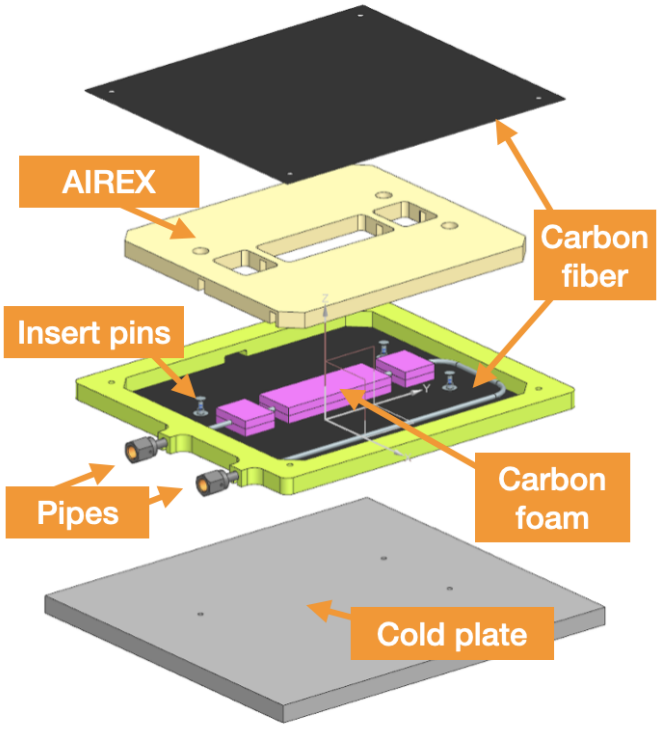

Figure 5.7: Exploded view of the thermal mockup.

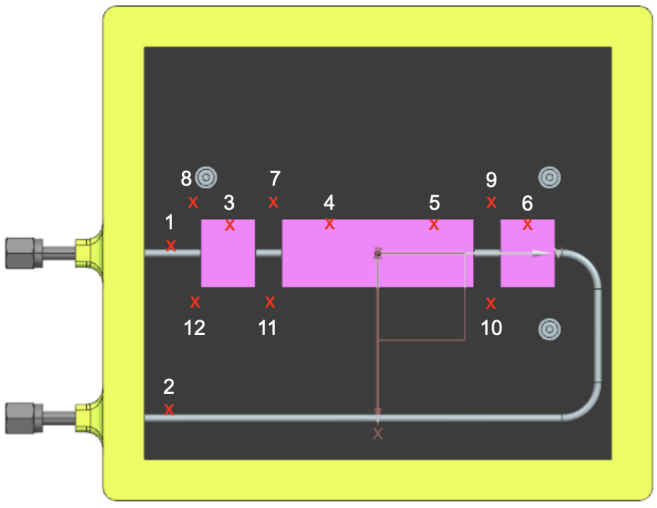

Figure 5.8: View of the second layer of the thermal mockup with the position of the 12 PT100 temperature sensors installed.

The module PS_26_05_DSY_00002 was mounted on the thermal mockup using a thermal pad as TIM and placed inside the sector test setup as shown in Figure 5.9.

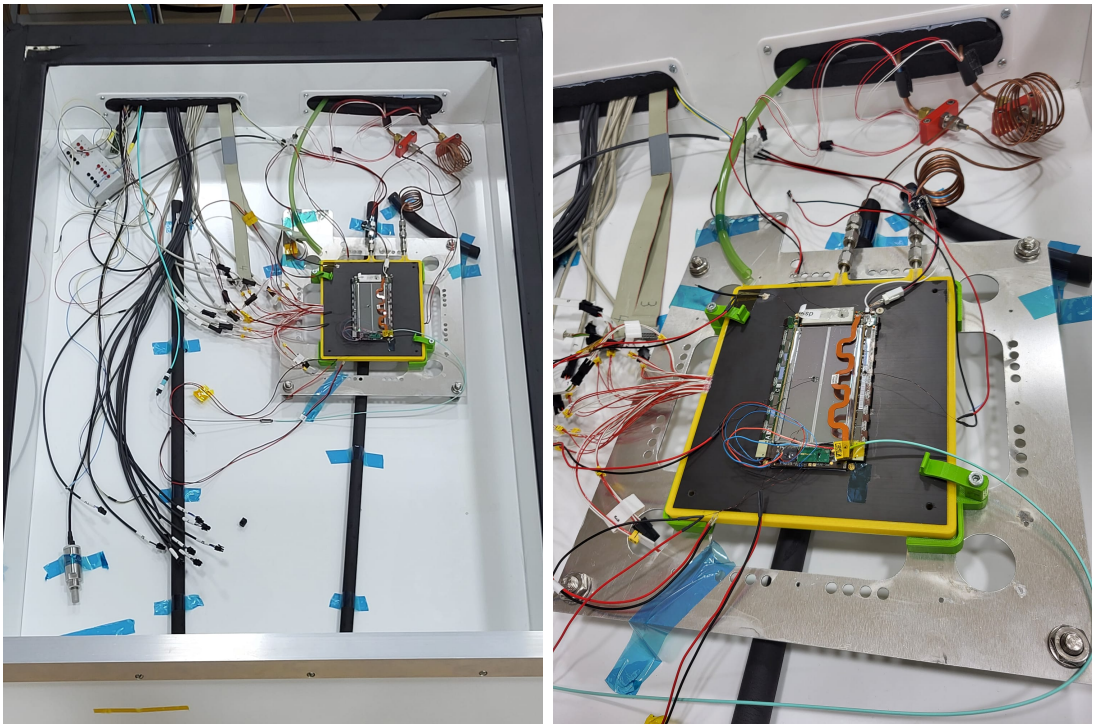

Figure 5.9: View of the thermal mockup with the module PS_26_05_DSY_00002 installed inside the sector test (left) and zoomed view of the mockup structure with the module (right).

5.3.1 Temperature measurements on the thermal mockup

The temperature measurements were conducted following the same procedure as in section 5.2.1, through a thermal cycle controlled by the MARTA cooling system. The cycle began at room temperature and proceeded by cooling down to a set point of -35 °C. Various tests, such as noise and IV measurements, were performed while the module was maintained at this low temperature, followed by a gradual warm-up to +20 °C. Throughout the process, the dew point consistently remained below -50°C, ensuring a dry environment to prevent condensation. When the module was biased, it was done at a voltage of -300V. The temperatures at the module were recorded using the same thermistors as described in section 5.2.1. Additionally, the temperature from the PT100 sensors placed on the structure was also monitored and recorded.

Figure 5.10 presents the temperature measurements for the thermal mockup while the

PS_26_05_DSY_00002 module was installed. Initially, with the MARTA system turned off and the module unpowered, all PT100 sensors registered temperatures above 20°C. The module was switched off, however, before starting this measurement, the module was powered on without cooling to test it before starting the measurement and some residual heat leads to the structure being warmer than the room temperature. Once the MARTA set point was adjusted to -35 °C, temperature in all sensors began to decrease. However, differences in cooling rates and final temperature can be observed.

Sensor 4, embedded in the carbon foam and located under the silicon, which is known to dissipate minimal heat (as discussed in Chapter 4), was the fastest to cool down and reached the lowest temperature of -30 °C. In contrast, Sensor 6, also embedded in carbon foam but positioned under the lpGBT, a known hot spot in the module, maintained a higher temperature of -25 °C.

Sensors 1 and 2, located on the inlet and outlet pipes, showed similar temperatures, both around -25 °C, with the outlet pipe being colder than the inlet due to the phase change of CO_2. Sensors 7, 9, 10, and 11, installed on the carbon fiber material beneath the silicon sensor, recorded temperatures of -18 °C. Lastly, Sensors 12 and 8 exhibited the highest temperatures, as they were placed in the carbon fiber material at the beginning of the loop.

The effects of heat dissipation during various tests performed with the module in the mockup structure are also evident in the temperature measurements, providing insights into the module's thermal behavior. Sensors 1 and 2, located on the inlet and outlet pipes, do not show any significant change in temperature throughout the test, as they are positioned away from the module and on the cooling pipes themselves.

At around 80 minutes, when the module is powered on, an increase in temperature is observed across nearly all sensors. However, this impact is minimal, with the sensors embedded in the carbon foam (4 and 6) experiencing only a slight rise of 0.5 °C. The sensors positioned beneath the silicon sensor (7, 9, and 10) show a more noticeable increase of 2 °C. Sensor 11, which is closer to the operational Front-End Hybrid (FEH), records a slightly larger increase of 3 °C. The most significant temperature rise is observed in sensors 8 and 12, located beneath the DCDC converter, where temperatures climb up to -12 °C.

A similar pattern is seen after 100 minutes when the module is configured, and an IV measurement is performed, representing the module's maximum power consumption and the peak of its heat generation. At around 150 minutes, the module is powered off, leading to a decrease in temperature, which falls even lower than the initial unpowered state, due to the support structure and the ambience being cooled down. When the module is powered on again at around 180 minutes and immediately reconfigured, the mockup structure warms up again, although slightly less than during the first power-up, with

temperatures 0.5 °C lower, which is consistent with the global trend. The temperature remains stable during the noise measurement, conducted at around 225 minutes. Finally, at 240 minutes, the module is powered off, and at minute 255, the MARTA set point is reset to +20°C, initiating a uniform warming up of the structure.

Figure 5.11 presents the temperature measurements for the PS_26_05_DSY_00002 module installed in the mockup structure, following the same timeline as in Figure 5.10. As the cooling begins, with the module unpowered, the thermistors located in the sensor show the highest slope, but only reach -19 °C. The second group, comprising the thermistors next to the insert pin and in the SSA, stabilizes at -15 °C. The DCDC converter and the lpGBT exhibit similar behavior, both reading -12 °C. The highest temperature is recorded in the VTRx+, which remains at -9 °C. It should be noted that the module is not powered at this stage. Hence, these differences in temperature arise only from the coupling through the module's components.

Upon powering the module, the VTRx+ temperature rises significantly, reaching almost 20 °C due to the heat dissipation from the laser being active. Both the lpGBT and the DCDC converter also warm up, reaching -1 °C. The thermistor located at the edge of the sensor shows higher temperature increase, compared to those in the SSA or near the insert pin, due to its proximity to the ROH, where the VTRx+ and lpGBT are located. The silicon sensor temperature reaches -12 °C.

During the configuration of the module and the IV measurement, the DCDC converter experiences a temperature increase of more than 5 °C due to the higher power consumption. Similarly, the SSA's temperature rises by over 5 °C as it becomes fully operational. The temperature sensor placed at the center of the strip PS sensor reaches nearly -10 °C. After the measurement, when the module is powered off, the cooling process results in similar temperatures but slightly lower than before powering on initially, with the silicon below -20 °C and the VTRx+ below -10 °C. When the module is powered on again and a noise measurement is performed, the heat dissipation behavior mirrors that of the first measurement.

Figure 5.12 shows the temperature measurement for the thermistor glued on the VTRX+ and the two PT100 located in the mockup beneath the ROH. It shows the difference between the temperature registered in the carbon foam (sensor 6), the one in the carbon fiber facing (sensor 9) and the one in the VTRx+, one of the hottest components of the module. The heat dissipated by the VTRx+ affects the temperature on the mockup structure. Even when the module is powered off, there remains a considerable temperature difference between the module itself and the mockup structure, indicating that the thermal coupling from the carrier structure to the module is not optimal.

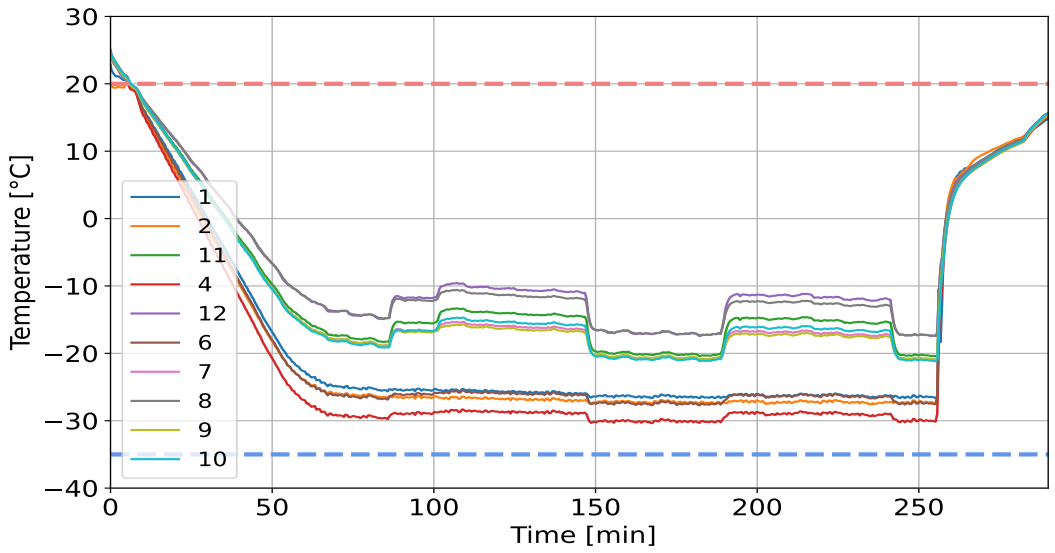

Figure 5.10: Temperature as a function of time, measured via 10 PT100 located on the thermal mockup following the scheme shown in Figure 5.8. The red (blue) dotted line marks the temperature of 20 °C (-35 °C).

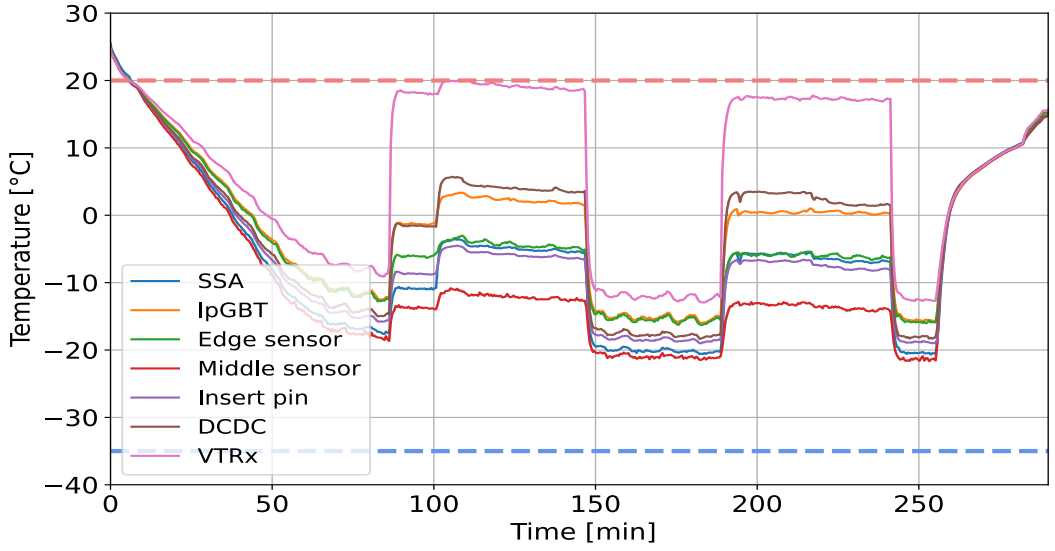

Figure 5.11: Temperature as a function of time, measured via the seven thermistors glued on onto PS_26_05_DSY_00002 following the color scheme shown in Figure 4.19. The red (blue) dotted line marks the temperature of 20 °C (-35 °C).

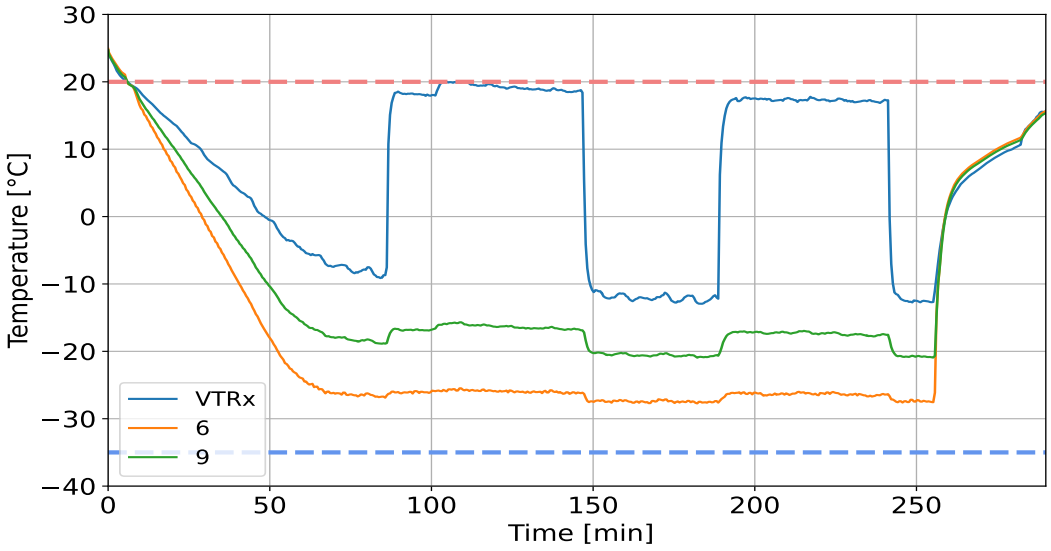

Figure 5.12: Temperature as a function of time, measured via one thermistors glued on the VTRx of PS_26_05_DSY_00002 and 2 PT100 located on the thermal mockup as shown in 5.8. The red (blue) dotted line marks the temperature of 20 °C (-35 °C).

The observed higher temperatures in the thermal mockup compared to those recorded in the Dee sector (section 5.2.1) can be attributed to several factors related to the structural and material differences between the two setups. Firstly, during the installation of the module in the mockup, one of the corners of the baseplate, specifically at an insert point intended for securing the module to ensure optimal physical contact, was found to be broken. This compromised the thermal interface, leading to suboptimal heat transfer from the module to the cooling structure.

Secondly, the mockup incorporates only three carbon foam blocks for thermal management, whereas the Dee features a more extensive array of such blocks distributed across its surface. This limited use of carbon foam in the mockup reduces its capacity to effectively dissipate heat from the module.

Lastly, the Dee cooling sector represents a complete cooling sector with a substantially larger surface area compared to the compact mockup. The greater size and more comprehensive cooling infrastructure of the Dee facilitate more efficient heat removal, contributing to the lower temperatures of the ambience and therefore of the module during its operation. In contrast, smaller scale and simplified design of the mockup inherently limit its cooling efficiency, resulting in the relatively higher temperatures recorded during the tests.

5.4 Integration test

A comprehensive integration test was conducted on a Dee prototype, representing the first instance of integrating both 2S and PS modules onto a Dee structure. This test was carried out at DESY, Hamburg from June 5th to June 9th, 2023 in collaboration with several institutes.

The prototype used in this test featured two cooling sectors connected in series to the MARTA system. As this prototype was integrated with preliminary modules, the results from these tests are not expected to fully reflect the performance of the final modules.

Thirteen prototype modules assembled at different assembly centers have been integrated for this test: four PS modules assembled at DESY, two PS modules assembled at INFN Bari, two 2S modules assembled at RWTH Aachen, and five 2S modules assembled at KIT. Each module underwent measurements in both warm and cold conditions using the Burn-in setup described in Section 4. Due to time constraints, the full Burn-in procedure was not performed but only one temperature cycle. Then, the modules were installed on the Dee, where further measurements were conducted at room temperature and at +15 °C. These measurements included IV curves, noise assessments, temperature readings from a module equipped with seven thermistors, and grounding evaluations. At a time of this test, the Dee cold box had not yet been built and a proper enclosed box was not available to cool the entire Dee under controlled dew point conditions. Since the dew point of the clean room was 10 °C, the temperature could be only lowered to 15 °C.

Due to the collaborative nature of this work and its presentation in internal meetings, not all measurements are described in detail here. In this work, the noise values recorded in the Burn-in and Dee setups for the modules assembled at DESY are presented, enabling a comparison with values obtained in the sector test and mockup structure.

The noise measurements presented reflect the average noise levels per hybrid and module built at DESY. An SSA is deemed noisy if it exceeds a threshold of 5 ThDAC. For the MPAs, noise levels should range between 2 and 4 ThDAC to be considered acceptable

Noise measurements on SSA chips

Figure 5.13 presents the mean noise values for all SSA chips per hybrid across the DESY modules:

- PS_26_05_DSY_00002 (referred as DSY2 in the following)
- PS_40_05_DSY_00003 (DSY3)

- PS_40_05_DSY_00004 (DSY4)
- PS_40_05_DSY_00005 (DSY5)

These measurements were performed across different setups and temperatures. Not all modules could be measured in every setup, primarily due to time constraints during the integration test, which was limited to one week for the test of all the 13 modules. In the case of the mockup structure, measurements were conducted exclusively with module DSY2.

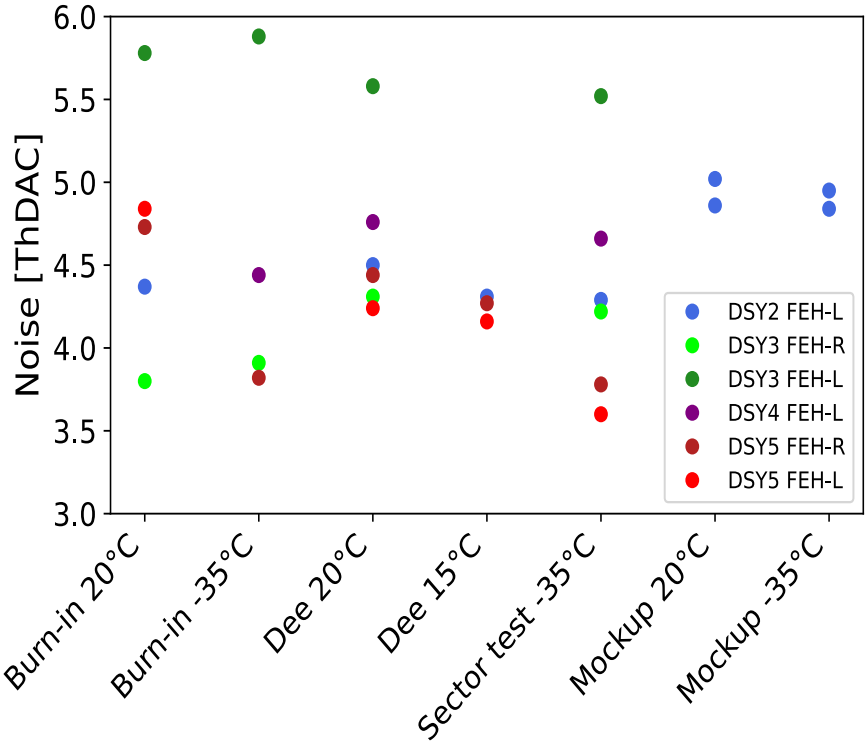

Figure 5.13: SSA noise values of the different hybrids of 4 different PS modules assembled at DESY, as a function of the measurements performed at different temperatures and different setups.

The module DSY4, which has only one functioning hybrid (FEH-L), was tested at three different points: in the Burn-in setup at -35 °C with a noise value of 4.4 ThDAC[2], in the Dee at 20 °C with 4.8 ThDAC, and in the sector test with 4.7 ThDAC. As expected,

[2]Precision on noise measurements is of the order of 0.1 ThDAC

the highest noise occurred at room temperature, but all measurements remained within acceptable limits.

The module DSY5 was tested at every stage. During the Burn-in at -35 °C, only one hybrid was measured due to time constraints, with the highest noise recorded at 20 °C (4.74 ThDAC). Lowering the temperature to -35 °C reduced the noise to 3.82 ThDAC. In the Dee, noise ranged from 4.26 ThDAC at 15 °C to 4.44 ThDAC at 20 °C, with similar results in the sector test.

The module DSY3, with two functional hybrids, was not measured in the Dee at 15 °C due to time constraints. A significant difference in noise levels was observed between the hybrids across tests, with FEH-L showing around 6 ThDAC and FEH-R ranging between 3.8 and 4.3 ThDAC, though some unexpected noise behaviors were noted.

The DSY2 module was not tested in the Burn-in setup at -35 °C due to existing data and time constraints, but the noise remained consistent across measurements, averaging around 4.4 ThDAC, with slightly higher values in the sector test at -35 °C. In the mockup structure, measurements at 20 °C showed noise levels around 5 ThDAC, while at -35 °C, the noise was approximately 4.8 ThDAC.

All SSA hybrids tested, with the exception of the FEH-L of module DSY3, fall within the acceptable noise range. Noise levels across the different setups and temperatures have been shown to be compatible, indicating consistent performance of the modules. However, the elevated noise levels of the SSAs in the mockup structure, particularly at cold temperatures, require further investigation. One possible explanation for these higher noise levels could be related to the inserts and grounding issues within the mockup, which should be examined in future studies.

Noise measurements on MPA chips

Figure 5.14 shows the mean noise values for all MPA chips per hybrid across the modules assembled at DESY. These measurements were taken across different setups and temperatures, similar to the procedure applied for the SSA. Again, not all the modules were measured in every setup. For the mockup structure, measurements were conducted only with module DSY2.

For the MPA chips, the temperature does not have a significant effect on noise levels, as becomes evident from the consistent noise measurements across different setups and temperatures. Additionally, the choice of setup itself does not seem to influence the noise, since all the modules, regardless of the test setup consistently exhibited noise levels of about 2.5 ThDAC.

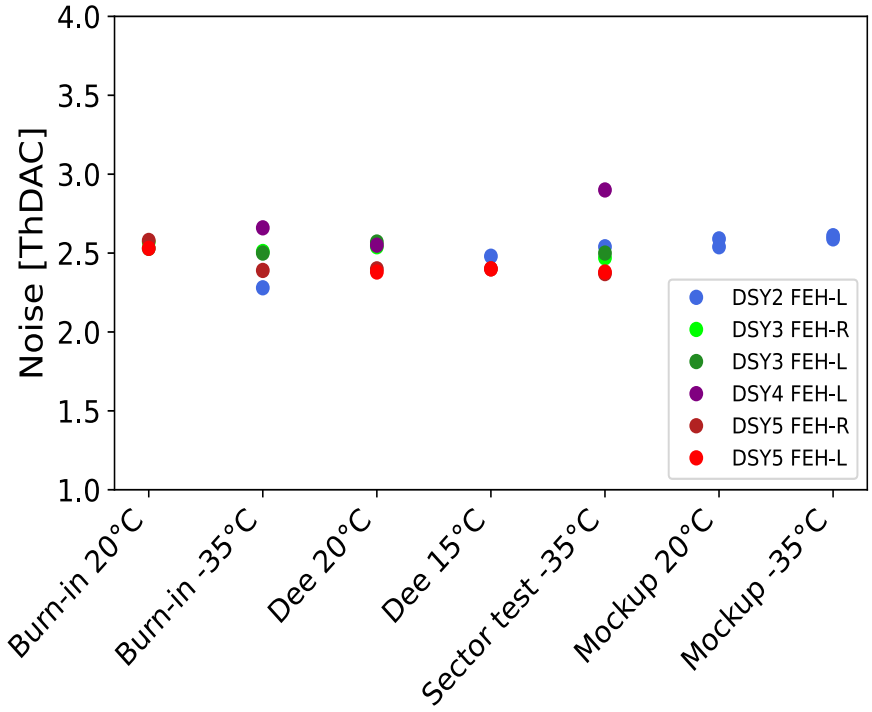

Figure 5.14: MPA noise values of the different hybrids of 4 different DESY modules, as a function of the measurements performed at different temperatures and different setups.

For the MPAs, noise levels across the different setups and temperatures fall within the acceptable range.

5.5 Conclusion and prospects

The integration tests conducted with the CMS Outer Tracker modules, with a particular emphasis on the DSY2 module, have provided critical insights into both the thermal behavior and the noise performance under various operational conditions. These tests were essential in validating cooling strategies and understanding the thermal dynamics that will be crucial for the final deployment of the modules in the CMS detector.

During these tests, the Burn-in setup demonstrated its effectiveness being utilized at full capacity to test 10 modules simultaneously during the integration test. Despite the high testing throughput, performing a single temperature cycle and noise measurement along with the IV measurement for each module, the system maintained consistent cooling performance.

The DSY2 module, which was extensively evaluated, confirmed that the cooling system effectively maintains module temperatures within the desired range. The module efficiently coped with the heat dissipation from critical components such as the DCDC converter, lpGBT, and VTRx+. Even under varying thermal conditions in the Dee and sector-test setups, the noise levels remained within an acceptable range, further validating the cooling design.

However, some anomalies were detected, particularly in the mockup structure, where temperature levels higher than expected were observed. These deviations were attributed to imperfections in the physical contact between the module and the cooling surface, highlighting the importance of mechanical integrity and proper installation for optimal thermal performance. Additionally, while thermal pads were used during these tests, further studies with gap fillers as TIM are planned for the mockup structure to determine the optimal solution for final installation. Even in the worst coupling scenario, which is expected to improve with the use of thermal gap filler, when the module's hotspots exceed 15 °C, the silicon sensor itself does not heat up to more than -15 °C, which is critical for the proper operation of the modules after irradiation.

Noise measurements compared across various setups and temperatures provide a comprehensive evaluation of the SSA and MPA chips' performance. The results indicated that all SSA hybrids maintain noise levels well within acceptable thresholds, validating the designs and materials used, except for the FEH-L of module DSY3. However, this is a known issue and is being investigated. The MPA hybrids consistently performed within the desired noise range, further affirming their reliability across different testing environments.

The average noise values from the scans show good agreement across the different setups, indicating consistent performance. However, the noise levels measured in the mockup structure are slightly elevated and require further investigation. One possible explanation for this discrepancy could be issues related to the grounding of the module to the mockup. To address this, additional noise measurements will be conducted with updated module versions and alternative TIM, which can further improve the thermal coupling and thus the module's performance.

CHAPTER 6

Tracker alignment in CMS: interplay with pixel local reconstruction

Contents

6.1 Introduction

The CMS detector houses the world's largest silicon tracking system, which plays a pivotal role in vertex reconstruction and momentum measurement of charged particles. For the tracker to fully leverage the excellent hit resolution of its silicon sensors, the precise positioning and orientation of these sensors must be accurately known. Achieving such precision requires frequent updates to the alignment parameters of the tracker to correct for movements due to magnet cycles, temperature variations, and pixel irradiation. A key aspect of this alignment process is the track-based alignment procedure, which uses reconstructed particle tracks to derive alignment corrections at the sensor level.

Due to mechanical limitations, an initial alignment only provides a coarse precision, typically ten times larger than the silicon sensors' intrinsic resolution, around 10 μm [171]. Furthermore, as mentioned previously, operational changes, such as ramping the CMS magnet and radiation damage, cause systematic sensor shifts that necessitate ongoing corrections. Consequently, automated and manual alignment procedures are implemented to maintain optimal tracker performance. During Run 2 of the LHC, an automated online alignment process, which focused on large-scale movements of the pixel detector, was employed to support offline alignments. However, as part of preparations for Run 3, this automated procedure has been enhanced to achieve higher granularity in alignment which provides finer spatial resolution than low granularity.

In this chapter, the methodology behind track-based alignment is discussed, including the alignment algorithms and validation methods used in CMS. Special attention is given to the challenges posed by the tracker's evolving conditions, such as radiation-induced sensor aging, discussing the interplay between tracker alignment and pixel local reconstruction.

This thesis addressed significant contributions to the alignment calibrations and validations for Run 3, in particular, investigation of the impact of radiation on the Lorentz drift, which is discussed in more details in the following.

6.2 CMS Tracker detector for Run 3

In the current (Run 3) configuration, the CMS tracker consists of 1856 silicon pixel and 15148 silicon strip detector modules. This chapter focuses on the pixel detector, the closest subdetector to the interaction point. It is composed of a barrel region (BPIX) and forward endcaps (FPIX), which together form the core tracking components nearest the interaction point, as shown in Figure 6.1. The BPIX consists of four concentric barrel layers (L1-L4) at radii of 29, 68, 109, and 160 mm, containing a total of 1184 modules. The FPIX includes three disks (D1-D3) installed on each end of the detector at distances of 291, 396, and 516 mm from the center, comprising 672 modules [105].

The pixel detector operates in a harsh radiation environment, and during the current data-taking period (Run 3), the integrated luminosity is doubled as compared to Run 2 (2015-2018). Consequently, the pixel detector was refurbished during the second Long Shutdown (LS2), from 2019 to 2021, to extend its operational lifetime. This refurbishment included the complete replacement of the innermost layer (L1) in the BPIX, replacement of damaged modules (primarily in layer 2), and upgrades to the power supplies from 600V to 800V. The detector was reinstalled in 2021 after these updates to ensure optimal performance during Run 3 [172].

To meet the ambitious physics goals of the CMS experiment, the tracker must deliver excellent tracking performance, which requires precise knowledge of the absolute coordinates

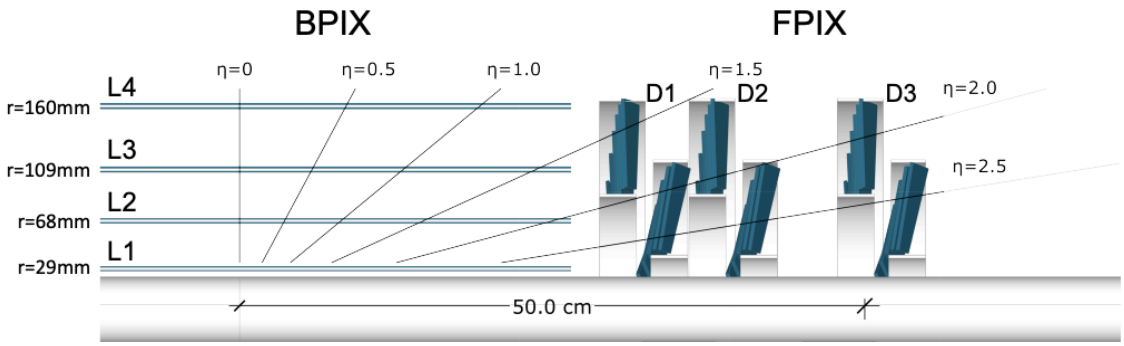

Figure 6.1: Pixel detector geometry.Figure taken from [105].

of the silicon sensors within the global CMS coordinate system. Therefore, track-based alignment procedures are employed to achieve the necessary precision for optimal detector performance. In particular, the pixel detector requires extremely precise alignment at the level of a few μm.

6.3 Track-based alignment

The CMS collaboration utilizes a track-based alignment method to ensure the precise positioning of the sensors in the CMS tracker, which is crucial for accurate tracking and vertex reconstruction. The primary goal of this track-based alignment approach is to reduce the mechanical alignment's uncertainty from $\mathcal{O}(100\ \mu\text{m})$ to the design resolution of the silicon sensors, $\mathcal{O}(10\mu\text{m})$. Without such precision, errors in track and vertex reconstruction could degrade performance, especially in the identification of b jets or during online triggering processes.

The misalignment of the detector modules leads to discrepancies between the measured hit positions and the fitted particle trajectories. These discrepancies, known as residuals, serve as a measure of the misalignment, as illustrated in Figure 6.2. To correct those, the alignment parameters are determined by minimizing the sum of squared normalized track-hit residuals using the χ^2 function [173]:

$$\chi^2(p,q) = \sum_{\text{tracks}} \sum_{\text{hits}} \left(\frac{m_{ij} - f_{ij}(p,q_j)}{\sigma_{ij}} \right)^2 , \tag{6.1}$$

where m represents the measured hit positions, f is the predicted hit from the fitted track, and σ is the uncertainty associated with the hit measurement. The parameters q account for track-related variables like curvature, while p are the alignment corrections.

Figure 6.2: Schematic representation of a fitted trajectory (solid blue) with misaligned modules on the left and aligned modules on the right. The true trajectory of the charged particle is represented by a dashed blue line, while the predicted and measured hits are depicted as blue-red and orange-red dots, respectively. The residuals between these two types of hits are shown as solid red lines. Figure taken from [174].

Given that the CMS tracker consists of thousands of modules, with complex geometries requiring the alignment of the order of 10^5 parameters, this minimization task is computationally intensive. The MillePede-II algorithm [175,176], a core tool in CMS, handles this challenge by constructing and solving a system of linear equations, which is derived from an initial set of track and alignment parameters. The algorithm works in two phases: the *mille* step, where residuals and derivatives are computed, and the *pede* step, where the global matrix equation is solved either exactly or numerically, yielding the final alignment corrections. Although the alignment results presented in this work were obtained using the MillePede-II algorithm, an independent algorithm, known as the HipPy algorithm [177], was primarily used during the detector's commissioning and served to cross-check the results produced by MillePede-II.

The alignment involves translational, rotational and surface deformation corrections for each sensor. Offline alignments, performed periodically with high granularity, use specialized datasets such as cosmic ray muons or dimuon resonances to cover various regions of the detector. For shorter timescales and larger structures, an automated online alignment process operates. This online system, in contrast, relies solely on collision data (specifically minimum bias data) and updates the positions of larger components like the pixel detector's half-barrels or forward disks. The pixel detector, being the closest to the interaction point and most sensitive to radiation, requires particularly frequent and precise alignment, especially after its upgrades during the shutdowns, due to changes in the running conditions, e.g. fluctuations in temperature or in magnetic field. For in-

stance, magnet cycles (ramping up and down the magnet for maintenance reasons) can cause movements of the high level structures (half-barrels and half-disks) up to few mm. The tracker is cooled during data taking, however cooling may be interrupted for maintenance purposes. Movements of the modules of $\mathcal{O}(10\ \mu\text{m})$ after temperature variations have been observed [171]. In addition, the modules' performance is affected over time by the radiation dose received during operation, known as aging of the modules. This effect produces a change of the Lorentz drift, which plays an important role in the pixel local reconstruction and the alignment calibration.

6.4 Impact of radiation effects

The CMS tracker operates in a high-radiation environment, particularly in regions near the interaction point. Over time, radiation exposure leads to changes in the detector modules, which directly impacts the alignment and position resolution of the tracker. One of the most significant effects of radiation is the shift in the Lorentz angle (LA), which describes the deflection of charge carriers as they traverse the silicon sensors under the influence of both electric and magnetic fields.

Charged particles passing through the detector create electron-hole pairs that are collected by an electric field, forming clusters of hits in neighboring pixels. The measured Lorentz angle (θ_{LA}, shown in Figure 6.3), defined as the angle between the electric field and the drift direction of the charge carriers, is critical to accurately reconstructing hit positions. However, due to radiation damage, the Lorentz drift (lateral shift experienced by charge carriers) changes over time, leading to degradation in the hit position resolution. As the radiation damage increases, the cluster sizes expand, causing systematic shifts in the hit positions in the direction of the Lorentz angle. Additionally, the magnitude of this drift depends on factors such as the strength of the electric field, the thickness of the silicon, and the mobility of the charge carriers, all of which degrade with increasing radiation dose [173].

To mitigate these effects, the CMS collaboration periodically recalibrates the sensors and increases the sensor bias voltage to maintain optimal performance [178]. However, beyond a certain radiation level, full charge collection cannot be recovered, leading to a permanent degradation in position resolution. Some residual effects of radiation, particularly those associated with the changes in the Lorentz angle, can be partially corrected through the track-based alignment procedure.

The track-based alignment method can absorb shifts in hit positions caused by radiation-induced changes. Since the Lorentz angle shift behaves in opposite direction for modules with inward- and outward-pointing electric fields, the track-based alignment allows independent adjustments for these modules. This compensation effectively corrects the bias

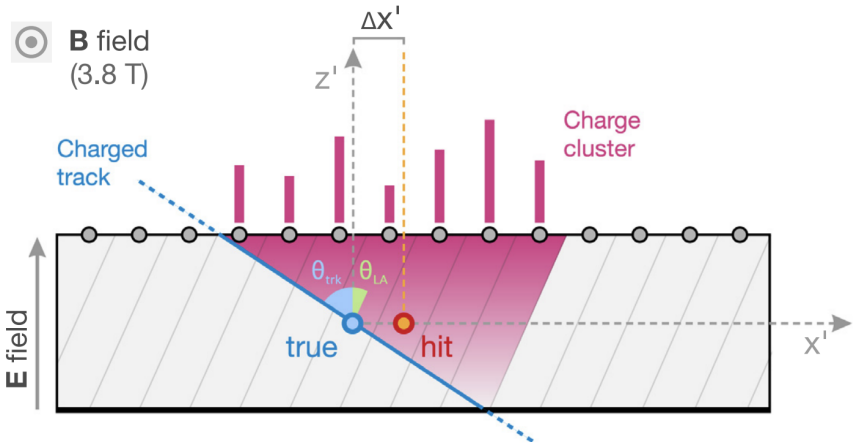

Figure 6.3: Transverse slice of a silicon module in an external magnetic field, illustrating the trajectory of a charged particle (blue line) at an incident angle of θ_{trk}. The true hit positions are represented by blue-cyan dots, while the shifted hit positions, with a residual of Δx, are shown as red-orange dots. Grey lines indicate the direction of the Lorentz drift, with θ_{LA} representing the angle relative to the electric field. The magenta-shaded area highlights the volume where charge carriers are released, and the magenta bars depict the corresponding cluster charge. Figure taken from [173].

in hit positions due to Lorentz drift. However, the impact of residual effects not fully absorbed by the alignment can be monitored.

6.5 Monitoring tracking performance

The alignment corrections derived from the track-based method result in an updated geometry of the tracker components, which must undergo thorough validation. Various techniques have been developed to assess the accuracy of the alignment by comparing key performance metrics under the new conditions to those expected in an ideal, perfectly aligned scenario.

Several methods are used to evaluate the precision of the track-based alignment. Some are specifically designed to detect systematic misalignments, including weak modes, systematic distortions that can transform valid tracks into another set of valid tracks with minimal impact on the χ^2 minimization, making them difficult to identify through standard residual checks.

A detailed discussion of these systematic distortions and the methods used to detect them can be found in [179]. The following sections focus on one key validation method,

particularly in the context of assessing the effect of the Lorentz drift.

6.5.1 Distribution of Median of Residuals

One of the primary methods for validating local alignment accuracy in individual tracker modules is through track-hit residuals. These residuals are calculated by refitting a track without the hit under investigation and measuring the distance between the predicted and actual hit positions in local module coordinates. The distribution of median residuals (DMRs) is then analyzed for different tracker substructures.

A perfectly aligned system would show DMR distributions centered around zero, while any shifts indicate systematic misalignment. The width of the distribution reflects remaining random misalignments and statistical uncertainty. DMR validation can also distinguish between inward- and outward-pointing modules based on the orientation of their electric fields, helping to identify residual biases caused by radiation effects in the silicon sensors. Additionally, finer granularity in alignment and specialized data sets often lead to a narrower distribution, indicating improved alignment accuracy.

The width of the distribution also contains an intrinsic component related to the limited number of tracks, meaning that valid comparisons between distributions can only be made when the same number of hits per module is used in their production.

6.5.2 Prompt Calibration Loop

During data taking, the operating configurations of the pixel detector evolve over time, necessitating periodic updates to the alignment constants. This is managed by defining intervals of validity (IOV) for each set of alignment constants.

To compensate for positional shifts in the pixel detector components, an automated alignment workflow is employed. This workflow updates the alignment parameters within approximately 48 hours, using the MillePede-II algorithm at Tier-0 as part of the Prompt Calibration Loop (PCL). It focuses solely on aligning the pixel detector, without addressing the strip detector, being one of the main reasons for the need for a fast update of the alignment parameters.

In Run 2 and the early stages of Run 3, the alignment routine performed a track-based alignment at the level of large structures, such as half barrels and half cylinders, with a total of 36 alignment parameters. This approach is referred to as the Low Granularity Prompt Calibration Loop (LG PCL).

With the increased radiation levels accumulated during Run 3 compared to Run 2, the Lorentz drift in the tracker modules became more pronounced. To mitigate this, more frequent re-alignments and finer granularity were required. As a result, the High Granularity Prompt Calibration Loop (HG PCL) was deployed after a commissioning phase. Like the LG PCL, it performs track-based alignment, but at the level of smaller structures such as ladders and panels, increasing the number of alignment parameters to around 5,000.

6.6 Results

To evaluate how well the alignment absorbs the effects of radiation damage in the Lorentz drift, the performance of three different tracker geometries from Run 3 are compared in Figure 6.4:

- Alignment during data the taking, using the alignment constants provided by the automated online alignment, running as part of the Prompt Calibration Loop (PCL). For the first period of data taking ($\sim$11 fb^{-1} before the technical stop), the pixel detector was aligned at the level of half barrels and half cylinders in the Low Granularity (LG) PCL configuration.
- Mid-year re-reconstruction, where the alignment corrections were applied for the first portion of 2022 data ($\sim$9 fb^{-1}), aligning the pixel and strip subdetectors at the single-module level. This was achieved using 120 million collision tracks from pp collisions at $\sqrt{s} = 13.6\,\text{TeV}$ and 8.5 million cosmic ray tracks at a 3.8 T magnetic field. For the last $\sim$2 fb^{-1} before the technical stop, alignment constants were provided by the High Granularity (HG) PCL, running offline after data collection.
- End-of-year re-reconstruction, where alignment constants were derived for the post-technical stop data ($\sim$30 fb^{-1}), provided by the HG PCL configuration running online as part of the PCL workflow. The starting geometry after the technical stop did not correspond to the final mid-year alignment, but rather to the HG PCL alignment configuration.

The variable μ represents the mean value (estimated through a Gaussian fit) of the DMRs calculated for each module within a given tracker substructure. For each IOV, the mean value is extracted for different alignment geometries and plotted as a function of the delivered integrated luminosity.

Figure 6.4 shows the DMR for the FPIX as a function of the delivered integrated luminosity. The initial online alignment using the LG PCL at the start of data taking exhibits deviations from zero due to changing conditions during the run. These deviations are

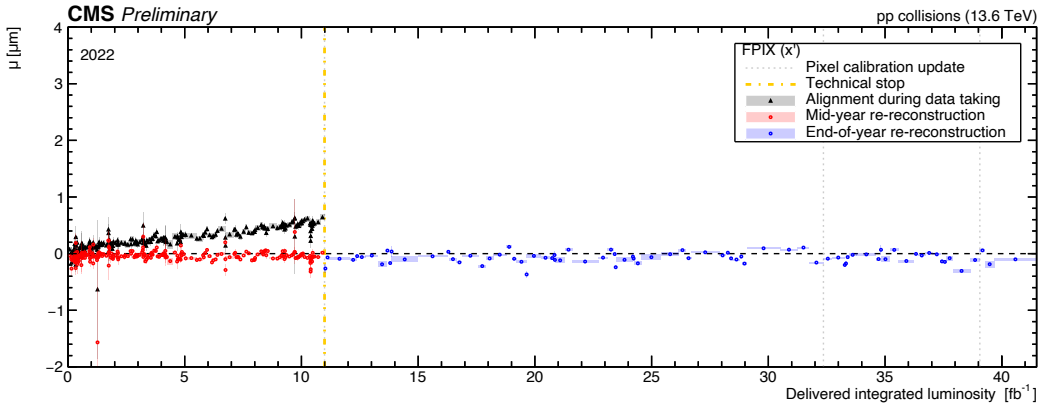

Figure 6.4: Mean value of the median residuals distribution in the local-x (x') direction of the forward pixel detector (FPIX) as a function of the delivered integrated luminosity. The local x axis aligns with $\vec{E} \times \vec{B}$, where $\vec{E}$ represents the electric field of the sensor and $\vec{B}$ denotes the axial magnetic field [173]. Vertical gray dotted lines mark changes in the pixel tracker calibration, while the yellow line indicates a four-week technical stop. The uncertainty is represented by the standard mean error of the plotted values, and different colors correspond to various alignment campaigns. Figure taken from [180].

corrected by the offline alignment performed after reprocessing. In contrast, the HG PCL consistently keeps the mean value of median residuals closer to zero, demonstrating improved stability compared to the automated LG PCL alignment.

As stated in section 6.4, the direction of the Lorentz angle shift is influenced by the orientation of the electric field, resulting in opposite shifts in hit positions for inward- and outward-pointing modules. In the barrel region, it is possible to obtain DMR distributions separately for modules with electric fields directed radially inward or outward, as illustrated in Figure 6.5. Significant degradation in alignment is observed after one month of data taking; however, the mid-year re-reconstruction effectively addresses these changes. The dashed lines indicate the DMR values for both inward- and outward-pointing modules across the different alignment geometries. The difference in the mean values of the median residuals, defined as $\Delta\mu = \mu_{\text{inward}} - \mu_{\text{outward}}$, serves as an indicator of the effectiveness in mitigating Lorentz angle effects. A mean value that deviates from zero suggests the presence of residual biases caused by the cumulative effects of radiation on the silicon sensors.

Figure 6.6 presents the DMR of $\Delta\mu$ for the BPIX as a function of delivered integrated luminosity. The online alignment using the LG PCL at the start of data taking and the offline alignment after reprocessing exhibit deviations from zero, indicative of shifts in the Lorentz angle due to radiation damage. An improvement in the difference of mean values for the mid-year re-reconstruction is noted around $\sim 9\,\text{fb}^{-1}$, coinciding with the initiation

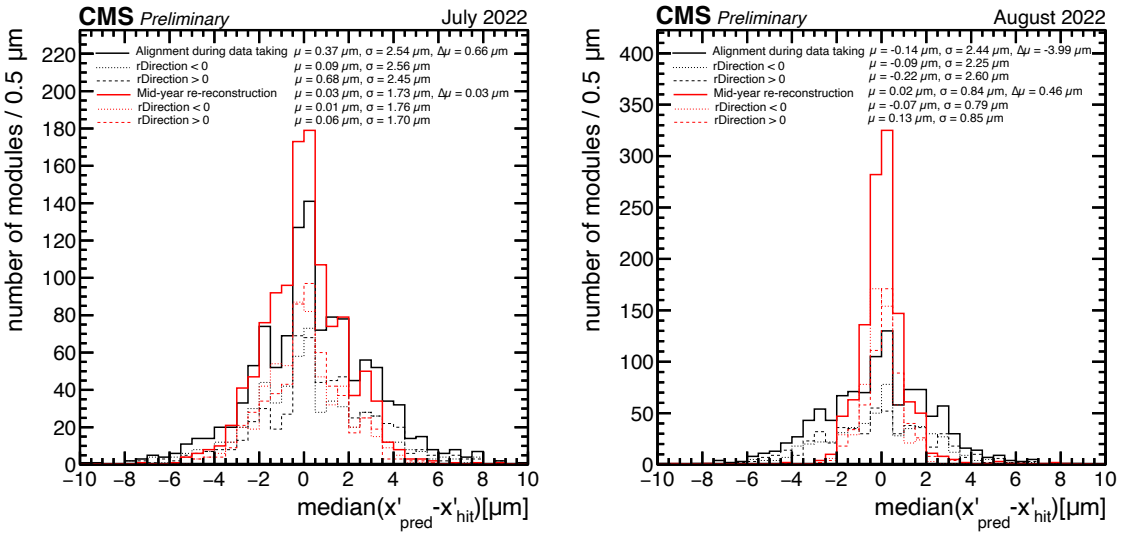

Figure 6.5: The distribution of median residuals in the local x' direction of the barrel pixel detector is presented for two distinct periods: July (left) and August (right) 2022, prior to the four-week technical stop. The black line represents the results from the automated alignment within the Low Granularity Prompt Calibration Loop (LG PCL), while the red line reflects the geometry used in the mid-year re-reconstruction. The means (μ) and standard deviations (σ) shown are parameters from a Gaussian fit to the distributions. Additionally, $\Delta\mu$ indicates the difference between the mean values obtained for modules with the electric field oriented radially inward and outward in the local x (x') direction. Figure taken from [180].

of the HG PCL offline alignment. The online HG PCL effectively corrects the position bias that developed during data taking and remained unaddressed by local reconstruction.

In Figure 6.7, the $\Delta\mu$ for BPIX layer 1 is displayed. This layer experiences more pronounced radiation effects since it is positioned closest to the interaction point and therefore incurs the highest radiation exposure. The mid-year re-reconstruction incorporates updates to the detector geometry with greater granularity than that of the alignment during data taking, enabling it to largely compensate for the effects of accumulated radiation damage within the alignment procedure.

During the transition in the pixel tracker calibration, the online High Granularity Prompt Calibration Loop (HG PCL) requires some time to adapt to the new conditions in the alignment, specifically around 32 fb^{-1} and 39 fb^{-1}. However, it demonstrates a rapid recovery thereafter.

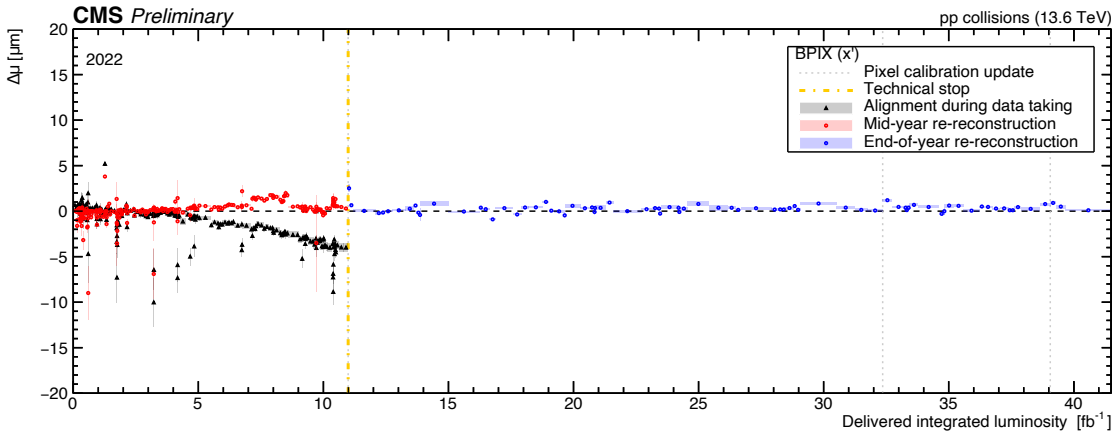

Figure 6.6: $\Delta\mu$ for the pixel barrel modules is presented as a function of the delivered integrated luminosity. The uncertainty is derived from the square root of the quadratic sum of the uncertainties calculated for the inward and outward-pointing modules separately. Vertical gray dotted lines indicate changes in the pixel tracker calibration, while the yellow line marks a four-week technical stop. Each color represents a different alignment campaign. Figure taken from [180].

6.7 Conclusion

The alignment of the CMS tracker is a crucial aspect of detector calibration, aiming to achieve precise measurements of tracker module positions within a few micrometers. This precision is accomplished through track-based alignment, which is detailed in the first part of this chapter. However, tracker alignment is complex, facing both computational and configuration challenges. The computational side involves determining a large number of parameters, while the configuration side often lacks clear guidance on optimal strategies related to alignment granularity, track topologies, and statistical methods.

A particularly challenging period for CMS tracker alignment occurred in 2021 when the entire pixel detector was upgraded and replaced. This transition required rapid derivation of alignment corrections shortly after installation, before data-taking could commence, necessitating a fast and effective approach. During this critical time, the author played a pivotal role by conducting comprehensive preparatory studies using simulated events. These studies compared various scenarios to identify the optimal realignment strategy. The identified strategy was subsequently applied to the first alignment measurements obtained from cosmic ray data collected prior to the proton-proton collision run. Initially, significant misalignments present after installation were corrected, leading to precise measurements of pixel tracker positions down to the level of individual modules. This effort significantly improved the precision of hit position measurements before the proton-proton collision run, allowing for the collection of collision data with a well-aligned tracker from

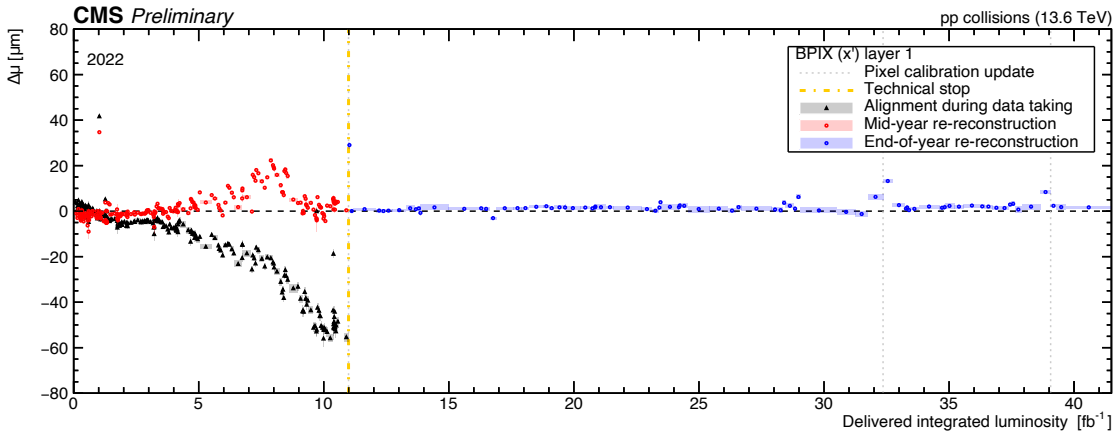

Figure 6.7: $\Delta\mu$ for layer 1 of the pixel barrel modules is presented as a function of the delivered integrated luminosity. The uncertainty is calculated as the square root of the quadratic sum of the uncertainties from the inward and outward-pointing modules. Vertical gray dotted lines mark changes in the pixel tracker calibration, while the yellow line indicates a four-week technical stop. Each color represents a different alignment campaign. Figure taken from [180].

the outset. Throughout the data-taking period, continuous alignment corrections and calculations of Alignment Precision Estimates (APEs) were performed.

Overall, the findings highlight the importance of monitoring Lorentz drift and the need for continuous alignment to maintain the pixel tracker's performance.

CHAPTER 7

Measurement of the $t\bar{t}$+jet cross section and the top quark pole mass

Contents

This chapter describes the measurement of the production cross section of $t\bar{t}$ pair in association with an additional jet and extraction of the top quark mass. The first CMS measurement of this kind, documented in Ref. [90], was based on pp collisions at the LHC at a center of mass energy of 13 TeV, collected by CMS in 2016 and corresponding to 35.9 fb^{-1}. The work presented in this thesis exploits the pp collisions at 13 TeV, in 2016-2018 (full Run 2 data), corresponding to the integrated luminosity of 138 fb^{-1}. Furthermore, the present measurement uses a new and more precise recalibration of the CMS Run 2 data, known as the *Ultra Legacy* reconstruction, which became available in 2021. Therefore, the present results profit from significantly reduced statistical and systematic uncertainties.

This chapter is structured as follows: the outline of the analysis strategy is presented in section 7.1, while in section 7.2 the data sets and event selection are discussed. The kinematic reconstruction of the $t\bar{t}$ system using a Neural Network (NN) is discussed in section 7.4. In section 7.5 the classification procedure using the NN is explained, while the unfolding is discussed in section 7.6. Systematic uncertainties are discussed in section 7.7. Finally, the results are presented in section 7.8.

7.1 Analysis strategy

Similar to other indirect measurements of the top quark mass, in this analysis, the value m_t^{pole} is extracted by comparing the unfolded parton-level cross sections with fixed-order theory predictions. The differential cross section of the $t\bar{t}$ system in association with one additional jet ($t\bar{t}$+jet) is measured as a function of the kinematic variable ρ defined in Section 1.4. This observable is strongly sensitive to m_t^{pole} (Section 1.3), which was experimentally explored by the ATLAS [181] and CMS [90] collaborations.

At first, the inclusive event selection is performed, explained in Section 7.2. Since the unfolding of the ρ distribution to parton level is performed, a kinematic reconstruction of the $t\bar{t}$ system and an event classification to distinguish signal and background are required. For this purpose, two multivariate analysis (MVA) methods are used, as explained in Sections 7.4 and 7.5. The kinematic reconstruction and the event classification are then fed into the unfolding, which is based on a profile maximum likelihood fit (Section 7.6). The differential cross section is measured within the visible phase space, which is defined by the geometric acceptance of the detector and the requirement on the reconstructed objects. Subsequently, this measurement is extrapolated to the full phase space, as defined at the parton level. The resulting differential cross section are compared with fixed order theory predictions using different parton distribution function sets and the pole mass of the top quark is extracted.

7.2 Data set, simualtion samples and event selection

This measurement uses the LHC pp collision data at $\sqrt{s}$= 13 TeV recorded by the CMS detector in 2016, 2017 and 2018, and corresponding to an integrated luminosity of 138 fb^{-1}. The data collected in 2016 is split into two periods, *2016preVFP* and *2016postVFP*, due to significant differences in detector conditions. In 2016preVFP period, the strip tracker experienced a lower signal-to-noise ratio and fewer track hits due to readout chip saturation. This issue was mitigated in 2016postVFP by adjusting the feedback preamplifier

bias voltage (VFP) [182]. In the subsequent running, continuous detector conditions were achieved within each 2017 and 2018 periods.

The top quark decays in the di-leptonic channel are used, to achieve best signal purity. For selecting the relevant events, dedicated sets of di-lepton and single lepton triggers are used. A logical "OR" operation is employed to select events in the di-lepton channel, combining different trigger terms. Collected data is organized into streams, based on specific event criteria or triggers. Events flagged with di-lepton paths are excluded when processing single lepton data streams. Additionally, to prevent overlap between single lepton data streams, events are assigned to one of the three di-lepton channels based on the definition of a distinct lepton pair per event. The trigger path selection of the high level trigger (HLT) is detailed in Appendix B.1.

Signal simulation

The Monte Carlo (MC) samples for $t\bar{t}$ pair production are generated at next-to-leading-order (NLO) using the POWHEG [183] event generator. In these simulations, the top quark mass value is fixed to m_t=172.5 GeV and the structure of the proton is described by NNPDF3.1 [184] PDF set at NNLO. The modeling of parton shower (PS) and hadronization is carried out using PYTHIA 8.2 [92] with the CP5 tune for describing the underlying event (UE) [70]. The matching of the matrix element (ME) calculations to PS is performed using the FxFx merging algorithm [69]. The h_{damp} parameter, regulating the ME-PS matching scale, is set to 1.379 m_t^{MC}. Finally, GEANT4 [73] is used to simulate the CMS detector response.

The generated cross section is corrected to the value of next-to-next-to-leading-order (NNLO) + next-to-next-to-leading logarithmic (NNLL) prediction, calculated by using TOP++ software [185], while the expected event yields are normalized to the corresponding integrated luminosity of the data.

Background simulation

The background MC samples and their cross sections are summarized in Table 7.1. For simulation of single top quark production in s- and t- (ST) and tW channels, POWHEG is used, while the di-boson (WW, WZ, and ZZ) samples are modeled by using PYTHIA 8.

The events containing W+jet production are simulated individually for different jet multiplicities, while the inclusive (W+jets), and the multiplicity-binned ones (W+0/1/2jets), are used together, to increase the statistics. The contribution from Drell-Yan (DY) events is simulated depending on the di-leptonic invariant mass, 10 GeV $< m_{ll} <$ 50 GeV and

$m_{ll} > 50$ GeV, and divided into different jet categories. The samples for the $t\bar{t}$ associated production with Z or W boson are simulated using MG5_aMC at NLO. For these samples, PS and hadronization are also simulated with Pythia 8 by using the FxFx merging prescription.

The cross sections are corrected to the highest-order available fixed-order calculations, such as NNLO for W+jets [186], NLO for Z+jets, approximate NNLO for single top quark tW channels [187], and NLO for diboson production [188].

Event selection

The $t\bar{t}$+jet process in the di-leptonic channel is characterized by two b tagged jets, two leptons and two neutrinos, as shown in Fig. 7.1, and an additional jet. The event selection is based on the physics objects, defined in Section 2.3. Processes like $t\bar{t}$ with no additional energetic jet ($t\bar{t}$+0jet) and tW with additional QCD radiation lead to identical final states and signatures, thus representing irreducible backgrounds. Z+jets background appears predominantly in the same-flavor channels, while in $e^{\pm}\mu^{\mp}$ channel it arises from $Z \to \tau\tau$. The events with W+jets and the semileptonic $t\bar{t}$ decays are further sources of background due to the lepton misidentification. Other background contributions constitute the diboson production and $t\bar{t}V$ production.

The event selection is critical to maximize the phase space of the process and to suppress the background contributions. Only events with well-understood properties are chosen, such as the ones where the experimental data is well described by the MC simulation. This involves ensuring adequate efficiency in the reconstruction and identification, which may need additional correction to both MC events and, if required, to the data.

The first step is to check if the event is triggered, and if there is a PV of good quality, additional missing transverse momentum filters are also applied. This check ensures that only high-quality events are selected, meaning filtering out events that might be poorly reconstructed.

Subsequently, the leptons originating from the $t\bar{t}$ decay must be identified. For that purpose, an opposite-charged lepton pair, reconstructed within the tracker acceptance, $|\eta| < 2.4$, is required. The leading (subleading) lepton is required to have a transverse momentum $p_T > 25$ GeV (20 GeV). Tight cut-based identification [118] is applied to the muon candidates, to mitigate possible contributions of fake muons (non-prompt muons coming either from jets or from secondary processes) and ensure a high-purity muon selection. To remove contributions from QCD multijet events, an extra isolation requirement is needed, $I_{rel} < 0.15$, where I_{rel} is obtained by summing the transverse momenta of charged and neutral hadrons and photons inside a cone of $\Delta R < 0.4$ with respect to the muon direction. An Identification Multivariate Analysis (ID MVA), based on Boosted Decision Trees

Process	Cross section [pb]
$t\bar{t}$ dilepton	88.96
$t\bar{t}$ hadronic	377.57
$t\bar{t}$ semileptonic	366.54
$t\bar{t}$Z (hadronic)	0.5297
$t\bar{t}$Z (leptonic)	0.2529
$t\bar{t}$W (hadronic)	0.4062
$t\bar{t}$W (leptonic)	0.2043
ST (t channel)	136.02
ST (s channel)	10.32
ST antitop	80.95
tW top/antitop	35.85
DY + jets (M_{ll} $\in$[10,50] GeV)	18610.1
DY + jets (M_{ll} $>$ 50 GeV)	6077.22
DY + 0 jets	5129.0
DY + 1 jet	951.5
DY + 2 jets	361.4
W + jets (inclusive)	61526.7
W + 0 jets	53330.0
W + 1 jet	8875.0
W + 2 jets	3338.0
WW	118.7
WZ	47.13
ZZ	16.523

Table 7.1: MC sample cross sections of the signal and backgrounds considered in this analysis. The $t\bar{t}$ dilepton is both used for signal and background.

with a working point of 90% in signal efficiency, is used to ensure high-purity samples of prompt electrons (originating from the primary interaction). This leads to improvement with respect to the cut-based method of 5% [189].

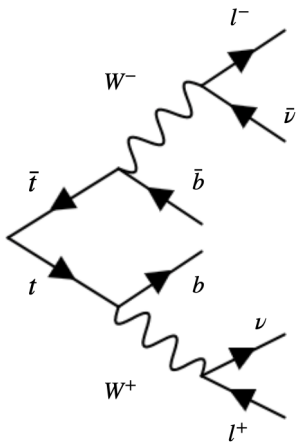

Figure 7.1: Representation of the dileptonic decay of the $t\bar{t}$ system.

If more than two leptons are reconstructed in an event, the ones with the highest p_T are selected. The event is classified as e^+e^-, $\mu^+\mu^-$ or $e^\pm\mu^\mp$ depending on the type of the lepton pairs selected. The di-lepton system is required to have an invariant mass above 20 GeV. This cut is imposed to suppress the DY processes and events from decays of heavy flavor resonances. In the same-flavor lepton decay channels, events are excluded if the di-lepton invariant mass falls within the region 76 GeV $< m_{ll} <$ 106 GeV, this way avoiding the Z boson mass window. In addition, the same-flavor channel events are required to have $p_T^{\text{miss}} > 40$ GeV to further reduce the Drell-Yan (DY) contribution.

All jet candidates undergo a set of "tight" identification criteria to suppress misreconstructed objects [190]. The jets reconstructed by using the PUPPI algorithm with $\Delta R >$ 0.4 are selected within absolute rapidity $|y| < 2.4$ and are required to have $p_T > 30$ GeV.

The b quark jets are identified by using the DeepJet tagger [124], based on multiclassification DNN. It substitutes track-based lifetime information with low-level characteristics of various charged and neutral particle flow jet constituents, complemented by attributes of secondary vertices linked to a jet. A "medium" working point is chosen, which corresponds to misidentification efficiency probability of 1% for light-flavor jets and around 15% for c quarks. The efficiency of correctly tagging flavor jets is above 80%. The event must contain at least one b tagged jet.

7.3 Data-simulation comparison

To mitigate discrepancies arising from deficiencies in the event simulation or from detector inefficiencies, several corrections are implemented using the so-called scale factor (SF). These SFs are derived for each object by comparing the examined observable between simulation and data, and applied to simulation, multiplicatively, as event weights. In particular, deficits in MC to describe reconstruction efficiency, identification and isolation of leptons in the data are accounted for in the SFs. Those effects are considered uncorrelated and different SF for muon and electron efficiencies are derived. Lepton energy-scale and resolution corrections are also applied to the MC simulation.

Jet Energy Scale (JES) corrections are applied to the measured energy of jets to correct for detector response and to account for discrepancies in the simulation of hadronization and showering. This ensures that the reconstructed jet energy reflects the energy of the original partons as accurately as possible.

The Jet Energy Resolution (JER) is defined as the relative uncertainty in the measurement of the energy of a jet. The reconstructed energy distribution has an inherent width expected due to differences in hadronization and detector response from jet to jet. The width is adjusted to match what is observed in the data.

During the 2018 data-taking period, the hadronic calorimeter Endcaps experienced reduced performance within certain η and ϕ ranges ($-3 < \eta < -1.3$ and $-1.57 < \phi < -0.87$) due to electrical issues. This issue, known as the Hadronic Calorimeter Endcaps Minus (HEM) issue, led to a significant increase in the multijet background. Jets in this affected region are reconstructed with underestimated transverse momentum, resulting in an overestimated missing transverse energy (E_T^{miss}). Jets in this region are vetoed to eliminate spurious E_T^{miss} in the signal region.

The SFs for the true flavor of the jets as a function of their p_T are derived, in order to adjust the b jet tagging efficiency in simulation to match that observed in data. The SFs for light flavor misidentification are determined by analyzing inclusive QCD multijet events. Similarly, the SFs for b and c jets are derived using muon-enriched QCD multijet events. Once the jet-based SFs are determined, they are converted into event-based corrections as follows. The probabilities of correctly identifying all b jets in an event in both data (P_{data}) and simulation (P_{MC}) are computed for a selected working point. The ratio of these probabilities is then used as a weight to correct the simulated events. The probabilities P_{MC} and P_{data} are determined as

$$P_{MC} = \prod_{f}^{\text{flavor}} \prod_{i}^{\text{tagged}} \epsilon_i^f(p_T) \prod_{j}^{\text{untagged}} [1 - \epsilon_j^f(p_T)] \tag{7.1}$$

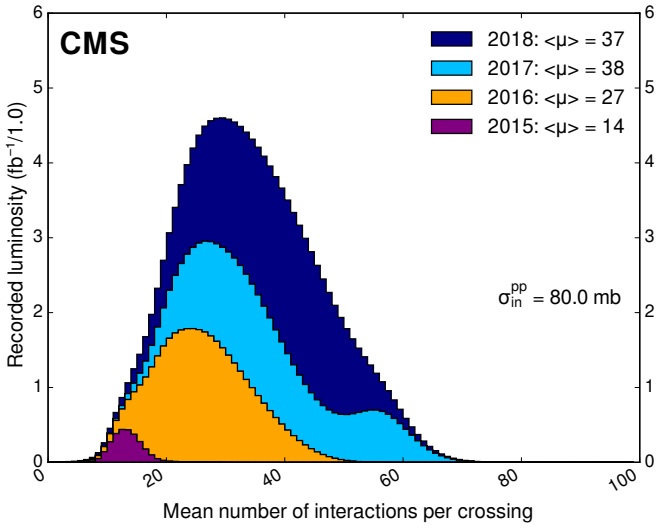

Figure 7.2: The average pileup for pp collisions recorded in 2015 (purple), 2016 (orange), 2017 (light blue), and 2018 (navy blue), including the overall mean values for each year of data taking. Figure taken from [191].

and

$$P_{data} = \prod_{f}^{\text{flavor}} \prod_{i}^{\text{tagged}} \epsilon_i^f(p_T) SF_i^f(p_T) \prod_{j}^{\text{untagged}} [1 - SF_j^f(p_T)\epsilon_j^f(p_T)], \tag{7.2}$$

where ϵ_i^f is the b tagging efficiency and SF_i^f is the SF for the jet i with flavor f.

Pileup reweighting

The number of interactions per bunch crossing, pileup (PU), differs between the simulation and real operation conditions. The actual pileup distribution, expressed in terms of the mean number of inelastic interactions per crossing μ in data can be inferred from the luminosity measurements. The simulation is adjusted to match the data by applying the event weights, obtained as ratios of normalized μ distributions in data and in simulations.

In Figure 7.2 the normalized pileup distributions for each data-taking year during Run 2 are presented, illustrating the differences between the data-taking periods due to changes of the operating conditions and instantaneous luminosities. The significant differences in PU conditions, resulting in tensions in the data-simulation agreement for the four data-taking periods, observed in all precision measurements of CMS based on Run 2 data, lead to reconsidering the 1-dimensional PU reweighting procedure.

In the present analysis, a new reweighting method is introduced, based on investigations of Ref. [192]. Instead of 1-dimensional reweighting in μ, this analysis considers two-dimensional correction factor. The PU corrections are derived in bins of double-differential distributions of the number of good reconstructed primary vertices, N_{vtx}, and the overall flux of energy through the detector at a given time, ρ_{det}, obtained from the ratio between simulation and data. The binning is chosen such that the uncertainty per bin is smaller than 1%.

In Figures 7.3 and 7.4, the two variables are for the data-taking periods of preVFP and postVFP 2016 respectively. In Figures 7.5 and 7.6, these variables are shown for 2017 and 2018, respectively. The two-dimensional binning results in step-like features in the corrected distributions, reflecting the discrete boundaries of the bins.

Measurement of the trigger efficiency

Dedicated trigger SFs are determined in the observable phase space. The trigger selection is designed to achieve the highest possible efficiency for collecting $t\bar{t}$ events. This efficiency is obtained by comparing the events selected by the trigger system to those that would have been selected based on the lepton selection criteria applied during the offline analysis (i.e., after the data is recorded and processed). It is measured using an orthogonal set of p_T^{miss} triggers, which allows an unbiased measurement in both data and simulation, if the p_T^{miss} baseline triggers are uncorrelated to the signal lepton triggers. The trigger efficiency can be obtained as

$$\epsilon_{\text{trig}} = \frac{N_{\text{Events}}(\text{trig}_{p_T^{\text{miss}}} \cap \text{trig}_{\text{lep}} \mid \text{pass sel.})}{N_{\text{Events}}(\text{trig}_{p_T^{\text{miss}}} \mid \text{pass sel.})}, \tag{7.3}$$

where the numerator is the number of events passing the offline selection, the signal and the baseline triggers. The denominator includes the number of events passing the offline selection and the baseline triggers.

To account for the differences in the efficiency of the trigger selection between data and simulation, SFs are derived as a function of the lepton p_T^{miss}. These factors are defined as the ratio of the trigger efficiency observed in experimental data to that in simulation. The results are shown in Appendix B.2.

Comparison between data and simulation

The agreement between the data and simulation is monitored by using the kinematic distributions. In Figures 7.7 and 7.8, p_T distributions for leading leptons and jets are

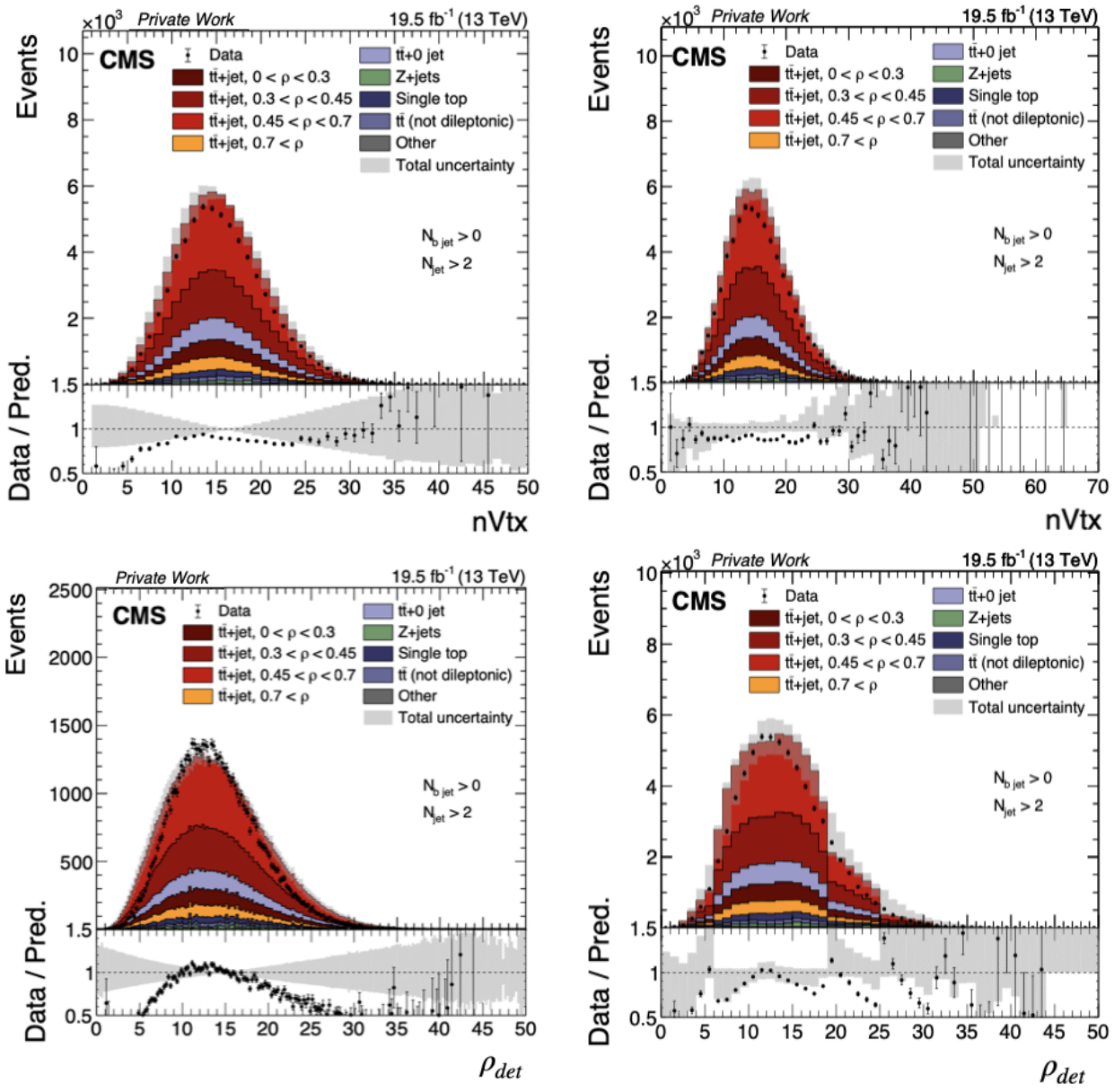

Figure 7.3: Pileup-relevant distributions in simulation (shaded histograms) and data (black symbols) for 2016 preVFP. Upper panel: number of primary vertices, N_{vtx}, before (left) and after (right) correction. Lower panel: the mean energy density, ρ_{det}, before (left) and after (right) the correction. In the lower insets, the ratios of data to simulation are shown.

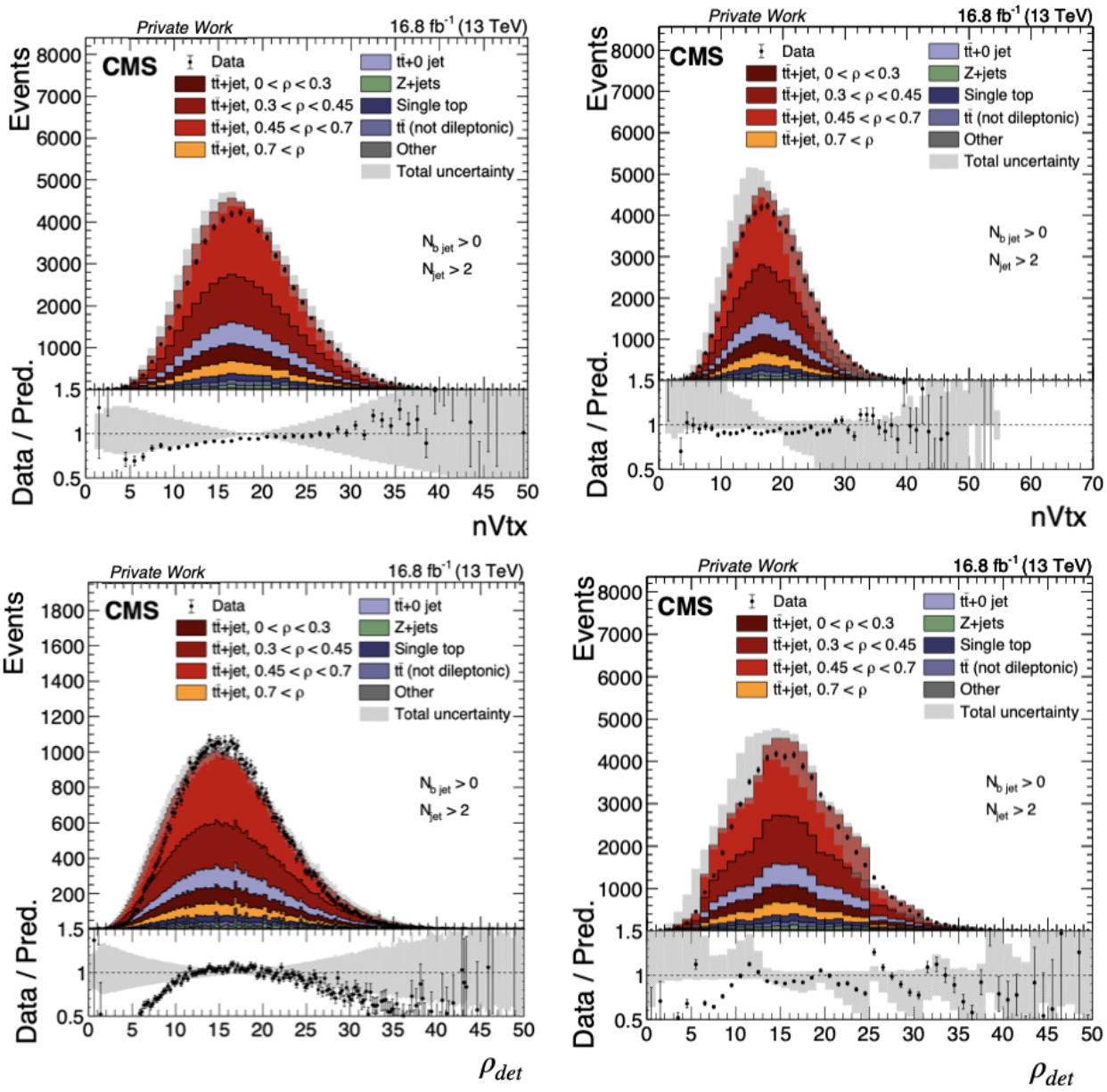

Figure 7.4: Same as in Figure 7.3, for 2016 postVFP.

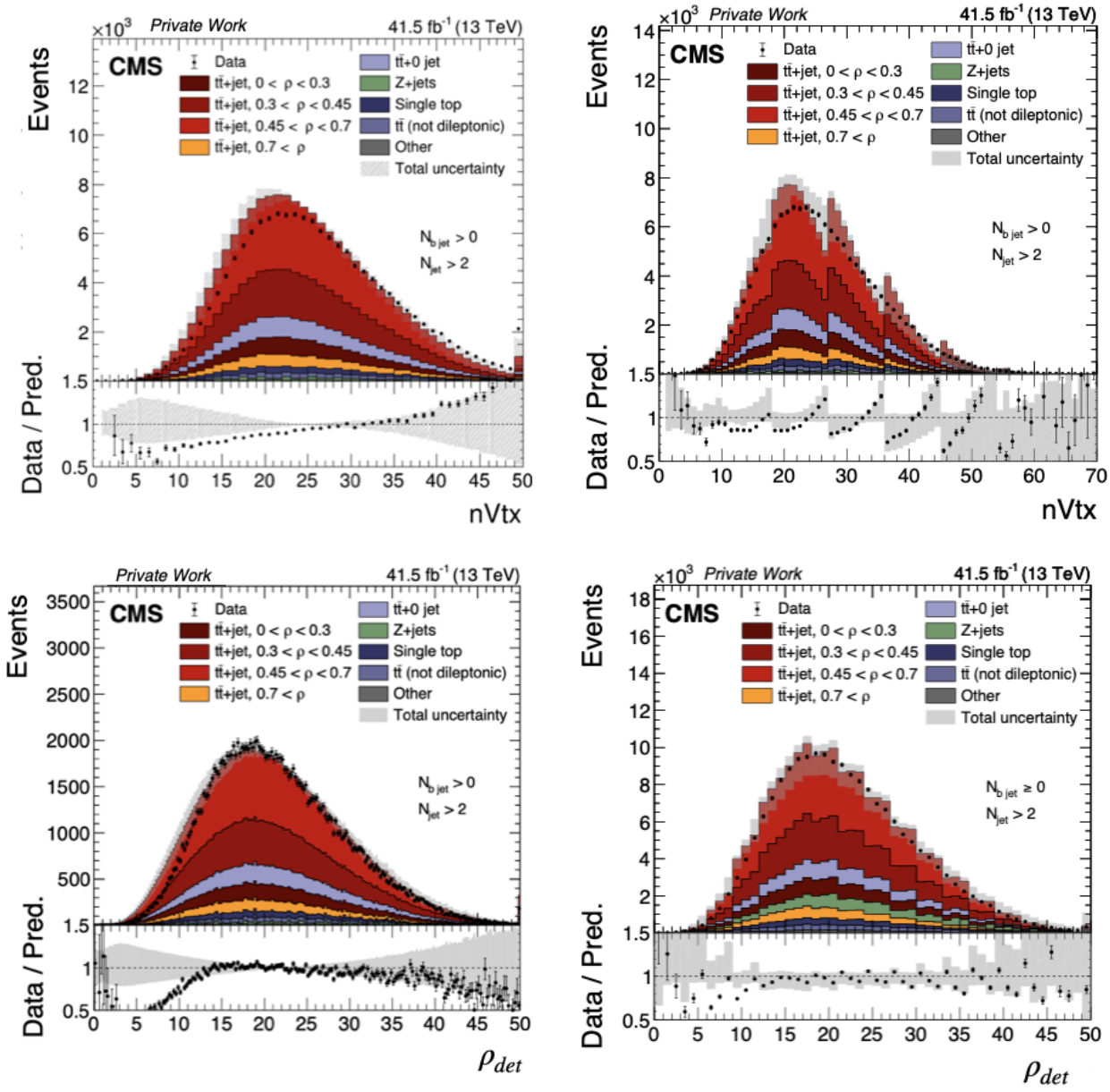

Figure 7.5: Same as in Figure 7.3, for 2017.

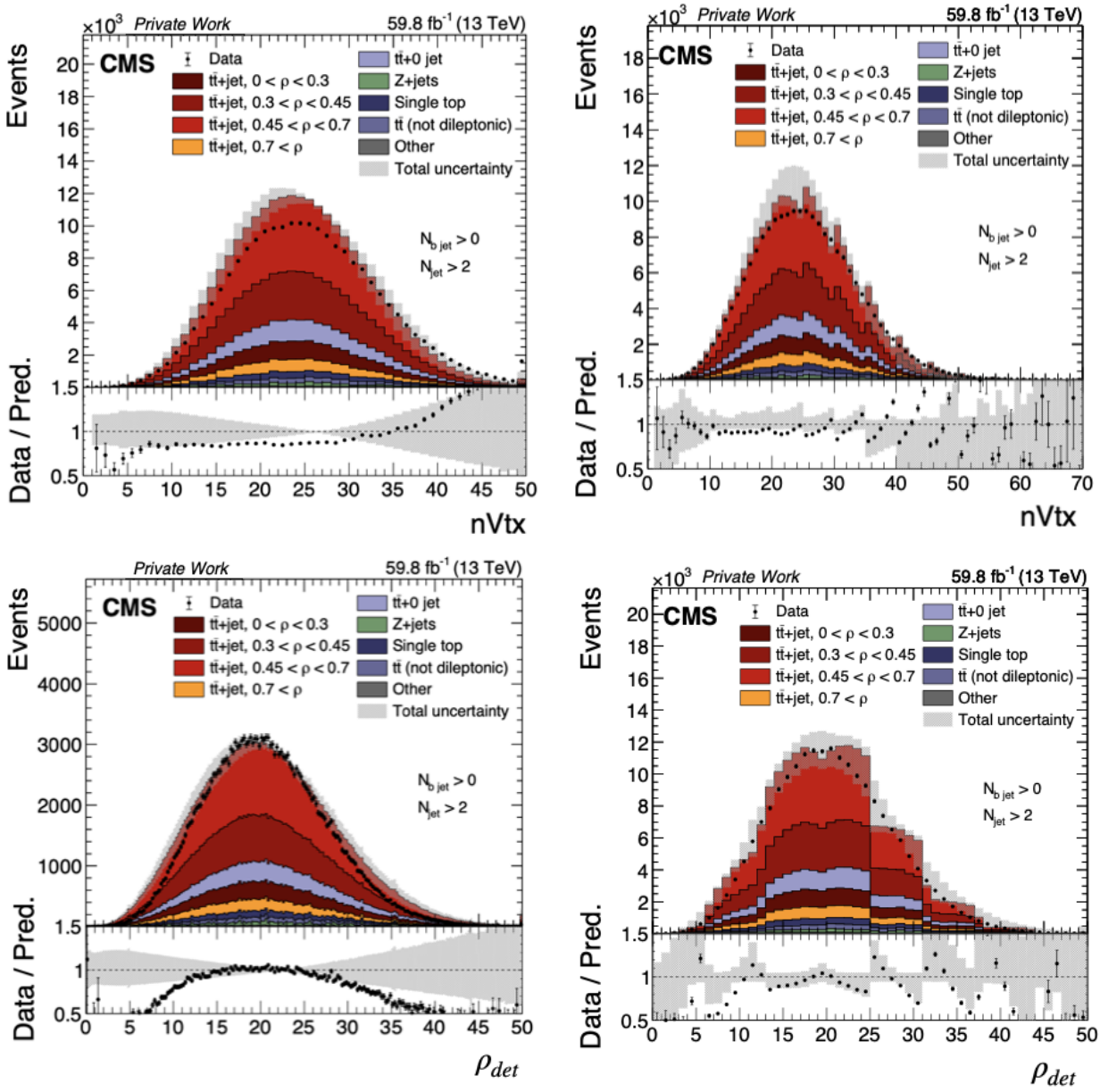

Figure 7.6: Same as in Figure 7.3, for 2018.

shown for the three lepton channels, combined. While very good general agreement in the shapes is observed, the minor discrepancy in the normalization between the data and simulation does not impact the analysis. Slight trends in the ratios of jet and lepton momenta have been observed already in previous measurements [90]. The jet and b tagged jet multiplicity are shown in Figures 7.9 and 7.10, where good agreement between the simulation and the data is found.

7.4 Reconstruction of the top quark kinematics

The unfolding of the ρ distribution at parton level requires the kinematic reconstruction of the $t\bar{t}$ system. This reconstruction is challenging due to the presence of neutrinos, which cannot be measured directly. Instead, their kinematics is inferred from the missing transverse momentum in the event. Each leptonic W boson decay produces a neutrino, leaving two neutrinos in the final state. In dileptonic decays of $t\bar{t}$ pair, this introduces an ambiguity in their reconstruction that degrades the resolution of the final state observables. Other sources can further affect the estimation of the p_T^{miss}, for example neutrinos originating from other processes, or inefficiencies in the detector.

There are two analytical kinematic reconstruction approaches to solve the $t\bar{t}$ system: the full kinematic reconstruction and the loose kinematic reconstruction. The full kinematic reconstruction determines the four-momenta of the top quark and antiquark, using among others the mass of the top quark as constraint. By taking the smallest $t\bar{t}$ invariant mass possible ambiguities are solved [193]. On the other hand, the loose kinematic reconstruction only determines the kinematics of the $t\bar{t}$ system as a whole [64] and not the individual kinematics of the top quark and antiquark.

In the context of the earlier $t\bar{t}$+jet analysis, an alternative reconstruction approach is developed, also used in the analysis of this thesis [90]. This technique is based on a regression NN to optimize the resolution of the ρ observable as shown in Figure 7.11.

7.5 Event classification and categorization

In this thesis, a MVA technique, specifically a regression NN, is used to enhance the discrimination capability between the $t\bar{t}$+jet signal and Z+jets and $t\bar{t}$+0jet backgrounds, where the latter is the main background. The architecture of the classification network has three output nodes, corresponding to the three process classes ($t\bar{t}$+jet, Z+jets, and $t\bar{t}$+0 jet), which improves the signal-to-background discrimination. The setup of the NN and the variables used are detailed in [90].

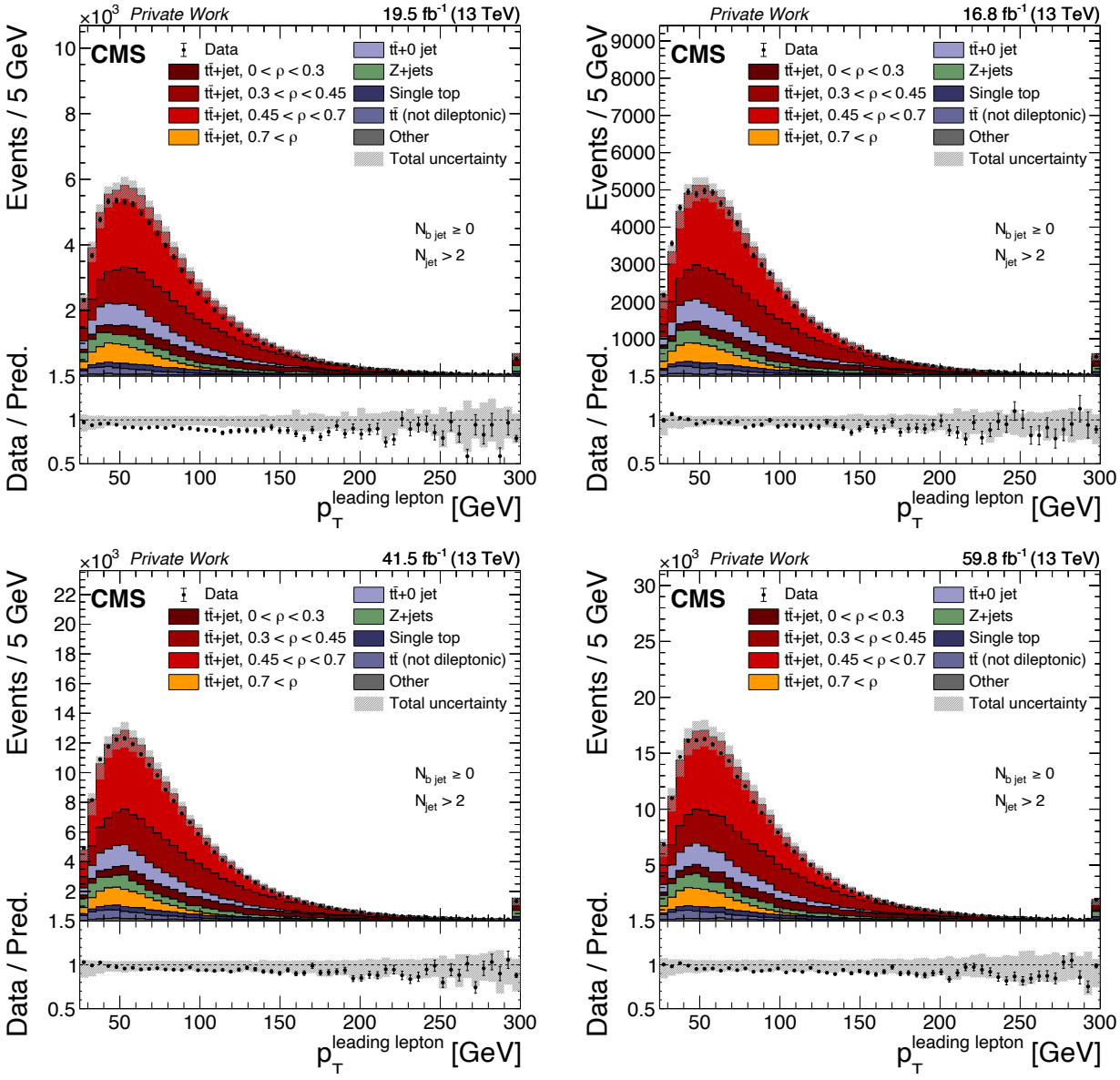

Figure 7.7: Comparison between the observed (black symbols) and predicted (filled histograms) events. The distributions of the transverse momentum p_T of the leading lepton are shown for different data-taking periods. The simulation is corrected by the b jet scale factors. Statistical uncertainties in the data are represented by vertical error bars, while the hatched bands indicate the systematic uncertainty in the simulation, including the uncertainty in the integrated luminosity. Overflow contributions are included in the last bins. In the lower insets, the ratio of the event yields in data to the sum of predicted signal and background yields is presented.

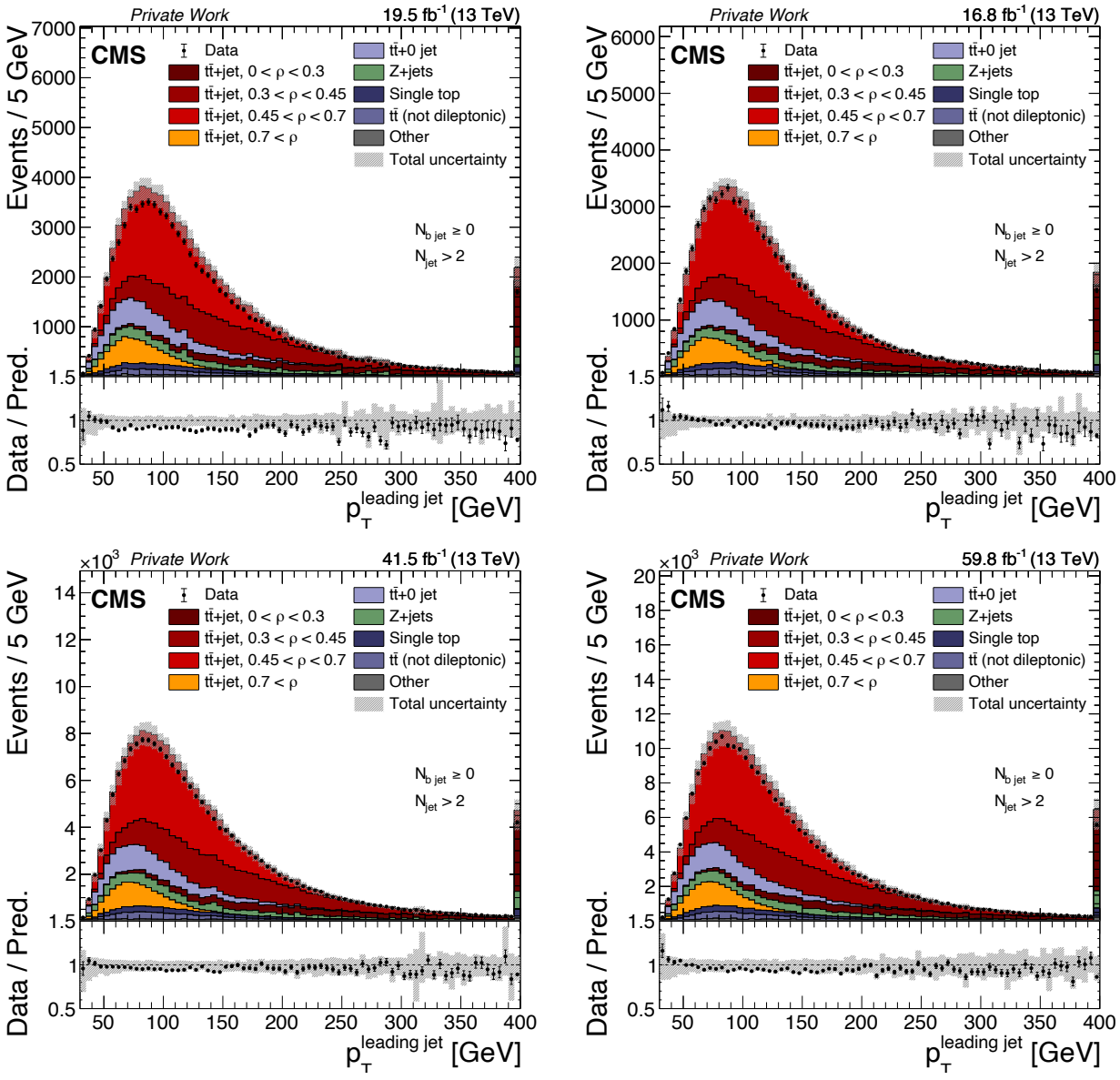

Figure 7.8: Transverse momentum of the leading jet, using same notations as in Figure 7.7.

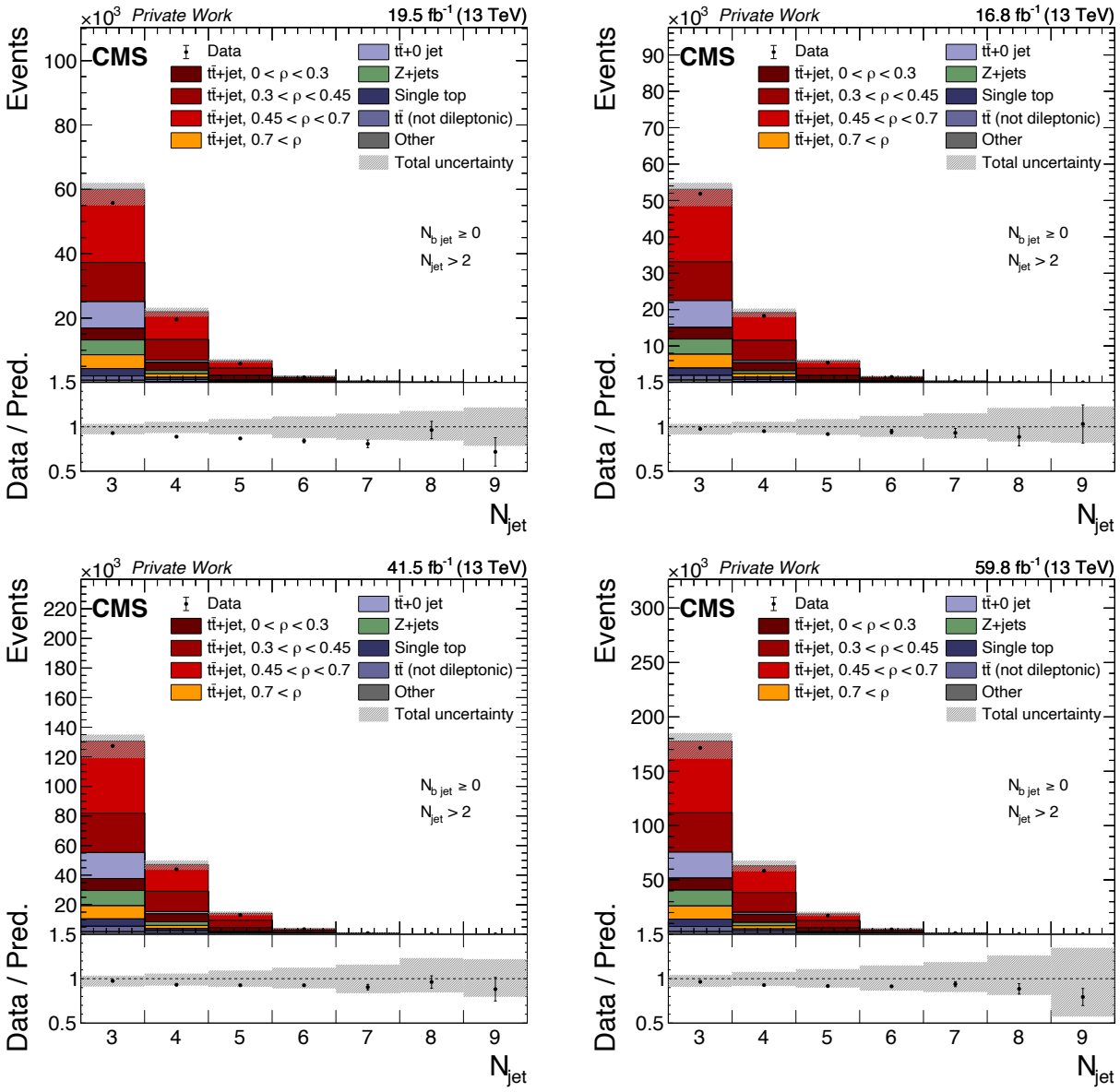

Figure 7.9: The number of observed and predicted events are presented in the same manner as in Figure 7.7. The distributions shown are the number of jets.

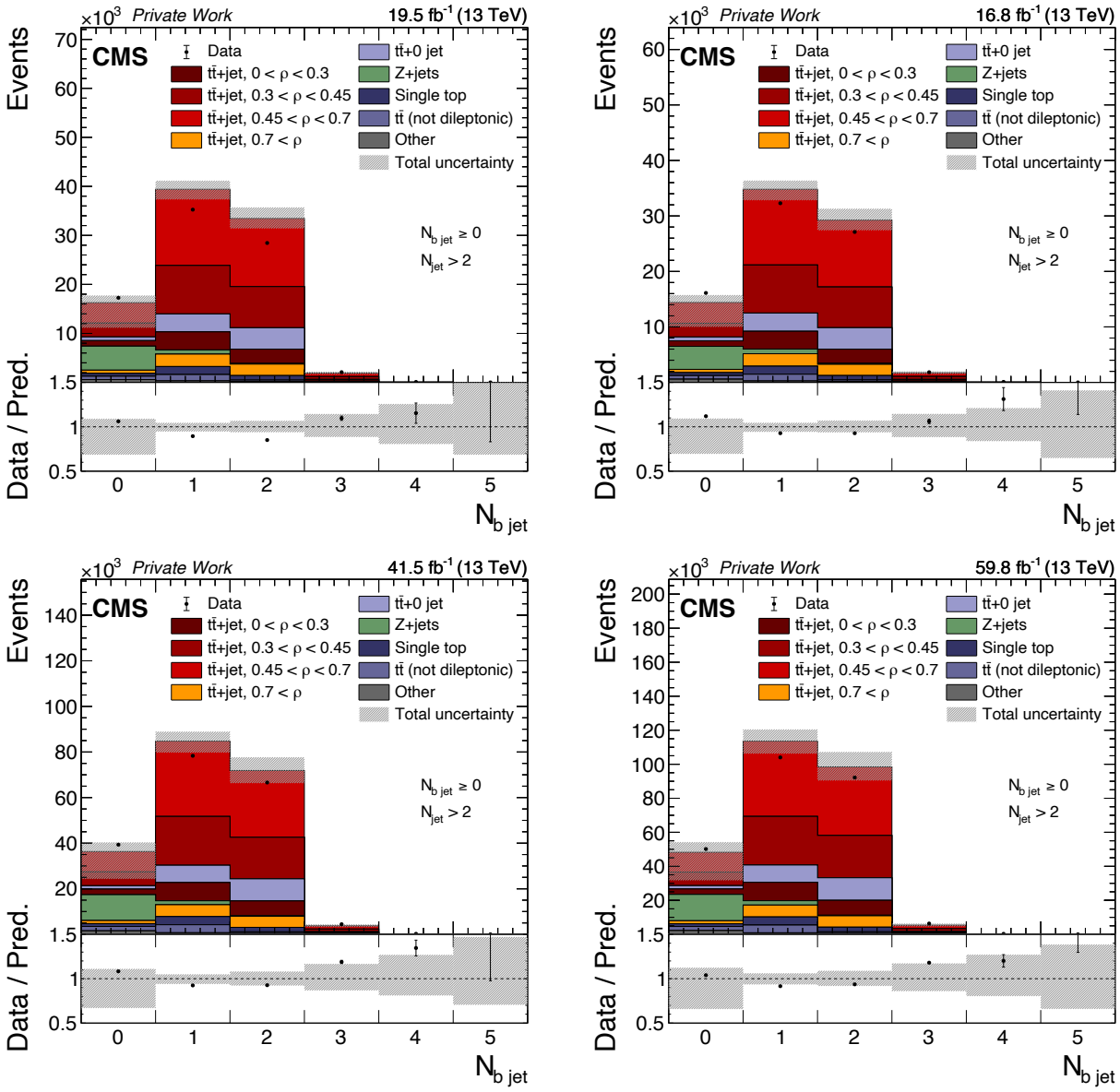

Figure 7.10: The number of observed and predicted events are presented in the same manner as Figure 7.7. The distributions shown are the number of b tagged jets.

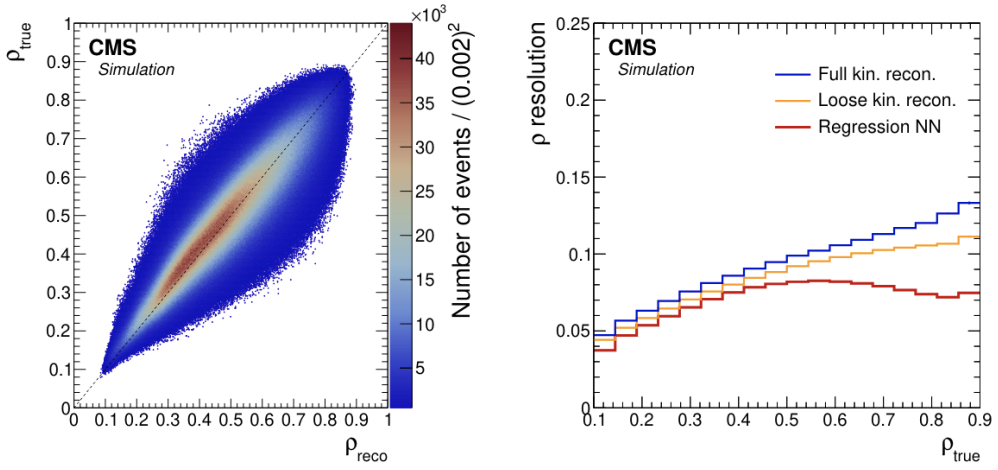

Figure 7.11: The correlation between ρ_{gen} and ρ_{reco} is shown for the regression NN reconstruction method (left). The ρ_{reco} resolution, defined in the text, as a function of the ρ_{gen} (right) for the full (blue line) and loose (orange line) kinematic reconstructions and the regression NN (red line) methods. the number of events per bin in the left plot is shown by the color scale. Figure taken from [90].

	No reconstructed ρ		Reconstructed ρ			
			$0 < \rho < 0.3$	$0.3 < \rho < 0.45$	$0.45 < \rho < 0.7$	$0.7 < \rho < 1$
	$N_{jet} = 1$	$N_{jet} = 2$	$N_{jet} > 2$			
$N_{b\ jet} = 1$	$p_T^{leading\ jet}$	$p_T^{subleading\ jet}$	R_{NN}	R_{NN}	R_{NN}	R_{NN}
$N_{b\ jet} > 1$		m_{lb}	R_{NN}	R_{NN}	R_{NN}	R_{NN}

Table 7.2: Event categories and distributions used in the maximum likelihood fit.

By maximizing the acceptance of signal events, also a significant number of background events are included in the final event selection. Differences in kinematics between signal and background events are used to group events with similar properties into different categories as shown in Table 7.2. The categorization relies on factors such as final-state object multiplicity (e.g., reconstructed leptons of specific flavors), number of produced jets, or the presence of b-tagged jets.

Events are separated into three categories based on the type of lepton pairs: e^-e^+, $e^\pm\mu^\mp$

and $\mu^-\mu^+$. This separation helps to constrain mostly orthogonal uncertainties in the reconstruction and identification of muons and electrons. It also helps in separating the Z+jets background, which affects same-flavor lepton channels differently than mixed-flavor channels.

Categorization in the number of b-tagged jets allows for better distinction between the single top quark (tW) process and $t\bar{t}$ decays. The first process is considered background and its final state typically contains one b-tagged jet, while the latter is characterized by exactly two b jets. Additionally, by categorizing events based on jet multiplicity, the signal ($t\bar{t}$+jet) can be distinguished from the main background ($t\bar{t}$+0 jet).

The final state for $t\bar{t}$+jet process contains at least three reconstructed jets and at least one b-tagged jet. For these events, the ρ observable is reconstructed using the NN regression. The output of this regression, known as relative signal response (R_{NN}) is fitted in the unfolding procedure. This signal is subdivided into four categories based on the ρ_{reco} bin, which are also divided into two further categories with different number of b tagged jets. This separation enhances the sensitivity of the $t\bar{t}$+jet by creating regions with different signal purity.

Events with less than three jets are considered background and therefore labeled as "No reconstructed ρ" category. This category contains the various background contributions and minimizes their extrapolation into the signal region. For the categories with only one b-tagged jet, the transverse momenta (p_T) of the leading jet and subleading jet for N_{jet}=1 and N_{jet}=2, respectively, are fitted to constrain the JES uncertainties. The event categories alongside the chosen observables are shown in Table 7.2. Relatively large bins are used to allow a maximum of 0.5 % of statistical uncertainty for shapes distribution in the simulated events. If the statistical uncertainty is higher, the observables in Table 7.2 are reduced to the total event yield. Further criteria for the choice of binning are purity and stability. Purity refers to the proportion of signal events that are both generated and reconstructed within a particular bin, divided by the total number of signal events generated in that bin. Stability assesses the proportion of signal events that are both generated and reconstructed in the same bin, divided by the total number of signal events reconstructed in that bin:

$$\text{purity} = \frac{N_i^{reco\&gen}}{N_i^{gen}}, \quad \text{stability} = \frac{N_i^{reco\&gen}}{N_i^{reco}}. \tag{7.4}$$

In the absence of bin-to-bin migrations and no background, both purity and stability would be unity. The chosen binning implies four bins both at parton and reconstruction level. In Figure 7.12, the corresponding values of purity and stability per bin are shown. Purities in the last bin are about 50%, which is attributed to the limited jet energy resolution since the ρ_{reco} category contains three reconstructed jets, and the reconstructed p_T^{miss}.

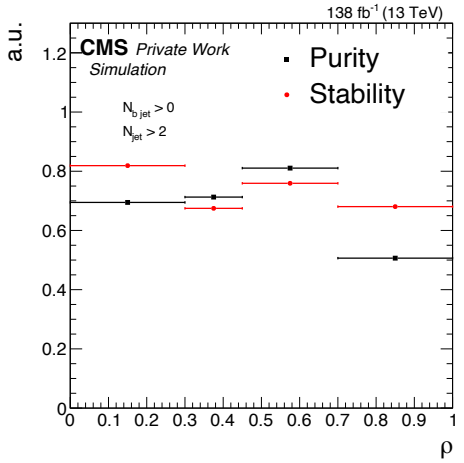

Figure 7.12: The purity and stability determined from the nominal samples, incorporating the statistical uncertainty for the number of simulated events, are shown.

The reconstructed ρ distribution with the chosen binning for the different years and lepton channels is shown in Figure 7.13. Good agreement between data and simulation is observed. The final input distributions for the fit per data taking period, categorized by events, are presented in Figures 7.14 and 7.15. Here, the data distributions are overlapped with simulated signal and pre-fit background distributions.

7.6 Unfolding and cross section measurement

The top quark pole mass is usually extracted from the measured differential cross section by comparing the unfolded parton-level cross section with fixed order theory predictions. In order to perform this comparison, an unfolding procedure has to be applied to remove experimental effects from the measured detector-level distributions. The statistical method used in this measurement to solve the unfolding problem is a profile maximum likelihood fit. This strategy has been previously used in other measurements [44, 90]. In general, unfolding aims to reconstruct a true distribution corrected for experimental distortions like resolution effects, misreconstruction, inefficiencies, and detector acceptance. This process involves using a response matrix R, which links the generator-level distribution to the detector-level distribution. The problem is often approached as a maximum likelihood estimation. In the unfolding procedure, the response matrix R is typically constructed using information obtained from MC simulations. It can be defined for a distribution as:

$$R_{ij} = \frac{N_j^{rec}}{N_i^{gen}} \tag{7.5}$$

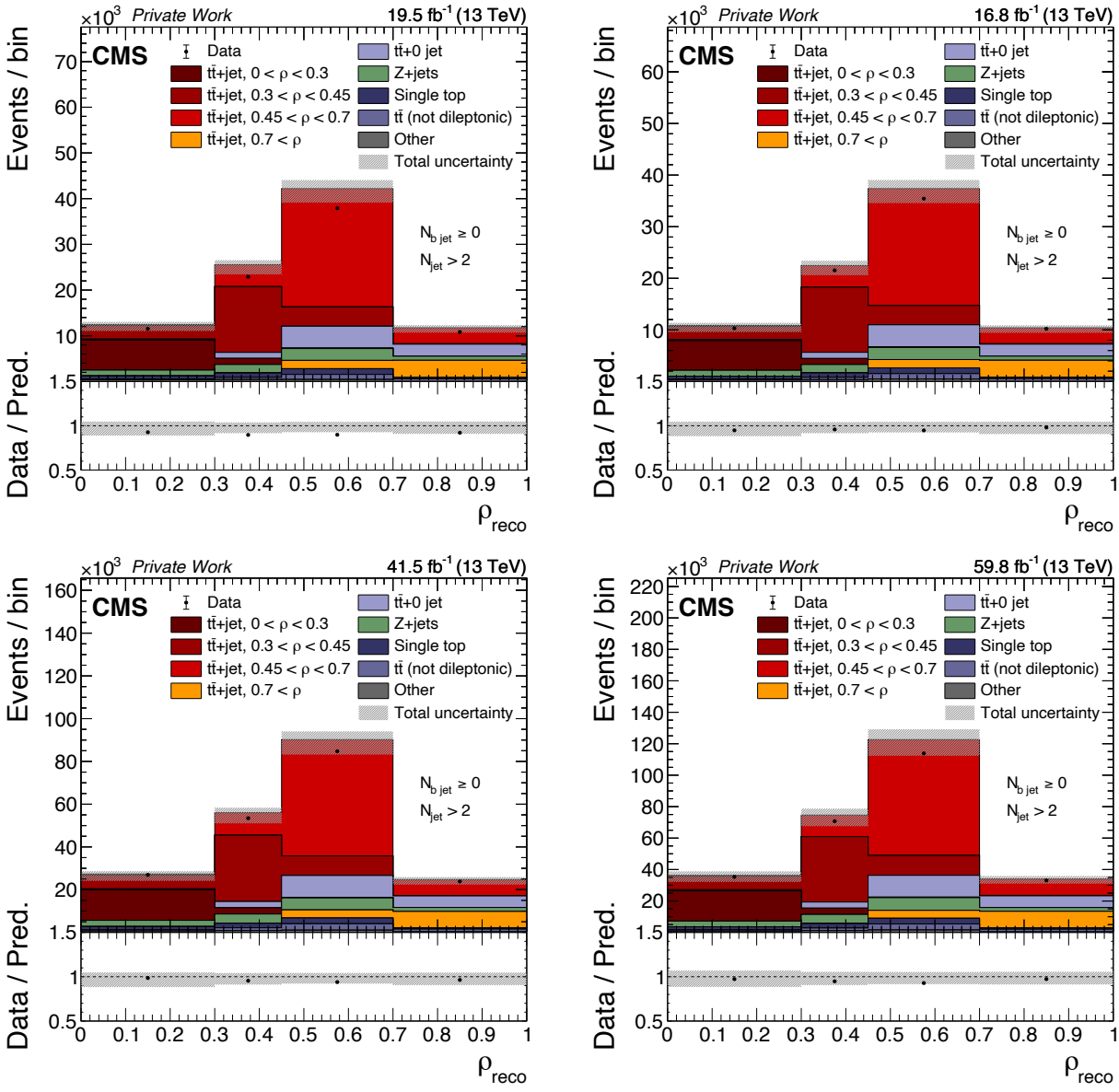

Figure 7.13: The observed (points) and predicted (stacked histograms) signal and background yields are depicted as a function of ρ_{reco} for the four different periods from upper left to lower right: 2016 preVFP, 2016 postVFP, 2017 and 2018. The vertical bars on the points denote the statistical uncertainty in the data, while the hatched band represents the total uncertainty in the sum of the simulated signal and background predictions. The lower panels display the ratio of the data to the sum of the signal and background predictions.

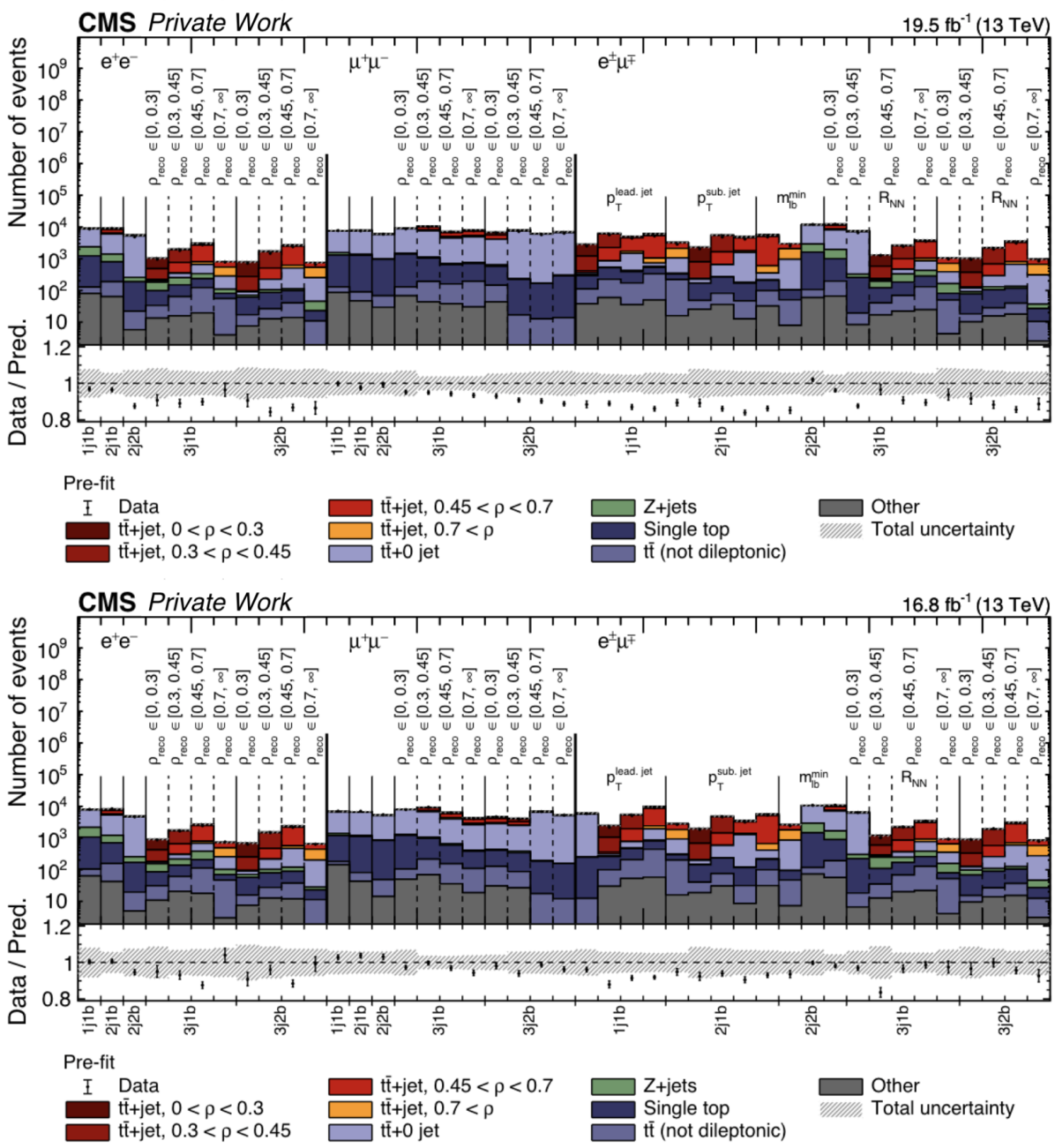

Figure 7.14: The pre-fit distributions from data (points) and simulated signal and background (colored histograms) utilized in the maximum likelihood fits are illustrated for 2016post and 2016pre. These distributions are displayed for each dilepton type and event category, where the x-axis label indicates events with m jets and n b jets. The vertical bars on the points indicate the statistical uncertainty in the data, while the hatched band represents the total uncertainty in the sum of the simulated signal and background predictions. The lower panel presents the ratio of the data to the sum of the simulated predictions.

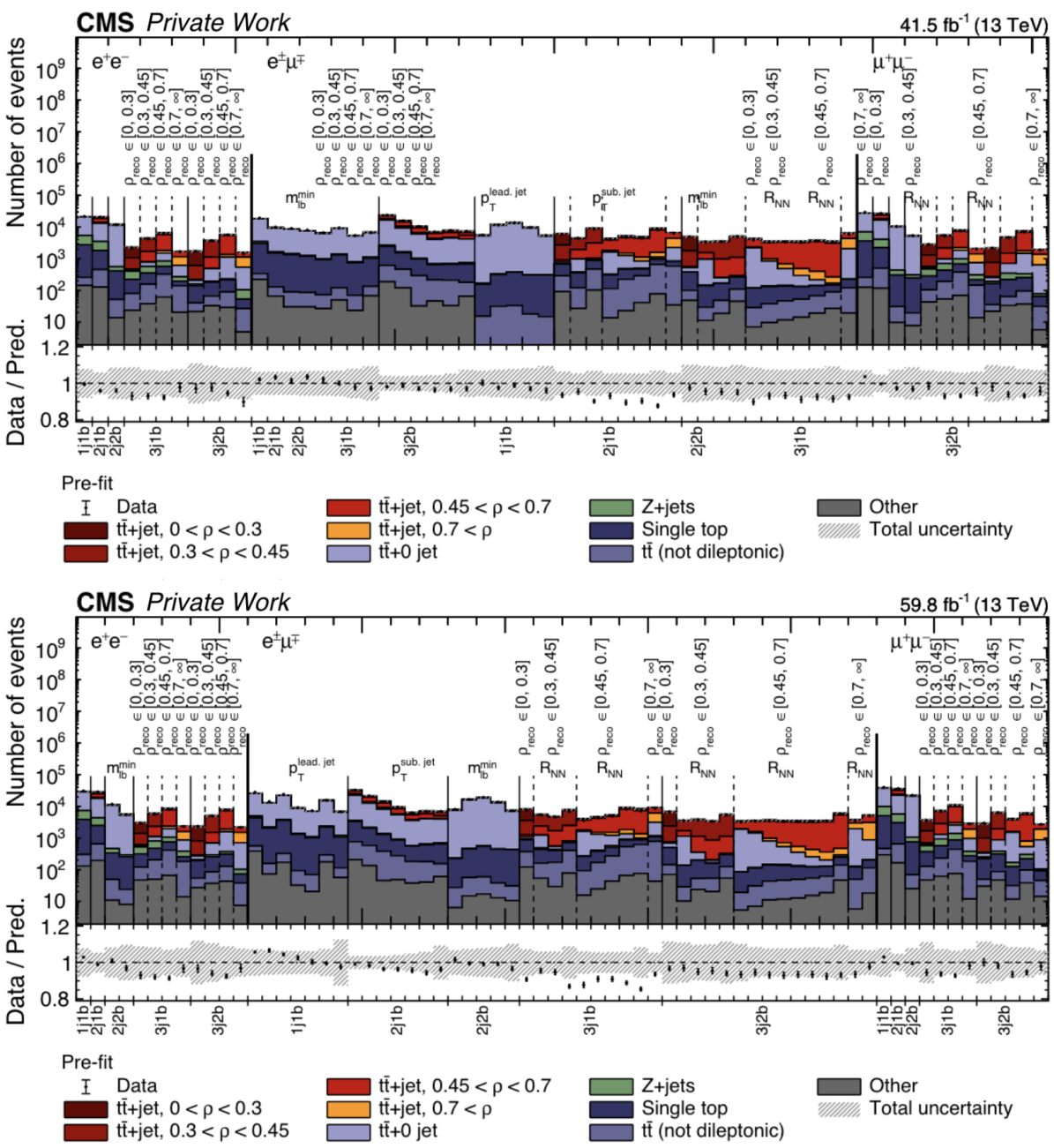

Figure 7.15: The pre-fit distributions from data (points) and simulated signal and background (colored histograms) utilized in the maximum likelihood fits are illustrated for 2017 and 2018. These distributions are displayed for each dilepton type and event category, where the x-axis label indicates events with m jets and n b jets. The vertical bars on the points indicate the statistical uncertainty in the data, while the hatched band represents the total uncertainty in the sum of the simulated signal and background predictions. The lower panel presents the ratio of the data to the sum of the simulated predictions.

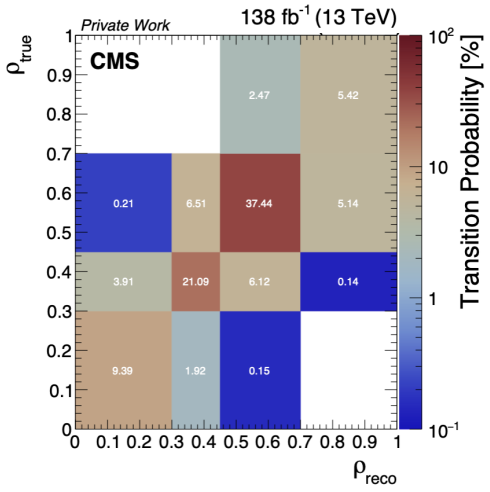

Figure 7.16: The response matrix displays the transition probability and bin-to-bin migrations as determined from the MC simulation.

where N_i^{gen} is the number of events generated in bin i and N_j^{rec} the events reconstructed in bin j [194]. The diagonal elements indicate the probabilities for events to be reconstructed in the correct bins in the detector-level spectrum. The relation between the true distribution, $\vec{y}$, and the reconstructed distribution, $\vec{x}$, can be written as $\vec{x} = R \cdot \vec{y} + b$, where b is the number of background events in the reconstructed spectrum. The true distribution, $\vec{y}$, is inferred from the reconstructed distribution, $\vec{x}$. This process involves the inversion of the response matrix.

A diagonal response matrix for the chosen signal events is desirable to address migrations concerning the parton level spectrum. The response matrix in the present analysis is shown in Figure 7.16. The *condition number* serves as a measure of numerical stability of the response matrix [195]. In this analysis, it is found to be 8 which makes it suitable for applying the unregularized maximum likelihood unfolding [196].

The signal strength μ is defined as the ratio between the observed cross section of the process and the one corresponding to the normalization of the MC prediction:

$$\mu_k = \frac{\sigma_k^{t\bar{t}+1jet}}{\sigma_k^{t\bar{t}+1jet}(MC)} \quad . \tag{7.6}$$

This ratio is extracted from the maximum likelihood fit, where k denotes the different bins in the ρ observable. A statistical model is constructed, assuming that the observed number of events in each bin is described by a Poisson distribution in the absence of systematic uncertainties.

Systematic uncertainties represent sources of error or bias in experimental measurements. Unlike statistical uncertainties, which arise from random fluctuations, systematic uncertainties affect the entire dataset, leading to biases or shifts in the observed values. Systematic uncertainties are often modeled by the inclusion of additional nuisance parameters in the fit which modulate their effects. Each nuisance parameter represents a specific source of uncertainty in the analysis. The expected number of events or event yield in a bin i can be described as:

$$\nu_i = \sum_k s_i^k(\sigma_k^{t\bar{t}+jet}, m_t^{MC}, \vec{\lambda}) + \sum_j b_i^j(w_j, \vec{\lambda}, m_t^{MC}), \tag{7.7}$$

where s_i^k is the expected number of signal events in the bin k for a reconstructed ρ value in bin i. It depends on the cross section, σ_k, the top quark mass used in the simulation (m_t^{MC}) and on the nuisance parameters, λ. The number of expected background process events defined as b_j, where j denotes the background source, depends on its normalization, w, and on the nuisance parameters $\vec{\lambda}$. In the case of $t\bar{t}$ and tW processes, b_j also depends on m_t^{MC}.

Uncertainty sources can be categorized into normalization and shape contributions. Normalization uncertainties affect the expected counts of a given process across all bins equally, leading to a uniform scaling of the observed distribution. In contrast, shape uncertainties result in variations that are not uniform across the different bins used by the fit. The expected modification to bin content in the final binning that is used by the profile likelihood fit is called the *template* associated to a given uncertainty.

The inclusion of systematic uncertainties in the likelihood function is done via multiplicative probability density functions for each source of uncertainty. These probability density functions, also called penalty terms, ensure that the nuisance parameters stay within a reasonable range around their estimated values, taking into account the uncertainty on each. For normalization uncertainties, the expected bin count is assumed to vary following a log normal distribution across all bins.

Modifications of the distribution due to particular shape uncertainties in the distribution can be modeled by altering parameters in the MC simulations that are used to generate the uncertainty templates. For each nuisance parameter, uncertainty templates are generated for up and down variations, which are used to estimate the effect of varying the underlying nuisance parameter by one standard deviation in either direction from the nominal estimate. These discrete variations are turned into a continuous estimate in each bin as a function of the nuisance parameter. This technique, known as morphing, combines the different templates to construct a single, continuous model for expected bin content that smoothly varies with the nuisance parameter [197]. The underlying nuisance parameter is taken to follow a normalized Gaussian probability density function.

The likelihood function is a product of probability density functions. The first term is a Poisson distribution that corresponds to the event count in each bin. The following density functions correspond to the distributions that nuisance parameters are assumed to follow. The likelihood function is defined as:

$$L = \prod_i \frac{e^{-\nu_i}\nu_i^{n_i}}{n_i!} \prod_m \pi_m(\lambda_m) \prod_j \pi_j(w_j), \tag{7.8}$$

where n_i is the observed number of events, and $\pi_j(w_j)$ and $\pi_m(\lambda_m)$ are the probability density functions for the normalization and shape nuisance parameters respectively.

The minimum invariant mass (m_{lb}^{min}) of the lepton and the b tagged jet used in events with 2 jets and more than one b tagged jet, increases the sensitivity to the top quark mass parameter in the MC, m_t^{MC}. To mitigate the correlation between the fitted signal strength, μ_k, and the value of m_t^{MC}, the latter is introduced as an additional free parameter in the fit. Two MC samples are used, one obtained with m_t^{MC}= 169.5 GeV and another one with m_t^{MC}= 175.5 GeV. The resulting differential cross section is independent of m_t^{MC} and can be compared directly to fixed-order predictions.

The parameters of interest (POI) are determined simultaneously by a single fit. The MC cross sections in Eq. (7.6) are derived from the nominal NLO POWHEG+PYTHIA 8 MC simulation and the nuisance parameters are constrained simultaneously with the cross section values in each kinematic bin. The values of the POIs that maximize the likelihood function are determined by minimizing $-\ln L$ using the CMS statistics software package called "Combine" [198], based on the RooStats package [199].

7.7 Systematic uncertainties

The analysis considers uncertainties arising from both signal and background modeling, as well as experimental inefficiencies. Some uncertainties only affect the normalization of the MC distributions, and are assessed by scaling the entire contributions up and down. These are referred to as normalization or rate uncertainties. Others impact both the shape and normalization of the distribution, known as shape uncertainties. In such cases, alternative MC templates are constructed with varied shapes to quantify the uncertainty in each background source or signal contribution.

The detector conditions have changed during the data-taking periods used, caused by detector upgrades, necessary maintenance during the technical stop and variations in operating conditions such as temperature or magnet cycles. Therefore certain corrections have to be derived separately for each data taking period, so that related uncertainties are treated as uncorrelated. Theoretical uncertainties, on the other hand, are mostly treated as fully correlated.

Sources of Experimental Uncertainty

The experimental systematic uncertainties are estimated by varying the SFs or applying weights, used to correct discrepancies between data and simulation. The following experimental uncertainties are taken into account.

Luminosity

The measured value of the luminosity has inherent uncertainties arising from detector effects on the luminometer and beam conditions. To address these uncertainties, a partial correlation scheme is implemented as described in [200]. This approach accounts for both correlated and uncorrelated sources of uncertainty.

Pileup

As mentioned in section 7.3, to determine the uncertainty related to the pileup reweighting, two nuisance parameters, related to n_{Vtx} and ρ_{det}, are introduced. These uncertainties are based on weights derived comparing simulation with data. Each uncertainty is treated as correlated among the data-taking periods.

Trigger efficiency

The trigger SFs discussed in Section 7.3 have associated uncertainties. The latter include systematic (PU modeling and number of jets) and statistical (limited size of samples used to derive the SF) contributions. The SF uncertainties are treated as uncorrelated among the data-taking periods and among the lepton channels.

Lepton identification

For the selection, the leptons must fulfil certain reconstruction, identification and isolation criteria. Each of these has a corresponding scale factor (SF) with associated uncertainty. The efficiencies for electron and muon selection are determined using the "tag-and-probe" method [201]. Corresponding SFs are found to be consistent with unity within 10% for electrons and 3% for muons. The uncertainties associated with these SFs typically range from 2% to 5% for electrons and 0.5% to 1.5% for muons [108, 118]. These uncertainties are individually varied within their respective ranges in the simulation for each lepton flavor and type of uncertainty.

Lepton energy scale and resolution

Uncertainties arising from correcting the electron and muon energy scales and resolutions are assessed independently by varying them in the simulation. Typically, the uncertainty in the energy resolution is around 0.5% for electrons and between 1-3% for muons [108, 118]. These variations in energy are accounted for in the calculation of the missing transverse momentum (p_T^{miss}).

Jet energy scale

To address uncertainties related to the jet energy scale (JES), the momenta of jets in simulated samples are rescaled as a function of their p_T and y. The JES uncertainties represent 23 sources detailed in [202], those related to the kinematic regions are not included in this analysis. Similar to the lepton energy scale, the changes of the jet momenta are also propagated to p_T^{miss}. These uncertainties are considered as being partially correlated across the data taking periods.

Jet energy resolution

The uncertainty in the Jet Energy Resolution (JER) is evaluated in the same way as the JES, but varying the width of the jet momenta distribution instead of its mean, using simulated samples across two distinct pseudorapidity regions: the central region ($|\eta| < 1.3$) and the forward region ($|\eta| > 1.3$). This variation results in an effect on the resolution ranging from 2% to 6%, depending on the specific η region [202]. These uncertainties are treated as uncorrelated across the data taking periods.

Uncertainties in b tagging

To address differences in b-tagging efficiencies and mistagging rates between data and simulation, SFs are determined to align the b-tagging performance in simulation with that observed in data. For heavy flavor (b and c) jets, the uncertainties are treated as fully correlated between data taking periods, while those for light-quark and gluon jets are considered uncorrelated with b jets. The uncertainty for mistagging light-quark jets typically ranges from 5% to 10%, while for tagging heavy-quark jets it ranges from 1% to 5% [123]. These uncertainties are further divided into four subsources, accounting for effects related to pileup, JES, number of selected events, and factors arising from the SF derivation method and modeling.

Unclustered missing transverse momentum

Unclustered missing transverse momentum refers to the energy deposits in the detector that are not associated to well-reconstructed and identified objects such as jets, electrons, muons, or photons. This unclustered energy can originate from low-energy particles that are not part of reconstructed jets, detector noise and other spurious signals. A separate energy scale uncertainty assigned to this unclustered energy is propagated to p_T^{miss} as the momenta of jets, muons and electrons. The unclustered missing transverse momentum uncertainties are treated as uncorrelated among the data-taking periods.

L1 Prefiring

During 2016 and 2017, a gradual timing shift in the ECAL was not accurately accounted for in the Level 1 trigger primitives. This led to a notable portion of high η trigger primitives being incorrectly associated with the previous bunch crossing. As Level 1 trigger rules prohibit two consecutive bunch crossings from firing, an unintended consequence of this issue was the potential for events to self-veto if a significant amount of ECAL energy was detected in the region of $2 < |\eta| < 3$. This effect, referred to as *prefiring*, is dependent on both η and p_T [203].

A similar issue is observed in the muon system, where the bunch crossing assignment of muon candidates may be incorrect due to the limited time resolution of the muon detectors. While this effect was most prominent in 2016, it persists with smaller contribution in both 2017 and 2018 [204].

Theoretical Uncertainties

The evaluation of theoretical assumptions in the modeling involves implementing suitable variations of the model parameters in the nominal POWHEG+PYTHIA 8 simulation, or by varying the nominal simulations with event weights. This can be accomplished by using dedicated simulated samples with adjusted parameters or by applying weights to modify the reference simulation. The total cross section per individual process contribution, whether it be background or signal, is kept constant at the nominal value before event selection when implementing these variations, to avoid double-counting effects. This ensures consistency in the overall normalization across different simulations and variations. All considered theoretical sources of uncertainty are outlined below.

Matrix element μ_R and μ_F scales

The uncertainty contributions due to missing higher order corrections are evaluated by examining variations in μ_r and μ_f in the matrix element calculations. These scales are varied up and down independently by a factor of 2. Similarly, for Z+jets and single top processes, scale variations are performed, with each scale varied individually by a factor of two up and down of its nominal value.

Variation of the Parton Shower scales

Uncertainties in the modeling of the PS are assessed by varying the corresponding scales for initial-state radiation (ISR) and final-state radiation (FSR), individually. They are varied by a factor of two up and down of their nominal values. The uncertainties in FSR and ISR are considered to be independent for $t\bar{t}$, single top, and DY processes.

Parton Distribution Functions

The influence of the uncertainties in the parton distribution function (PDF) set on the signal acceptance is assessed by reweighting the $t\bar{t}$ signal sample by using the 100 uncertainty eigenvectors of the NNPDF3.1 PDF set [184], used in the MC simulation, including the uncertainties associated with variations of $\alpha_s(mZ)$. Each eigenvector is treated as an individual nuisance parameter in the fit.

Matrix element and Parton shower matching

The h_{damp} parameter controls the matrix element and parton shower matching in POWHEG+PYTHIA 8. The nominal value used for this parameter is determined in a dedicated tuning procedure and is set to $1.379^{+0.926}_{-0.5052}$ [70]. Dedicated MC samples are generated with higher and lower values of h_{damp}, to estimate the related uncertainty.

Underlying event tune

The UE refers to the components of a collision event that are not directly associated with the primary hard scatter interaction. The uncertainty arising from the choice of the UE tune CP5 [70] is evaluated with dedicated POWHEG+PYTHIA 8 simulations for $t\bar{t}$ and single top processes. In these simulations, the tuned parameters of the UE tune CP5 are varied up and down according to uncertainties determined in the tuning process.

b quark fragmentation

In the nominal CP5 tune of Pythia 8 used for $t\bar{t}$ and single top simulations, the fragmentation of a b quark into b-flavored hadrons is modeled by the Bowler–Lund function, with the parameter r_b set to 1.056 [205]. To assess the corresponding uncertainty, the relevant transfer function is varied up and down and applied as event weight.

Alternatively, the Peterson fragmentation function can be used with its default parameter. The fragmentation function in the nominal $t\bar{t}$ and single top simulations is adjusted accordingly through reweighting. These uncertainties are treated as fully correlated between the data-taking periods.

b semi-leptonic branching ratio

The branching ratio of semi-leptonic b decays influences the response of b-jets. To accurately capture its impact, this quantity is varied within its measured uncertainty [17]. It is treated as fully correlated among the data-taking periods.

Top quark p_T reweighting

In analyses of Run 1 data, it was observed that the top quark p_T spectra in data is softer than predicted by the NLO MC generators. While the central MC prediction was not altered, an additional uncertainty [193] was introduced to cover this difference, derived from the ratio of data to NLO MC prediction.

Color reconnection

Color reconnection (CR) refers to the phenomenon where the color charge of partons can rearrange before hadronization, affecting the final state. The CR uncertainties arise in the modeling of hadronization. In the default CR model as implemented in Pythia 8 and used in the reference $t\bar{t}$ and single top simulation, early resonance decays (ERD) are switched off. To assess the impact of ERD, dedicated additional samples with ERD enabled are generated, and the difference relative to the nominal setup is considered as a systematic uncertainty.

Additionally, two more CR schemes are taken into account: a gluon-move scheme [206] and a QCD-inspired scheme [207]. For each scheme, dedicated samples are generated, and the systematic uncertainty is estimated likewise by comparing the results to those obtained with the nominal setup.

Top quark mass parameter in the MC

To eliminate the correlation between the fitted signal strength parameters and the top quark mass used in the Monte Carlo simulation (m_t^{MC}), the latter is introduced as a free-floating parameter in the fit. The central value for m_t^{MC} is set to 172.5 GeV with a prior uncertainty of ± 1 GeV. Templates based on simulated samples with masses of 169.5 GeV and 175.5 GeV are used. These templates are rescaled using a factor of 1/3 while reducing noise from statistical fluctuations affecting dedicated samples with smaller m_t^{MC} variations.

Background cross sections

The uncertainties in the background normalization for the analysis arise from several sources. For the inclusive $t\bar{t}$ production in the semileptonic and hadronic decay channels, the total uncertainty includes contributions from two primary sources: the scale uncertainty, assumed to be in the range of $+2.5\%$ to -3.6%, and the combined uncertainties from the PDFs and α_s, which are assumed to be $+0.47\%$ to -0.46%. These are combined quadratically to determine the overall uncertainty.

For single top quark production and smaller background contributions, such as diboson and W+jets production, a conservative uncertainty of 30% is applied and modeled with a log-normal prior probability density function, following methodologies established in previous analyses. In the case of Z+jets background, separate uncertainties are assigned to each b-jet multiplicity category to reduce reliance on the leading-order Z+jets simulation predictions. Additionally, uncertainties of 5%, 10%, 30%, and 50% are assigned for events with 0, 1, 2, and 3 or more jets, respectively. These values are derived using scale variations from next-to-leading-order W+jets predictions for lower jet counts, while the higher multiplicities are treated conservatively [88].

For the $t\bar{t} + 0$ jet background, no prior probability density function is used. Instead, its normalization is left as a free parameter in the fit to allow for constraint from the background-dominated categories. This approach ensures a consistent treatment of uncertainties across all background contributions while allowing the fit to adjust as needed for specific data-taking categories.

MC statistical uncertainty

The statistical uncertainty arising from the limited number of simulated events is addressed by using the Beeston-Barlow method [208]. This method involves assigning a single nuisance parameter to each bin of the fitted distribution, which encapsulates the

overall statistical uncertainty on the predicted number of events for all processes. These nuisance parameters are constructed based on either a Poisson or Gaussian probability distribution, depending on the number of events in the bin.

Uncertainty	Type	Year	Correlation
Luminosity	rate	all	partial
Pileup	shape	all	total
Muon identification	shape+rate	all	partial
Muon energy scale and resolution	shape+rate	all	partial
Electron identification	shape	all	total
Electron energy scale and resolution	shape	all	total
Jet energy scale	shape+rate	all	partial
Jet energy resolution	shape+rate	all	no
p_T^{miss}	shape+rate	all	no
b jet identification	shape+rate	all	partial
Trigger efficiency	shape+rate	all	no
L1 Prefiring	shape+rate	2016 and 2017	total
b quark fragmentation	shape	all	total
b semileptonic BR	shape	all	total
μ_R and μ_F	shape	all	total
FSR and ISR	shape	all	total
PDFs	shape+rate	all	total
UE CPS	shape	all	total
ME and PS matching	shape	all	total
p_T reweighting	shape	all	total
CR	shape	all	total
Background normalization	rate	all	total

Table 7.3: Sources of systematic uncertainties considered in the analysis. The type of uncertainty is described as being a constant normalization factor (rate) or variations that modify both the normalization and the shape of the distribution (shape+rate). Partial correlations are described in the text.

Extrapolation uncertainties

Extrapolation uncertainties are introduced to account for the impact of modeling uncertainties, specifically focusing on how these uncertainties affect the signal acceptance. These uncertainties are evaluated by adjusting model parameters (Nuisance Parameters) and assessing the resulting variations in the signal. In this process, post-fit constraints

on these uncertainties, based on events reconstructed in the visible phase space, are not considered. The procedure involves varying a single Nuisance Parameter by one standard deviation up and down while keeping the others fixed. The variations in the signal cross-section due to these changes are then used to define the additional extrapolation uncertainties.

In Table 7.3, the aforementioned uncertainty sources and how these are correlated across the data-taking periods are summarized.

7.8 Results

The cross section of $t\bar{t}$+jet production is measured differentially as function of ρ through the maximum likelihood fit to the MC signal and background predictions. The post-fit distributions are illustrated in Figures 7.17 and 7.18 for different data-taking periods. A very good agreement between the data and the MC predictions is observed for all years.

Figure 7.19 illustrates the ratio between the results obtained by using 2016preVFP, 2016postVFP, 2017, and 2018 datasets, separately, where the ratios for each POI are shown, evaluated across different categories corresponding to distinct bins of ρ. These categories are defined as follows: *rate_ttj0* ($0 < \rho < 0.3$); *rate_ttj1* ($0.3 < \rho < 0.45$); *rate_ttj2* (covers $0.45 < \rho < 0.7$); and *rate_ttj3* ($0.7 < \rho < 1$). Additionally, the overall background rate associated with the events that include no additional jets ($\mathrm{t\bar{t}}$ + 0 jet events) is marked by *rateTT0Jet*.

While the results obtained in 2017 and 2018 are consistent with each other, a tension with that of 2016 (in particular, 2016preVFP), is observed, which is attributed to the normalization issue. In particular, a notable incompatibility in the first bin (rate_ttj0) is observed between results obtained in 2017 and 2018, once compared to 2016. These incompatibilities have also been observed in other high precision measurements by the CMS experiment using the full Run 2 data. While the detailed investigation of the reasons is yet ongoing, there is no recommendation to exclude a particular data set from the analysis while extracting the cross sections, reported in the following.

Results on the cross section

The absolute differential cross section for $t\bar{t}$+jet production, $d\sigma_{t\bar{t}+jet}/d\rho$, is depicted in Figure 7.20 (left), compared with next-to-leading-order (NLO) QCD predictions. These predictions are computed using the $t\bar{t}$+jet process implemented in POWHEG-BOX [209], and the ABMP16NLO PDF set [210], assuming different values for m_t^{pole}=169.5, 172.5, and 175.5 GeV. Alternatively, the NLO prediction is obtained by using the CT18NLO

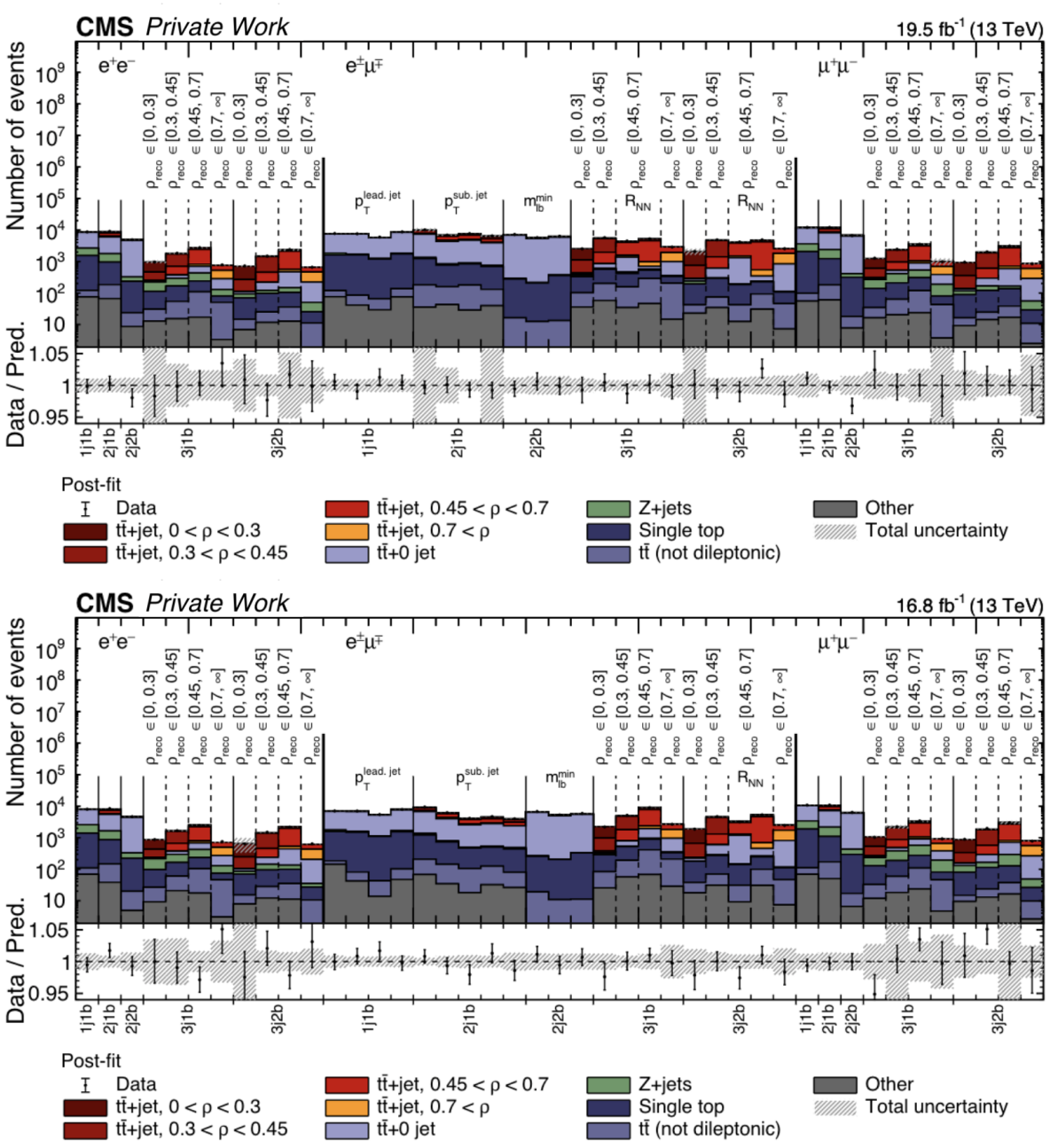

Figure 7.17: The post-fit distributions from data (points) and simulated signal and background (colored histograms) after the maximum likelihood fit are illustrated for 2016preVFP and 2016postVFPs. The number of observed and predicted events are presented in the same manner as Figure 7.14.

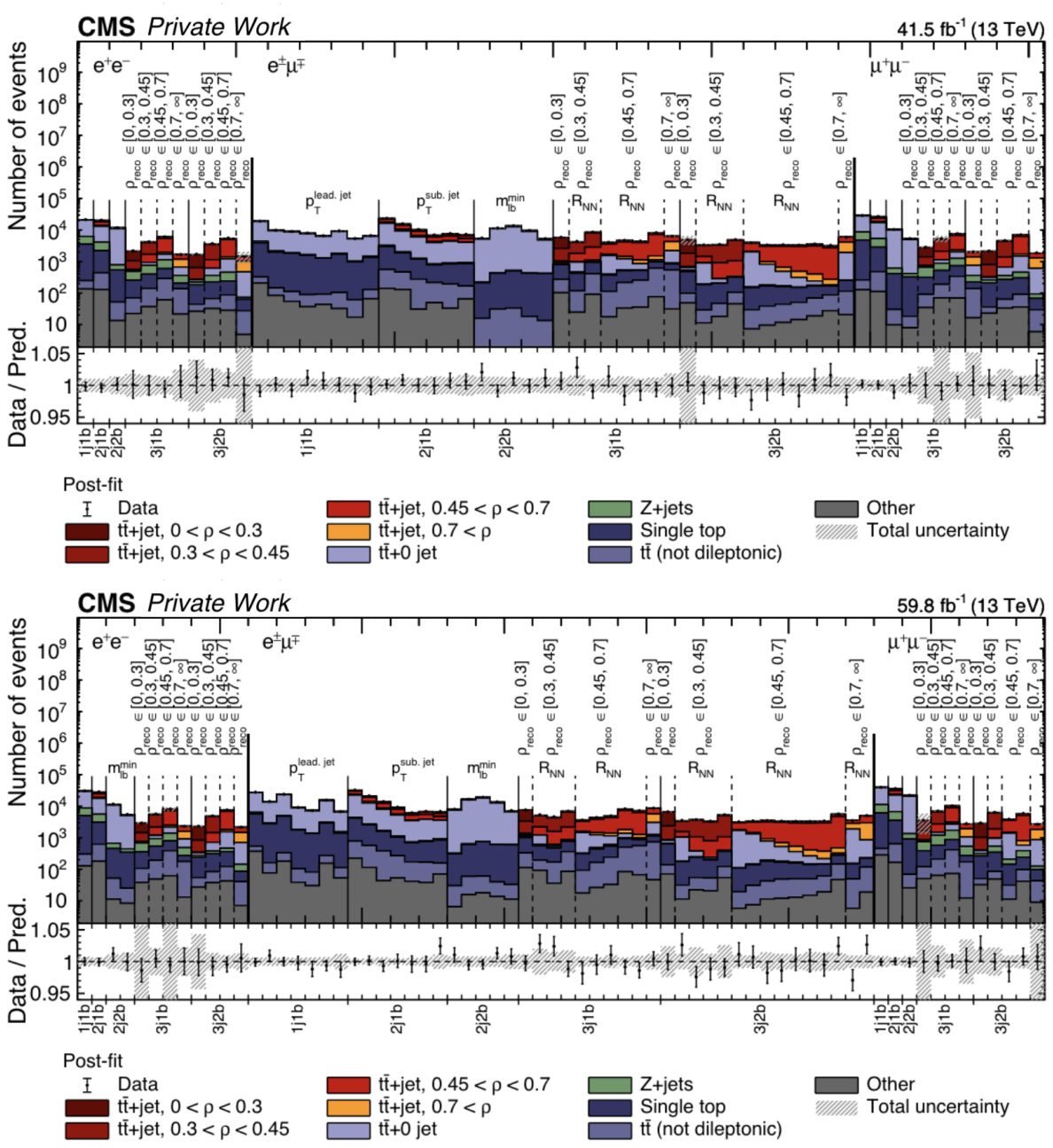

Figure 7.18: The post-fit distributions from data (points) and simulated signal and background (colored histograms) after the maximum likelihood fit are illustrated for 2017 and 2018. The number of observed and predicted events are presented in the same manner as Figure 7.14.

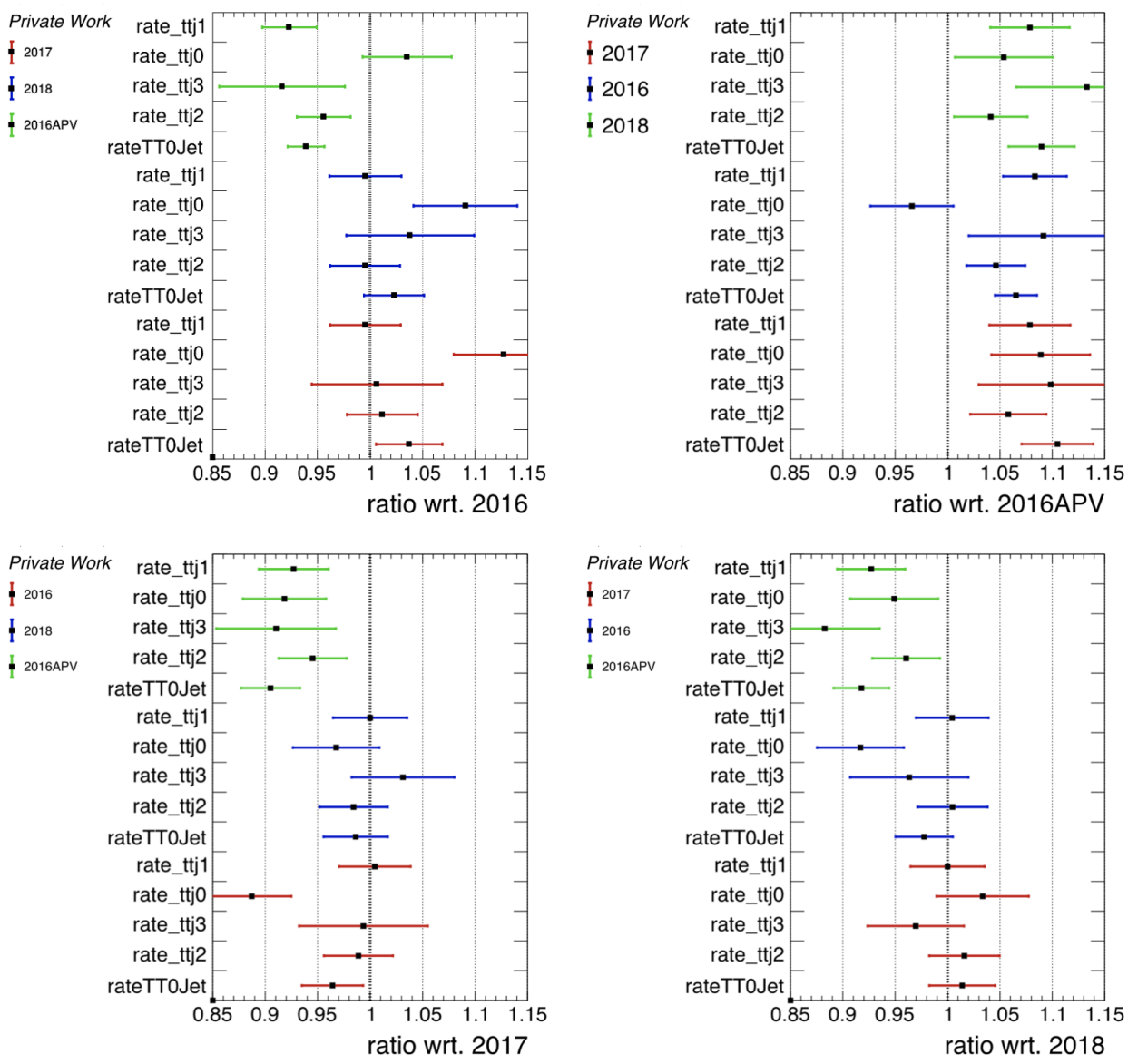

Figure 7.19: Ratio between the 4 different data taking periods with respect to each of them. Each plot displays the ratios for individual Parameters of Interest (POIs) evaluated across different ρ bins.

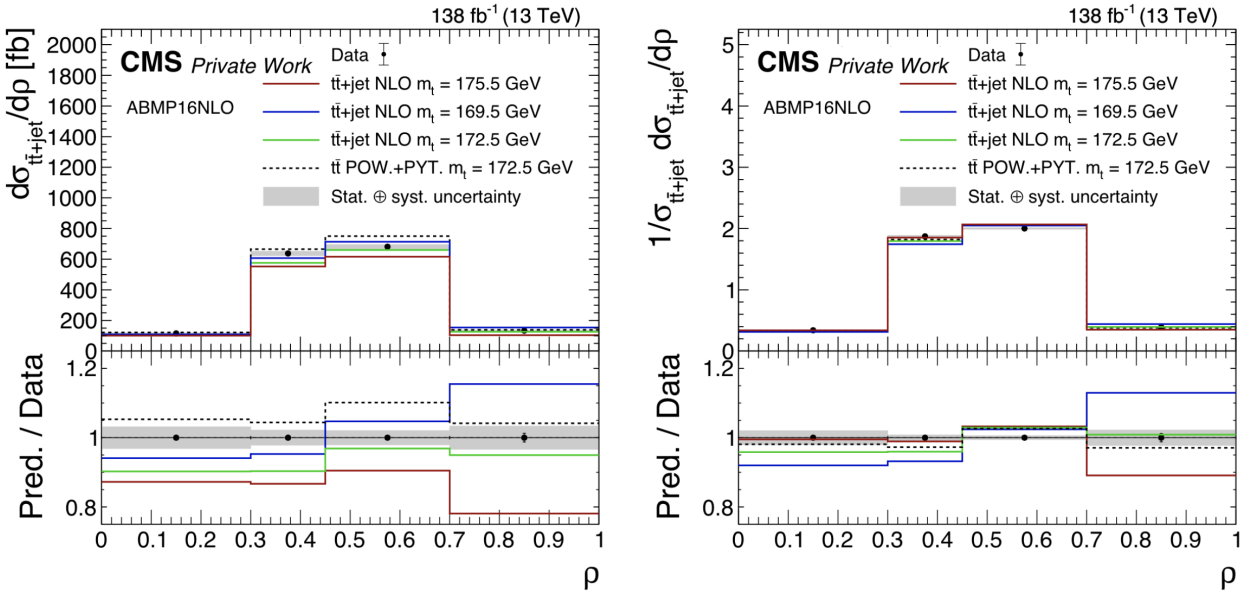

Figure 7.20: Absolute (left) and normalized (right) $t\bar{t}$+jet differential cross sections as a function of ρ for both the data (points) and theoretical predictions. The vertical bars on the data points represent the statistical uncertainty, while the shaded region indicates the total uncertainty in the measurement. The lower panels show the ratio of the theoretical predictions to the data.

PDF set [211]. The Dynamic QCD scale $H_T^B/2$ is chosen, with H_T^B defined as the scalar sum of the transverse masses of the top quark, antiquark, and p_T of the additional jet, as suggested in Refs. [212] and [94].

While the total uncertainty is the result of the fit, properly accounting for all the correlations, individual contributions of different uncertainties can be assessed for illustration. The Contribution of statistical uncertainties is calculated by fixing all systematic nuisance parameters to their post-fit values. The systematic uncertainty is derived by subtracting the statistical uncertainty quadratically from the total uncertainty. The contributions of relative uncertainties $\Delta\sigma_k^{t\bar{t}+jet}$ in the parton-level cross section $\sigma_k^{t\bar{t}+jet}$ are determined by performing the fit again, now fixing the nuisance parameters related to the source of interest to their post-fit values. Each partial uncertainty is calculated by subtracting the result from the total uncertainty obtained with this method. The quadratic sum of these individual contributions differs from the total uncertainty due to correlations between the nuisance parameters, which are considered during the fitting process but ignored when isolating individual sources.

Figure 7.21 presents the fitted parameter values, $\Delta\hat{r}_k$, expected and observed constraints, and the impact on the signal strength parameters r_k for the 30 most relevant nuisance

parameters in the fit. The nuisance parameter values $\hat{\theta}$ are compared to their pre-fit input values θ_0, normalized by their uncertainties $\Delta\theta$. The impact $\Delta\hat{r}_k$ for each nuisance parameter reflects the difference between the nominal best-fit value of r_k and the best-fit value when only that particular nuisance parameter is set to its fitted value $\hat{\theta}$, while all others remain free. Note, that no prior probability distribution function is assigned to the $\mathrm{t\bar{t}} + 0$ jet normalization and m_t^{MC}.

In the normalized cross section, the total uncertainty is significantly reduced due to cancellation of most of the normalization uncertainties. In the present analysis, the values and uncertainties of the normalized differential cross section are derived from the obtained absolute cross sections by utilizing the covariance matrices obtained in the fit. In particular, the normalized differential cross section for each bin is calculated by dividing the absolute differential cross section by the sum of all bin values. Prior to this normalization, the uncertainties are symmetrized using the HESSE method [213]. The uncertainties in the normalized cross sections are obtained through Gaussian error propagation as

$$\sigma_f^2 = \left|\frac{df}{dx}\right|^2 \sigma_x^2 + \left|\frac{df}{dy}\right|^2 \sigma_y^2 + 2\frac{df}{dx}\frac{df}{dy}\sigma_{xy} \ , \tag{7.9}$$

where $\sigma_{xy} = \sigma_x \sigma_y \rho_{xy}$ represents the covariance between x and y, and ρ_{xy} denotes their correlation. Here, x and y refer to the cross section in a particular bin and the total cross section, respectively. This approach is valid due to the sufficiently large number of events, which justifies the Gaussian approximation of the likelihood function. Correlation matrices for both statistical and total uncertainties are presented in Figure 7.22 for the absolute cross section and in Figure 7.23 for the normalized cross section.

Furthermore, the theoretical uncertainties are reduced, e.g. the α_S-dependence of the predicted normalized cross section is mitigated, as compared to the absolute cross section. Reduction of experimental and theoretical uncertainties is the advantage of the normalized cross section for further extraction of the top quark mass.

Extraction of the top quark mass

The value of the top quark pole mass m_t^{pole} is obtained through a χ^2 fit of the NLO theoretical predictions for the normalized differential cross section to that of data. In the NLO prediction, m_t^{pole} is varied between 168.5 and 176.5 GeV.

For correlated data, the general formula for the goodness-of-fit χ^2 is adjusted by including a covariance matrix V, which accounts for correlations between data points: $\chi^2 = \Delta^T V^{-1} \Delta$, where Δ represents the difference between the observed and expected values. A good fit is typically indicated when $\chi^2_{\mathrm{min}} \approx k$, and the uncertainty in the fit can

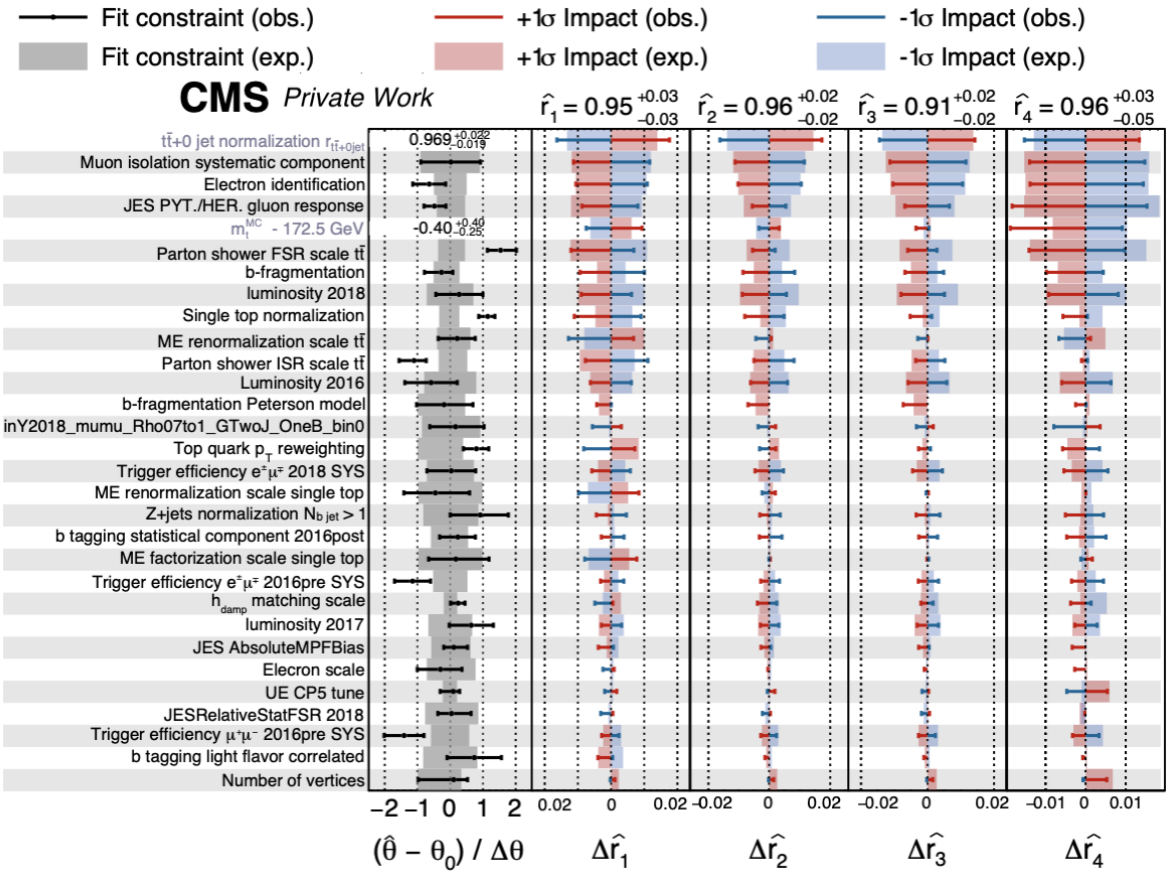

Figure 7.21: Fitted nuisance parameters and their impacts, $\Delta\hat{r}_k$, for the signal strengths $\hat{r}_k$, ordered by their relative summed impact, for the 30 most significant ones. The resulting fitted values of $\hat{r}_k$, along with their total uncertainties, are shown. Red (blue) lines present the variation in $\Delta\hat{r}_k$ when the nuisance parameter is shifted up (down) by its fitted uncertainty $\Delta\theta$. Gray, red, and blue shaded regions represent the expected values from fits to pseudo-data to illustrate the uncertainty associated with the impacts of the nuisance parameters. For nuisance parameters associated with $t\bar{t} + 0$ jet normalization and m_t^{MC}, the post-fit values are shown, as no prior probability distribution function is assigned to these parameters.

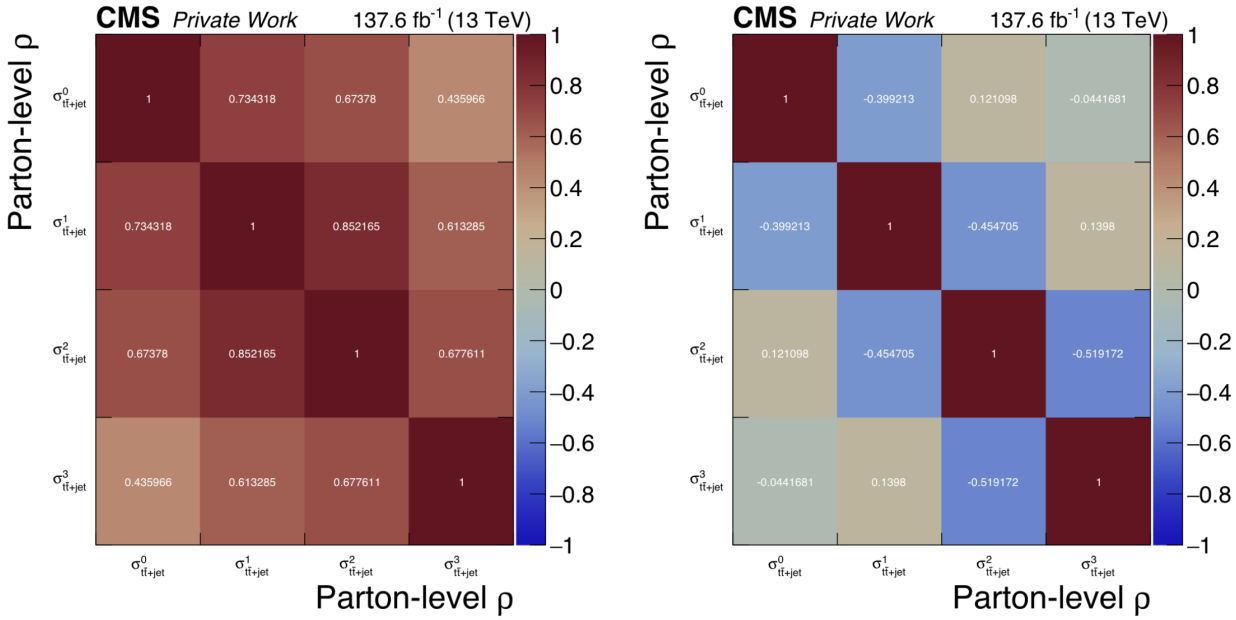

Figure 7.22: Correlation matrices for the total uncertainty (left) and statistical uncertainty (right) between the bins of the absolute differential cross section.

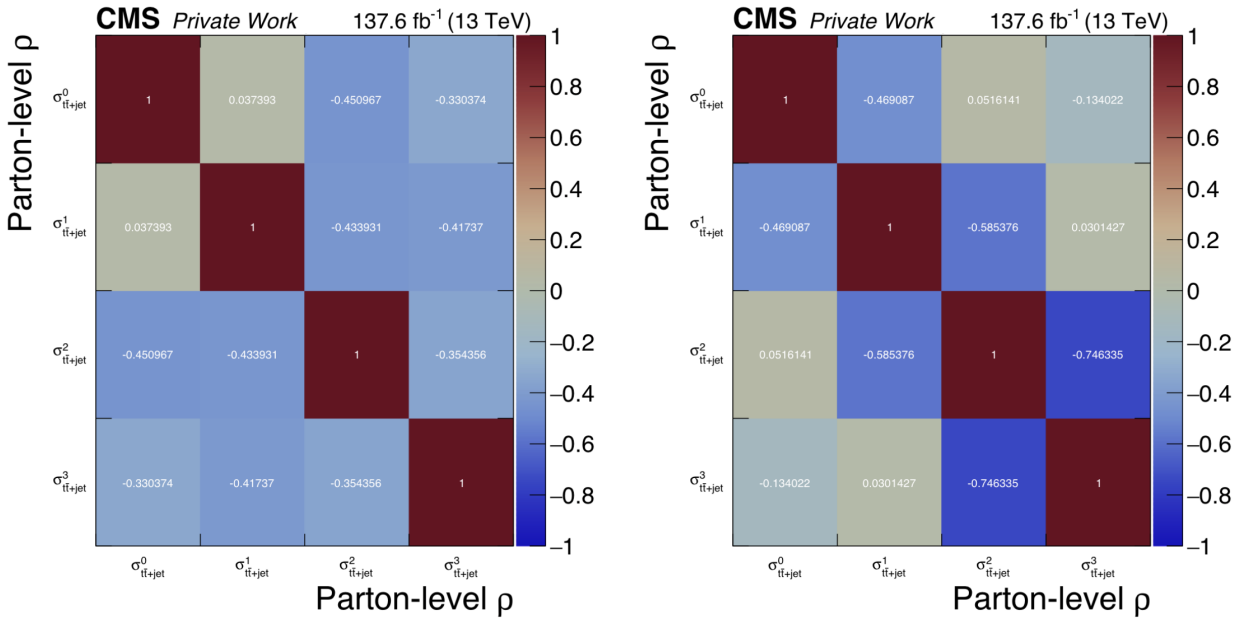

Figure 7.23: Correlation matrices for the total uncertainty (left) and statistical uncertainty (right) between the bins of the normalized differential cross section.

be estimated using the condition $\chi^2 = \chi^2_{\text{min}} + 1$ for a 68% confidence level in the case of a single parameter fit.

Since the normalized differential cross section introduces correlations between measurements across different bins, the first bin is excluded from the χ^2 fit. Note that the choice of the excluded bin does not affect the fit result.

In the fit, the PDF uncertainties in the NLO cross section are evaluated for each bin, taking into account the eigenvectors of the PDF set. These uncertainties are incorporated into the total covariance matrix V used in the χ^2 fit, assuming full correlation across all bins. For the CT18NLO PDF set, uncertainties are initially calculated at 90% confidence level (CL) and rescaled to 68% CL for consistency, and symmetrized by selecting the larger absolute value. Similarly, the extrapolation uncertainties are symmetrized by averaging the positive and negative variations, and these uncertainties are included in the total covariance matrix V, assuming full correlation between all bins.

The results of the fit using NLO predictions based on ABMP16NLO or CT18NLO PDFs are shown in Figure 7.24. The resulting values for m_t^{pole} correspond to the minimum of the χ^2 distributions. The total uncertainty in the fit is determined using the tolerance criterion $\Delta\chi^2 = 1$. To estimate the impact of missing higher-order corrections in the theoretical predictions, the χ^2 fits are repeated using theoretical predictions where the QCD scales μ_R and μ_F are independently varied by factors of 0.5 and 2. The cases where $\mu_F/\mu_R = 4$ or 1/4 are excluded. The total scale uncertainty is calculated by taking the maximum difference in the extracted m_t^{pole} values compared to the nominal result.

Using the ABMP16NLO PDF set in the NLO prediction results in

$$m_t^{\text{pole}} = 172.73 \pm 0.59\ (\text{fit})^{+0.39}_{-0.35}\ (\text{scale}) = 172.73 \pm 0.71\ \ (\text{tot})\ \text{GeV} \quad [\text{ABMP16 }]. \quad (7.10)$$

Using CT18NLO PDF, alternatively, leads to

$$m_t^{\text{pole}} = 172.11 \pm 0.66\ (\text{fit})^{+0.41}_{-0.31}\ (\text{scale}) = 172.11 \pm 0.78\ \ (\text{tot})\ \text{GeV} \quad [\text{CT18}]\ . \quad (7.11)$$

The fit uncertainty includes both statistical and systematic uncertainties from the χ^2 fit, covering PDF and extrapolation uncertainties, while the scale uncertainty comes from variations in μ_R and μ_F.

To study the possible impact of incompatibilities observed in the normalization of different data taking periods, the value of m_t^{pole} has also been extracted for individual data-taking periods using the two PDF sets, and the results are compared in Figure 7.25, together with the full Run 2 result. Indeed, the results demonstrate good compatibility across the data-taking periods, demonstrating significant independence of the final result on normalization issues spotted in Run 2 data. The result is in agreement with earlier extractions of m_t^{pole} [83] and is the most precise one of its kind, to date.

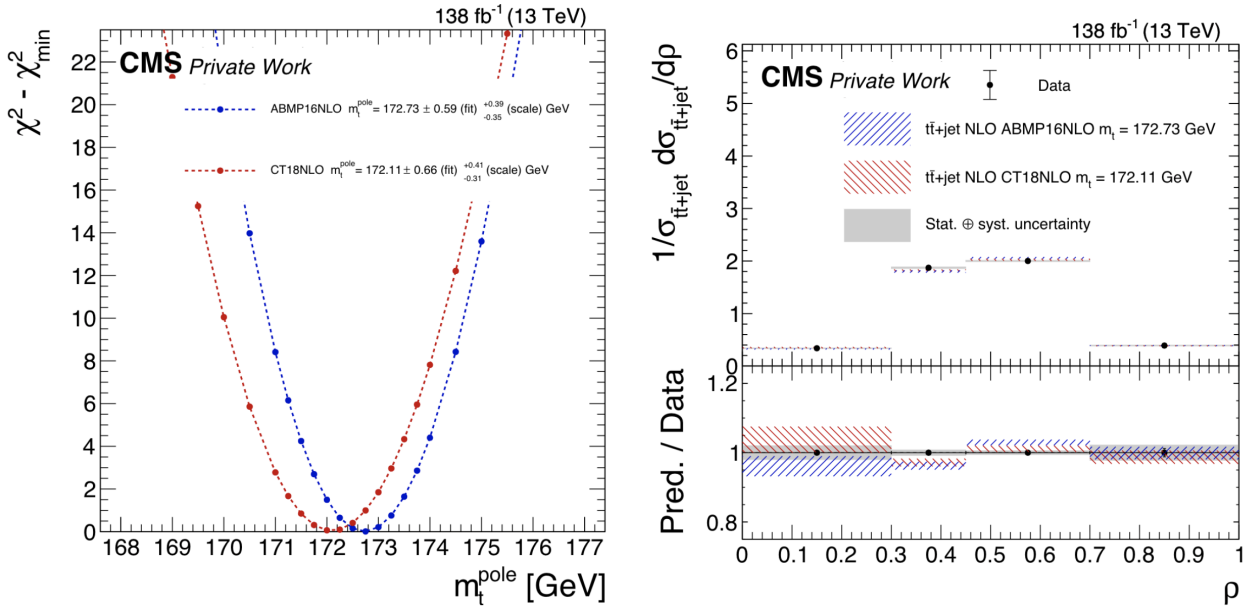

Figure 7.24: The χ^2 scan (left) of m_t^{pole} from the fit of the predicted normalized $t\bar{t}$+jet differential cross section to data. The NLO predictions are obtained by using ABMP16NLO (blue) and CT18NLO (red) PDF sets, alternatively. The normalized $t\bar{t}$+jet differential cross section as a function of ρ (right). The data (black symbols) are shown with their total uncertainty (shaded band), while the statistical errors are covered by the symbols. The theoretical predictions obtained by using ABMP16NLO (blue) and CT18NLO (red) and corresponding best-fit m_t^{pole} values are shown by the hatched bands.

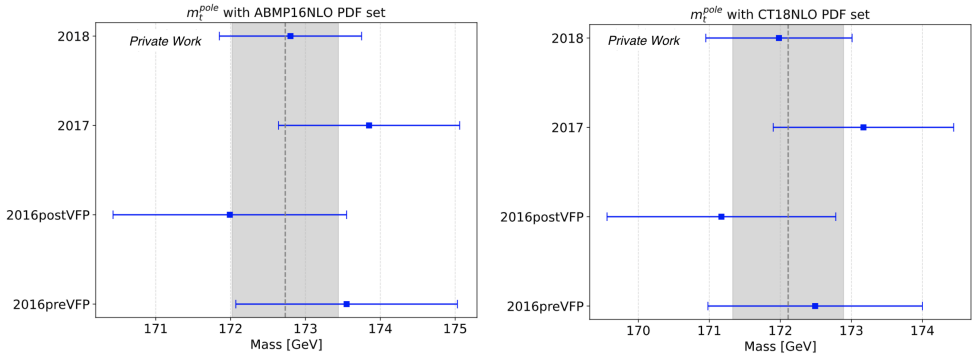

Figure 7.25: Values of m_t^{pole} extracted in four different data-taking periods (blue symbols), with their total uncertainty using ABMP16NLO (left) and CT18NLO (right). The results obtained in the fit to the full Run 2 data (dotted likes) are shown with their total uncertainties (shaded bands).

Uncertainty Source	$\Delta r^1_{t\bar{t}+jet}$	$\Delta r^2_{t\bar{t}+jet}$	$\Delta r^3_{t\bar{t}+jet}$	$\Delta r^4_{t\bar{t}+jet}$
Muon identification	3.1	2.2	2.0	3.2
Muon energy scale	3.3	2.3	2.2	3.2
Electron identification	2.8	1.8	1.7	3.0
Electron energy scale	4.0	3.2	2.9	3.7
Jet energy scale	3.5	3.0	2.8	3.6
Jet energy resolution	4.0	3.2	2.9	3.7
Jet identification	4.0	3.2	2.9	3.7
ptMiss	4.0	3.2	2.9	3.7
b jet identification	3.7	2.9	2.8	3.7
Trigger efficiency	4.0	3.2	2.9	3.7
Total experimental	2.7	1.7	1.4	2.1
tt0jet	2.6	1.4	1.6	3.2
zJets	3.0	1.9	1.8	2.9
single top	2.8	2.0	2.0	3.2
Total background normalization	2.6	1.5	1.6	3.3
Zjets ME scale	4.5	3.9	3.6	4.7
single top ME/FSR/ISR scales	2.8	2.1	2.0	3.2
PDF	3.3	2.6	2.6	3.6
ME scale	3.0	2.2	2.1	3.3
ISR scale	4.0	3.2	2.9	3.7
FSR scale	4.0	3.2	2.9	3.7
top pt	3.3	2.5	2.4	3.3
b fragmentation	3.0	2.2	2.0	3.1
matching scale	3.8	2.9	2.8	3.9
UE tune	3.0	2.1	2.0	3.2
Total theory and modelling	2.3	1.9	1.9	2.8
Luminosity	4.3	3.5	3.3	4.3
mtMC	3.4	2.4	2.2	3.3
Limited size of simulated samples	2.8	1.8	1.7	2.6
Total systematic	4.0	2.8	2.7	3.7
Statistical	0.7	0.5	0.4	1.3
Total	4.0	2.9	2.7	3.9

Summary

Advancing our understanding of the fundamental particles and forces that govern nature requires extensive collaboration across disciplines, with many projects in high-energy particle physics spanning decades from planning to execution. The success of these exper-

iments depends equally on development of detector technologies, scrutinizing the object reconstruction and calibration and advancing the data analysis methods. This thesis reflects on several aspects of modern particle physics, encompassing the design and qualification of new detector components, the alignment of the detectors, and finally, the analysis of collision data recorded by the experiment. In the following, the main achievements are summarized.

Contributions to the CMS Outer Tracker Upgrade

As a part of this thesis, the development of the burn-in setup for PS modules at DESY and the integration tests for CMS Outer Tracker modules were performed. The burn-in system was successfully commissioned, achieving reliable temperature cycling and dew point control, and demonstrating its capability for full-scale testing. Initial tests, though yet limited to single modules, highlight the potential to handle 20 modules with either parallel or alternating usage. Software and firmware improvements will continue to enhance the system's operational efficiency, with ongoing developments to finalize protocols, software installation and optimize the chiller settings.

In the integration tests, the cooling strategy and noise performance of the CMS Outer Tracker modules were validated under simulated operational conditions. The tests have confirmed the capability of the cooling system to maintain optimal temperatures across the key components, even in demanding setups. Several issues, such as overheating in the mockup structures, and grounding discrepancies, affecting the noise levels were identified. Planned improvements, including the use of alternative thermal interface materials and modifications of the module such as the cover layer of the hybrid tail, or the filter circuits on the POH, aim to address these issues. Together, these efforts have provided essential insights into the thermal and noise performance of the CMS Outer Tracker modules for the upgrade of the detector for the upcoming High-Luminosity LHC run.

Tracker Alignment and Pixel Local Reconstruction

Another part of the thesis has addressed the significant contribution to the CMS tracker alignment in the LHC Run 3. A track-based alignment, while being effective at reaching the precision required, presents computational and configuration challenges, which were particularly evident in 2021 when the entire pixel detector was upgraded. This thesis has contributed to the transition to High Granularity Prompt Calibration Loop (HG PCL), which improves the alignment accuracy by addressing Lorentz drift and reducing radiation-induced effects, maintaining high tracking precision of the order of μm throughout the current LHC Run 3.

Measurement of the Top Quark Mass

Finally, a precision measurement of the top quark pole mass was performed in this thesis. For this purpose, the events containing $t\bar{t}$+jet production were used, collected in pp collisions at the LHC at $\sqrt{s} = 13$ TeV and recorded by the CMS experiment in 2016-2018 (Run 2), corresponding to the integrated luminosity of 138 fb^{-1}.

This work followed the strategy of the first CMS measurement of this kind [90], based on a fraction of the available data. The value of the top quark mass was extracted through comparison of the parton-level normalized differential $t\bar{t}$+jet cross sections, measured as a function of the observable ρ, defined as the inverse of the invariant mass of the $t\bar{t}$ system and the additional jet, to the next-to-leading order QCD predictions. The top quarks are selected in their dileptonic decays.

The NLO prediction is obtained with two alternative sets of parton distribution functions. The value $m_t^{\text{pole}} = 172.73 \pm 0.71$GeV is obtained using the NLO prediction based on the ABMP16NLO PDF, while $m_t^{\text{pole}} = 172.11 \pm 0.78$GeV is obtained by using the prediction based on CT18NLO PDF.

These results agree with previous extractions of the top quark pole mass and are the most precise of their kind, to date.

APPENDIX A

Burn-in

A.1 Burn-in setup components

Figure A.1: RTD cabling scheme for the Burn-in box.

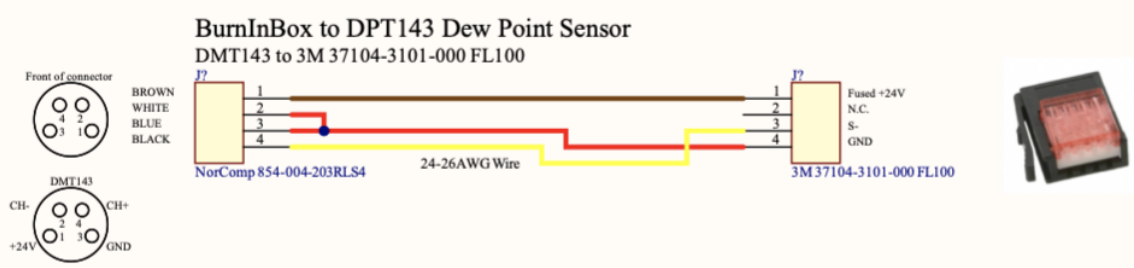

Figure A.2: Dew point sensor cabling scheme for the Burn-in box.

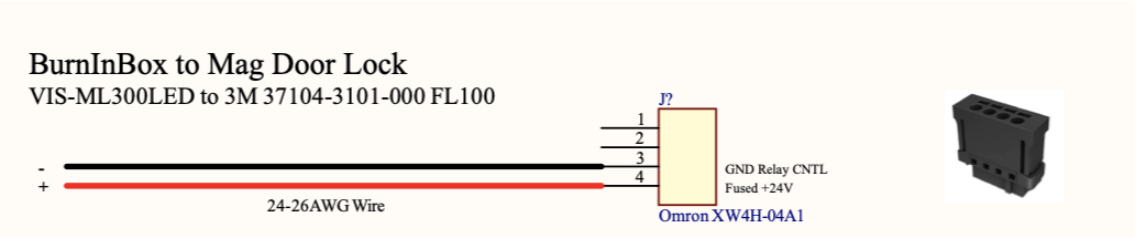

Figure A.3: Magnetic interlock cabling scheme for the Burn-in box.

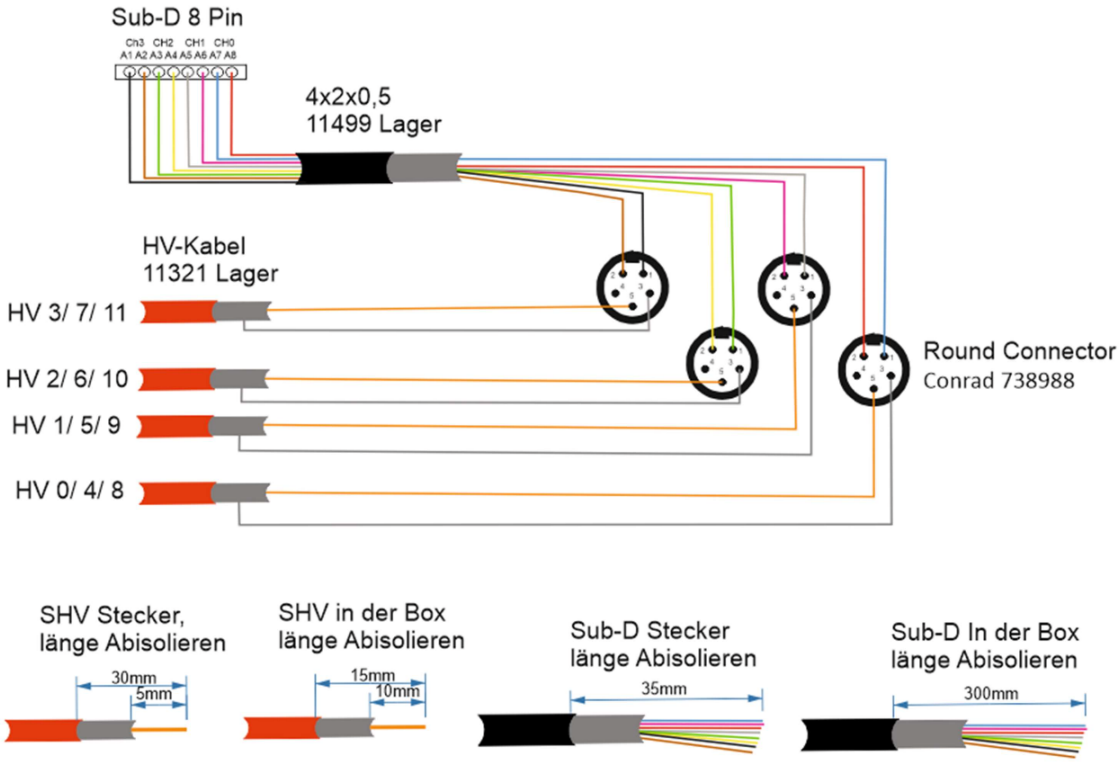

Figure A.4: Patch box cabling scheme.

A.2 Noise measurement during Burn-in test

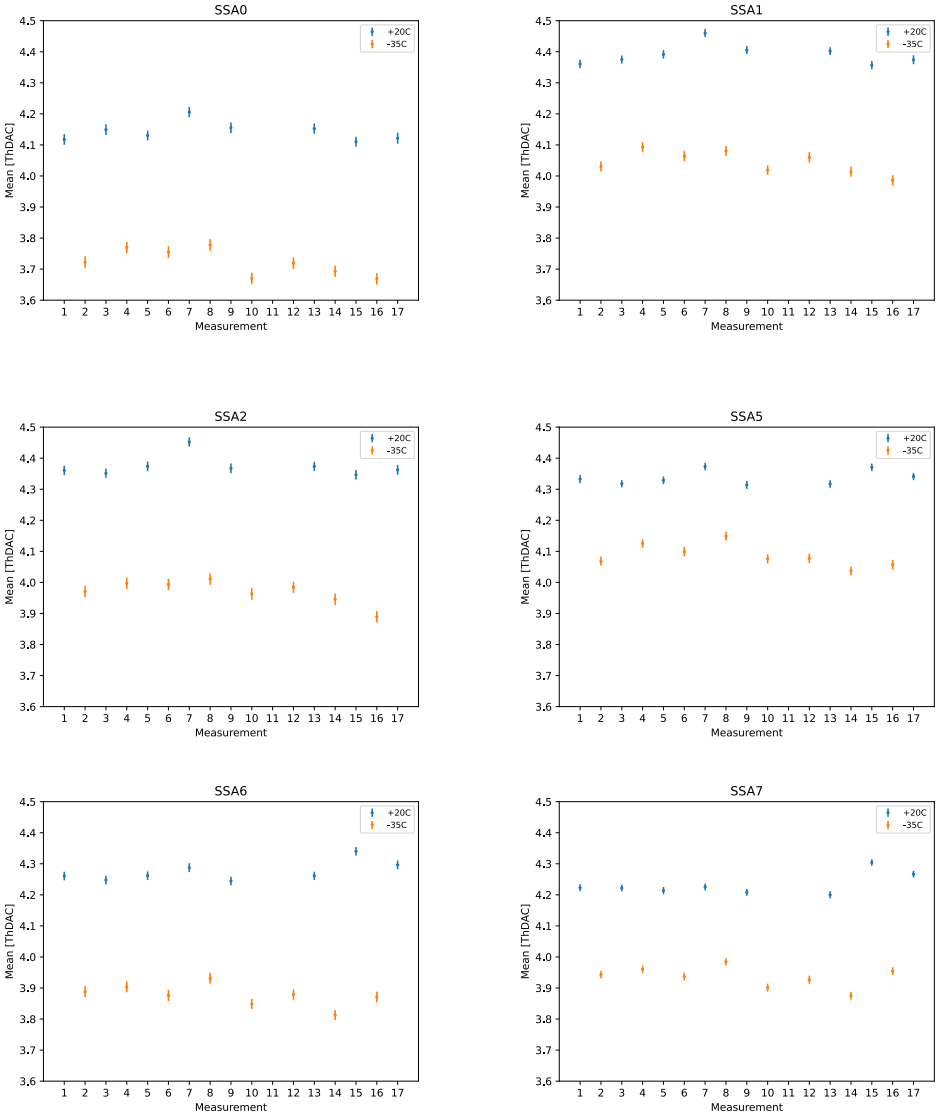

Figure A.5: Mean value of the noise per SSA.

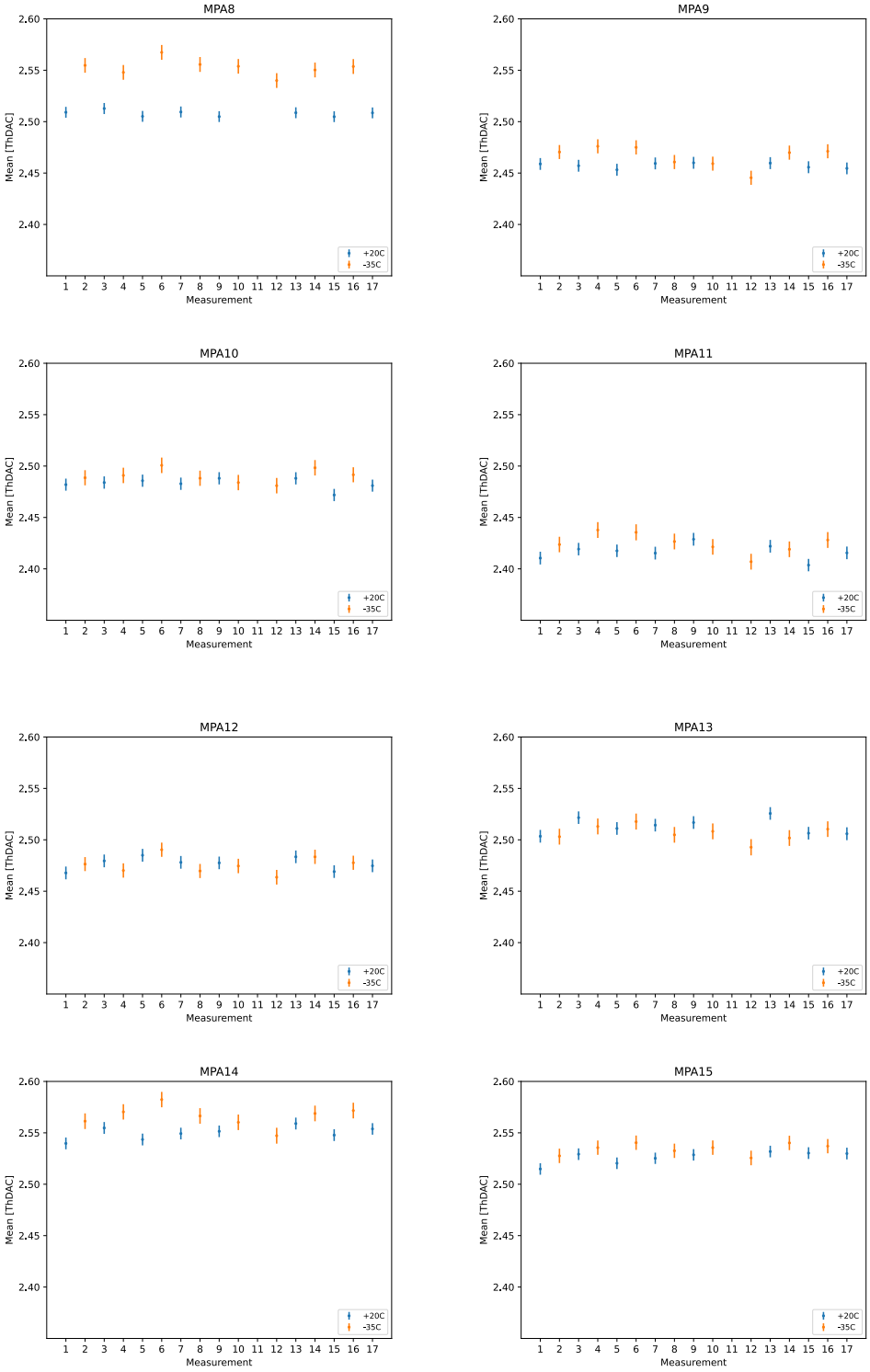

Figure A.6: Mean value of the noise per MPA.

APPENDIX B

Analysis

B.1 List of triggers used

Channel	Trigger path
$\mu^+ \mu^-$	HLT_Mu17_TrkIsoVVL_Mu8_TrkIsoVVL_DZ_Mass3p8_v* HLT_IsoMu24_v*
$e^+ e^-$	HLT_Ele23_Ele12_CaloIdL_TrackIdL_IsoVL_DZ_v* HLT_Ele23_Ele12_CaloIdL_TrackIdL_IsoVL_v HLT_Ele32_WPTight_Gsf_v
$\mu^\pm e^\mp$	HLT_Mu23_TrkIsoVVL_Ele12_CaloIdL_TrackIdL_IsoVL_DZ_v* HLT_Mu23_TrkIsoVVL_Ele12_CaloIdL_TrackIdL_IsoVL_v* HLT_Mu12_TrkIsoVVL_Ele23_CaloIdL_TrackIdL_IsoVL_DZ_v* HLT_Mu8_TrkIsoVVL_Ele23_CaloIdL_TrackIdL_IsoVL_DZ_v* HLT_Ele32_WPTight_Gsf_v HLT_IsoMu24_v*

Table B.1: Trigger paths considered in this analysis in 2018.

Channel	Trigger path
$\mu^+ \mu^-$	HLT_Mu17_TrkIsoVVL_Mu8_TrkIsoVVL_DZ_Mass3p8_v*
	HLT_Mu17_TrkIsoVVL_Mu8_TrkIsoVVL_DZ_Mass8_v*
	HLT_IsoMu27_v*
$e^+ e^-$	HLT_Ele23_Ele12_CaloIdL_TrackIdL_IsoVL_v*
	HLT_DoubleEle33_CaloIdL_MW_v*
	HLT_Ele32_WPTight_Gsf_L1DoubleEG_v*
	HLT_Ele35_WPTight_Gsf_v*
$\mu^\pm e^\mp$	HLT_Mu23_TrkIsoVVL_Ele12_CaloIdL_TrackIdL_IsoVL_DZ_v*
	HLT_Mu23_TrkIsoVVL_Ele12_CaloIdL_TrackIdL_IsoVL_v*
	HLT_Mu12_TrkIsoVVL_Ele23_CaloIdL_TrackIdL_IsoVL_DZ_v*
	HLT_Mu8_TrkIsoVVL_Ele23_CaloIdL_TrackIdL_IsoVL_DZ_v*
	HLT_Ele32_WPTight_Gsf_L1DoubleEG_v*
	HLT_Ele35_WPTight_Gsf_v*
	HLT_IsoMu27_v*

Table B.2: Trigger paths considered in this analysis in 2017.

Channel	Trigger path
$\mu^+ \mu^-$	HLT_Mu17_TrkIsoVVL_Mu8_TrkIsoVVL_DZ_v*
	HLT_Mu17_TrkIsoVVL_TkMu8_TrkIsoVVL_DZ_v*
	HLT_IsoMu24_v*
	HLT_IsoTkMu24_v*
$e^+ e^-$	HLT_Ele23_Ele12_CaloIdL_TrackIdL_IsoVL_DZ_v*
	HLT_DoubleEle33_CaloIdL_MW_v*
	HLT_DoubleEle33_CaloIdL_GsfTrkIdVL_v*
	HLT_Ele27_WPTight_Gsf_v*
	HLT_Ele25_eta2p1_WPTight_Gsf_v*
	HLT_Photon175_v*
$\mu^\pm e^\mp$	HLT_Mu8_TrkIsoVVL_Ele23_CaloIdL_TrackIdL_IsoVL_DZ_v*
	HLT_Mu8_TrkIsoVVL_Ele23_CaloIdL_TrackIdL_IsoVL_v*
	HLT_Mu12_TrkIsoVVL_Ele23_CaloIdL_TrackIdL_IsoVL_DZ_v*
	HLT_Mu12_TrkIsoVVL_Ele23_CaloIdL_TrackIdL_IsoVL_v*
	HLT_Mu23_TrkIsoVVL_Ele12_CaloIdL_TrackIdL_IsoVL_DZ_v*
	HLT_Mu23_TrkIsoVVL_Ele12_CaloIdL_TrackIdL_IsoVL_v*
	HLT_IsoMu24_v*
	HLT_IsoTkMu24_v*
	HLT_Ele27_WPTight_Gsf_v*
	HLT_Ele25_eta2p1_WPTight_Gsf_v*
	HLT_Photon175_v*

Table B.3: Trigger paths considered in this analysis in 2016 preVFP and postVFP.

B.2 Triggers Scale Factors

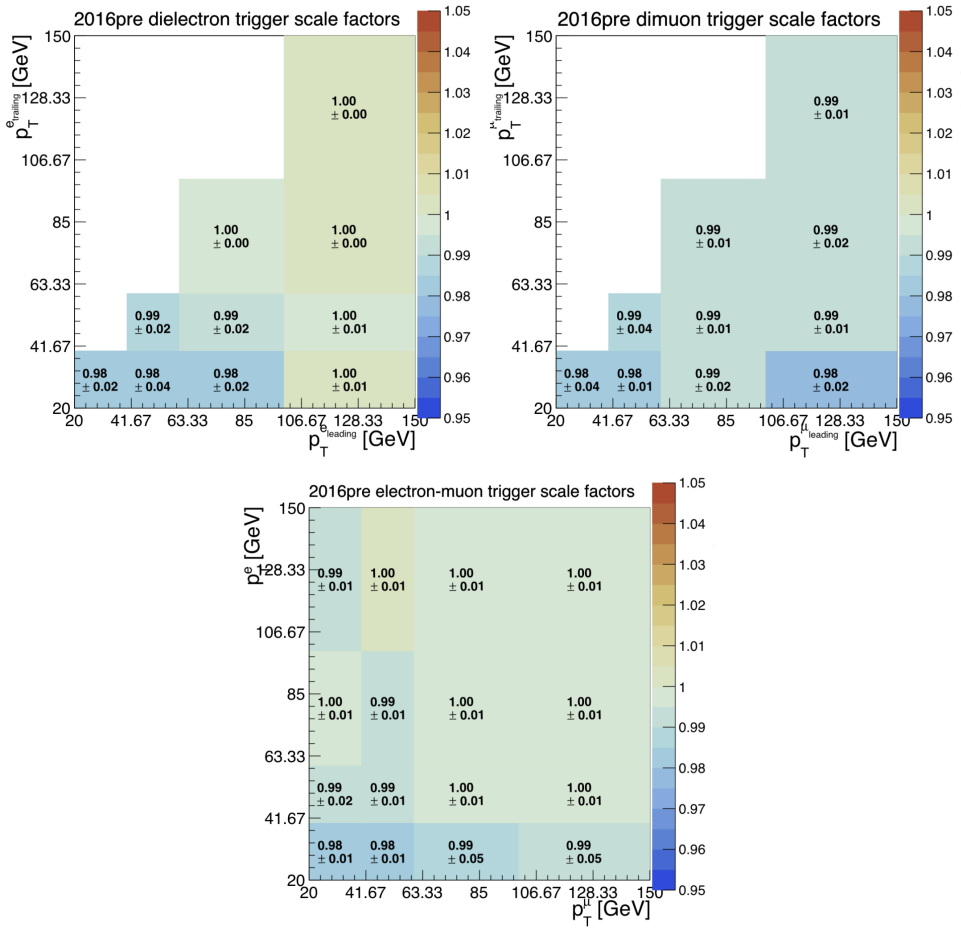

Figure B.1: The 2016preVFP trigger scale factors as a function of p_T for both leptons in the e^+e^- (top left), $\mu^+\mu^-$ (top right), and $\mu^\pm e^\mp$ (bottom) channels. The uncertainties shown include both statistical and additional systematic uncertainties combined in quadrature.

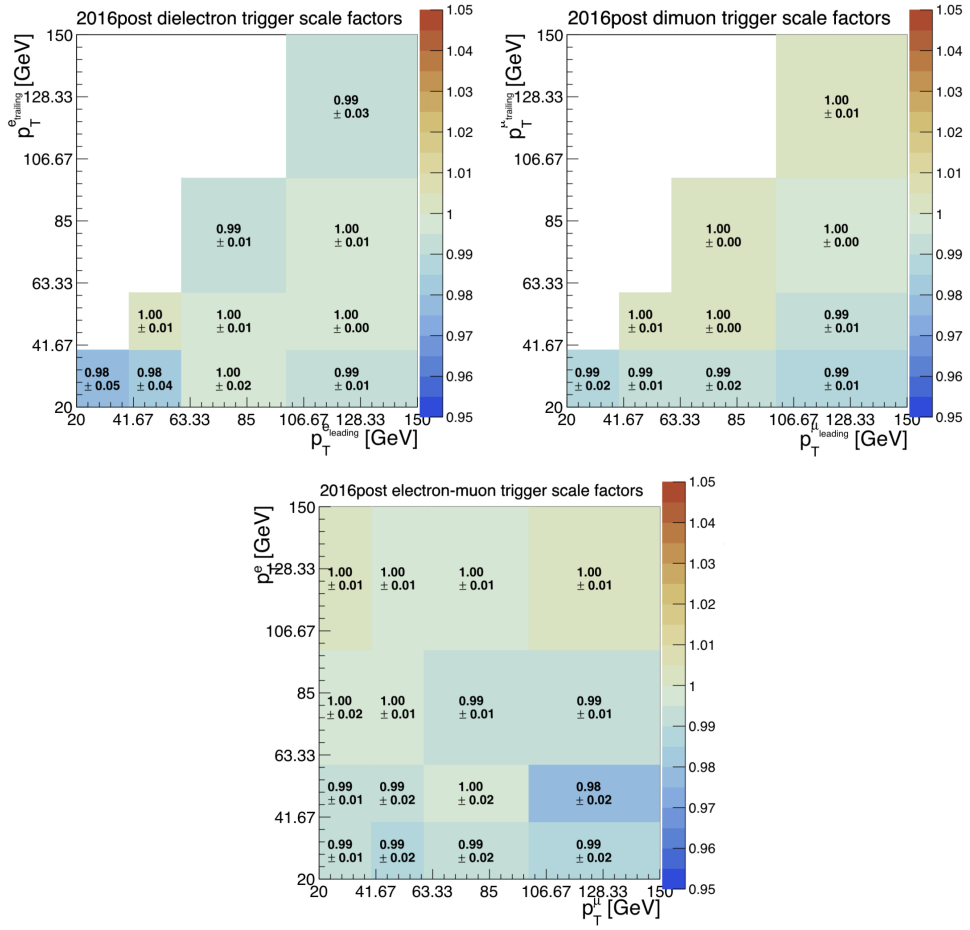

Figure B.2: The 2016postVFP trigger scale factors as a function of p_T for both leptons in the e^+e^- (top left), $\mu^+\mu^-$ (top right), and $\mu^\pm e^\mp$ (bottom) channels. The uncertainties shown include both statistical and additional systematic uncertainties combined in quadrature.

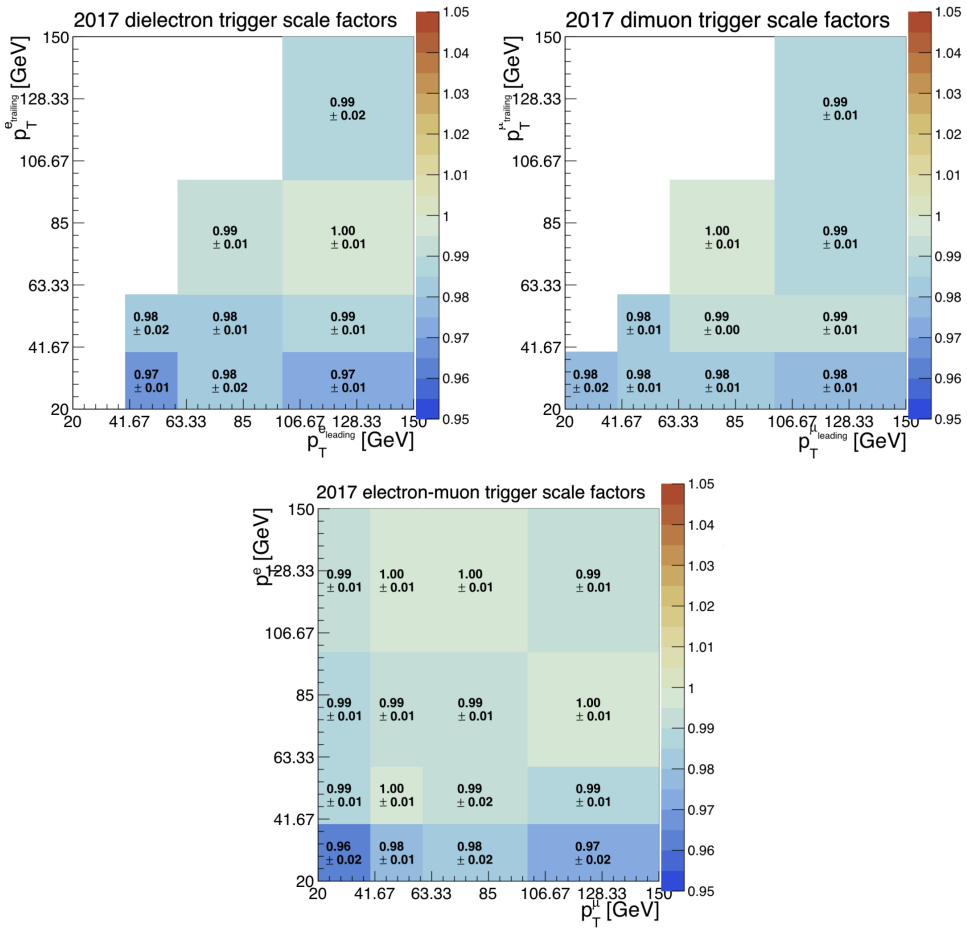

Figure B.3: The 2017 trigger scale factors as a function of p_T for both leptons in the e^+e^- (top left), $\mu^+\mu^-$ (top right), and $\mu^\pm e^\mp$ (bottom) channels. The uncertainties shown include both statistical and additional systematic uncertainties combined in quadrature.

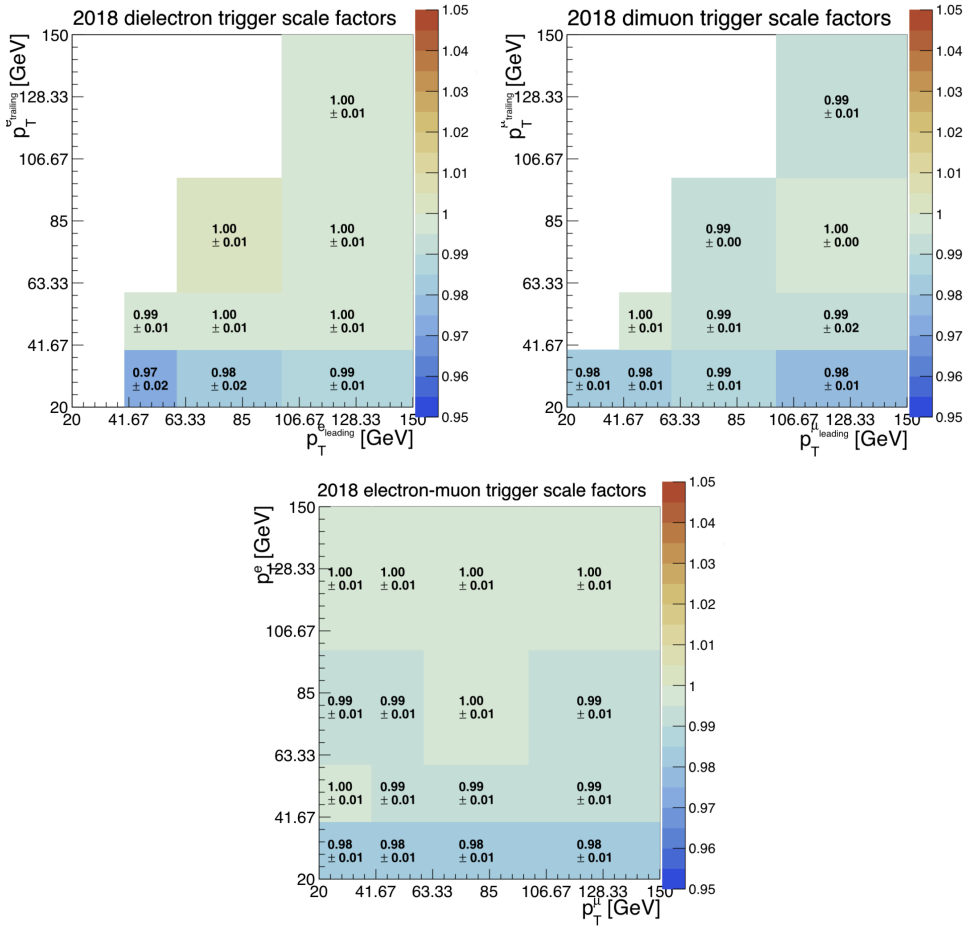

Figure B.4: The 2018 trigger scale factors as a function of p_T for both leptons in the e^+e^- (top left), $\mu^+\mu^-$ (top right), and $\mu^\pm e^\mp$ (bottom) channels. The uncertainties shown include both statistical and additional systematic uncertainties combined in quadrature.

B.3 Cross section per year

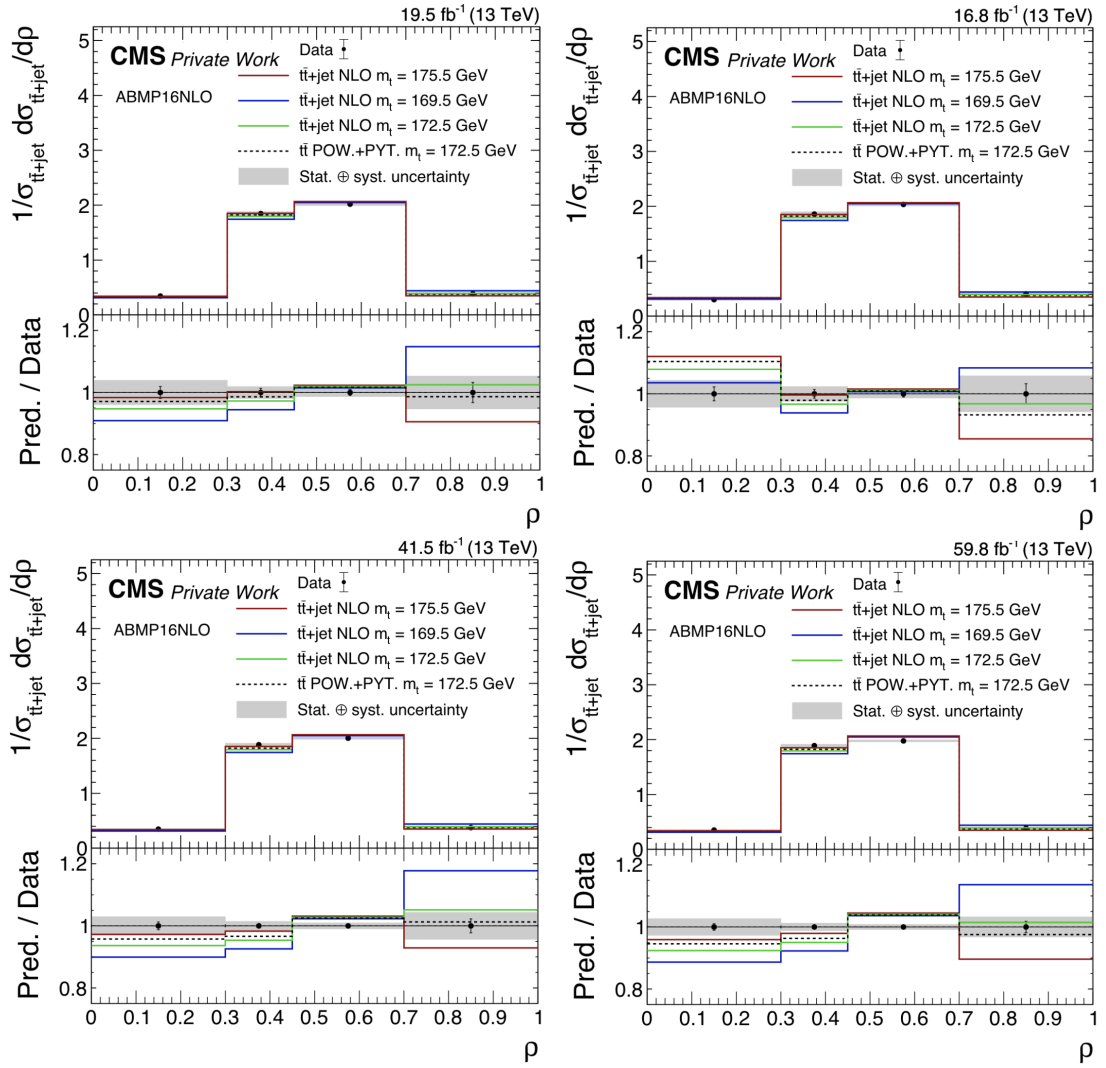

Figure B.5: Normalized $t\bar{t}$+jet differential cross section as a function of ρ for both the data (points) and theoretical predictions for 2016preVFP on the upper left, 2016postVFP on the upper right, 2017 on the lower left and 2018 on the lower right. The vertical bars on the data points represent the statistical uncertainty, while the shaded region indicates the total uncertainty in the measurement. The lower panels show the ratio of the theoretical predictions to the data.

Bibliography

[1] A. Einstein, *Die Grundlage der allgemeinen Relativitätstheorie*. Annalen der Physik und Chemie. J.A. Barth (1916). Book.

[2] G. 't Hooft and M. Veltman, "Regularization and renormalization of gauge fields." *Nuclear Physics B* **44** (1972), no. 1 189–213. doi: 10.1016/0550-3213(72)90279-9.

[3] E. Noether, "Invariante variationsprobleme." *Nachrichten von der Gesellschaft der Wissenschaften zu Göttingen, Mathematisch-Physikalische Klasse* **1918** (1918) 235–257. Paper.

[4] M. E. Peskin and D. V. Schroeder, *An Introduction to quantum field theory*. Addison-Wesley, Reading, USA (1995). doi: 10.1201/9780429503559.

[5] S. Wuchterl, "Top quark pole mass from $t\bar{t}$+jet using a machine learning based reconstruction for $t\bar{t}$ kinematics." (2023). DESY-THESIS-2023-0036.

[6] F. Englert and R. Brout, "Broken symmetry and the mass of gauge vector mesons." *Phys. Rev. Lett.* **13** (Aug, 1964) 321–323. doi: 10.1103/PhysRevLett.13.321.

[7] P. W. Higgs, "Broken symmetries and the masses of gauge bosons." *Phys. Rev. Lett.* **13** (Oct, 1964) 508–509. doi: 10.1103/PhysRevLett.13.508.

[8] ALEPH, DELPHI, L3, OPAL, SLD, LEP Electroweak Working Group, SLD Electroweak Group, and SLD Heavy Flavour Group Collaboration, "Precision electroweak measurements on the z resonance." *Physics Reports* **427** (2006), no. 5 257–454. doi: 10.1016/j.physrep.2005.12.006.

[9] C. S. Wu, E. Ambler, R. W. Hayward, D. D. Hoppes, and R. P. Hudson, "Experimental test of parity conservation in beta decay." *Phys. Rev.* **105** (Feb, 1957) 1413–1415. doi: 10.1103/PhysRev.105.1413.

[10] S. L. Glashow, "Partial-symmetries of weak interactions." *Nuclear Physics* **22** (1961), no. 4 579–588. doi: 10.1016/0029-5582(61)90469-2.

[11] S. Weinberg, "A model of leptons." *Phys. Rev. Lett.* **19** (Nov, 1967) 1264–1266. doi: 10.1103/PhysRevLett.19.1264.

[12] A. Salam, *Weak and electromagnetic interactions*, pp. 244–254. doi: 10.1142/9789812795915_0034.

[13] M. Schwartz, *Quantum Field Theory and the Standard Model*. Quantum Field Theory and the Standard Model. Cambridge University Press (2014). Book.

[14] M. Gell-Mann, "The interpretation of the new particles as displaced charge multiplets." *Il Nuovo Cimento (1955-1965)* **4** (1956), no. 2 848–866. doi: 10.1007/BF02748000.

[15] T. Nakano and K. Nishijima, "Charge Independence for V-particles*." *Progress of Theoretical Physics* **10** (11, 1953) 581–582. doi: 10.1143/PTP.10.581.

[16] J. Ellis, "Higgs physics." (2013). doi: 10.48550/arXiv.1312.5672.

[17] P. D. Group, "Review of Particle Physics." *Progress of Theoretical and Experimental Physics* **2020** (08, 2020) 083C01. doi: 10.1093/ptep/ptaa104.

[18] ATLAS Collaboration, "Observation of a new particle in the search for the standard model higgs boson with the atlas detector at the lhc." *Physics Letters B* **716** (2012), no. 1 1–29. doi: 10.1016/j.physletb.2012.08.020.

[19] CMS Collaboration, "Observation of a new boson at a mass of 125 GeV with the CMS experiment at the LHC." *Physics Letters B* **716** (2012), no. 1 30–61. doi: 10.1016/j.physletb.2012.08.021.

[20] M. Kobayashi and T. Maskawa, "CP-Violation in the Renormalizable Theory of Weak Interaction." *Progress of Theoretical Physics* **49** (02, 1973) 652–657. doi: 10.1143/PTP.49.652.

[21] N. Cabibbo, "Unitary symmetry and leptonic decays." *Phys. Rev. Lett.* **10** (Jun, 1963) 531–533. doi: 10.1103/PhysRevLett.10.531.

[22] B. Pontecorvo, "Inverse beta processes and nonconservation of lepton charge." *Zh. Eksp. Teor. Fiz.* **34** (1957) 247. Paper.

[23] Z. Maki, M. Nakagawa, and S. Sakata, "Remarks on the Unified Model of Elementary Particles." *Progress of Theoretical Physics* **28** (11, 1962) 870–880. doi: 10.1143/PTP.28.870.

[24] Super-Kamiokande Collaboration, "Evidence for oscillation of atmospheric neutrinos." *Phys. Rev. Lett.* **81** (Aug, 1998) 1562–1567. doi: 10.1103/PhysRevLett.81.1562.

[25] SNO Collaboration, "Direct evidence for neutrino flavor transformation from neutral-current interactions in the sudbury neutrino observatory." *Phys. Rev. Lett.* **89** (Jun, 2002) 011301. doi: 10.1103/PhysRevLett.89.011301.

[26] KATRIN Collaboration, "Direct neutrino-mass measurement with sub-electronvolt sensitivity." *Nature Physics* **18** (2022), no. 2 160–166. doi: 10.1038/s41567-021-01463-1.

[27] J. Schwichtenberg, *Physics from Symmetry*. Undergraduate Lecture Notes in Physics. Springer (2018). doi: 10.1007/978-3-319-66631-0.

[28] M. Gell-Mann, "Symmetries of baryons and mesons." *Phys. Rev.* **125** (Feb, 1962) 1067–1084. doi: 10.1103/PhysRev.125.1067.

[29] G. 't Hooft and M. Veltman, "Regularization and renormalization of gauge fields." *Nuclear Physics B* **44** (1972), no. 1 189–213. doi: 10.1016/0550-3213(72)90279-9.

[30] S. Soldner-Rembold, "QCD studies and α_s measurements at lep." in *High Energy Physics*, p. 652–656, World Scientific Publishing Company, May, 2005. doi: 10.1142/9789812702227_0116.

[31] CMS Collaboration, "Measurement and QCD analysis of double-differential inclusive jet cross sections in pp collisions at $\sqrt{s}$=8 TeV and cross section ratios to 2.76 and 7 TeV." *Journal of High Energy Physics* **2017** (Mar., 2017). doi: 10.1007/jhep03(2017)156.

[32] O. Behnke, A. Geiser, and M. Lisovyi, "Charm, beauty and top at hera." (2015). arXiv:1506.07519.

[33] DELPHI Collaboration, "Study of b-quark mass effects in multijet topologies with the delphi detector at lep." *The European Physical Journal C* **55** (2008), no. 4 525–538. doi: 10.1140/epjc/s10052-008-0631-5.

[34] DELPHI Collaboration, "Determination of the b quark mass at the m_z scale with the delphi detector at lep." *The European Physical Journal C - Particles and Fields* **46** (2006), no. 3 569–583. doi: 10.1140/epjc/s2006-02497-6.

[35] ALEPH Collaboration, "A measurement of the b-quark mass from hadronic z decays." *The European Physical Journal C* **18** (Dec., 2000) 1–13. doi: 10.1007/s100520000533.

[36] OPAL Collaboration, "Determination of the b quark mass at the z mass scale." *The European Physical Journal C* **21** (July, 2001) 411–422. doi: 10.1007/s100520100746.

[37] A. Brandenburg, P. Burrows, D. Muller, N. Oishi, and P. Uwer, "Measurement of the running b-quark mass using $e^+e^- \to b\bar{b}g$ events." *Physics Letters B* **468** (Nov., 1999) 168–177. doi: 10.1016/s0370-2693(99)01194-6.

[38] ZEUS Collaboration, "Measurement of beauty and charm production in deep inelastic scattering at hera and measurement of the beauty-quark mass." *Journal of High Energy Physics* **2014** (2014), no. 9. doi: 10.1007/jhep09(2014)127.

[39] A. Gizhko, A. Geiser, S. Moch, I. Abt, O. Behnke, A. Bertolin, J. Blümlein, D. Britzger, R. Brugnera, A. Buniatyan, P. Bussey, R. Carlin, A. Cooper-Sarkar, K. Daum, S. Dusini, E. Elsen, L. Favart, J. Feltesse, B. Foster, A. Garfagnini, M. Garzelli, J. Gayler, D. Haidt, J. Hladkỳ, A. Jung, M. Kapichine, I. Korzhavina, B. Levchenko, K. Lipka, M. Lisovyi, A. Longhin, S. Mikocki, T. Naumann, G. Nowak, E. Paul, R. Plačakytė, K. Rabbertz, S. Schmitt, L. Shcheglova, Z. Si, H. Spiesberger, L. Stanco, P. Truöl, T. Tymieniecka, A. Verbytskyi, K. Wichmann, M. Wing, A. Żarnecki, O. Zenaiev, and Z. Zhang, "Running of the charm-quark mass from HERA deep-inelastic scattering data." *Physics Letters B* **775** (2017) 233–238. doi: 10.1016/j.physletb.2017.11.002.

[40] U. Langenfeld, S. Moch, and P. Uwer, "Measuring the running top-quark mass." *Phys. Rev. D* **80** (Sep, 2009) 054009. doi: 10.1103/PhysRevD.80.054009.

[41] J. Fuster, A. Irles, D. Melini, P. Uwer, and M. Vos, "Extracting the top-quark running mass using $t\bar{t}$ + 1-jet events produced at the large hadron collider." *The European Physical Journal C* **77** (Nov., 2017). doi: 10.1140/epjc/s10052-017-5354-z.

[42] M. M. Defranchis, "First measurement of the running of the top quark mass." (2020). presented on 30 Apr 2020.

[43] M. M. Defranchis, J. Kieseler, K. Lipka, and J. Mazzitelli, "Running of the top quark mass at NNLO in QCD." (2022). doi: 10.48550/arXiv.2208.11399.

[44] CMS Collaboration, "Running of the top quark mass from proton-proton collisions at $\sqrt{s}$= 13 TeV." *Physics Letters B* **803** (Apr., 2020) 135263. doi: 10.1016/j.physletb.2020.135263.

[45] D. J. Gross and F. Wilczek, "Asymptotically free gauge theories. i." *Phys. Rev. D* **8** (Nov, 1973) 3633–3652. doi: 10.1103/PhysRevD.8.3633.

[46] H. D. Politzer, "Reliable perturbative results for strong interactions?." *Phys. Rev. Lett.* **30** (Jun, 1973) 1346–1349. doi: 10.1103/PhysRevLett.30.1346.

[47] H1 Collaboration, "Evidence for a narrow anti-charmed baryon state." *Physics Letters B* **588** (2004), no. 1 17–28. doi: 10.1016/j.physletb.2004.03.012.

[48] LHCb Collaboration, "Observation of $j/\psi\phi$ structures consistent with exotic states from amplitude analysis of $B^+ \to j/\psi\phi K^+$ decays." *Phys. Rev. Lett.* **118** (Jan, 2017) 022003. doi: 10.1103/PhysRevLett.118.022003.

[49] LHCb Collaboration, "Observation of $j/\psi p$ resonances consistent with pentaquark states in $\Lambda_b^0 \to j/\psi K^- p$ decays." *Phys. Rev. Lett.* **115** (Aug, 2015) 072001. doi: 10.1103/PhysRevLett.115.072001.

[50] I. I. Bigi, M. A. Shifman, N. G. Uraltsev, and A. I. Vainshtein, "Pole mass of the heavy quark: Perturbation theory and beyond." *Physical Review D* **50** (Aug., 1994) 2234–2246. doi: 10.1103/physrevd.50.2234.

[51] A. Hoang, A. Jain, C. Lepenik, V. Mateu, M. Preisser, I. Scimemi, and I. W. Stewart, "The MSR mass and the $\mathcal{O}(\lambda_{QCD})$ renormalon sum rule." *Journal of High Energy Physics* **2018** (2018), no. 4 3. doi: 10.1007/JHEP04(2018)003.

[52] J. C. Collins, D. E. Soper, and G. Sterman, "Factorization of hard processes in QCD." (2004). doi: 10.48550/arXiv.hep-ph/0409313.

[53] Y. L. Dokshitzer, "Calculation of the Structure Functions for Deep Inelastic Scattering and e^+e^- Annihilation by Perturbation Theory in Quantum Chromodynamics.." *Sov. Phys. JETP* **46** (1977) 641–653. Paper.

[54] G. Altarelli and G. Parisi, "Asymptotic freedom in parton language." *Nuclear Physics B* **126** (1977), no. 2 298–318. doi: 10.1016/0550-3213(77)90384-4.

[55] V. N. Gribov and L. N. Lipatov, "Deep inelastic electron scattering in perturbation theory." *Sov. J. Nucl. Phys.* **15** (1972) 438–450. doi: 10.1016/0370-2693(71)90576-4.

[56] M. Vakili, C. G. Arroyo, P. Auchincloss, L. de Barbaro, P. de Barbaro, A. O. Bazarko, R. H. Bernstein, A. Bodek, T. Bolton, H. Budd, J. Conrad, D. A. Harris, R. A. Johnson, J. H. Kim, B. J. King, T. Kinnel, G. Koizumi, S. Koutsoliotas, M. J. Lamm, W. C. Lefmann, W. Marsh, K. S. McFarland, C. McNulty, S. R. Mishra, D. Naples, P. Nienaber, M. J. Oreglia, L. Perera, P. Z. Quintas, A. Romosan, W. K. Sakumoto, B. A. Schumm, F. J. Sciulli, W. G. Seligman, M. H. Shaevitz, W. H. Smith, P. Spentzouris, R. Steiner, E. G. Stern, U. K. Yang, and J. Yu, "Nuclear structure functions in the large-x large-Q^2 kinematic region in neutrino deep inelastic scattering." *Phys. Rev. D* **61** (Feb, 2000) 052003. doi: 10.1103/PhysRevD.61.052003.

[57] M. Tzanov, D. Naples, S. Boyd, J. McDonald, V. Radescu, R. A. Johnson, N. Suwonjandee, M. Vakili, J. Conrad, B. T. Fleming, J. Formaggio, J. H. Kim, S. Koutsoliotas, C. McNulty, A. Romosan, M. H. Shaevitz, P. Spentzouris, E. G. Stern, A. Vaitaitis, E. D. Zimmerman, R. H. Bernstein, L. Bugel, M. J. Lamm, W. Marsh, P. Nienaber, N. Tobien, J. Yu, T. Adams, A. Alton, T. Bolton, J. Goldman, M. Goncharov, L. de Barbaro, D. Buchholz, H. Schellman, G. P. Zeller, J. Brau, R. B. Drucker, R. Frey, D. Mason, S. Avvakumov, P. de Barbaro, A. Bodek, H. Budd, D. A. Harris, K. S. McFarland, W. K. Sakumoto, and U. K. Yang, "Precise measurement of neutrino and antineutrino differential cross sections." *Phys. Rev. D* **74** (Jul, 2006) 012008. doi: 10.1103/PhysRevD.74.012008.

[58] H1 and ZEUS Collaboration, "Combination of measurements of inclusive deep inelastic $e^{\pm}p$ scattering cross sections and QCD analysis of HERA data." *The European Physical Journal C* **75** (2015), no. 12 580. doi: 10.1140/epjc/s10052-015-3710-4.

[59] D0 Collaboration, "Inclusive jet cross section in $p\bar{p}$ collisions at $\sqrt{s}$ =1.8 TeV." *Phys. Rev. Lett.* **68** (Feb, 1992) 1104–1108. doi: 10.1103/PhysRevLett.68.1104.

[60] L. A. Harland-Lang, A. D. Martin, P. Motylinski, and R. S. Thorne, "Parton distributions in the LHC era: MMHT 2014 PDFs." *The European Physical Journal C* **75** (May, 2015). doi: 10.1140/epjc/s10052-015-3397-6.

[61] S. Dulat, T.-J. Hou, J. Gao, M. Guzzi, J. Huston, P. Nadolsky, J. Pumplin, C. Schmidt, D. Stump, and C.-P. Yuan, "New parton distribution functions from a global analysis of quantum chromodynamics." *Physical Review D* **93** (Feb., 2016). doi: 10.1103/physrevd.93.033006.

[62] NNPDF Collaboration, "Parton distributions from high-precision collider data: NNPDF collaboration." *The European Physical Journal C* **77** (Oct., 2017). doi: 10.1140/epjc/s10052-017-5199-5.

[63] S. Alekhin, J. Blümlein, S. Moch, and R. Plačakytė, "Parton distribution functions, α_s and heavy-quark masses for LHC run II." *Physical Review D* **96** (July, 2017). doi: 10.1103/physrevd.96.014011.

[64] CMS Collaboration, "Measurement of $t\bar{t}$ normalised multi-differential cross sections in pp collisions at $\sqrt{s}$=13 TeV, and simultaneous determination of the strong coupling strength, top quark pole mass, and parton distribution functions." *The European Physical Journal C* **80** (July, 2020). doi: 10.1140/epjc/s10052-020-7917-7.

[65] CMS Collaboration, "Measurement and QCD analysis of double-differential inclusive jet cross sections in proton-proton collisions at *sqrts*= 13 TeV." *Journal of High Energy Physics* **2022** (2022), no. 2 142. doi: 10.1007/JHEP02(2022)142.

[66] CMS Collaboration, "Measurement of the triple-differential dijet cross section in proton-proton collisions at $\sqrt{s} = 8$ TeV and constraints on parton distribution functions." *The European Physical Journal C* **77** (2017), no. 11 746. doi: 10.1140/epjc/s10052-017-5286-7.

[67] S. Höche, *Introduction to Parton-Shower Event Generators*, ch. Chapter 5, pp. 235–295. doi: 10.1142/9789814678766_0005.

[68] S. Hoeche, F. Krauss, N. Lavesson, L. Lonnblad, M. Mangano, A. Schaelicke, and S. Schumann, "Matching parton showers and matrix elements." (2006). doi: 10.48550/arXiv.hep-ph/0602031.

[69] R. Frederix and S. Frixione, "Merging meets matching in MC@NLO." *Journal of High Energy Physics* **2012** (2012), no. 12 61. doi: 10.1007/JHEP12(2012)061.

[70] CMS Collaboration, "Extraction and validation of a new set of CMS pythia8 tunes from underlying-event measurements." *The European Physical Journal C* **80** (2020), no. 1 4. doi: 10.1140/epjc/s10052-019-7499-4.

[71] B. Andersson, G. Gustafson, G. Ingelman, and T. Sjöstrand, "Parton fragmentation and string dynamics." *Physics Reports* **97** (1983), no. 2 31–145. doi: 10.1016/0370-1573(83)90080-7.

[72] G. Marchesini, B. Webber, G. Abbiendi, I. Knowles, M. Seymour, and L. Stanco, "Herwig 5.1 - a monte carlo event generator for simulating hadron emission reactions with interfering gluons." *Computer Physics Communications* **67** (1992), no. 3 465–508. doi: 10.1016/0010-4655(92)90055-4.

[73] GEANT4 Collaboration, "Geant4—a simulation toolkit." *Nuclear Instruments and Methods in Physics Research Section A: Accelerators, Spectrometers, Detectors and Associated Equipment* **506** (2003), no. 3 250–303. doi: 10.1016/S0168-9002(03)01368-8.

[74] S. W. Herb, D. C. Hom, L. M. Lederman, J. C. Sens, H. D. Snyder, J. K. Yoh, J. A. Appel, B. C. Brown, C. N. Brown, W. R. Innes, K. Ueno, T. Yamanouchi, A. S. Ito, H. Jöstlein, D. M. Kaplan, and R. D. Kephart, "Observation of a dimuon resonance at 9.5 GeV in 400-GeV proton-nucleus collisions." *Phys. Rev. Lett.* **39**. doi: 10.1103/PhysRevLett.39.252.

[75] H. Harari, "A new quark model for hadrons." *Physics Letters B* **57** (July, 1975) 265–269. doi: 10.1016/0370-2693(75)90072-6.

[76] CDF Collaboration, "Observation of top quark production in $\overline{p}p$ collisions with the collider detector at fermilab." *Phys. Rev. Lett.* **74** (Apr, 1995) 2626–2631. doi: 10.1103/PhysRevLett.74.2626.

[77] D0 Collaboration, "Observation of the top quark." *Phys. Rev. Lett.* **74** (Apr, 1995) 2632–2637. doi: 10.1103/PhysRevLett.74.2632.

[78] A. de Gouvêa, D. Hernández, and T. M. P. Tait, "Criteria for natural hierarchies." *Phys. Rev. D* **89** (Jun, 2014) 115005. doi: 10.1103/PhysRevD.89.115005.

[79] G. Degrassi, S. Di Vita, J. Elias-Miró, J. Espinosa, G. F. Giudice, G. Isidori, and A. Strumia, "Higgs mass and vacuum stability in the standard model at NNLO." *Journal of High Energy Physics* **2012** (2012), no. 8 98. doi: 10.1007/JHEP08(2012)098.

[80] J. Haller, A. Hoecker, R. Kogler, K. Mönig, T. Peiffer, and J. Stelzer, "Update of the global electroweak fit and constraints on two-Higgs-doublet models." *Eur. Phys. J. C* **78** (2018), no. 8 675, [arXiv:1803.01853]. doi: 10.1140/epjc/s10052-018-6131-3.

[81] The ALEPH, DELPHI, L3, OPAL Collaborations, the LEP Electroweak Working Group Collaboration, "Electroweak Measurements in Electron-Positron Collisions at W-Boson-Pair Energies at LEP." *Phys. Rept.* **532** (2013) 119, [arXiv:1302.3415]. arXiv:1302.3415.

[82] A. Arbuzov, M. Awramik, M. Czakon, A. Freitas, M. Grünewald, K. Mönig, S. Riemann, and T. Riemann, "Zfitter: a semi-analytical program for fermion pair production in e+e− annihilation, from version 6.21 to version 6.42." *Computer Physics Communications* **174** (2006), no. 9 728–758. doi: 10.1016/j.cpc.2005.12.009.

[83] CMS Collaboration, "Review of top quark mass measurements in CMS." arXiv:2403.01313. doi: 10.48550/arXiv.2403.01313.

[84] D0 Collaboration, "Useful diagrams of top signals and backgrounds." accessed on September, 2024.

[85] CMS Collaboration, "A profile likelihood approach to measure the top quark mass in the lepton+jets channel at $\sqrt{s}$=13 TeV." tech. rep., CERN, Geneva, 2022. PAS: CMS-PAS-TOP-20-008.

[86] A. H. Hoang, "What is the top quark mass?." *Annual Review of Nuclear and Particle Science* **70** (2020), no. Volume 70, 2020 225–255. doi: 10.1146/annurev-nucl-101918-023530.

[87] ATLAS Collaboration, "A precise interpretation for the top quark mass parameter in ATLAS Monte Carlo simulation." tech. rep., CERN, Geneva, 2021. doi: ATL-PHYS-PUB-2021-034.

[88] CMS Collaboration, "Measurement of the $t\bar{t}$ production cross section, the top quark mass, and the strong coupling constant using dilepton events in pp collisions at $\sqrt{s}$=13 TeV." *The European Physical Journal C* **79** (2019), no. 5 368. doi: 10.1140/epjc/s10052-019-6863-8.

[89] S. Alioli, P. Fernandez, J. Fuster, A. Irles, S. Moch, P. Uwer, and M. Vos, "A new observable to measure the top-quark mass at hadron colliders." *The European Physical Journal C* **73** (2013), no. 5 2438. doi: 10.1140/epjc/s10052-013-2438-2.

[90] CMS Collaboration, "Measurement of the top quark pole mass using $\mathrm{t\bar{t}}$+jet events in the dilepton final state in proton-proton collisions at $\sqrt{s}$= 13 TeV." *Journal of High Energy Physics* **2023** (2023), no. 7 77. doi: 10.1007/JHEP07(2023)077.

[91] S. Dittmaier, P. Uwer, and S. Weinzierl, "Next-to-leading-order QCD corrections to $\mathrm{t\bar{t}}$ production at hadron colliders." *Phys. Rev. Lett.* **98** (Jun, 2007) 262002. doi: 10.1103/PhysRevLett.98.262002.

[92] T. Sjöstrand, S. Ask, J. R. Christiansen, R. Corke, N. Desai, P. Ilten, S. Mrenna, S. Prestel, C. O. Rasmussen, and P. Z. Skands, "An introduction to PYTHIA 8.2." *Computer Physics Communications* **191** (June, 2015) 159–177. doi: 10.1016/j.cpc.2015.01.024.

[93] G. Bevilacqua, H. B. Hartanto, M. Kraus, and M. Worek, "Off-shell top quarks with one jet at the LHC: a comprehensive analysis at NLO QCD." *Journal of High Energy Physics* **2016** (2016), no. 11. doi: 10.1007/jhep11(2016)098.

[94] S. Alioli, J. Fuster, M. V. Garzelli, A. Gavardi, A. Irles, D. Melini, S.-O. Moch, P. Uwer, and K. Voß, "Phenomenology of $\mathrm{t\bar{t}}$j+ x production at the LHC." *Journal of High Energy Physics* **2022** (2022), no. 5 146. doi: 10.1007/JHEP05(2022)146.

[95] LHC Study Group Collaboration, "The Large Hadron Collider: Conceptual design.". doi: CERN-AC-95-05-LHC.

[96] LHC, "Facts and figures about the LHC." accessed on September, 2024.

[97] ATLAS Collaboration, "The ATLAS Experiment at the CERN Large Hadron Collider." *JINST* **3** (2008) S08003. doi: 10.1088/1748-0221/3/08/S08003.

[98] LHCb Collaboration, S. Amato et al., "LHCb technical proposal: A Large Hadron Collider Beauty Experiment for Precision Measurements of CP Violation and Rare Decays.". doi: CERN-LHCC-98-04.

[99] ALICE Collaboration, K. Aamodt et al., "The ALICE experiment at the CERN LHC." *JINST* **3** (2008) S08002. doi: 10.1088/1748-0221/3/08/S08002.

[100] CMS Collaboration, "Public CMS luminosity information." Peak luminosity, accessed on November, 2024.

[101] CMS Collaboration, "Public CMS luminosity information." Cumulative luminosity, accessed on November, 2024.

[102] CMS Collaboration, "The CMS detector design." accessed on September, 2024.

[103] CMS Collaboration, "CMS tracker detector performance results." (2020). Public results.

[104] H. Kästli, M. Barbero, W. Erdmann, C. Hörmann, R. Horisberger, D. Kotlinski, and B. Meier, "Design and performance of the CMS pixel detector readout chip." *Nuclear Instruments and Methods in Physics Research* **565** (2006), no. 1 188–194. doi: 10.1016/j.nima.2006.05.038.

[105] CMS Collaboration, "CMS technical design report for the pixel detector upgrade.". doi: 10.2172/1151650.

[106] CMS Collaboration, "The CMS tracker: addendum to the Technical Design Report.". TDR: CMS-TDR-5-add-1.

[107] CMS Collaboration, "The Phase-2 Upgrade of the CMS Tracker." *Nuclear Instruments and Methods in Physics Research* (6, 2017). doi: 10.17181/CERN.QZ28.FLHW.

[108] CMS Collaboration, "Electron and photon reconstruction and identification with the CMS experiment at the CERN LHC." *Journal of Instrumentation* **16** (May, 2021) P05014. doi: 10.1088/1748-0221/16/05/p05014.

[109] CMS Collaboration, "The CMS ECAL performance with examples." *Journal of Instrumentation* **9** (feb, 2014) C02008. doi: 10.1088/1748-0221/9/02/C02008.

[110] CMS Collaboration, "The CMS Experiment at the CERN LHC." *JINST* **3** (2008) S08004. doi: 10.1088/1748-0221/3/08/S08004.

[111] CMS-HCAL Collaboration, "Design, performance, and calibration of CMS hadron-barrel calorimeter wedges." *The European Physical Journal C* **55** (2008), no. 1 159–171. doi: 10.1140/epjc/s10052-008-0573-y.

[112] CMS-HCAL Collaboration, "Design, performance, and calibration of CMS forward calorimeter wedges." *The European Physical Journal C* **53** (2008), no. 1 139–166. doi: 10.1140/epjc/s10052-007-0459-4.

[113] CMS Collaboration, "Upgrades of the CMS muon detectors: from Run 3 towards HL-LHC." *PoS* **EPS-HEP2019** (2020) 156. doi: 10.22323/1.364.0156.

[114] CMS Collaboration, "CMS. The TriDAS project. Technical design report, vol. 1: The trigger systems.". CERN-LHCC-2000-038.

[115] CMS Collaboration, "Particle-flow reconstruction and global event description with the CMS detector." *JINST* **12** (oct, 2017). doi: 10.1088/1748-0221/12/10/P10003.

[116] T. Mc Cauley, "Collisions recorded by the CMS detector on 14 Oct 2016 during the high pile-up fill." CMS Collection.

[117] CMS Collaboration, "Description and performance of track and primary-vertex reconstruction with the CMS tracker." *Journal of Instrumentation* **9** (oct, 2014) P10009. doi: 10.1088/1748-0221/9/10/P10009.

[118] CMS Collaboration, "Performance of the CMS muon detector and muon reconstruction with proton-proton collisions at $\sqrt{s}$ =13 TeV." *Journal of Instrumentation* **13** (June, 2018) P06015–P06015. doi: 10.1088/1748-0221/13/06/p06015.

[119] W. Adam, R. Frühwirth, A. Strandlie, and T. Todorov, "Reconstruction of electrons with the gaussian-sum filter in the CMS tracker at the LHC." *Journal of Physics G: Nuclear and Particle Physics* **31** (July, 2005) N9–N20. doi: 10.1088/0954-3899/31/9/n01.

[120] M. Cacciari, G. P. Salam, and G. Soyez, "The anti-ktjet clustering algorithm." *Journal of High Energy Physics* **2008** (Apr., 2008) 063–063. doi: 10.1088/1126-6708/2008/04/063.

[121] CMS Collaboration, "Pileup Removal Algorithms." tech. rep., CERN, Geneva, 2014. PAS: CMS-PAS-JME-14-001.

[122] CMS Collaboration, "Performance of missing transverse momentum reconstruction in proton-proton collisions at $\sqrt{s}$ = 13 TeV using the CMS detector." *Journal of Instrumentation* **14** (jul, 2019) P07004. doi:10.1088/1748-0221/14/07/P07004.

[123] CMS Collaboration, "Identification of heavy-flavour jets with the CMS detector in pp collisions at 13 TeV." *Journal of Instrumentation* **13** (may, 2018) P05011. doi: 10.1088/1748-0221/13/05/P05011.

[124] E. Bols, J. Kieseler, M. Verzetti, M. Stoye, and A. Stakia, "Jet flavour classification using deepjet." *Journal of Instrumentation* **15** (dec, 2020) P12012. doi: 10.1088/1748-0221/15/12/P12012.

[125] CMS Collaboration, "How CMS weeds out particles that pile up.". CMS news.

[126] N. Wermes and H. Kolanoski, *Particle Detectors*. Springer, Heidelberg (2016). Book.

[127] H. Spieler, *Semiconductor Detector Systems*. Oxford University Press (08, 2005). doi: 10.1093/acprof:oso/9780198527848.001.0001.

[128] G. Lutz, *Semiconductor Radiation Detectors: Device Physics*. Springer, New York (1999). Book.

[129] F. Hartmann, *Evolution of Silicon Sensor Technology in Particle Physics*, vol. 275 of *Springer Tracts in Modern Physics*. Springer (2017). Book.

[130] H. Kolanoski and N. Wermes, *Particle detectors: fundamental and applications*. Oxford University Press (2020). Book.

[131] M. Miglierini, *Detectors of Radiation*. Reactor Physics Experiments Journal (2004). Book.

[132] T. Duffar, *Encyclopedia of Materials: Science and Technology*. Elsevier, Oxford (2001). doi: 10.1016/B0-08-043152-6/00343-0.

[133] P. Schütze, *Silicon Pixel Detectors - Performance after Irradiation and Application in Three-dimensional Imaging*, dissertation, Universität Hamburg, Hamburg (2019). Dissertation, Universität Hamburg, 2019.

[134] W. Shockley, "Currents to Conductors Induced by a Moving Point Charge." *Journal of Applied Physics* **9** (10, 1938) 635–636. doi: 10.1063/1.1710367.

[135] S. Ramo, "Currents induced by electron motion." *Proceedings of the IRE* **27** (1939), no. 9 584–585. doi: 10.1109/JRPROC.1939.228757.

[136] M. Moll, *Radiation damage in silicon particle detectors: Microscopic defects and macroscopic properties*, Ph.D. thesis, Hamburg U. (1999). Moll Thesis.

[137] A. Junkes, *Influence of radiation induced defect clusters on silicon particle detectors*, Ph.D. thesis, Hamburg U. (2011). Junkes Thesis.

[138] R. Turchetta, "Spatial resolution of silicon microstrip detectors." *Nuclear Instruments and Methods in Physics Research Section A: Accelerators, Spectrometers, Detectors and Associated Equipment* **335** (1993), no. 1 44–58. doi: 10.1016/0168-9002(93)90255-G.

[139] R. Mankel, "Pattern recognition and event reconstruction in particle physics experiments." *Reports on Progress in Physics* **67** (mar, 2004) 553. doi: 10.1088/0034-4885/67/4/R03.

[140] G. Apollinari, O. Brüning, T. Nakamoto, and L. Rossi, "High luminosity large hadron collider HL-LHC." (2015). doi: 10.5170/CERN-2015-005.1.

[141] CMS Collaboration, "The Phase-2 Upgrade of the CMS Barrel Calorimeters." tech. rep., CERN, Geneva, 2017. CMS-TDR-015.

[142] CMS Collaboration, "The Phase-2 Upgrade of the CMS Endcap Calorimeter." tech. rep., CERN, Geneva, 2017. doi: 10.17181/CERN.IV8M.1JY2.

[143] CMS Collaboration, "A MIP Timing Detector for the CMS Phase-2 Upgrade." tech. rep., CERN, Geneva, 2019. CMS-TDR-020.

[144] Y. Otarid, *Pixel-Strip Modules for the CMS Tracker Phase-2 Upgrade*, Ph.D. thesis, Universitt Hamburg (2023). Otarid Thesis.

[145] A. Mussgiller. private communication (2024).

[146] N. Hinton. private communication (2023).

[147] M. Guthoff, A. Mussgiller, and O. Reichelt, "Specifications for the production of support structures for silicon detector modules for the upgrade of the CMS tracker." (February, 2023).

[148] CMS Collaboration, "The tracker End-Cap Double Disks (TEDD) of the CMS Phase 2 Outer Tracker." (October, 2021).

[149] Huber, *Unistat Pilot One Operation Manual*, April, 2022. Huber manual.

[150] 3M, *3M Novec 7200 Engineered Fluid*. NOVEC 7200.

[151] ggmgastro, *Tiefkühlschrank specifications*. TKSG568N.

[152] AAVID, *HI-CONTACT 6-PASS COLD PLATE*. Cold plate.

[153] OMEGA, *Analog Temperature sensor OMEGA SA1-RTD*. SA1-RTD.

[154] Digikey, *Digital Temperature sensor DS18B20+*. DS18B20.

[155] VAISALA, *Dew Point Transmitters DMT143*. DMT143.

[156] T. Rizzo, "Thermal chamber controller for burn-in system of cms silicon modules." (2017). Report BIBC.

[157] CAEN, *LV Modules A2519C*. HV supply module.

[158] CAEN, *HV Modules A7435DN*. LV supply module.

[159] CAEN, *Multichannel Power Supply System SY5527*. Multichannel Power Supply System.

[160] HENSEL, *HENSEL box Mi 0100*. Hensel box.

[161] M. Pesaresi, M. B. Marin, G. Hall, M. Hansen, G. Iles, A. Rose, F. Vasey, and P. Vichoudis, "The FC7 AMC for generic DAQ & control applications in CMS." *Journal of Instrumentation* **10** (mar, 2015) C03036. doi: 10.1088/1748-0221/10/03/C03036.

[162] PCIMG, *The AMC standard*. AMC.

[163] PCIMG, *The μTCA standard*. uTCA.

[164] AMD Xilinx, *Kintex-7 FPGA*. FPGA.

[165] ANSI/VITA, *57.1-2008 FPGA mezzanine card*. FMC.

[166] K. Biery, E. Flumerfelt, A. Lyon, R. Rechenmacher, R. Rivera, M. Rominsky, L. Uplegger, and M. Votava, "The Fermilab Test Beam Facility Data Acquisition System Based on otsdaq." (2018). doi: 10.48550/arXiv.1806.07240.

[167] F. Faccio, S. Michelis, G. Blanchot, G. Ripamonti, and A. Cristiano, "The bPOL12V DCDC converter for HL-LHC trackers: towards production readiness." in *TWEPP 2019*, p. 070, 03, 2020. doi: 10.22323/1.370.0070.

[168] CEBEA Bochnia, *User's Manual for MARTA: Monoblock Approach for a Refrigeration Technical Application. A guide to operating the CO2 Cooling Unit*.

[169] A. Colijn and B. Verlaat, "Evaporative CO2 heat transfer measurements for cooling systems of particle physics detectors." *Journal of Physical Chemistry C - J PHYS CHEM C* (01, 2010). Paper.

[170] Multicomp PRO, *Silicone Thermal Interface Pads*. Pad.

[171] CMS Collaboration, "Alignment of the CMS tracker with LHC and cosmic ray data." *Journal of Instrumentation* **9** (jun, 2014) P06009. doi: 10.1088/1748-0221/9/06/P06009.

[172] CMS Collaboration, "The CMS Phase-1 pixel detector upgrade." *Journal of Instrumentation* **16** (feb, 2021) P02027. doi: 10.1088/1748-0221/16/02/P02027.

[173] CMS Collaboration, "Strategies and performance of the CMS silicon tracker alignment during LHC Run 2." *Nuclear Instruments and Methods in Physics Research* **1037** (2022) 166795. doi: 10.1016/j.nima.2022.166795.

[174] N. Bartosik, *Associated top-quark-pair and b-jet production in the dilepton channel at $\sqrt{s}$ = 8 TeV as test of QCD and background to tt+Higgs production*, dr., Universität Hamburg, Hamburg (2015). Universität Hamburg, Diss., 2015.

[175] V. Blobel and C. Kleinwort, "A new method for the high-precision alignment of track detectors." (2002). doi: 10.48550/arXiv.hep-ex/0208021.

[176] V. Blobel, "Software alignment for tracking detectors." *Nuclear Instruments and Methods in Physics Research Section A: Accelerators, Spectrometers, Detectors and Associated Equipment* **566** (2006), no. 1 5–13. TIME 2005.

[177] V. Karimäki, T. Lampen, and F.-P. Schilling, "The HIP Algorithm for Track Based Alignment and its Application to the CMS Pixel Detector." tech. rep., CERN, Geneva, 2006. Note: CERN-CMS-NOTE-2006-018.

[178] CMS Collaboration, "Pixel Detector Performance in Run 3.". DP: CMS-DP-2022-067.

[179] CMS Collaboration, "Strategies and performance of the CMS silicon tracker alignment during LHC Run 2." *Nuclear Instruments and Methods in Physics Research Section A: Accelerators, Spectrometers, Detectors and Associated Equipment* **1037** (2022) 166795. doi: 10.1016/j.nima.2022.166795.

[180] A. V. Barroso, "Tracker alignment in CMS: interplay with pixel local reconstruction." (2023). doi: 10.48550/arXiv.2303.16642.

[181] ATLAS Collaboration, "Measurement of the top-quark mass in $t\bar{t}$+ 1-jet events collected with the atlas detector in pp collisions at $\sqrt{s}$ = 8 TeV." *Journal of High Energy Physics* **2019** (2019), no. 11 150. doi: 10.1007/JHEP11(2019)150.

[182] CMS Collaboration, CMS, "Simulation of the Silicon Strip Tracker pre-amplifier in early 2016 data.". CMS-DP-2020-045.

[183] S. Frixione, P. Nason, and C. Oleari, "Matching NLO QCD computations with parton shower simulations: the POWHEG method." *Journal of High Energy Physics* **2007** (nov, 2007) 070. doi: 10.1088/1126-6708/2007/11/070.

[184] R. D. Ball, V. Bertone, S. Carrazza, L. D. Debbio, S. Forte, P. Groth-Merrild, A. Guffanti, N. P. Hartland, Z. Kassabov, J. Latorre, E. R. Nocera, J. Rojo, L. Rottoli, E. Slade, and M. Ubiali, "Parton distributions from high-precision collider data." *The European Physical Journal C* **77** (2017), no. 10 663. doi: 10.1140/epjc/s10052-017-5199-5.

[185] M. Czakon and A. Mitov, "Top++: A program for the calculation of the top-pair cross-section at hadron colliders." *Computer Physics Communications* **185** (2014), no. 11 2930–2938. doi: 10.1016/j.cpc.2014.06.021.

[186] Y. Li and F. Petriello, "Combining QCD and electroweak corrections to dilepton production in the framework of the FEWZ simulation code." *Phys. Rev. D* **86** (Nov, 2012) 094034. doi: 10.1103/PhysRevD.86.094034.

[187] N. Kidonakis, "Two-loop soft anomalous dimensions for single top quark associated production with a W^- or H^-." *Phys. Rev. D* **82** (Sep, 2010) 054018. doi: 10.1103/PhysRevD.82.054018.

[188] J. M. Campbell, R. K. Ellis, and C. Williams, "Vector boson pair production at the LHC." *Journal of High Energy Physics* **2011** (2011), no. 7 18. doi: 10.1007/JHEP07(2011)018.

[189] CMS Collaboration, "Performance of electron and photon reconstruction in Run 2 with the CMS experiment." tech. rep., CERN, Geneva, 2020. DP: CMS-DP-2020-037.

[190] CMS Collaboration, "Jet algorithms performance in 13 TeV data." tech. rep., CERN, Geneva, 2017. PAS: CMS-PAS-JME-16-003.

[191] CMS Collaboration, "Public CMS luminosity information." Interactions per crossing, accessed on November, 2024.

[192] CMS Collaboration, "First measurement of the top quark pair production cross section in proton-proton collisions at $\sqrt{s}$= 13.6 TeV." *Journal of High Energy Physics* **2023** (2023), no. 8 204. doi: 10.1007/JHEP08(2023)204.

[193] CMS Collaboration, "Measurement of the differential cross section for top quark pair production in pp collisions at $\sqrt{s} = 8$ TeV." *The European Physical Journal C* **75** (2015), no. 11 542. doi: 10.1140/epjc/s10052-015-3709-x.

[194] Schmitt, Stefan, "Data unfolding methods in high energy physics." *EPJ Web Conf.* **137** (2017) 11008. doi: 10.1051/epjconf/201713711008.

[195] G. H. Golub and C. F. V. Loan, *Matrix Computations*. Johns Hopkins University Press, Baltimore (2013). Book.

[196] Spanò, Francesco, "Unfolding in particle physics: a window on solving inverse problems." *EPJ Web of Conferences* **55** (2013) 03002. doi: 10.1051/epjconf/20135503002.

[197] J. S. Conway, "Incorporating Nuisance Parameters in Likelihoods for Multisource Spectra." in *PHYSTAT 2011*, pp. 115–120, 2011. doi: 10.5170/CERN-2011-006.115.

[198] CMS Collaboration, "The CMS statistical analysis and combination tool: COMBINE." (2024). doi: 10.48550/arXiv.2404.06614.

[199] L. Moneta, K. Cranmer, G. Schott, and W. VERKERKE, "The RooStats project." *PoS* **ACAT2010** (2011). doi: 10.22323/1.093.0057.

[200] CMS Collaboration, "CMS luminosity measurement for the 2017 data-taking period at $\sqrt{s} = 13$ TeV." tech. rep., CERN, Geneva, 2018. PAS: CMS-PAS-LUM-17-004.

[201] CMS Collaboration, "Measurements of inclusive W and Z cross sections in pp collisions at $\sqrt{s} = 7$ TeV." *Journal of High Energy Physics* **2011** (2011), no. 1. doi: 10.1007/jhep01(2011)080.

[202] CMS Collaboration, "Jet energy scale and resolution in the CMS experiment in pp collisions at 8 TeV." *Journal of Instrumentation* **12** (feb, 2017) P02014. doi: 10.1088/1748-0221/12/02/P02014.

[203] CMS Collaboration, "Performance of the CMS Level-1 trigger in proton-proton collisions at $\sqrt{s} = 13$ TeV." *Journal of Instrumentation* **15** (oct, 2020) P10017. doi: 10.1088/1748-0221/15/10/P10017.

[204] CMS Collaboration, "Performance of the CMS muon trigger system in proton-proton collisions at $\sqrt{s} = 13$ TeV." *Journal of Instrumentation* **16** (jul, 2021) P07001. doi: 10.1088/1748-0221/16/07/P07001.

[205] M. G. Bowler, "e^+e production of heavy quarks in the string model." *Zeitschrift für Physik C Particles and Fields* **11** (1981), no. 2 169–174. doi: 10.1007/BF01574001.

[206] S. Argyropoulos and T. Sjöstrand, "Effects of color reconnection on $t\bar{t}$ final states at the LHC." *Journal of High Energy Physics* **2014** (2014), no. 11 43. doi: 10.1007/JHEP11(2014)043.

[207] J. R. Christiansen and P. Z. Skands, "String formation beyond leading colour." *Journal of High Energy Physics* **2015** (2015), no. 8 3. doi: 10.1007/JHEP08(2015)003.

[208] R. J. Barlow and C. Beeston, "Fitting using finite Monte Carlo samples." *Comput. Phys. Commun.* **77** (1993) 219–228. doi: 10.1016/0010-4655(93)90005-W.

[209] S. Alioli, S.-O. Moch, and P. Uwer, "Hadronic top-quark pair-production with one jet and parton showering." *Journal of High Energy Physics* **2012** (2012), no. 1 137. doi: 10.1007/JHEP01(2012)137.

[210] S. Alekhin, J. Blümlein, and S. Moch, "NLO PDFs from the ABMP16 fit." *The European Physical Journal C* **78** (2018), no. 6 477. doi: 10.1140/epjc/s10052-018-5947-1.

[211] T.-J. Hou, K. Xie, J. Gao, S. Dulat, M. Guzzi, T. J. Hobbs, J. Huston, P. Nadolsky, J. Pumplin, C. Schmidt, I. Sitiwaldi, D. Stump, and C. P. Yuan, "Progress in the CTEQ-TEA NNLO global QCD analysis." (2019). doi: 10.48550/arXiv.1908.11394.

[212] G. Bevilacqua, H. B. Hartanto, M. Kraus, and M. Worek, "Off-shell top quarks with one jet at the LHC: a comprehensive analysis at NLO QCD." *Journal of High Energy Physics* **2016** (2016), no. 11. doi: 10.1007/jhep11(2016)098.

[213] F. James and M. Roos, "Minuit - a system for function minimization and analysis of the parameter errors and correlations." *Computer Physics Communications* **10** (1975), no. 6 343–367. doi: 10.1016/0010-4655(75)90039-9.

Acknowledgements

I extend my sincere gratitude to my supervisor, Katerina Lipka, for her guidance and expertise during my doctoral research. Even during the busiest periods, she made time to discuss my analysis, address my numerous questions, and provide feedback that was vital in shaping this work. I deeply appreciate her encouragement of my professional development and her guidance throughout this journey. Her meticulous proofreading significantly enhanced the quality of this thesis. I am also profoundly grateful for her understanding and support during challenging personal times that arose during my PhD. Although these challenges were unrelated to the work itself, her kindness and empathy were an enormous help.

I would also like to express my gratitude to my second supervisor, Paul Schütze, for his contributions to this work. I deeply appreciate the time spent reading my thesis and providing valuable feedback. His constructive comments helped guide the development of this work and improve its quality.

I would like to sincerely thank my PhD committee for their time and valuable input during my submission and my defense. Their thoughtful questions and discussions provided important insights that helped strengthen my work. I am especially grateful to Prof. Sven-Olaf Moch, who carefully read and evaluated my thesis. His detailed feedback and constructive criticism were instrumental in refining my thesis, and I truly appreciate his effort and dedication.

I would like to express my sincere thanks to Patrick Connor, Sandra Consuegra and Henriette Peterson for their mentorship and support throughout my work on tracker alignment. Their guidance and expertise in this area have been invaluable, and I am grateful for the opportunity to contribute to this project.

I am deeply grateful to the Tracker Group, particularly for their support during the development of the Burn-in system and the measurements performed. I spent many hours in the lab and engaged in meetings with the team, navigating through various challenges. Their collaboration and dedication played a significant role in my learning experience, and I am thankful for the opportunity to work with such a skilled and committed group. I would especially like to thank Younes and Ginger, who welcomed me into the group and made me feel part of this family; Reimer, for his constant help with any questions I had regarding the chiller, pipes, and mechanical structures; Anastasiia, for her assistance with all the MARTA measurements, her insightful discussions in the lab, and her patience with me; and Moritz, for guiding me whenever I was lost or stuck.

I would also like to extend my sincere thanks to the Top Group. The guidance and support from both senior members and colleagues during group meetings were priceless. Whenever I encountered a problem with the analysis or faced difficulties in understanding certain aspects, they were always more than willing to help. Whether sitting down with me to troubleshoot issues or offering suggestions for improvement and alternative approaches, their continuous support was critical to my progress and growth throughout the project.

Special thanks to Maria, Roman and Olaf for their consistent support and for always inquiring not only about my analysis but also my well-being.

I would also like to express my thanks to the HGF group, they were always willing to offer their expertise, provide suggestions, and discuss new ideas, helping me refine my work and expand my understanding of the broader context of my thesis.

Thanks to Anna and Birgit for always being ready to help with a smile. Bureaucracy felt less scary thanks to you.

To my office mates over the years, starting with Josry, Toni, Xiaomin, David, and Finn, thanks for creating an environment that made the office a place I always looked forward to going. Special thanks to Sebastian, who was instrumental in helping me with my analysis, offering countless hours of discussion and support. Beyond work, I truly appreciated our time together outside the office, whether going for dinner or drinks. I cannot thank Jiwon enough, having someone to vent to, share frustrations with, and rely on for constant support made all the difference. Thank you for always being there, and willing to help me no matter the situation.

I want to thank all the CMS PhD and ECR community including Valentina, Alberto, Daniil, Mikel, Iakov, Konstantin, Aliya, Alessia, Federico, Jeremy, Laurids, Dominic, Keila, Daina, Lakshmi, Maryam, Gabri, Benno, Andre, Aenne, Mykyta, Andrea, Soham, Lovisa, Hugo, Malinda, Matin, Jacopo, Stephan, Sara, Di, Qun and more for making lunches and coffees more enjoyable and for always be there to talk to, to share a smile or hug or simply sit in silence together, you became my friends.

Special thanks to Beatriz, Federica and Valerie, my first friends here in Hamburg, they adopted me during a really hard time and we became besties, Hamburg is not the same without you girls, I miss you and I love you!

My crew, Moritz, Nico, Lucia, Nayla and Matthias thanks for existing, I love you guys thanks a lot for all the support and for the fun times very much needed through this last period of my thesis. Muchas gracias!

To Carlos, Yahya, Thea, Adri, Bianca, Lukas, Michele and Charles: Thank you for the endless hours talking about life, about the future and fixing the world, it was therapeutic and helped me go through this 4 years.

Thanks to all my friends around the world. To those who were already in my life before I started the PhD and to those who appeared during this period. Many friends from El Prat, from University, the friends I met at CERN and in Geneva, the friends I met in Hamburg and my football team Altona93, the Kreisliga meister!

Special thanks to all the people who made me the researcher I am today, starting with my high school teacher Emilio, the first professor who believed in me in University Ricardo

and Michael Moll who made me a researcher. Thanks to the SSD group where I found a second family, thanks Yana, Marcos, Isidre, Julio, Pedro and many more.

I want to thank my therapist, Irene. Without her, I couldn't have made it. She guided me through really dark periods, and her support was crucial in helping me navigate depression and anxiety.

My friends from far away: Emma ens coneixem des que tenim tres anys i el que ens queda, sempre, t'estimo. Sara, no me puedo imaginar llegar hasta aquí sin ti, esos "días de estudio" han dado sus frutos, te quiero mucho. Irene esta era nuestra década y vaya si lo está siendo, te quiero mucho. Lucia, gracias por siempre creer en mí, te quiero mucho. Marta que bonito era Ginebra cuando estábamos todas juntas, gracias por tu fe inquebrantable en mí, te quiero mucho. A todas gracias gracias gracias por siempre estar aquí conmigo, por apoyarme desde la distancia como si estuvieseis aquí, por siempre tener palabras de ánimos y por supuesto por haberme visitado aquí en Hamburgo, os quiero muchísimo.

Carmen no tengo palabras, las hemos pasado de todos colores, pero hemos sobrevivido creo que estoy tan orgullosa de ti como lo estás tú de mí, y que bonito vernos consiguiendo lo que queríamos juntas. Gracias por estar aquí siempre.

Andrea incondicional, parece que llevemos toda una vida juntas. Las veces que hemos llorado juntas y hemos acabado descojonándonos. Viviendo nuestras vidas paralelas, te quiero siempre a mi lado y sé que lo estarás siempre. ¡Te quiero muchísimo, gracias por existir!

Evan, thank you so much for everything, from advising me against pursuing a PhD to celebrating my submission with me. You've been an amazing colleague, always willing to help with the technical aspects of my thesis. You taught me how to be diplomatic in emails and meetings, and you even helped me refine my already perfect English. Most importantly, you were the best partner anyone could ask for during the challenges of a PhD journey. You were there when I was super excited because something finally worked and when I was devastated because nothing was going right. Whether I came home smiling with pride or crying because I felt I was not good enough, you were always there with a hug, a kind word, or a pat on the shoulder. I know it wasn't easy to deal with me during this time, so thank you for staying by my side. T'estimo!

Gracias por todo a mi Abuela que siempre estuvo poniendo velitas para que aprobase todos los exámenes y sé que me ha puesto una vela para que acabe esta tesis, a mi abuelo que me ha enseñado lo que es la palabra resiliencia y ahí está el campeón reinventándose y recibiéndome con el abrazo más grande de todos cada vez que me ve. A mis tíos y primos que sé que están orgullosísimos de mí y siento su apoyo constante. A mis padres, Juan y Pili, he llegado hasta aquí gracias a vosotros. Siempre me dijisteis: si quieres puedes y aquí estoy pudiendo y acabando mi doctorado. Soy la persona que soy por todos los

valores que me habéis inculcado y me llena de orgullo decir que soy vuestra hija y que tengo a los mejores padres del mundo, os quiero muchísimo. ¡Paula tu también tienes mucha culpa de este éxito, a pesar de estar tan lejos te siento cerca, gracias por el apoyo incondicional y por hacerme mejor persona, te quiero mucho!

Doing a PhD is a huge endeavor, and one person alone cannot accomplish it. This thesis is a result of the support and contributions from every single person in my life. I am deeply grateful to all who helped me throughout this journey.

Thank you all!